Synthesis of 1D microgel strands and their motion analysis in solution

Dissertation zur Erlangung des akademischen Grades "doctor rerum naturalium" (Dr. rer. nat.) an der Mathematisch-Naturwissenschaftlichen Fakultät der Universität Potsdam

vorgelegt von

Diplom-Chemiker

Marco Philipp Hermann Schürings

Published online at the
Institutional Repository of the University of Potsdam:
https://doi.org/10.25932/publishup-43953
https://nbn-resolving.org/urn:nbn:de:kobv:517-opus4-439532

Die vorliegende Arbeit wurde unter Betreuung von Herrn Prof. Dr. Alexander Böker in der Zeit von Oktober 2010 bis Oktober 2015 am Lehrstuhl für Makromolekulare Materialien und Oberflächen an der RWTH Aachen durchgeführt.

Eidesstattliche Erklärung

Hiermit erkläre ich, dass die vorgelegte Dissertation von mir selbständig und ohne unzulässige Hilfe verfasst wurde. Ferner wurde keine anderen als die von mir angegebenen Quellen und Hilfsmittel verwendet.
Zudem versichere ich, dass diese Arbeit in der vorgelegten oder einer ähnlichen Fassung noch nicht zu einem früheren Zeitpunkt an einer anderen in- oder ausländischen Hochschule als Dissertation eingereicht worden ist.

Tag der Disputation: 25.11.2019

Gutachter:

1. Universitätsprofessor Dr. rer. nat. Alexander Böker (Universität Potsdam)
2. Universitätsprofessor Dr. rer. nat. Andrij Pich (RWTH Aachen)
3. Universitätsprofessor Dr. rer. nat. Thomas Hellweg (Universität Bielefeld)

Meinen Eltern, meiner Schwester und meinen Fürsprechern

Danksagung

Einen besonderen Dank möchte ich an meinem Doktorvater Prof. Dr. Alexander Böker für die ausgezeichnete und institutsübergreifende Betreuung meiner Dissertation richten. Für den fachlichen Austausch in vielen anregenden und konstruktiven Gesprächen sowie für das entgegengebrachte Vertrauen bedanke ich mich sehr. Zudem möchte ich mich bei allen bedanken, die mich bei der Fertigstellung der vorliegenden Arbeit unterstützt haben.

Prof. Dr. Andrij Pich an der RWTH Aachen möchte ich für seine Unterstützung im Bereich der Mikrogelsynthese und die Möglichkeit bedanken mit seinem Team zusammenzuarbeiten. Außerdem danke ich ihm für seine Bereitschaft, als Zweitgutachter zu fungieren.
Bei Prof. Dr. Thomas Hellweg von der Universität Bielefeld möchte ich mich sehr für die Übernahme des Drittgutachtens bedanken.

Ich bedanke mich auch bei meinen weiteren Kooperationspartnern Dominic Schmitz und Dominik Kehren für die gute Zusammenarbeit bei der Synthese funktionaler Kolloide. Ich danke Prof. Dr. Dominik Wöll, Prof. Dr. Gero von Plessen, Dr. Bing Liu und Oleksii Nevskyi für ihre Unterstützung bei Charakterisierung der Bewegungseigenschaften anisotroper Mikrogelstränge.
Bei Prof. Dr. Bart Jan Ravoo und Jenny Krings von der Uni Münster möchte ich mich für die Kooperation im Bereich der Wirt-Gast-Systeme bedanken.
Für die Charakterisierung des Adsorptionsverhaltens von Mikrogelen möchte ich mich beim Team von Prof. Dr. Regine von Klitzing bedanken.

Ich danke meinen ehemaligen Studenten und Bürokollegen für die gute Zusammenarbeit und gesellige Zeit. Für den motivierenden Ansporn in vielen fachlichen und persönlichen Kollaborationen gilt ein besonderer Dank an Dr. Patrick Wünnemann und Prof. Dr. Christian Pester.
Mein großer Dank gilt schließlich meiner Familie für die Unterstützung jeglicher Art während meiner gesamten Promotionszeit.

Zusammenfassung der Dissertation: Synthesis of 1D microgel strands and their motion analysis in solution von Marco Philipp Schürings vorgelegt an der Mathematisch-Naturwissenschaftlichen Fakultät der Universität Potsdam

In dieser Arbeit wurde die Herstellung von Nanostrukturen aus stimuli-responsiven Mikrogelen gezeigt. Mikrogele sind bekannt dafür auf verschiedene Reize aus der Umgebung reagieren zu können, so werden sie z.B. in der Industrie seit langem als Superabsorber eingesetzt. Da diese Mikrogele über eine Volumenäderung auf den externen Reiz reagieren, kann so eine gezielte mechanische Antwort erreicht werden. Durch eine sorgfältige Auswahl der Polymermatrix ist es möglich die Mikrogele so zu gestalten, dass sie präzise auf die gesetzten Stimuli reagieren (z.B. Wirkstoffabgabe über pH- und Temperaturänderungen oder selektive Kontraktionen durch Zufuhr von elektrischem Strom[125]).

In dieser Arbeit wurde das Ziel verfolgt, flexible Nanofilamente zu schaffen, die ähnlich wie Muskelfilamente zu schnellen anisotropen Kontraktionen fähig sind. Für die Herstellung solcher Stränge wurden nanostrukturierte Template (PDMS-Wrinkles) verwendet, da diese einfach und kostengünstig herzustellen und in ihren Abmessungen vielseitig skalierbar sind. Darüber hinaus ist die Strukturbildung via Wrinkles ein bekanntes lithographiefreies Verfahren, das die Herstellung von Nanostrukturen in reproduzierbarer Weise und mit hoher Fernordnung auf Nanoskala ermöglicht.

In Kapitel 2.1 wurde erstmals gezeigt, dass Mikrogele als weiche bzw. schwammartige Materialien zu dicht gepackten Mikrogelarrays mit einstellbaren lateralen Dimensionen ausgerichtet werden können. Obwohl die Mikrogele bei der Anordnung auf ebene Oberflächen unterschiedliche Verformbarkeiten zeigten, behielten sie ihre Thermoresponsivität und ihr Quellverhalten bei.

Zur Herstellung von Mikrogelsträngen wurde eine interpartikuläre Konnektivität angestrebt. In Kapitel 2.2 wurde dies durch verschiedene Vernetzungsmethoden (d.h. Vernetzung durch UV-Bestrahlung und Wirt-Gast-Komplexierung) erreicht. Mit VCL/AAEM-Mikrogelen ist es möglich stabile, eindimensionale Mikrogelstränge herzustellen und zur weiteren Analyse in Wasser zu redispergieren. In diesem Kapitel wurde gezeigt, dass eindimensionale Partikelanordnungen in der Zickzackformation im Gegensatz zu Anordnungen in einer Perlenkettenstruktur oder zweidimensionaler Bandstruktur den besten Kompromiss in Bezug auf die Stabilität der Mikrogelstränge in Lösung bei gleichzeitigem Erhalt einer ausreichenden Flexibilität darstellt.

In Kapitel 2.3 wurden für die Bewegungsanalysen Mikrogelstränge in Zickzackformation verwendet. Zusammenfassend lässt sich sagen, dass die Flexibilität der Mikrogelstränge eher mit der mechanischen Biegefähigkeit eines halbflexiblen Kabels als mit dem eines Fadens vergleichbar ist. Die hier untersuchten Stränge bestehen aus Dutzenden oder sogar Hunderten von diskreten Einzelpartikeln, die durch Vernetzung miteinander verbunden sind und für die es in der Nanotechnologie nur wenige Parallelen gibt.

Wie hier dargestellt, ermöglichen die diversen Anordnungsmethoden eine vielseitige Mikrogelarchitektur (z.B. Mikrogelnetze, Doppel- und Dreifachstränge). In Zukunft könnte man komplexere Template (z.B. keramische Rhomben und sternförmige Wrinkles) verwenden, um die Möglichkeiten der nanoskaligen Mikrogelanordnungen zu erweitern und deren Seitenverhältnisse präzise zu steuern (z.B. zur Herstellung von homogenen Mikrogelstäbchen).

Contents

List of abbreviations

AAEM	Acetoacetoxyethyl methacrylate
AFM	Atomic force microscopy
AMPA	2,2´-azobis(2-methylpropyonamidine) dihydrochloride
AuNP	Gold nanoparticles
AuNR	Gold nanorods
BIS	N,N´-methylenebis(acrylamide)
CD	Cyclodextrine
CTAB	Cetyltrimethylammoniumbromide
DMF	Dimethylformamide
DMSO	Dimethylsulfoxide
EtOH	Ethanol
GISAXS	Grazing-incidence small-angle scattering
MWCO	Molecular weight cut-off
NIPAAm	N-Isopropylacrylamide
PDI	Polydispersity index
PDMS	Polydimethylsiloxane
R_H	Hydrodynamic radius
RhB	Rhodamine B
TEM	Transmission electron microscopy
VCL	N-vinylcaprolactam
VPTT	Volume phase transition temperature

1 Motivation and Objectives

1.1 Aim

The development of flexible one-dimensional nanostructures is an important step towards the design of responsive and adaptive materials such as artificial muscles, flexible sensors and rollable screens. Ageing society could benefit from robots being not only intelligent in terms of recognizing one's needs but also in adapting upon contact their grip strength, temperature, softness.[1] Implants degrading according to the degree of recovery or adapting to a child's growth are scenarios not far in the future. Increasing digitalization breathes life into formerly analogous objects and augments their properties, e.g. illuminated walls changing their degree of transparency, cleaning robots recognizing their environment.

With the evolution of artificial intelligence and its growing involvement in everyday life, it will become increasingly important to enable a transfer and integration of its abilities into equally smart materials. Therefore, these materials have to be adaptive towards the outer environment, moveable and flexible. Similar to the silicon chip providing the computing power for the artificial intelligence to act, the abilities of these smart materials on a macroscopic scale need the support on the micro- or nano-dimension. Thus, being able to design complex nanostructures in a controlled manner is a crucial first step towards the fabrication of macroscopic smart materials.

In this work the construction of one-dimensional nanostructures based on stimuli-responsive microgels is discussed. Microgels are colloidal cross-linked polymer particles able to swell in the respective solvent they are dispersed in. They were chosen as they provide a broad platform for the integration of various stimuli. Upon choosing polymers such as polyacrylic acid, responsiveness towards pH is acquired, NIPAAm and VCL are known materials changing their solubility in water according to temperature which leads to a swelling or shrinking of the respective microgels. By combination, e.g. copolymerization, multiple stimuli can be incorporated into one microgel. Furthermore, the advantage of

microgels lies in the fact that their velocity to react upon a stimulus is high due to their small size. This is an important factor for the later macroscopic material to adapt/respond rapidly to environmental changes. The material's properties such as rigidity, or affinity to certain surfaces can be adjusted by a proper choice of the polymeric matrix as well.

By connecting single microgels, flexible 1D nanostrands can be obtained. However, to gain control over these nanostrands, additional tools are needed, which will be discussed later. In this work, order is imposed upon the nanostrands by using wrinkled templates for a guided assembly.

This thesis is structured as follows. In the first chapter, the microgels used herein are described in detail as well as routes to structure a surface on the nanoscale in a controlled manner. Furthermore, methods known to this date to generate 1D nanostrands are shown.

The results of this work are presented in the second chapter. First, the interaction of microgels with the wrinkled templates is described and several methods are presented how to align the microgels to different structures with the help of the wrinkles.

In the following subchapter these aligned microgels are connected to 1D strands. The cross-linking methods needed therefore are discussed in detail.

Last, the obtained microgel strands from subchapter 2.2 were detached from their support and their behavior in solution was studied. The characterization of the flexible and moveable 1D nanostrands in solution is described in subchapter 2.3.

In Chapter 4 and 5 the experimental details and methods used for characterization can be found. Chapter 3 summarizes the findings of this work and gives an outlook to future directions.

1.2 Microgels

Carothers recognized that the gelation of polymers into three-dimensional networks is the result of a cross-linking reaction (e.g. covalent and non-covalent cross-linking).[2] Based upon these observations, microgels or nanogels can be defined as intermolecular cross-linked macromolecules with colloidal dimensions. Their capability to undergo a volume phase transition (VPT) by isotropic contraction upon external stimuli is a well-established research field. The manifold areas of application result from the capability of the spherical microgels to swell isotropically in their respective solvent (Figure 1). The cross-linking prevents the complete dissolution of the gel into individual polymer chains.[3]

The uptake of the solvent into the polymer matrix (swelling) depends on entropic and enthalpic processes based on a complex equilibrium between polymer-polymer-, polymer- and solvent and solvent-solvent interactions. These interactions can be disturbed through external stimuli such as changes in temperature,[4] pH,[5] ionic strength[6] or electromagnetic fields.[7] Microgels which react upon these external changes in a reversible manner are often called smart or stimuli-responsive materials.

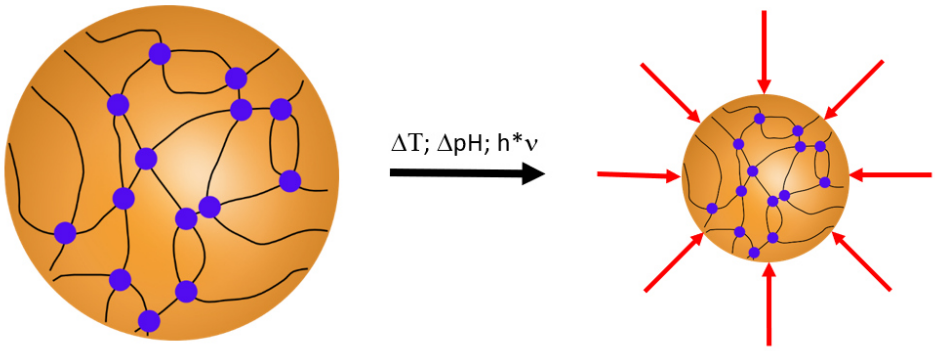

Figure 1: Schematic depiction of isotropic microgel contraction.

One of the most studied temperature-responsive polymers is poly(N-vinylcaprolactam) (PVCL),[5, 8, 9] second only to poly(N-isopropylacrylamide) (PNIPAAm).[10] Both polymers show a similar lower critical solution temperature (LCST) of 30-31°C.[11] Above this temperature these polymers turn insoluble. Due to the temperature increase, molecular

motion is breaking the hydrogen bonds between water and the amide groups of the corresponding polymers (entropy is dominant). The extended polymer chains turn into polymer globuli to minimize the water-polymer interaction. This polymer-based property transcends to the microgel/nanogels as the volume phase transition temperature (VPTT), which is predominantly determined by the LCST of the corresponding polymer. Upon reaching the VPTT, the polymer-polymer interactions start to predominate over polymer-water interactions leading to an expulsion of water from the microgels and subsequent shrinkage and precipitation of the latter.[12] The microgels have a sponge-like structure as shown in Figure 2, which enables them to take up large amounts of solvent of up to several times their own weight by swelling.[13]

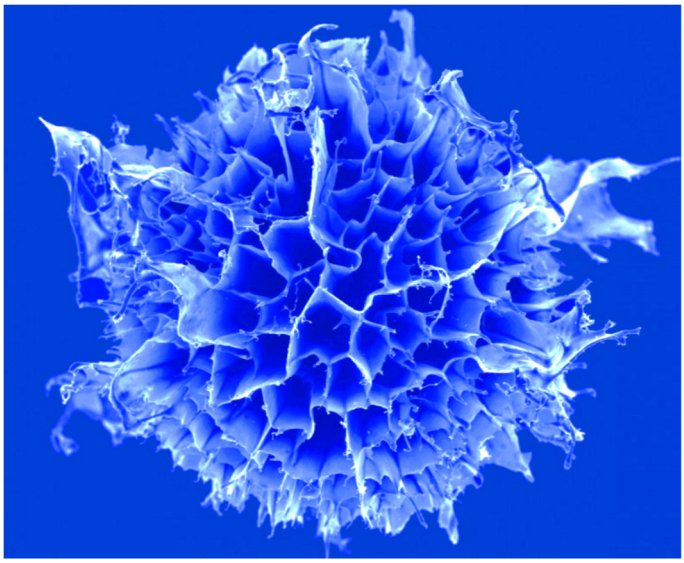

Figure 2: Depiction of a dried microgel (Source Prof. Andrij Pich - Lehr- und Forschungsgebiet Funktionale und Interaktive Polymere und DWI - Leibniz-Institut für Interaktive Materialien e.V.).[14]

Due to the LCST being close to the range of human body temperature, both PVCL and PNIPAAm are considered to have high potential for future bio-applications. Therefore, it is not surprising that most of the microgels are based upon these two polymers. The major advantage of microgels/nanogels over macroscopic hydrogels is their rapid response within milliseconds on external stimuli due to their small size. The response time is proportional

to the square of the microgel dimensions[15] and thus is influenced by the diffusion process as shown by Tanaka et al.[3]

Due to the amphiphilic nature of the VCL monomers, many synthesis approaches in different solvents can be conducted. There are several methods for the synthesis of microgels: dispersion polymerization ,[16-18] precipitation polymerization (surfactant free emulsion polymerization)[5, 8, 12, 19-25] and inverse microemulsion polymerization .[26] Dispersion polymerization is typically conducted in organic solvents and enables the preparation of micron-sized particles with narrow size distributions. With the emulsion polymerization the synthesis of smaller microgels with diameters below 150 nm is feasible,[27] but it has the drawback that a complete removal of the surfactant is difficult. Precipitation polymerization, which was predominantly used in this work, is conducted in water and yields microgel sizes between 50-1000 nm.[11] Since this method is free of surfactants, a subsequent cleaning step is not necessary. The radical reaction is initiated at temperatures around 70°C with a water-soluble initiator. The soluble monomers grow to longer chains and eventually precipitate out of the reaction solution as the reaction is conducted above the LCST of the polymers.

In this work, PNIPAAm and PVCL microgels were used, with the focus on PVCL. In contrast to PNIPAAm, PVCL is stable against hydrolysis since the amide group of the PVCL, responsible for its hydrophilic behavior, is directly attached to the hydrophobic polymer chain (Figure 3). It was found that PVCL resists hydrolysis in aqueous solution with HCL (1N) at 100°C during 60 h.[28] NIPAAm on the other hand produces small amide derivatives upon hydrolysis. While both NIPAAM and VCL monomers show a concentration dependent cytotoxic behavior, using the hydrolysis-resistant PVCL is an important step towards the enhanced biocompatibility of this polymer compared to PNIPAAm.[29] Kong et al.[30] replaced the cytotoxic CTAB used for the stabilization and synthesis of Au-NRs with a PEG-functionalized PVCL coating gaining biocompatibility for Au-NRs. Although PVCL is still awaiting FDA approval, recent reviews were dedicated to the future and present biomedical,[31, 32] pharmaceutical[33, 34] and technical[11, 35-37] applications of PVCL containing systems. PVCL-based hydro -and microgels have been considered for the entrapment of enzymes and cells,[9, 38-40] as a drug delivery vehicle,[16, 41-45]

for tissue engineering [46-49], bioanalytical sensors[50-53] and minireactor for organic synthesis.[21, 22]

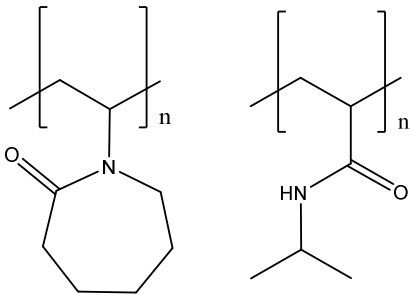

Figure 3: Chemical formulae of PVCL (left) and PNIPAAm (right) polymers.

Although PVCL has been known for a long time as a thermoresponsive polymer, the first cross-linked hydrogel was reported 1996.[54] The reason why this polymer was not in focus for years is that the polymerization kinetics of VCL is often not favorable during copolymerization. During radical copolymerization the VCL forms less stable propagating radicals compared to acrylates, e.g. methacrylate. This leads to a higher incorporation of the second comonomer regardless of the initial concentration and monomer feed and thus to low conversions.[55] For this reason, the AAEM comonomer in VCL/AAEM microgels is predominantly incorporated in the center forming a rigid core.[56] In a similar reaction the intra particle cross-linker BIS is slightly more active compared to the NIPAAm monomer which leads to a gradual decrease in cross-linking density from the core to the outer region of the microgel making NIPAAm microgels exceedingly fuzzy and soft.[57]

Pure PVCL polymers, hydrogels and microgels often show a high PDI which can influence the thermosensitivity of the resulting gels in a negative way.[58-61] Tager et al. showed that for this polymer the precipitation temperature is heavily dependent on the concentration and molecular weight of the polymer.[58, 62]

Chee et al. showed that the coil to compact globuli transition for PVCL expands over a temperature range of 15°C compared to PNIPAAm with a sharp transition within 2°C.[63] Based upon these findings, a continuous phase transition of VCL microgels was expected.

This is the case, but in contrast to the bulk polymer the transition is less broad.[64] This contradicting observation still has to be explained through further investigations.

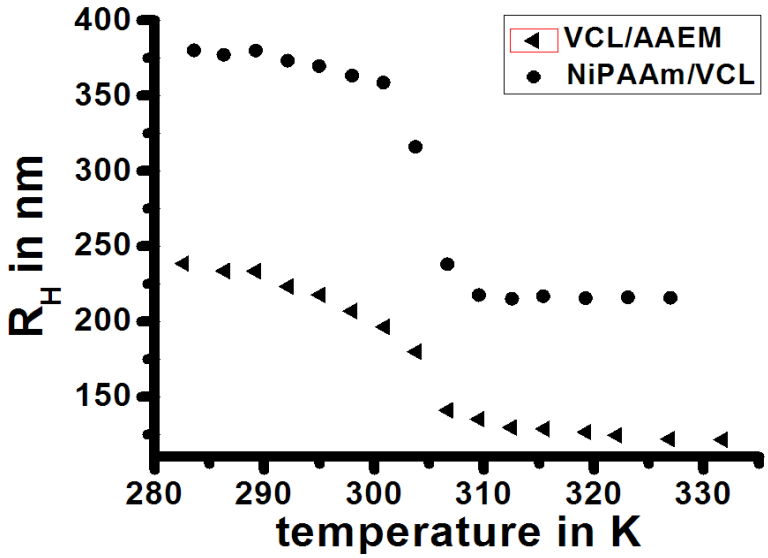

Figure 4: Comparison of the VPTT of VCL/AAEM and NIPAAm/VCL microgels observed by DLS measurements.[64]

In contrast to the continuous phase transition of VCL/AAEM microgels, NIPAAm microgels exhibit a sharp transition which makes them less tunable over a broad temperature spectrum. By incorporation of a second polymer with a different VPTT in a core-shell structure, NIPAAm microgels are able to express a continuous collapse.[65]

Besides the continuous transition temperature, which makes the VCL/AAEM microgels interesting for sensor applications and also for the use as artificial muscles, the acetoacetoxy group enables multiple possibilities. With AAEM the chelate complexation of nanoscopic metals, e.g. Ag,[20] Au,[66, 67] FePt,[68] and Gd-NPs[69] via the keto form and a possible in-situ reduction through the enol form is feasible. Furthermore, inorganic nanoparticles beyond metals can be incorporated as well, such as hydroxyapatite,[70, 71] magnetite,[72, 73] ZnS,[74] and ZnO.[24]

The comonomer AAEM decreases the VPTT of the PVCL-based microgels from 32°C to 28°C.[5] Due to the pronounced keto-enol tautomerism of the aceto acetoxy group (Figure 5: 75% ketone : 25% enol), cross-linking is also feasible via various groups such as isocyanates, activated alkenes, aldehydes, and amines.[75]

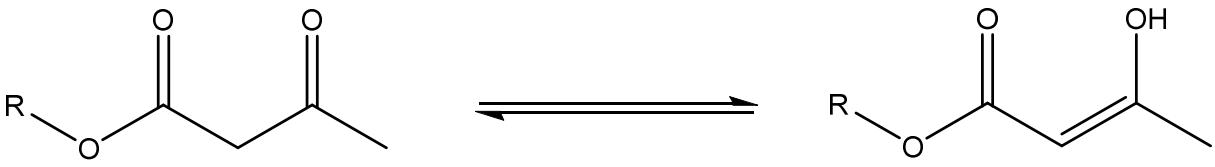

Figure 5: Keto-enol tautomerism of the acetoacetoxy group.

VCL/AAEM microgels provide a versatile platform for functional modifications via copolymerization with selected comonomers, e.g. NIPAAm[8, 16] and vinyl α-cyclodextrin[76, 77] while maintaining a narrow PDI.

1.3 Nanostructured surfaces

For structuring surfaces on the nanoscale, there are two major approaches: top down and bottom up. With top-down methods, bulk material is shaped subsequently into nanoscopic dimensions by using mainly lithographic methods (e.g. optical grids with photo resins, electron beam, scanning probe and plasma etching methods).[78] This approach enables the nanostructuring of large surface areas. This is the reason why top-down methods are intensely used for the lithographic fabrication of microchips. The architecture of state-of-the-art computer chips (2019) reaches into 14 nm broad conductor tracks. However, these methods demand an expensive experimental setup (e.g. lithographic templates, clean rooms and complex irradiation techniques) to prevent defects in the nanostructure and suffer from structural limitations such as useable surface area and high rigidity, which limits their practical applications.

In bottom-up approaches, nanostructuration is achieved through atomic or molecular self-organization processes such as supramolecular self-assembly of microgels,[79-81] colloids[82, 83] and dendrimers,[84] atomic layer deposition, sol–gel nanofabrication, DNA-scaffolding.[78] While this method enables a precise tuning of the resulting nanostructure, the use of single building blocks demands at the same time a high control over the process parameters and a high purity of the components. For this reason, the major drawback of this method is the slow speed, the relatively low yields and small nanostructured surface areas. Nevertheless, to this research field belongs the future because self-organization processes enable higher versatility and flexibility towards mimicking biological structures.

As an alternative, nanostructured surfaces can be obtained through lithography-free methods. The process of controlled wrinkling represents a straightforward alternative for the fabrication of flexible templates. Hereby, the differences in moduli in semi-flexible materials is used to create sinusoidal surface structures. This phenomenon is commonly referred to as wrinkling or buckling. Wrinkles are most commonly observed in our own ageing process, where the relatively rigid protective layer of our skin resides on top of flexible tissue (e.g. muscles). During ageing, the difference in E-moduli between the rigid protective layers (skin) and the support layers begin to increase so that the movement of the flexible bottom tissue cannot be followed by the rigid top layer leading to the development of wrinkles.[85, 86] We try circumventing this process through rehydrating the top layer with cosmetic products, thus decreasing the difference in flexibility. Cerda und Mahadevan studied this universal phenomenon and postulated that the surface layer forms wrinkles to reduce the stress occurring during deformation (e.g. this is also the case during the formation of mountains caused by tectonic plate displacement).[87, 88]

This phenomenon can be exploited for the generation of highly periodic micro- and nanostructures. Whitesides et al. used PDMS to generate periodic wrinkles by expanding the PDMS substrate by heat and subsequently oxidizing the top layer. Upon relaxation, the difference between the rigid top layer and the flexible bottom layer caused the formation of highly periodic sinusoidal micro- and nanostructures.[89] Genzer at al. optimized the process by using a stretching apparatus instead of heat for a more controlled formation of

nanowrinkles (Figure 6).[85, 90] The uniaxial stretching is imperative for a controlled formation of sinusoidal structures.[91-93]

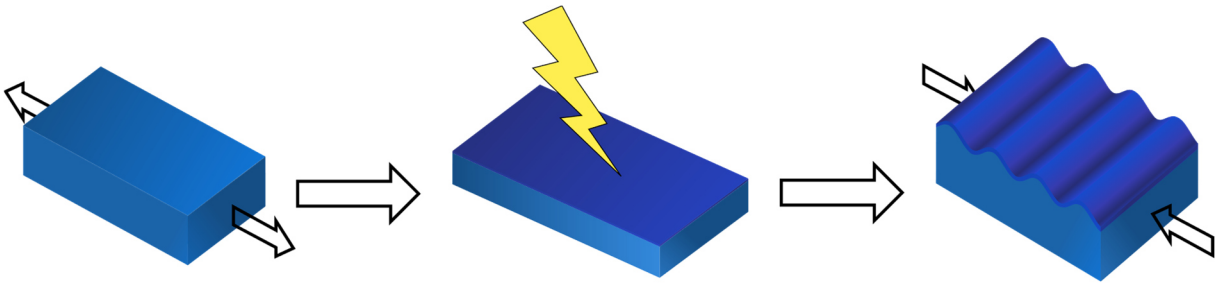

Figure 6: Schematic depiction of wrinkle formation. From left to right: stretching, oxidizing, relaxation of the PDMS substrate.

By defining the distance between two maxima (wrinkle peaks) as the wavelength λ and the difference between minima and maxima (wrinkles grooves and peaks) as the amplitude A, the formation of wrinkles on oxidized PDMS surfaces can be mathematically described (Figure 7).

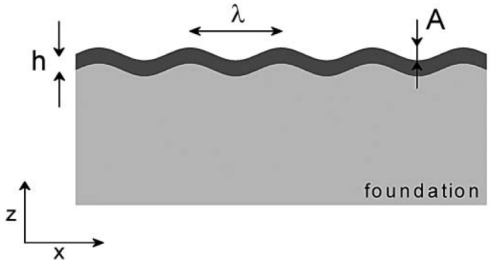

Figure 7: Schematic illustration the buckling of a thin skin on an flexible foundation.[85]

Genzer and Groenewold stated that for the formation of nanoscale wrinkles only a very thin SiO_x layer is needed.[85] The layer thickness and thereby the wavelength correlates directly to the plasma treatment time (Figure 8).[94]

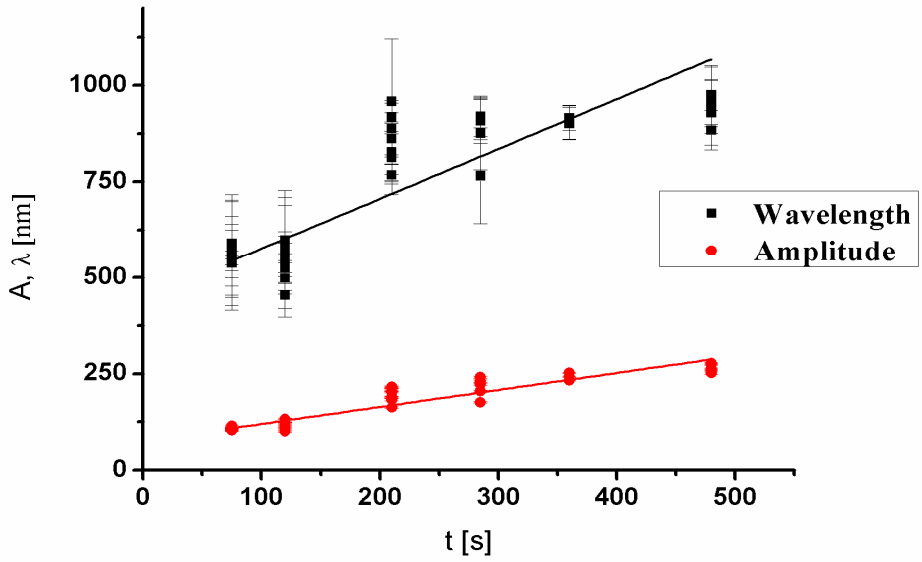

Figure 8: Wavelength and amplitude of PDMS wrinkles as a function of plasma treatment time.[94]

The wrinkles used in this work were all fabricated by plasma treating stretched PDMS surfaces. Thereby, the Si-Me groups of the PDMS are oxidized to $Si_xO_yC_z$ and CO_x forming a high concentration of hydrophilic silanol groups at the surface.[90, 95-97] Residual PDMS oligomers can diffuse through the porous oxide layer turning the surface hydrophobic again over time.[95, 98] In literature, it is described that the process of regaining hydrophobicity takes several hours.[89] However, experiments conducted within the scope of this doctoral thesis showed that the process takes several minutes after plasma treatment. The reason behind this accelerated process could be that after relaxation of the substrate, the oligomers are forcefully pushed through the porous layer due to internal pressure. Thus, in this case, it was probably not a diffusion driven process.

By understanding the fundamental processing parameters, many different nanostructured surfaces can be fabricated based on this method.

Through diaxial stretching, the fabrication of fishbone and checkerboard surface structures is feasible (Figure 9). [89, 93, 99]

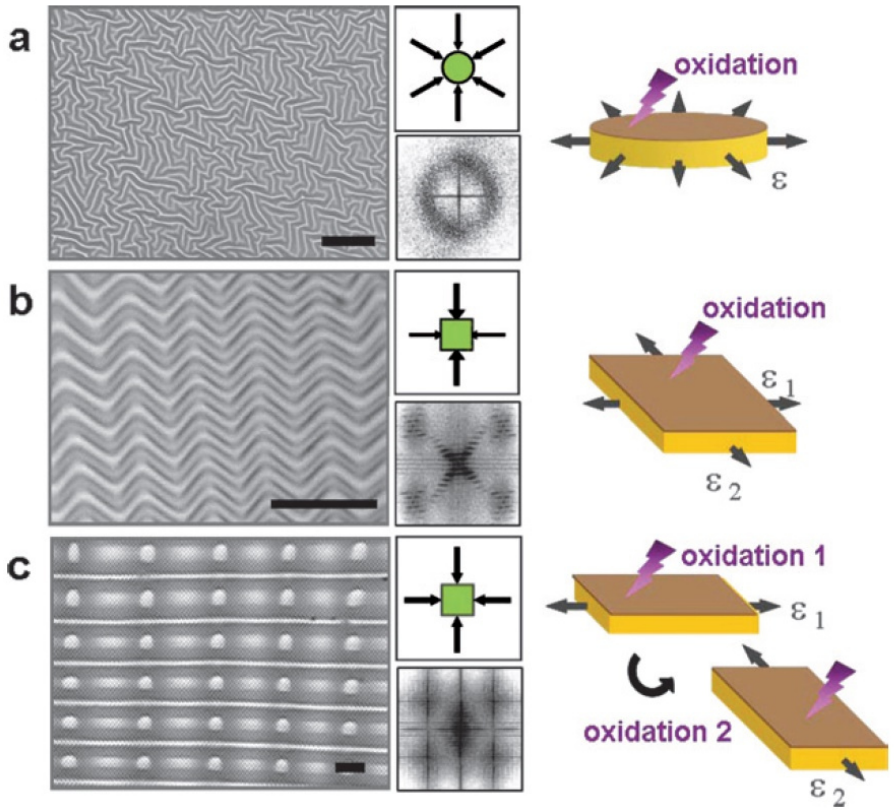

Figure 9: Optical micrographs of surface patterns generated by single and multi-axial strain fields (indicated by schematics) coupled with plasma (a, b) or UVO (c) exposure. Patterns (a, b) are generated by a single exposure step and yield isotropic and chevron topologies (in addition to lines in Fig. 1a). Pattern (c) yields a checkerboard pattern consisting of peaks and saddles, which has been produced by two successive exposure–strain steps. Scale bars are 20 mm.[93]

Yin et al. showed that hierarchical or fractal structured surfaces are feasible by a two-step process, wherein the stretched PDMS surfaces are first plasma-treated, followed by a semi relaxation, which generates the first generation microwrinkles. Sequential oxidation via ultraviolet ozone followed by a total relaxation of the initially applied stretching forms the second generation of perpendicular aligned nanowrinkles (Figure 10).[100] By miniaturization of this approach, lotus-like effects can be expected.

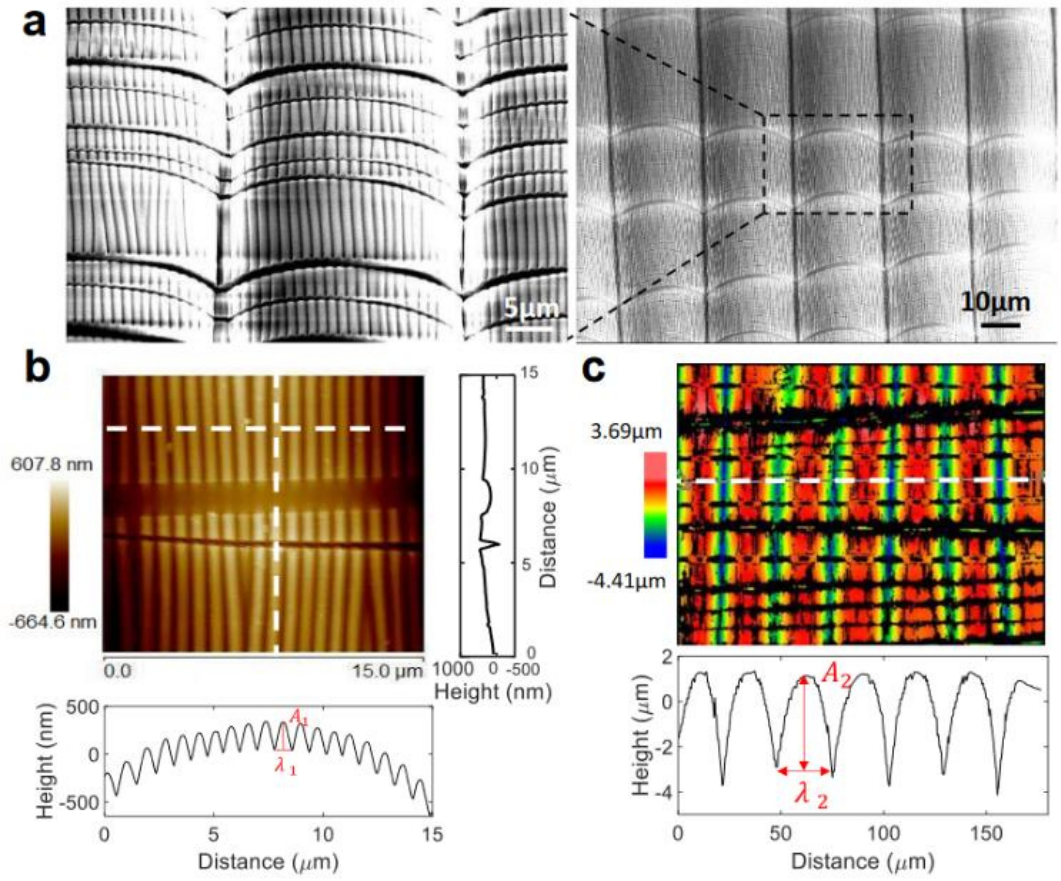

Figure 10: (a) SEM images of hierarchical wrinkles. Left: magnified view. (b) Corresponding AFM images of hierarchical wrinkles with measured horizontal and vertical cross-sectional profiles along the white dashed line shown to the bottom and to the right, respectively. (c) Corresponding optical profilometer images of hierarchical wrinkles with measured cross-sectional profile along the white dashed line shown to the bottom.[100]

In a similar approach, Feng et al. were able to align the second generation of nanowrinkles perpendicular to the first generation of microwrinkles (Figure 11).[101]

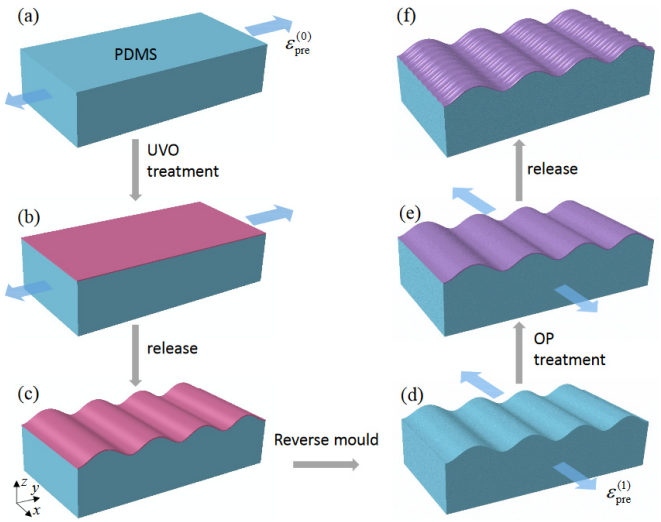

Figure 11: The key steps for fabricating periodic hierarchical wrinkling patterns by controlling the curvature of a soft bilayer system.[101]

Lu et al. showed that by applying an additional layer of photo resin onto the PDMS substrates and a subsequential exposure with UV light controlled by lithographic masks can lead to more complex microstructures (Figure 12).[102]

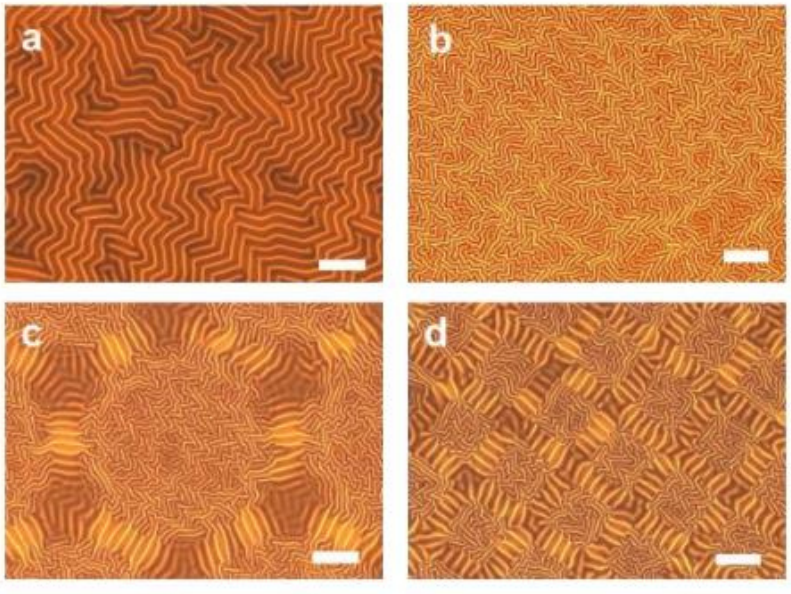

Figure 12: Optical images of the wrinkles on the multilayer before (a) and after blanket irradiation with visible light (b), selective irradiation with visible light by 100 mesh-sized hexagonal holes (c) and 300 mesh-sized square holes (d), respectively. Scale bar: 50 µm.[102]

Recent advances on nanoscale surface structuring of PDMS substrates were demonstrated by Böker et al. The fabrication of gradient wrinkles was possible through shielding of the underlining PDMS during plasma treatment. These gradient wrinkles were capable of particle separation via spin coating[103] and showed anisotropic wetting properties (Figure 13).[104]

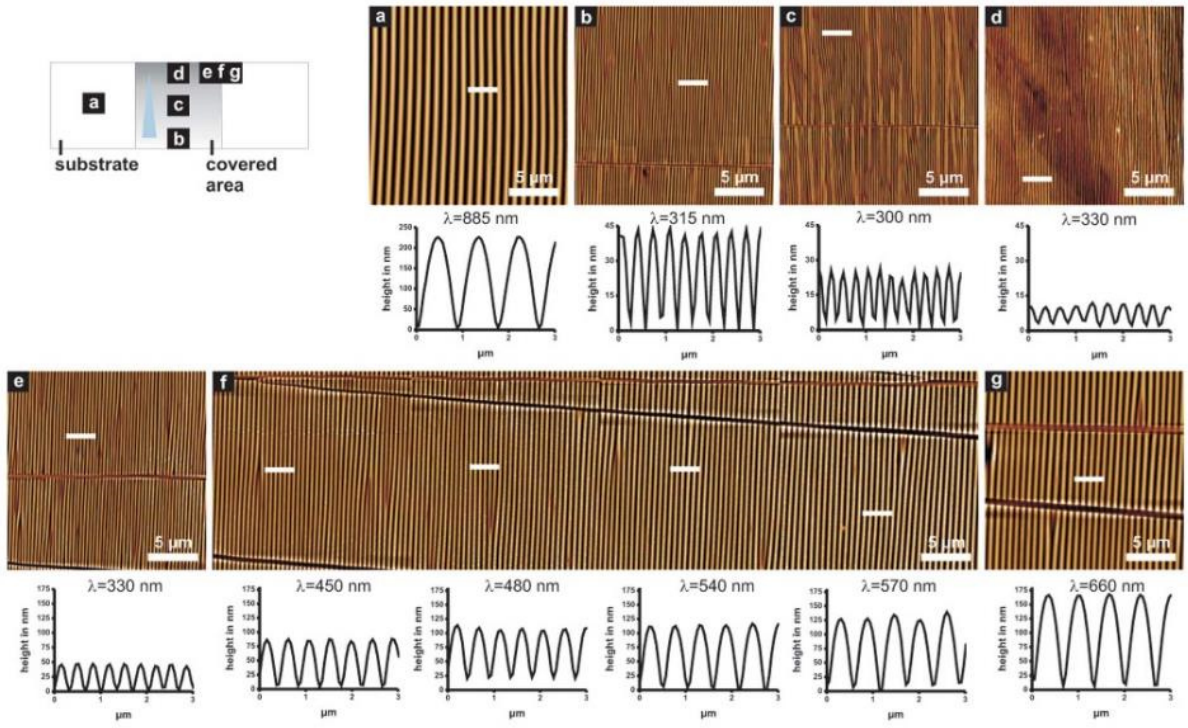

Figure 13: Sketch of the gradient sample (450 s plasma treatment) with letters indicating the points of measurement and corresponding AFM height images(a–g). In the sketch, the grey area represents the area covered by the silicon wafer, and the triangles show the direction-dependent trend and the steepness of the wrinkle gradients. While the blue triangle indicates the direction of increasing distance between wafer and substrate and a gradient in A, the orange triangles indicate gradients in A and 1. A cross-section is depicted underneath each AFM image. Height scale: (a) 300 nm, (b) and (e) 80 nm, (c) 50 nm,(d) 20 nm, (f) 150 nm, (g) 250 nm.[103, 104]

Böker et al. also showed that by using a 360° stretching apparatus and a targeted introduction of spherical defects into the PDMS substrates, star shaped nanopatterns can be obtained (Figure 14).[105]

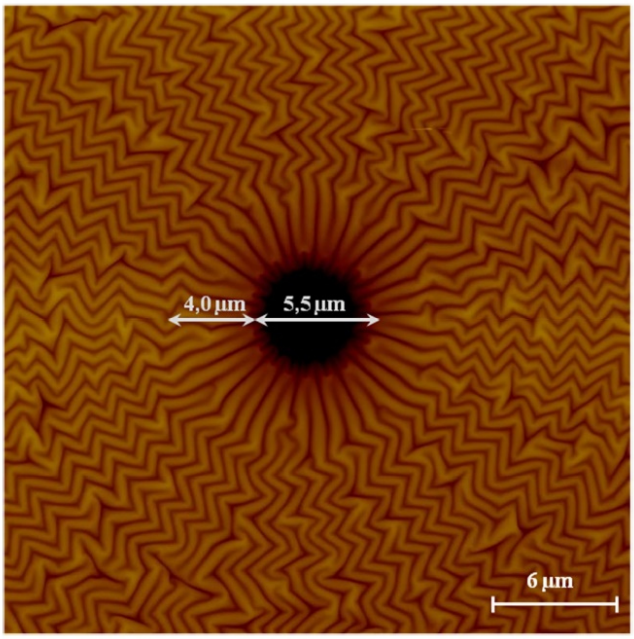

Figure 14: Star shaped wrinkled structures on nanoscale.[105]

These wrinkled structures can be used for the fabrication of efficient solar panels for minimization of thermal radiation,[106] for studies of cells[107, 108], bacteria[109, 110] and marine life,[110] and their adhesion on nanostructures to either prohibit unwanted adhesion or to enhance the proliferation of certain cell types. Furthermore, an minimization of surface friction in microfluidics is possible through nanowrinkles[111] and the fabrication of flexible and transparent conductive graphene films.[112, 113]

In conclusion, wrinkles allow to mimic many biological surface patterns and are scalable from the macroscale towards the lower nanometer dimensions.[114] They combine many favorable properties such as the mimicry of biological structures on multiple scales, their engineering at low cost and ease of fabrication as they are highly adaptable to the required experimental setup. In this work, wrinkles were preferred over the expensive lithographic methods and the hard-to-control self-assembly processes provided by bottom-up approaches. Therefore, the template-assisted fabrication of nanoarrays and 1D nanostructures with soft matter (e.g. microgels and hydrogels) were performed using wrinkled PDMS.

1.4 1D nanostructures and anisotropic microgels

The investigation of stimuli responsive materials with spatial dimensions in the order of a few nanometers up to several microns has become an important and established research field in nanoscience.[115] Improving the fundamental understanding of the mechanical, electrical, optical and magnetic properties of soft nanoscale structures offers high potential for the next generation of functional materials. In particular, microgels are most suitable for creating new nanoscale superstructures which, in the future, might lead to promising applications in diverse fields such as printable electronics,[116, 117] photonics,[118-120] biomedical applications, tissue engineering[121-123] and sensor technology.[124-126]

1D nanostructures with metal nanoparticles were obtained via template-assisted assembly which showed outstanding properties through their anisotropic shape in terms of conductivity, optical diffraction and superparamagnetism. Examples for these nanostructures were recently shown by Zhang et al. with the alignment of AuNRs in wrinkles through microfluidics.[127] Park et al. used wrinkles for the in-situ synthesis of AuNPs.[128] Fery et al. transferred AuNPs, AuNRs and magnetic NR to flat surfaces via wrinkles to obtain nanoscale conductor tracks and optical arrays with anisotropic plasmon coupling.[129-133]. Furthermore, wrinkles enable the assisted fabrication of metallic nanocups. [134]

The fabrication of patchy Janus particles by wrinkled templates was shown by Brüx et al.[135] Patchy particles are currently a hot topic in the self-assembly field with a construction kit like approach to functionalize the surface of nanoparticles. These particles can self-assemble in a dynamic way leading to various shapes.[136] It is even possible to mimic molecules on a supramolecular level with divalent, trivalent and tetravalent assemblies.[137]

Polystyrene as model for polymeric nanoparticles was used to obtain 1- and 2-dimensional patterned colloidal nanoarrays.[138, 139] Endo et al. showed the wrinkle assisted alignment of polystyrene beads and subsequent crosslinking into stiff 1D-

nanostrands via plasma treatment with no exceptional function in regards to flexibility, biocompatibility and stimuli responsive behavior.[140] Latter properties were achieved by Böker et al. using soft matter particles e.g. nanogels.[64, 141]

Hybrid particles combine the benefit of metal properties, such as conductivity and plasmon resonance with the stimuli responsive behavior of polymers forming semiflexible arrays by template assisted alignment on flat surfaces[119, 142] and hexagonal alignment of AuNR@pNIPAM on wrinkled surfaces.[143] The in-situ synthesis of hybrid hydrogel arrays via wrinkle confinement was show by Wünnemann et al.[144] Post-treatment of these hydrogels led to the fabrication of conductive Au-nanowires. Böker et al. showed that even biomaterials such as rod like viruses can be aligned in this manner.[145, 146]

In comparison to inorganic materials, soft polymeric matter exhibits virtually unrivalled biocompatibility [11, 31, 43] and, therefore, is gaining significant interest for drug delivery.[147] Böker et al. showed that the alignment of microgels can be controlled via wrinkle dimensions, de-wetting and capillary forces.[103] Due to their ability to rapidly swell and de-swell in response to external stimuli, microgels are potentially useful for actuation applications.[148] In the swollen state, the solvent can make up more than 90% of the microgel weight. The extent of their sponge-like swelling and deswelling is determined by the type of polymer and the cross-linking density.

Individual spherical microgels are capable of substantial size changes and of generating stroke forces during expansion and contraction. One-dimensional assemblies of interconnected microgels within microgel arrays, which have been demonstrated by Böker et al.[64] could be particularly well suited for actuation purposes (Figure 15).

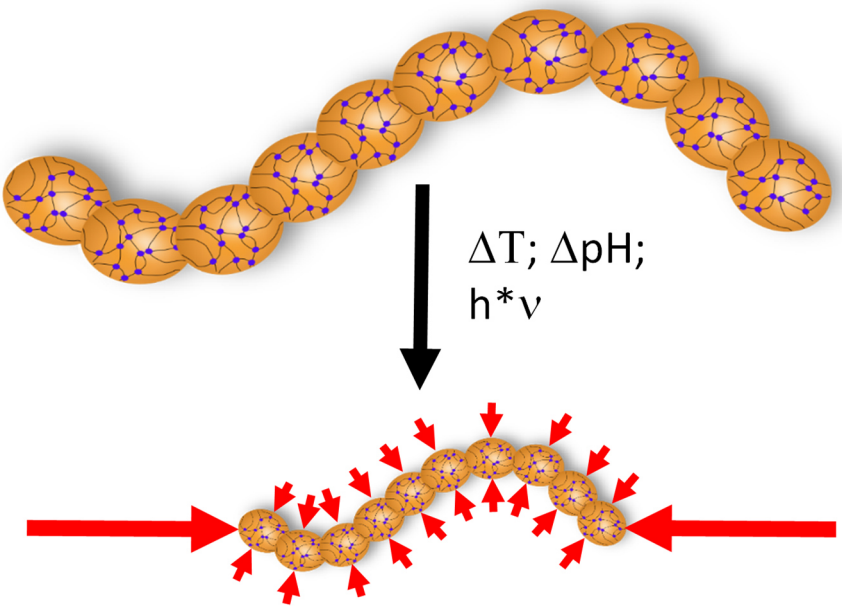

Figure 15: Schematic depiction of an anisotropic strand contraction triggered by an external stimulus (e.g. ΔT) inducing a fast contraction due to diffusion processes on a nanoscale volume.[3]

While the shape of one-dimensional microgel assemblies bears similarities to those of microfilaments made out of magnetic colloids and linkers,[149-151] which have recently been studied intensively for actuation applications in microfluidics, they differ from the latter in the types of movements they are able to generate (contractions and expansions). Additionally, their movements can be triggerable by temperature or pH changes.

A prerequisite for using one-dimensional microgel assemblies for actuation applications are methods to fabricate them with reproducible geometric shapes and stable links between the constituent microgels. Strategies for the synthesis of microgel assemblies can be adopted from anisotropic linear arrangements of colloids used for surface patterning and coating.[152-154] One such strategy is template-assisted or guided self-assembly,[155, 156] which gives good control over the positional order of particles in the dimension of the colloidal superstructures.[157-160] As previously introduced, templates for guided self-assembly can be fabricated using top-down approaches (e.g., lithography and etching) or controlled wrinkling.[90, 92, 93, 97, 110, 146] This work shows that using wrinkled substrates as templates, 1D

microgel arrays[104] and freely dispersed microgel strands[141] composed of single microgels as well as zigzag structures can be obtained. These one-dimensional strands were found to have lengths of up to 100 μm and represent a unique and novel material class which, up to this point, had never been fabricated or studied in detail.

The suitability of such microgel strands for possible actuation applications will depend, to a large extent, on their mechanical properties. Among these are the size of the force that the strand can exert during contraction along the strand axis and the velocity of the contraction. Furthermore, the strand has "passive" mechanical properties that describe the response of the structure to other forces: its tensile elasticity characterizes the response to a tensile force along the strand axis, its bending stiffness specifies the resistance to shearing forces, and its mobility gives its velocity under the combined effects of a moving force and hydrodynamic friction in the solvent. Bending stiffness and mobility are key properties that have been intensively studied in other one-dimensional systems of interest for actuation, e.g., microtubules[161], carbon nanotubes[162, 163] and magnetic colloid microfilaments.[149, 164] In the case of microgel strands, the values of these mechanical properties have not been determined yet. They are difficult to predict theoretically due to the granular structure of the strands and the unknown strength of the links between adjacent microgels. It is therefore necessary to determine them experimentally in order to gain information on the mechanical suitability of microgel strands for actuation purposes.

Microgel assemblies offer various possibilities for further exploiting the chemical diversity of microgels. Such arranged soft structures are known from nature, where flexible motion is enabled by one- or two-dimensional linear structures such as actin filaments and muscle fibers. In contrast to early actuation experiments with hydrogels at relatively low contraction speeds,[126] it can be expected that nanoscopic stimuli responsive microgel strands can respond much faster and thus represent the next step towards mimicking natural muscles.[3]

Strategies for the synthesis of microgel assemblies can be taken from anisotropic linear arrangements of colloids used for surface patterning and coating.[152-154] For the fabrication of colloidal arrangements, the already described two assembly methods are most commonly

used: (i) bottom-up template-free self-assembly procedures and (ii) top-down template-assisted or guided self-assembly. The former benefits from its greater simplicity, but lack in controlling the width and length of the anisotropic arrays and the positional order of the individual colloidal particles.[155, 156] In contrast, guided self-assembly represents a versatile approach towards a broad range of complex supramolecular structures, which are not feasible with template-free methods, by utilizing topographically structured surfaces.[64, 103, 139, 157-160, 165-171] The various methods of guided self-assembly all exhibit good control over positional order and dimension of the colloidal superstructures.[157-160] Template assisted methods utilities alignment techniques like spin-coating,[165] dip-coating[171] and confinement by templates [133, 166, 172], were the underlining physical laws (e.g. capillary forces, de-wetting processes, etc.) determine the alignment quality.[173, 174]

For 1D alignment of microgels, wrinkles based on PDMS have shown an impeccable positional order for both the particles and the arrays. This and the easy tunability of the wavelength (i.e. the distance between two wells) from nanometers to microns make wrinkled substrates based on PDMS especially suited for large-area surface structuring and particle size screening processes for optimal alignment of soft colloidal particles.[64, 87, 99, 103] These periodic nanostructured surfaces have served as templates for many different methods to functionalize surfaces[173, 175] such as microcontact printing (μCP),[92, 176] intaglio printing,[145, 146] spin-coating,[64, 103] dip-coating[171] and applications involving stretchable electronics,[177, 178] optical grids,[179] antifouling[180] and switching of surface wettability.[181, 182]

Due to the aforementioned chemical versatility and stimuli-responsiveness of microgels, their utilization as building blocks for the decoration of surfaces has become popular in recent years. For the fabrication of nanostructured surfaces with these soft colloids, interactions between the microgels and the substrate surface (e.g., via surface charges, pH) have to be considered.[64, 183-185] In order to tap into the full potential of their stimuli-triggered contraction, the anisotropic particle arrays should be exposed to a minimal interaction with any kind of surface which confines their motion. Non-confined and non-adhered 1D microgel arrays enable smart materials of a new type, which includes the possibility of anisotropic contraction along the longitudinal axis of a free dispersed 1D array.

In this work the synthesis and characterization of various freely dispersed 1D PVCL microgel arrays is described including pearl necklace-like, zigzag and ribbon-like formations fabricated by utilizing wrinkled surfaces as templates. Diffusion coefficients characterizing their lateral and rotational diffusion in the solvent are determined from an evaluation of their motion. Due to their anisotropic shape and expected ability to respond to external stimuli, these cross-linked microgel arrays promise to provide a playground for future investigations of biomimetic applications such as artificial muscles or sensors.

1.5 AFM methods

The main characterization tool used in this thesis is atomic force microscopy (AFM). In contrast to microscopy methods based on electromagnetic waves (e.g. optical and electron microscopy), this method is based on the interactions between a probe and the surface which is examined. Topologies on the nanoscale are sequentially scanned by a sharp nanoscale tip, thereby the resolution is defined by the dimension of the tip radius: the smaller the tip, the higher the resolution. Structures smaller than the tip radius cannot be resolved.[186] Ideally, the tip should consist of a single atom to enable the higher possible resolution on the nanoscale.

The advantages of an AFM are the ability to conduct different experiments and measurement at once (e.g. imaging, force measurements and surface manipulation). The measurement setup is based on one of the fundamental laws ins physics. In the classic contact mode method, the tip which is attached to a cantilever is brought in contact with the surface. The force F occurring between the tip and the surface can be described by Hook´s law (Equation 1) for a linear elastic spring cantilever, with k_c for spring constant of the cantilever and Δz for deflection.

Equation 1

$$F\ (z) = k_c \Delta z$$

The order of magnitude of the spring constant is a crucial factor for topology measurement of soft nanostructured surfaces. Choosing cantilevers with spring constants in the order of magnitude of the E-Moduli enables to detect the true undeformed dimension of the measured topology. The correlation between Hook´s law and Young´s equation is described in Equation 2, with L_0 for initial object length, ΔL for the extent of deformation and A for surface area.

Equation 2

$$E = \frac{stress}{strain} = \frac{FL_0}{A\Delta L} = \frac{k_c \Delta z L_0}{A\Delta L}$$

By determining the spring constant k_c via calibration, E-Moduli and adhesion measurements on soft particles are feasible as shown in this work.

The interactions between the tip and the measured surface can be describe via the Lennard-Jones potential (Figure 16) and can be categorized into attractive and repulsive forces. Interactions can be triggered by different forces (e.g. electrostatic forces, van-der-Waals-forces). In Figure 16, the total potential curve is depicted as a function of the tip distance *r*. It can be seen that at large distances the long-range van-der-Waals forces dominate (decreasing with $(1/r)^6$). Closer to the surface the short-range repulsive Pauli forces become predominant (decreasing with $(1/r)^{12}$). Based upon this knowledge, different measurement modi were developed, which are applicable dependent on the present surface situation. In contact mode, the tip stays in direct contact with the surface. Due to the predominant attractive forces the tip snaps into contact at a certain distance. That is why measurements in contact mode are conducted under repulsive conditions.

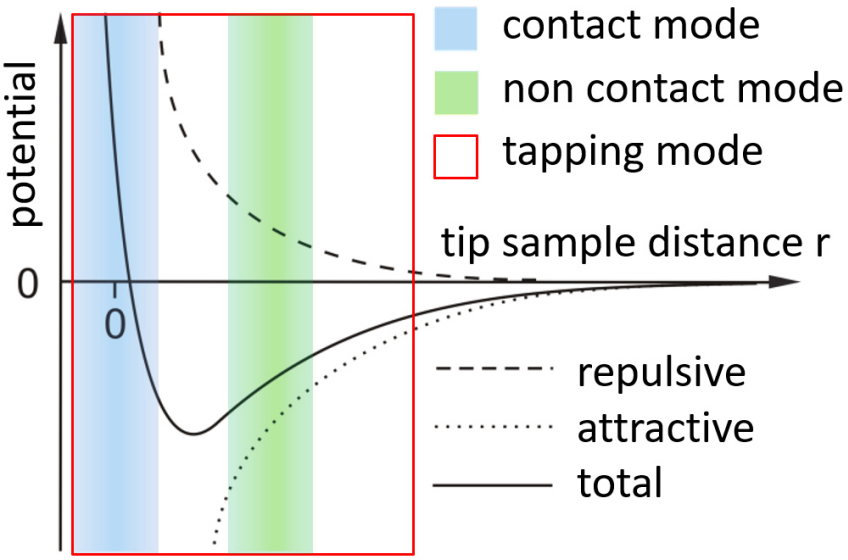

Figure 16: Lennard-Jones potential: forces between tip and sample in dependence of the distance.

When the cantilever is moved over a surface it is deflected (Δz) by the topography of the sample. In modern AFMs, the deflection is measured by a laser and reflected onto a photodiode. There, the measured signal is translated into a change in current and transformed into an image (e.g. height, moduli, adhesion etc.) via the respective software. The AFM used in this work had one tube piezo element for lateral and vertical cantilever motion.[186-188] Piezo elements are used when continuous and precise motions on nanoscale are required.

There are commonly two different types of contact modes:

In the constant-force mode the cantilever is moved with a defined force in the range of *nN* and constant deflection Δz across the surface. The height information is obtained via readjustment of the tube piezo. The piezo readjustment makes this method rather slow.

In constant-height mode the tube piezo is set on a constant value and the topography information is obtained via deflection of the cantilever. In contrast to the constant force mode the deflection needs no piezo readjustment which enables high scan rates. However, due to the direct application of the tip on the surface cantilever with high spring constants

kc can destroy sensitive materials. For this reason, this measurement mode was not used in this work.

Non-contact mode uses attractive long-range forces (e.g. van- der-Waals forces) for measurement. Thereby the cantilever is set to oscillate in resonance frequency. At around 100 nm the attractive forces dampen the oscillation which in turn provides the necessary topological information. The measurement is very slow and rather sensitive towards disturbances. For this reason, this measurement mode was not used in this work.

The TappingMode™ also uses an oscillating tip bit in contrast to the non-contact mode this mode is operated at distances where repulsive forces are dominant. The oscillation ensures a short contact with the surface minimizing surface damages occurring during contact mode. The measurement information is derived from the difference from the free oscillation and the dampened one during contact. This mode was used for nearly all height measurements in this work.

Since its development in the 1980s by Binnig et al. [189] the AFM technique has been further developed so that now complex experiments in liquid media,[190] on soft matter[191] and live samples are feasible.[192]

Since the tapping-mode is not suitable for determining the rigidity of soft particles in aqueous solutions the PeakForce™ QNM™ (Quantitative Nanomechanical Property Mapping) method was used.[193-195] According to literature advantages of this measurement method lies in mapping of moduli and adhesion in high resolution, force control in order to keep the indentations small for non-destructive measurement of soft particles (<1 MPa). PeakForce-QNM uses the tube piezo to move the cantilever towards the surface. In contrast to the tapping mode where the amplitude of the cantilever is kept constant, the PeakForce-QNM mode keeps the maximum force applied to the measured sample constant by controlling the vertical motion via the tube piezo. The probe intermittently touches the surface and the maximum force is controlled at each contact point. Since the maximum force is kept throughout the scan (in this work the tube piezo is set at 150pN and 300pN, respectively), the deflection of the cantilever can be well controlled, which is crucial for characterization of mechanical properties and the topological deformation of soft particles

(e.g. microgels in water). Zhao et al. showed that with this method it is even possible to characterize gas nanobubbles in liquid media.[195] As can be seen in Figure 17 a nanobubble can be deformed by applying different load forces. Analogous to this method, the microgel softness was determined in this thesis.

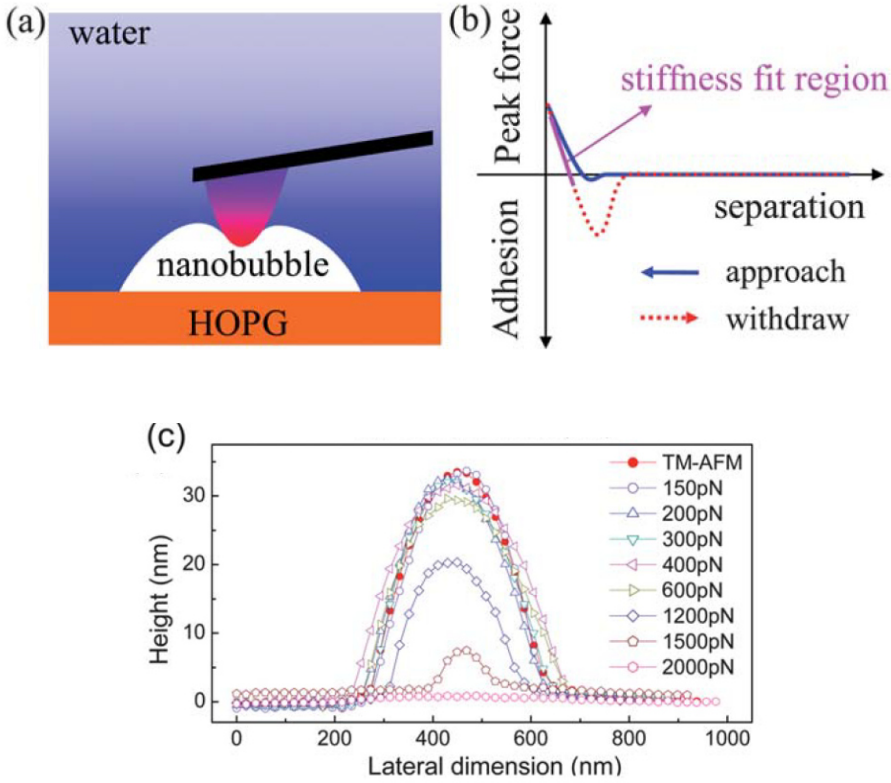

Figure 17: Schematic diagram of the AFM tip–nanobubble interaction and example force curves: (a) shows that a nanobubble is highly deformed under a high load from the AFM tip; (b) is an example force curve in PF-QNM which indicates the stiffness fit region. (c) is the profile analysis of a nanobubble obtained at different peak force setpoint.[195]

2 Results and Discussion

2.1 Guided self-assembly of microgels into 1D nanoarrays

Parts of this chapter have been published elsewhere.[64, 94]

2.1.1 Introduction

The ordered assembly of soft matter particles, e.g. microgels, into nanoarrays is a promising approach towards the formation of smart materials on a submicron scale. The alignment of microgels into various supramolecular nanostructures is highly sophisticated and depends on their dimensions and physical properties.[103, 122] In contrast to solid nanoparticles, microgels do not have a defined contour, which poses a particular complex challenge for well-known particle alignment methods. For this reason, phenomena like steric and electrostatic interactions and physical entanglement between the participating systems has to be taken into account when transferring well-established alignment methods for solid particles. e.g. alignment via wrinkles as template[140, 145] or confinement,[133, 166, 172] to fuzzy microgel particles.[64] Furthermore, some microgels exhibit density gradients[57] or are composed of core-shell structures with different E-moduli, which add even more complexity to the understanding of such systems.[4] These intrinsic microgel properties define their unique colloidal responsiveness towards various external stimuli, but also complicate the alignment of these particles into various nanostructures. Nevertheless, using the alignment methods discussed in this work may transfer these unique functionalities, e.g. stimuli responsiveness and deformability, to a new generation of flexible supramolecular nanostructures, which are able to react upon environmental changes.

It has been proven that topographically structured surfaces are very important tools in guiding the assembly of nanoparticles.[139, 157, 169, 170] Especially wrinkled surfaces, which serve as templates in this work, combine several benefits which are numerated in the following. The low fabrication costs, the easily accessible tunability of the dimensions and the high

periodicity over a long range (several cm^2) are the major advantages of these systems (Figure 18).

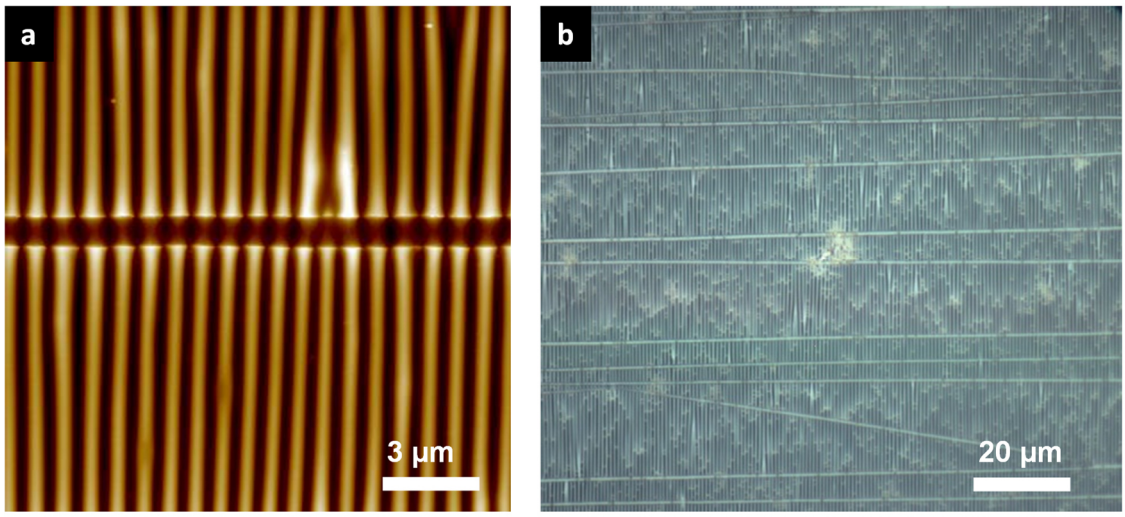

Figure 18a: AFM image of wrinkles. b: optical microscopy image of a similar sample. Perpendicular aligned micro scale cracks are visible which appear due to strain release (stress fractures).

In this chapter, VCL/AAEM microgels, which form sterically stabilized dispersion in water, soft NIPAAm microgels and their copolymeric NIPAAm/VCL derivates were aligned into supramolecular assemblies by using PDMS wrinkles. Two major alignment methods for microgels were optimized according to the individual microgel properties in the scope of this work (e.g. size, mechanical properties, rigidity, interparticle and interfacial interactions). [94] Furthermore, the properties of microgels and microgel arrays at the solid/air and at the solid/liquid interface were studied (e.g. adhesion on silica, rigidity). Finally, the influence of aligned microgels on wrinkled PDMS surfaces was studied via stretching experiments.

2.1.2 Assembly Method 1: microgel alignment via spin coating by using wrinkles as templates

Microgel assembly via spin-coating was primarily carried out by using a commercially available spin-coater (Modell WS-650SZ GNPP/lite, Laurell Technology Corp). For the topographically structured surfaces, wrinkling was induced by exploiting differences in

Young's moduli of plasma treated elastomeric PDMS. Details regarding the experimental setups can be found in Chapter 4; details regarding the theoretical background of buckling were previously discussed in Chapter 1.3. To circumvent a high amount of stress fractures, e.g. cracks, the nanowrinkled PDMS substrates were stabilized by placing the bottom of the substrate onto a glass slide.

For microgel alignment via spin-coating, the PDMS wrinkles had to be plasma treated a second time before starting the alignment process. This is necessary, because the SiO_x surface turns hydrophobic within several minutes due to diffusion of oligomeric PDMS through the thin glass layer. [95, 98] Afterwards, the substrates were placed into the spin-coater and the microgel dispersion was pipetted onto them. Microgel alignment during spin-coating is induced by centrifugal forces and subsequent solvent evaporation (Figure 19).[173, 174] Preliminary parameter settings, e.g. particle concentration and spin-coating conditions, were derived from the prior diploma thesis on this topic created by the author of this doctoral thesis.[94]

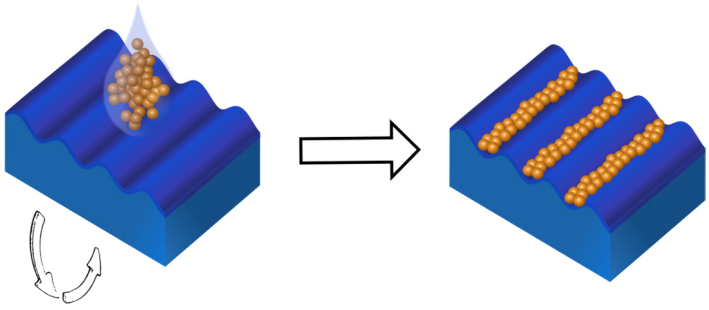

Figure 19: Schematic depiction of a spin-coating process. Left: application of microgel dispersion and start of the rotation program. Right: Microgel alignment at the end of the process.

From here on spin-coating including all follow up processes, e.g. printing, are referred to as Assembly Method 1. In the following, the applicability of this method towards aligning soft polymer particles is discussed by using different microgel types. As model systems the following microgels were used:

i) N-vinylcaprolactam/acetoacetoxyethyl methacrylate: **VCL/AAEM microgels**

ii) N-isopropylacrylamide/N-vinylcaprolactam: **NIPAAm/VCL microgels**

iii) N-isopropylacrylamide: **NIPAAm microgels**

iv) N-vinylcaprolactam/acetoacetoxyethyl methacrylate/cetyltrimethylammonium bromide. **VCL/AAEM/CTAB microgels**

The microgel types differ in mechanical properties, size, chemical composition and surface charges.

Wavelength and amplitude dependent alignment

Preliminary work showed that the alignment of microgels within the wrinkle grooves is dependent on the wavelength λ and amplitude *A* of the wrinkles.[94] As an example, the alignment of relatively rigid VCL/AAEM microgels on wrinkles with increasing λ and *A* is shown in Figure 20.

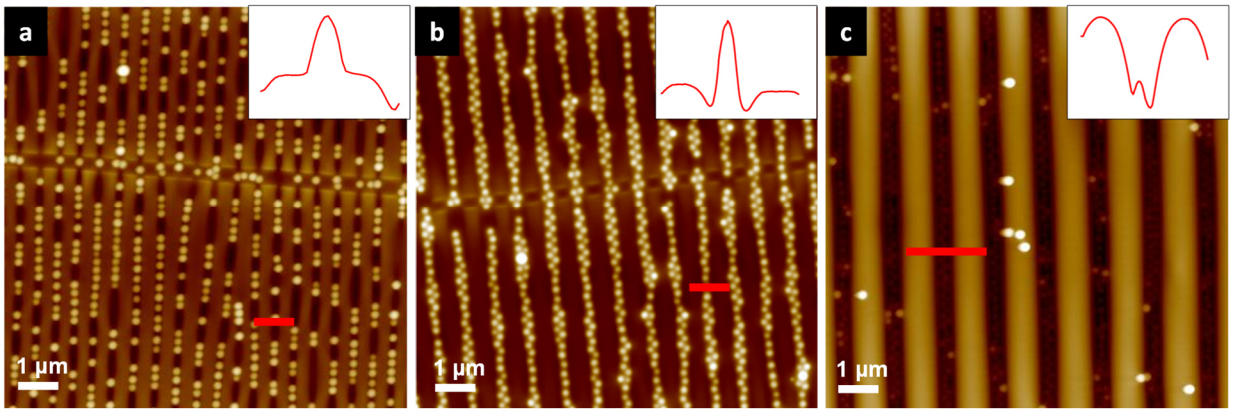

Figure 20: AFM height images of VCL/AAEM microgels with R_H ~ 250 nm which were spin-coated on substrates with increasing wavelengths λ and amplitudes *A*. a: wrinkles with λ ~ 500 nm, b: λ ~ 800 nm, c: λ ~ 1300 nm (Δz = 200 nm).[94]

VCL/AAEM microgels can be considered as relatively rigid due to the sterically demanding N-vinylcaprolactam rings and the concentration of AAEM in the core region of the

microgels.[56] AFM images verified the latter assumption (Figure 21). Upon adsorption on flat silica surfaces VCL/AAEM microgels (Figure 21d/f) nearly maintain their shape in dispersion and were very similar to the rigid silica particles (Figure 21a/f). They deform only slightly which can be observed as a small bulge enclosing the main body forming a fried egg like shape (Figure 21a/f red arrow). In contrast, the soft NIPAAm microgels flatten out entirely when adsorbing onto the silica surface (Figure 21b, c/f). Surprisingly, NIPAAm/VCL microgels with various copolymer ratios showed a similar adsorption behavior.

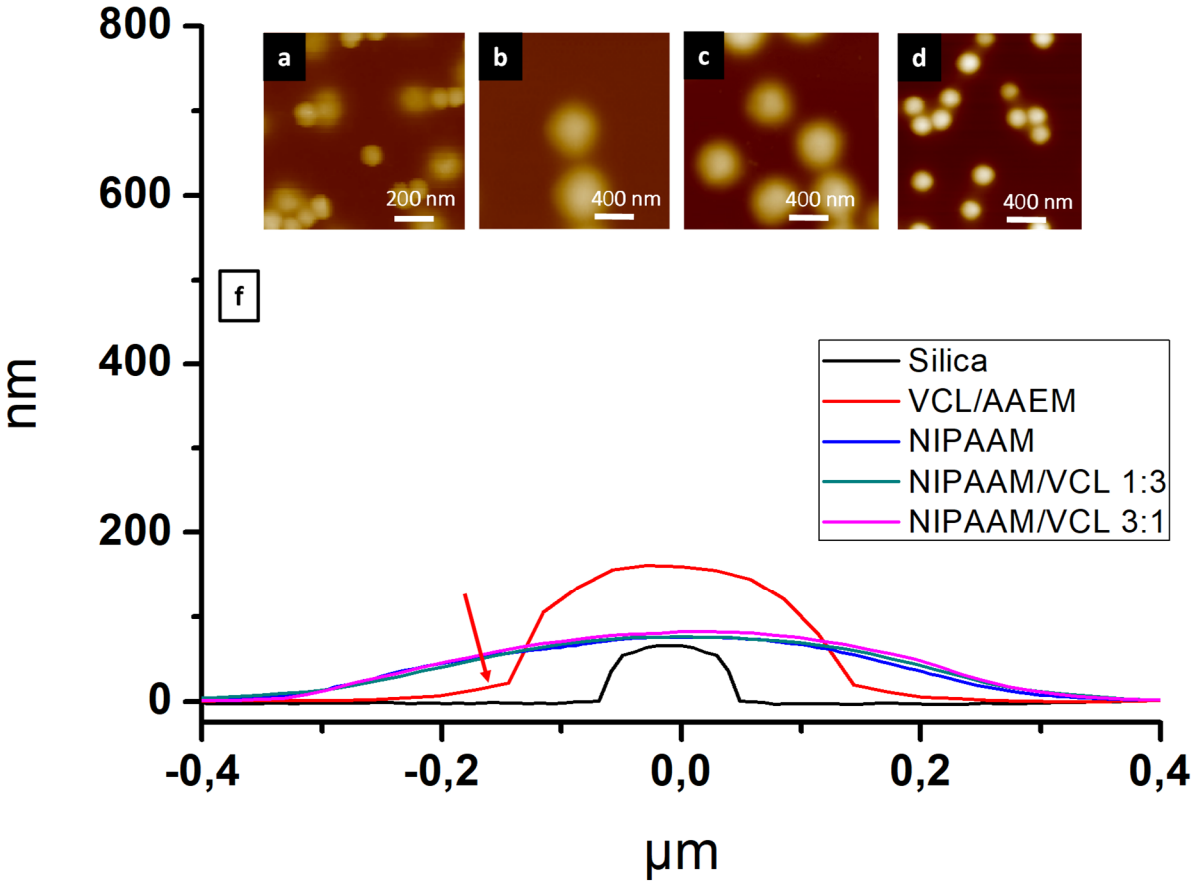

Figure 21: AFM images of a: silica particles; b: NIPAAm microgels; c: NIPAAm/VCL 1:3(3:1) microgels; d:VCL/AAEM microgels and f sections of all microgels compared to a section of a silica particle.

A close proximity alignment of VCL/AAEM microgels with a low defect rate begins when λ exceeds the hydrodynamic radius of the microgel by about 1.5 times. This is shown in

Figure 20b in comparison to Figure 20a. A dense alignment is necessary for the formation of 1D microgel arrays. With further increase of λ, the microgels submerge into the wrinkle grooves, because the amplitude A increases proportionally to the wavelength (Figure 8).

By carefully tuning the wavelength, a nearly defect free close proximity alignment of the VCL/AAEM microgels can be achieved (Figure 22). In this case, the λ/R_H ratio was around 1.8. Furthermore, this fine-tuning approach opened the way towards more complex alignment such as zigzag structures (Figure 22c). Böker et al. showed that by using gradient wrinkled surfaces the desired wavelength for the individual microgel types can be found out quickly.[103]

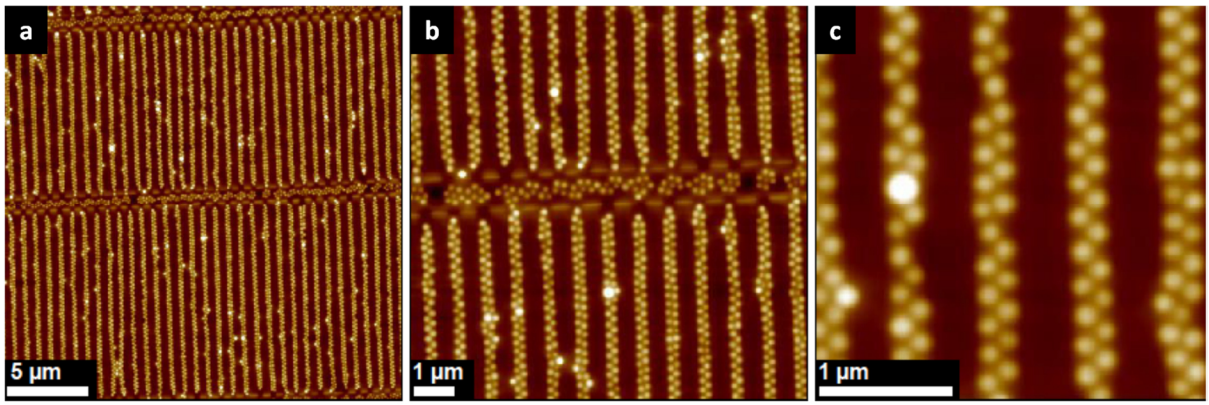

Figure 22a-c: AFM height images of VCL/AAEM microgel arrays (R_H ~ 250 nm) in zigzag formation which were spin-coated on wrinkled substrates with λ ~ 900 nm. a and b showed perpendicular aligned cracks (Δz = 250 nm).[94]

The section in Figure 20b showed that the microgels reside slightly above the wrinkled structure which is an important factor for their successful transfer onto other flat surfaces. In a subsequent experiment, the microgels arrays from Figure 22 were transferred onto an oxidized Si-Wafer (Figure 23).

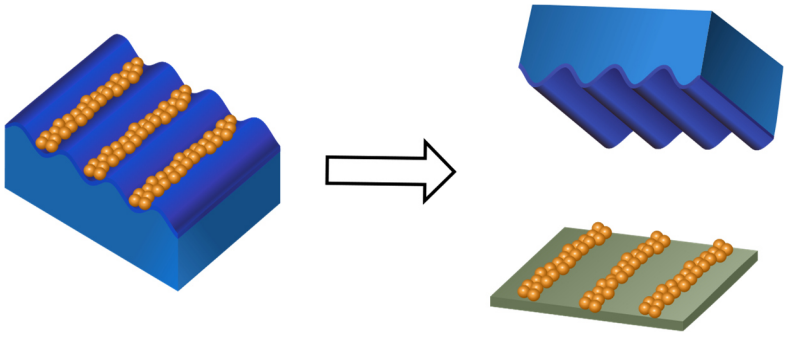

Figure 23: Schematic depiction of the printing process.

Due to the increase in hydrophobicity of the wrinkles over time, a few µL of water were very helpful to transfer the aligned arrays onto the desired surface. It is shown in Figure 24 that the formation from Figure 22 can be transferred without losing much of its structural integrity. Some small defects and lose microgels can be seen in Figure 22b, but considering that the particles had no interparticle connectivity, e.g. via cross-linking, the transferred arrays showed a low defect rate combined with a high periodicity determined by the template.

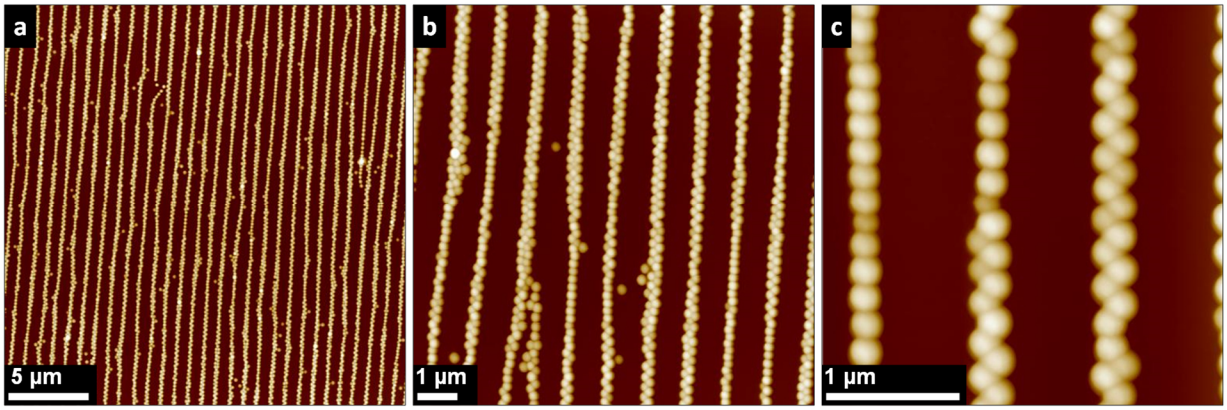

Figure 24a-c: AFM height images of VCL/AAEM microgel arrays (R_H ~ 250 nm) in zigzag formation which were transferred onto a Si-wafer. The space between the arrays remained equal to the wavelength of the substrate (λ~ 900 nm & Δz = 200 nm).[94]

Latter assumption was validated through comparing the mean distances between two arrays taken from relatively small areas (30µm²) via AFM-imaging with the average distance

derived out of GISAXS measurements which analyzed the whole sample area (2 cm^2; details can be found in the attachments).[94] In conclusion, it can be stated that the template dimensions (e.g. λ and A) determine the array formation (e.g. zigzag, ribbon, pearl necklace) and average distance between two arrays. Furthermore, by using wrinkled surfaces, a high periodicity combined with a low defect concentration can be achieved over large areas up to 2 cm^2. The maximum limit is only determined by the template size and defects are determined by the number of perpendicularly aligned cracks (Figure 22a and b). The experiment showed that this approach is suitable for the relatively rigid VCL/AAEM microgels.

However, when using softer microgels such as pure NIPAAm and NIPAAm/VCL 3:1 microgels, this method reaches its limitations for particle alignment, but at the same time offers insights regarding microgel properties and surface adhesion. For example, the analogue alignment experiment with pure NIPAAm microgels showed no dependency on the template dimensions. On the contrary the microgels adsorbed homogeneously in a monolayer for all wavelengths. Residual microgels were washed off due to the interparticle repulsion.[183, 184]

Presumably, the amide groups of the NIPAAm matrix form hydrogen bonds with the silanol groups of the Si-wafer. In order to explore this hypothesis, adhesion experiments with different microgel types were conducted in collaboration with the von Klitzing group. By using an oxidized Si-tip, the interaction between the silanol rich tip and the microgels were measured through the retraction curve after contact with the microgels. The relationship between contact area and load by DMT theory was verified by Enachescu et al. with an atomic force microscope (AFM).[196] In Figure 25 it can be seen that the normalized adhesion energy for the NIPAAm microgels was twice as high compared to the other microgel types which contained VCL. These results could explain the sticky character of NIPAAm microgels (Figure 26). These adhesion energies are in the same range as the theoretical adhesion energies calculated via DMT-model between polyester sheets (32.5 mJ/m^2) and polyester-silica sheets (20 mJ/m^2) undergoing interfacial separation.[197] The separation of graphite-silica interface would require around 80 mJ/m^2.[197]

Furthermore Horn et al. determined an adhesion energy of 25 mJ/m² for silica particles from their the elastic behavior within silica powder.[198] For the same model system (silica powder) Broersma et al. measured adhesion energies around 40 mJ/m².[199, 200]

Thus, the more rigid VCL microgels behave more like solid silica particles whereas the pure NIPAAm microgels shows a stickier behavior. One could argue that this behavior is based on attractive interactions between the silanol groups of the silica tip and the acrylic moieties of the microgel.

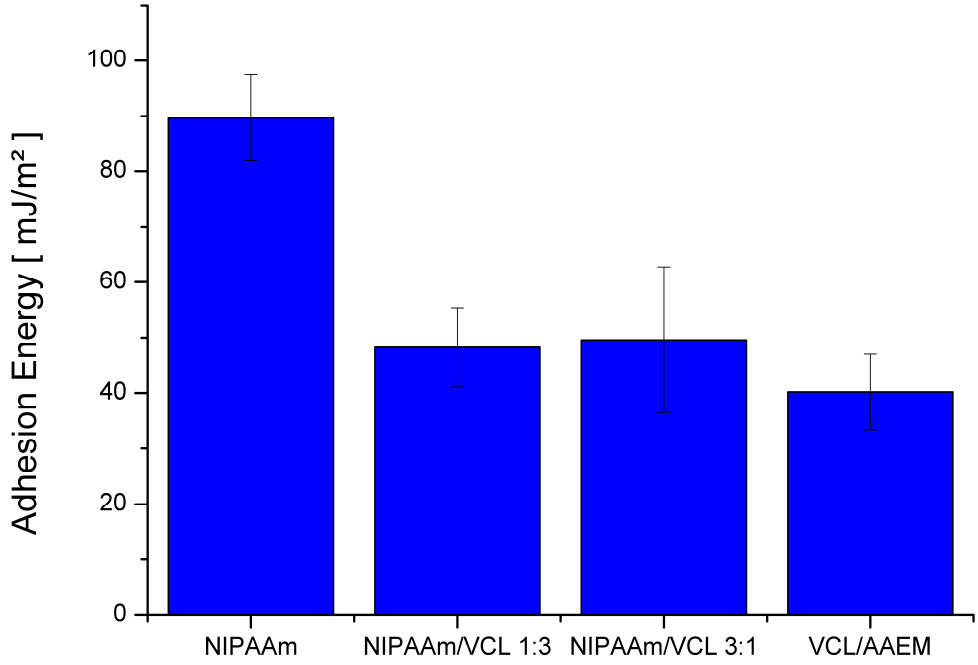

Figure 25: Adhesion energy measurements of the examined microgels provided by the von Klitzing group (TU Berlin). The normalized adhesion energies were calculated based on a 25 nm tip radius.

The homogeneous coverage of the wrinkled template is solely based upon the interaction between the Si-wafer surface and the NIPAAm. Figure 26a-c shows a gradual decrease of NIPAAm microgel concentration. The microgels tend to increase the contact area with the wrinkled surface as much as possible, thereby deforming into barely visible flat disks (Figure 26c), which was confirmed by the AFM sections in Figure 21 of non-confined NIPAAm microgels.

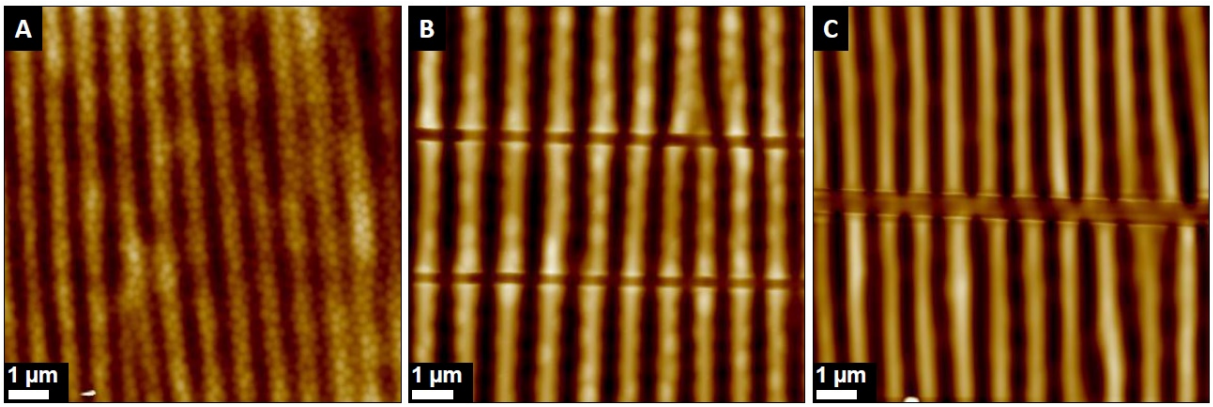

Figure 26: AFM height images of wrinkles (~900 nm) covered by NIPAAm microgels (R_H ~ 250 nm) which were spin-coated onto them. a: dispersion with 2 wt% NIPAAm microgels, b: dispersion with 0.5 wt% NIPAAm microgels, c: dispersion with 0.3 wt% NIPAAm microgels (Δz = 250 nm).[94]

NIPAAm/VCL 3:1 and 1:3 microgels with 25 and 75 wt-% VCL were used for similar experiments (Figure 28a-f). By copolymerizing the soft and thus flexible NIPAAm with the rigid VCL, an intermediate behavior in terms of rigidity and surface interaction was initially expected. Although this was disproved in Figure 21, both microgel types aligned similar to the VCL/AAEM microgels in terms of selective occupation of the wrinkle grooves (Figure 28a-f). When aligned on small wrinkles the microgels tend to bend while residing within the wrinkle grooves (Figure 27 and Figure 28a/d).

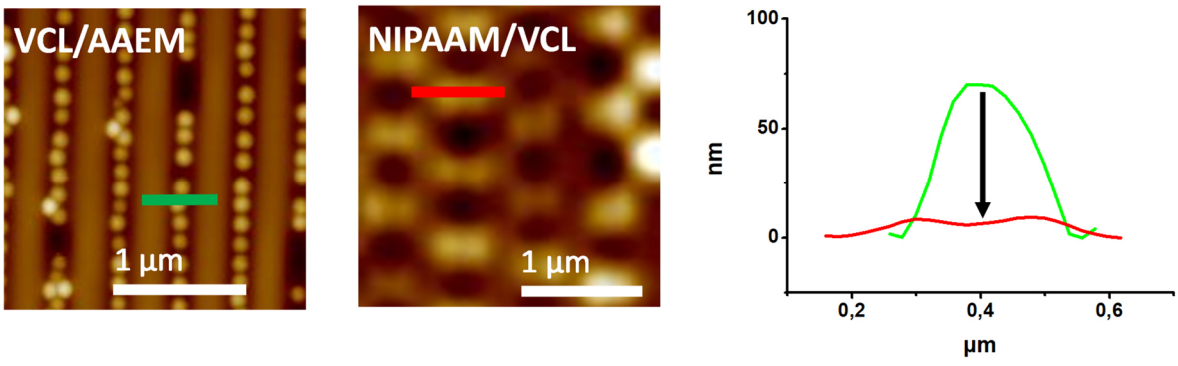

Figure 27: Comparison of the flexibility of VCL/AAEM vs NIPAAm/VCL microgels

This strong deformation is due to the flexible NIPAAm copolymer within the microgel matrix. However, as can be seen in all images, the alignment via spin-coating shows a lot of defects, which can be explained by steric repulsion between NIPAAm rich particles.[10] Furthermore, both microgel types show signs of an adsorption behavior somewhere between pure NIPAAm and VCL/AAEM microgels towards the Si-surface, as the corresponding images in Figure 28a-f show.

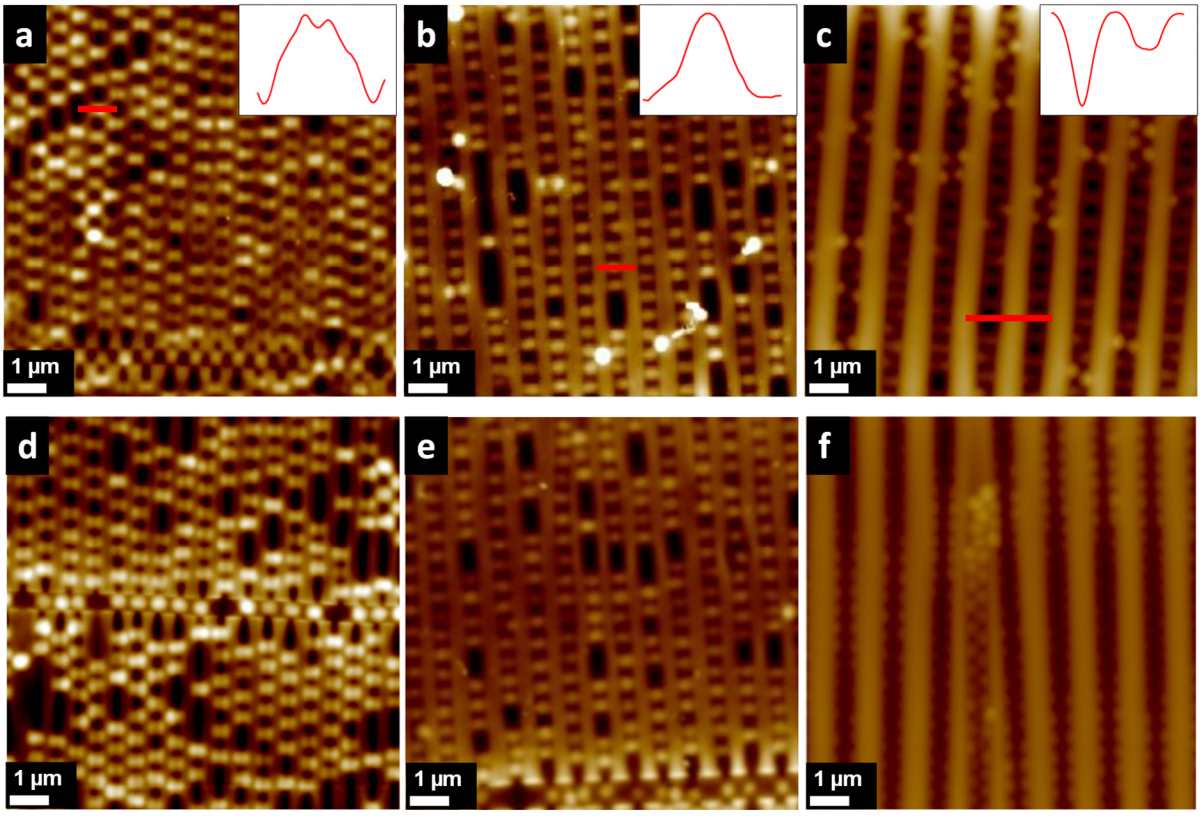

Figure 28a-c: AFM height images of NIPAAm/VCL 3:1 microgels with R_H ~ 350 nm which were spin-coated on substrates with increasing wavelengths λ and amplitudes *A*. a: wrinkles with λ ~ 500 nm, b: λ ~ 750 nm, c: λ ~ 1300 nm.[94] d-f: AFM height images of NIPAAm/VCL 1:3 microgels with R_H ~ 330 nm which were spin-coated on substrates with increasing wavelengths λ and amplitudes *A*. d: wrinkles with λ ~ 500 nm, e: λ ~ 750 nm, f: λ ~ 1300 nm (Δz = 250 nm).

In another approach, microgels were synthesized in presence of the surfactant CTAB in different concentrations, leading to smaller particle sizes.[56, 201] As can be seen in Figure 29, these microgels remain similarly rigid as the VCL/AAEM microgels.

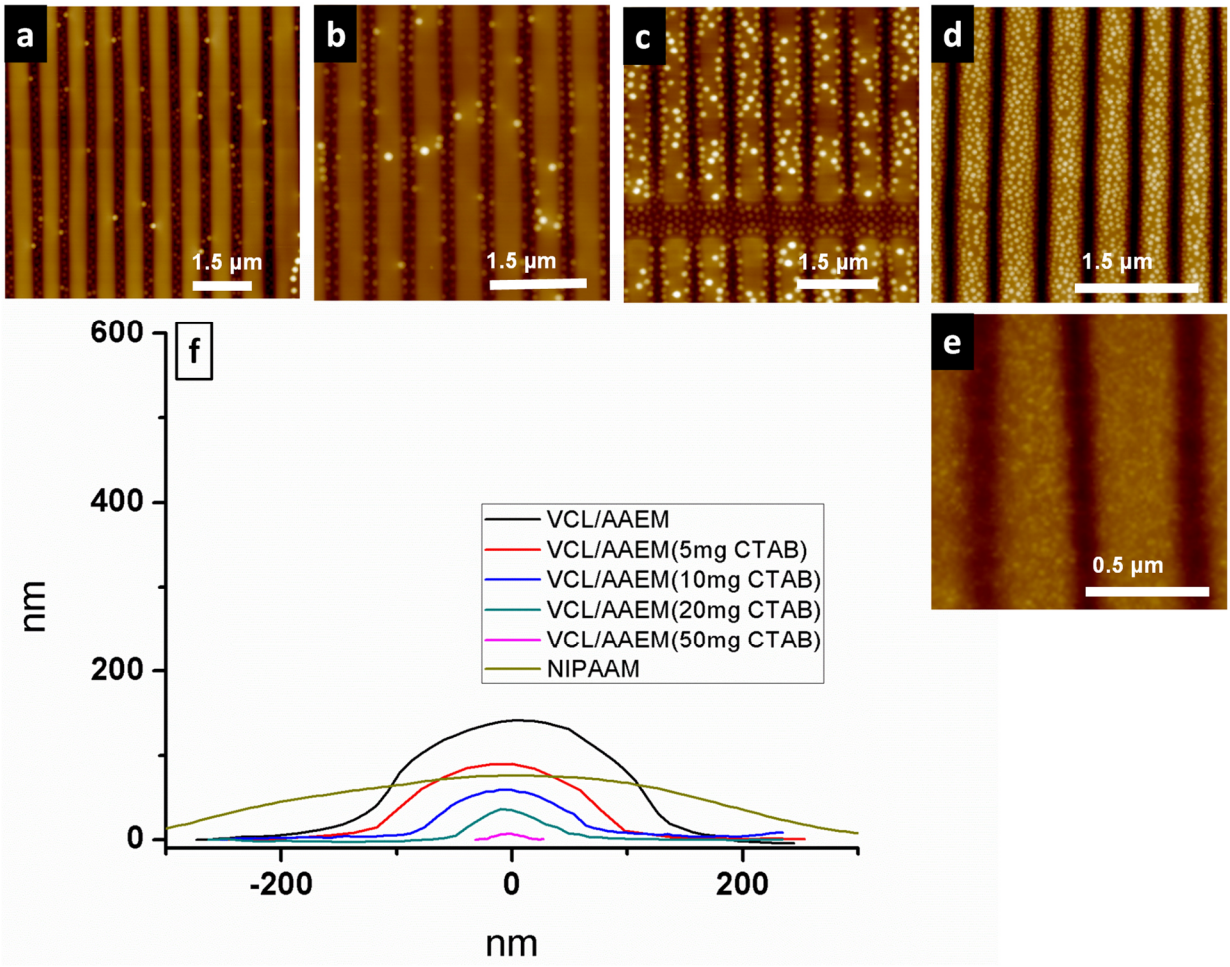

Figure 29a-e: AFM images of VCL/AAEM microgels with increasing CTAB content during synthesis compared to a section of a NIPAAm microgel (Δz = 300 nm). a: standard VCL/AAEM microgels; b: 5 mg CTAB; c: 10 mg CTAB; d: 20 mg CTAB; e: 50 mg CTAB; f: comparison of AFM sections.

The main idea of decreasing the microgel size was to obtain small microgels for alignment in wrinkles with lower λ. The AFM images in Figure 29a-e showed the alignment behavior via spin-coating of the VCL/AAEM microgels synthesized with increasing amount of

emulsifier. Although the microgel shrunk in size with increasing CTAB content, the alignment quality worsened. This is not surprising since CTAB brings a positive charge into the microgels which in turn leads to an interaction between the now positively charged microgels and the negatively charged substrate. Based upon these findings, a transfer onto a substrate was not pursued.

The Assembly Method 1 showed to be only suitable for relatively rigid VCL/AAEM microgels, as they were able to assemble uniformly and in close proximity within different wrinkle grooves. However, printing in good quality is only feasible at a specific wrinkle wavelength λ when the microgels reside above the nanostructure. In principle, printing with NIPAAm/VCL microgels is possible, but the defect rate was very high (see Chapter 7).

2.1.3 Assembly Method 2: microgel assembly via confinement by wrinkled substrates

As a second assembly method, wrinkles were used as a confinement/mold for microgel assembly. Therefore, the microgels were placed onto a glass substrate. Subsequently, the topographically structured surfaces were pressed on top and the setup was allowed to dry (Figure 30). Details regarding the experimental setups can be found in Chapter 4.

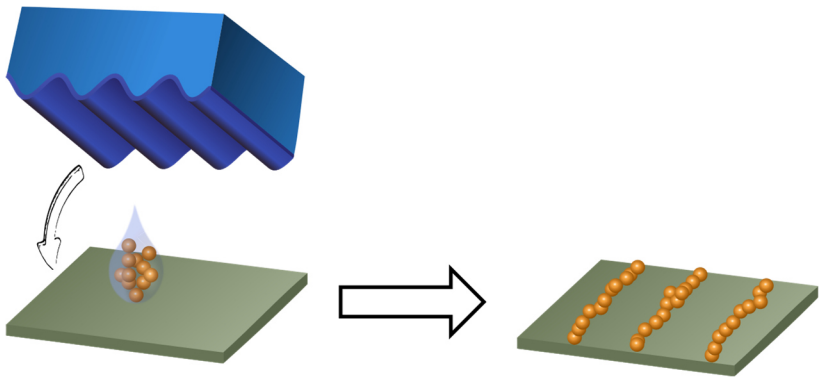

Figure 30: Schematic depiction of the molding/confinement process. left: a droplet microgel dispersion is placed between the template the substrate. Afterwards the template is pushed onto the substrate. Right: Microgel alignment at the end of a 24h drying process.

From here on the molding method including all follow up processes is referred to as Assembly Method 2. In the following, the applicability of this method towards aligning soft polymer particles is discussed by using different microgel types.

The Assembly Method 2 showed different assembly qualities depending on the microgel composition. The rather rigid VCL/AAEM microgels show an equidistant alignment of the particles with still distinguishable microgel particles within the arrays. However, a significant amount of residual microgels were not aligned and remained in between the arrays (Figure 31a). The pure NIPAAm microgels formed similar arrays but the single microgels were not distinguishable anymore. They were strongly deformed by the template (Figure 31b).[94] The surface of a substrate with aligned NIPAAm/VCL microgels arrays was scratched with a needle, to determine if the space in between the arrays was at the same height level as the surface of the Si-wafer. It can be seen in Figure 32 (cross section) that some microgels were flattened to the point that they formed a very thin polymer film in between the arrays. In contrast to the latter, both NIPAAm/VCL microgels formed arrays with no residual microgels in the interspatial areas (Figure 31c-d). Still, in both cases, the microgels were in a deformed state, whereby the NIPAAm/VCL 1:3 microgels with a predominant VCL amount seemed to retain their shape better (Figure 31d). The cracks in Figure 31c showed that without confinement there would be a random distribution of microgels on the substrate surface.

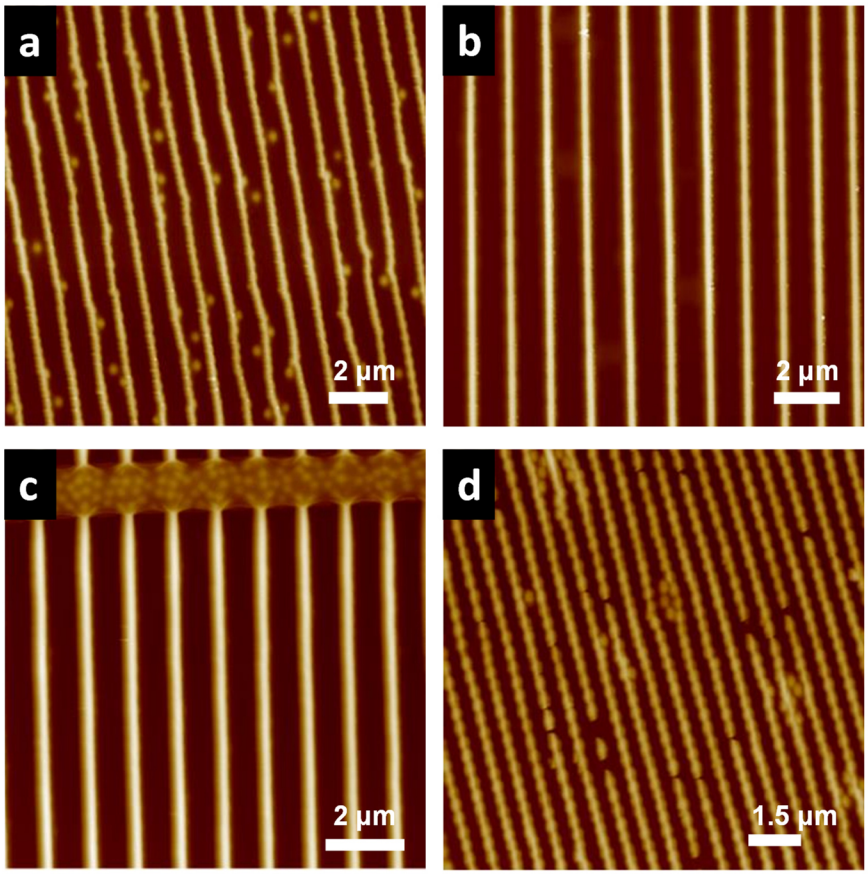

Figure 31a VCL/AAEM; b: NIPAAm; c: NIPAAm/VCL 3:1; d: NIPAAm/VCL 1:3 (Δz = 350 nm).

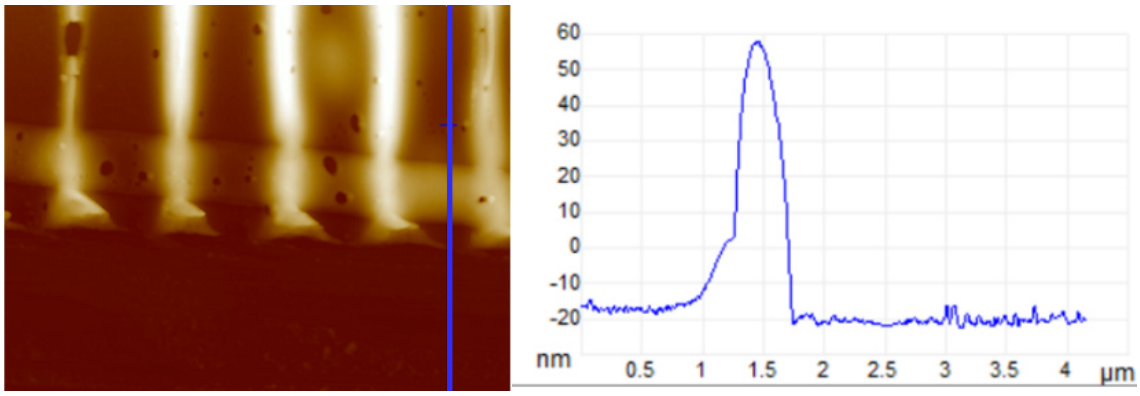

Figure 32: NIPAAm microgels molded on a Si-Wafer and scratched by a needle.

By adjusting the wavelength λ of the templates, the spacing in between the flexible NIPAAm/VCL 3:1 microgels could be controlled (Figure 33a-c). Due to their

deformability, the microgels were able to adapt to the narrow spacing down to approximately 300 nm. The fabrication of microgel arrays with tunable spacing is also feasible with the more rigid VCL/AAEM microgels. However, due to their rigidity, the particle size has to be adjusted carefully to fit the wrinkled dimensions (Figure 20a-c). For this purpose, the VCL/AAEM/CTAB 5, 10 and 20 mg CTAB were used for the respective arrays depicted in Figure 33d-f. The small wrinkles were fabricated according to previously published literature.[104]

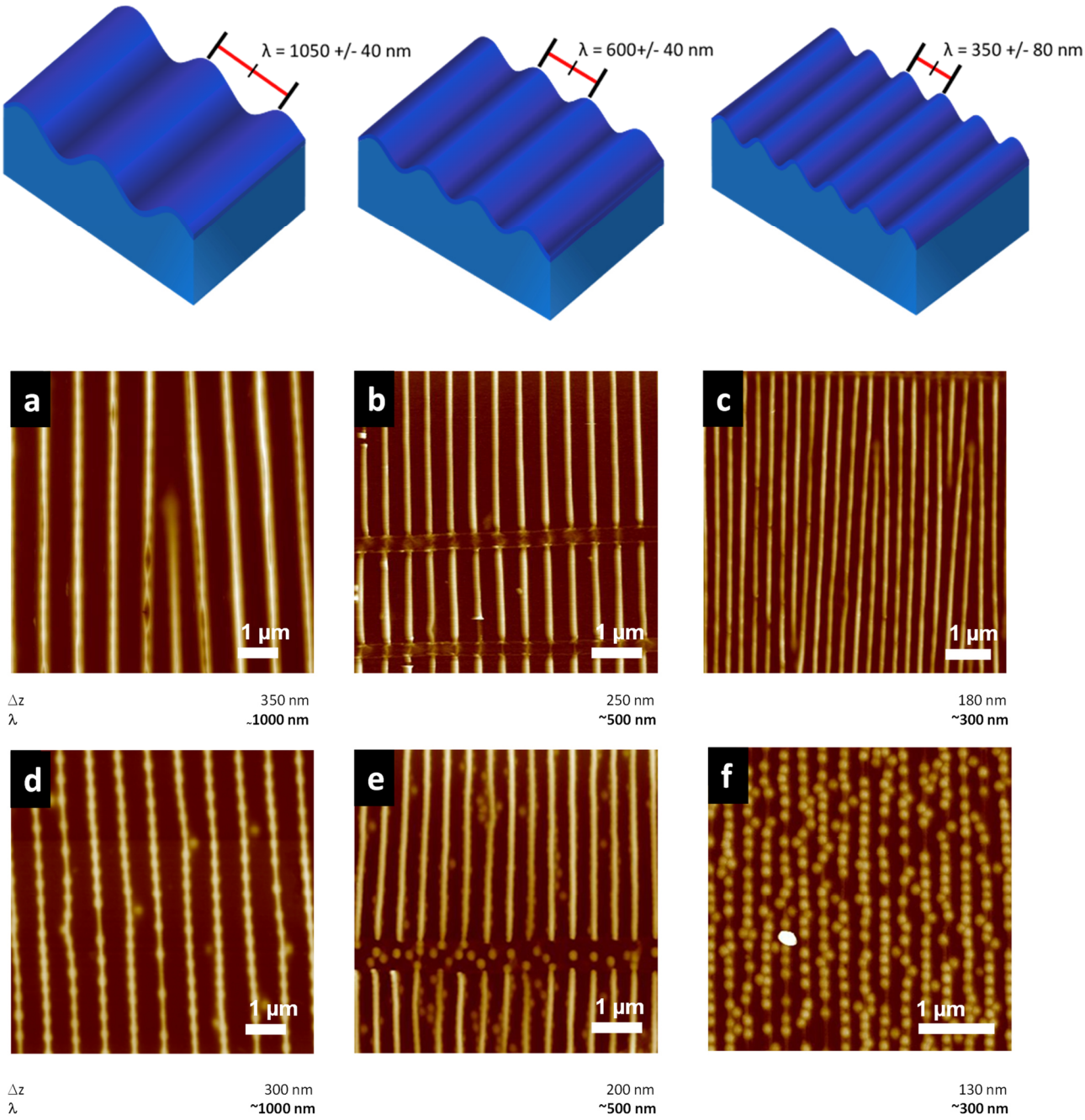

Figure 33: microgel arrays fabricated with Assembly Method 2 show tuneability of spacing between the arrays correlates directly with the wrinkle wavelength λ. a-c: deformed NIPAAm/VCL 3:1 microgels arrays with decreasing space between the individual arrays with a: R_H = 379 nm, b: R_H = 201 nm and c: R_H = 180 nm. d-f: VCL/AAEM arrays with decreasing space between the individual the arrays. d: R_H = 180 nm, e: R_H = 150 nm and f: R_H = 70 nm (see Chapter 7).

2.1.4 Thermo-responsiveness of microgel arrays on silica surfaces

With VCL/AAEM arrays obtained by Assembly Method 2, temperature dependent swelling experiments were conducted via AFM measurements in water in PeakForce-QNM mode. The question which was addressed by this experiment was whether the VCL/AAEM microgels were deformed by the molding process and if their inherent property to swell and collapse during temperature change was still present. The conventional AFM Tapping mode determines the morphology through changes of the amplitude and the phase of the cantilever in a resonant mode. These cantilevers are not sensitive to interactions between tip and the fuzzy microgel surface, which leads to a dampening of the resonance in tapping mode and thus to a high error in the desired height information obtained through this measurement mode. The standard silica cantilevers had to overcome 80 mJ/m² of adhesion energy (see Figure 25), which is easy to achieve because these cantilevers had spring constants larger than 50 N/m. To observe the fuzzy microgel shells with a more sensitive feedback in regard to the true microgel shape, cantilevers with a spring constant of about 0,1 N/m were used. In contrast to the standard tapping mode the PeakForce-QNM mode determines the morphology through driving the whole cantilever via the piezo element directly towards the sample, thus the height information is calculated through the true deflection of the cantilever after contact of the tip with the microgel. Therefore, the applied force could be regulated and was set at low loading force of 150 pN (with k~0.1 N/m, tip radius 5 nm and amplitude of 400 nm). The samples were heated by the liquid cell apparatus and the experimental temperatures were measured in the bulk liquid. Details regarding the measurement method can be found in Chapter 5.1. In Figure 34, AFM images of VCL/AAEM microgels after removing the mold are depicted. As can be seen, the microgels change their shape drastically after immersion in water (Figure 34). Comparison of the AFM images in the dry state with the wet state at 25 °C showed that the microgels regained their spherical shape during rehydration losing at the same time the interparticle connectivity (Figure 34a-b). Upon further increase in temperature, the appearance of the microgels does not change much. However, upon increasing temperature, the margin of

error regarding the height information increases, because the spring constant k is temperature dependent. This can be observed in Figure 34e, where the image is blurry.

The size change during the whole temperature experiment including the rehydration of the microgels after the application of water is depicted in the corresponding cross-sections (Figure 34f). It can be observed that the microgels increase around 75% in size after exposure to water. Furthermore, the microgels in the dry state showed indentation marks on both sides due to the imprint of the removed template (Figure 34a) which also forces the microgels to use the remaining space between each other forming lamellar structures. Although the VPTT of the VCL/AAEM microgels begins around 28°C,[12] no significant height changes could be observed in the temperature range of 25-33°C. The first significant decrease in height appeared at 36°C leading to a small collapse of ca. 30% with respect to the fully inflated microgels at 25°C. Compared to the maximum collapse capability of freely dispersed VCL/AAEM microgels of around 80% (Figure 4), 30% seemed rather small, but it has to be taken into account that the microgels are limited in their expansion through the surface adhesion on a Si-wafer. Furthermore, the set temperature of the heating stage could differ from the actual temperature of the solution because the system lost heat through convection and heat emission of the open setup (heating rate 3°C/min; equilibrium time 10 min). Additionally, the experiment could only be carried out until at 36°C the maximum limit of the heating stage was reached. For this reason, it could not be determined if the collapse was completed or not. Due to this, experiments with NIPAAm microgels were not carried out, since their VPTT starts at 32°C.[202]

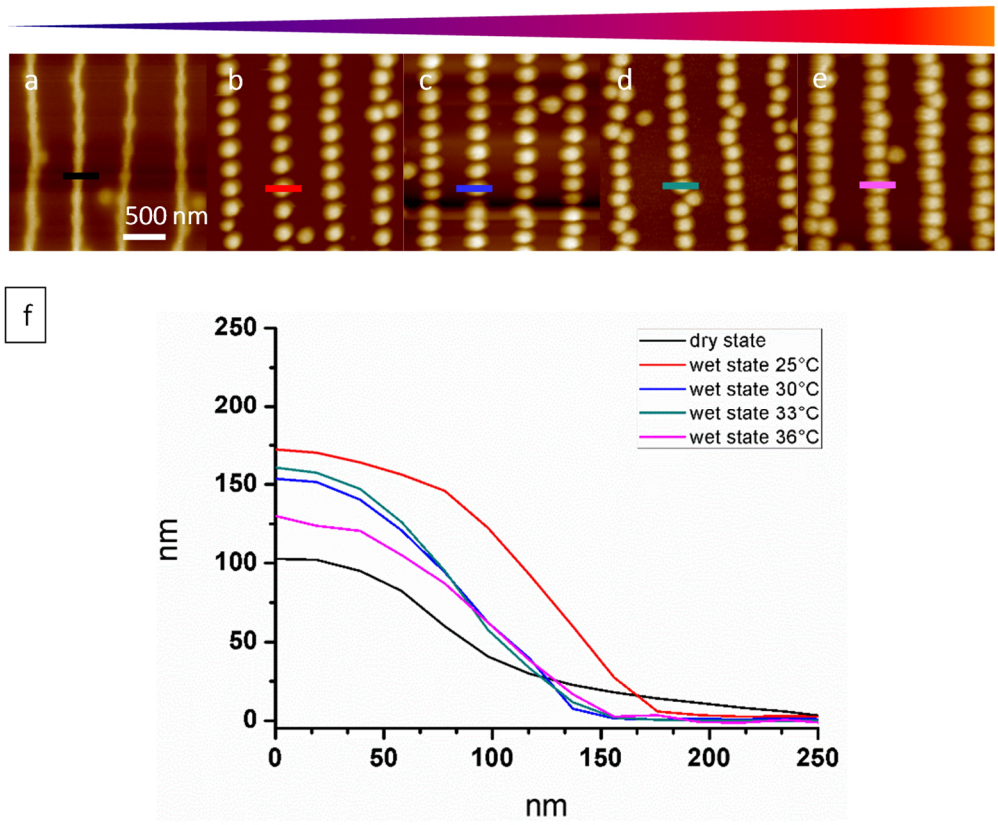

Figure 34: Swelling behavior of VCL/AAEM microgels after molding. a: dry state at 25°C, b: wet state at 25°C, c: wet state at 30°C, d: wet state at 33°C and e: wet state at 36°C. f: corresponding AFM cross-sections.

2.1.5 Softness and deformability of microgel arrays

In the following, experiments are discussed which focus on the softness and deformability of the microgels in arrays assembled with Assembly Method 2. Again, all AFM measurements were conducted by using PeakForce-QNM. In order to examine the degree of deformability of microgels in a hydrated state, the loading force of the cantilever was raised from 150 pN to 300 pN (with k~0.1 N/m, tip radius 5 nm and amplitude of 400 nm). According to literature by using PeakForce-QNM with spring constants around 0.1 N/m, detecting E-Moduli < 20 MPa should be feasible.[193] Details regarding the measurement method can be found in Chapter 5.1.

AFM images of VCL/AAEM microgel arrays in the dry state, in hydrated states before and after deformation are depicted in Figure 35a-c, with their corresponding cross-sections in Figure 35d. The pronounced increase in height by 30% after hydration in water was observed again (Figure 35d). The application of 300 pN load force led to a deformation of the microgels. 300 pN was the maximum force which could be applied by using the 0.1 N/m cantilevers. Interestingly, comparing the cross-section of both hydrated states with the reference measurement of VCL/AAEM microgels spin coated on Si-wafers, no differences were observed regarding the height. The reference microgels only seemed to be broader which could be a further indicator of the influence of the template imprint. Based on this observation, one can assume that the microgels which were spin-coated retained a certain amount of water comparable to the amount of the fully hydrated ones. Therefore, it seems that the template deflates the microgels during the assembly process, squeezing out a larger amount of water. The error which arises by comparing two different microgels was neglected based on the data obtained by DLS measurements (Figure 4), which indicate low polydispersity indices for VCL/AAEM microgels.

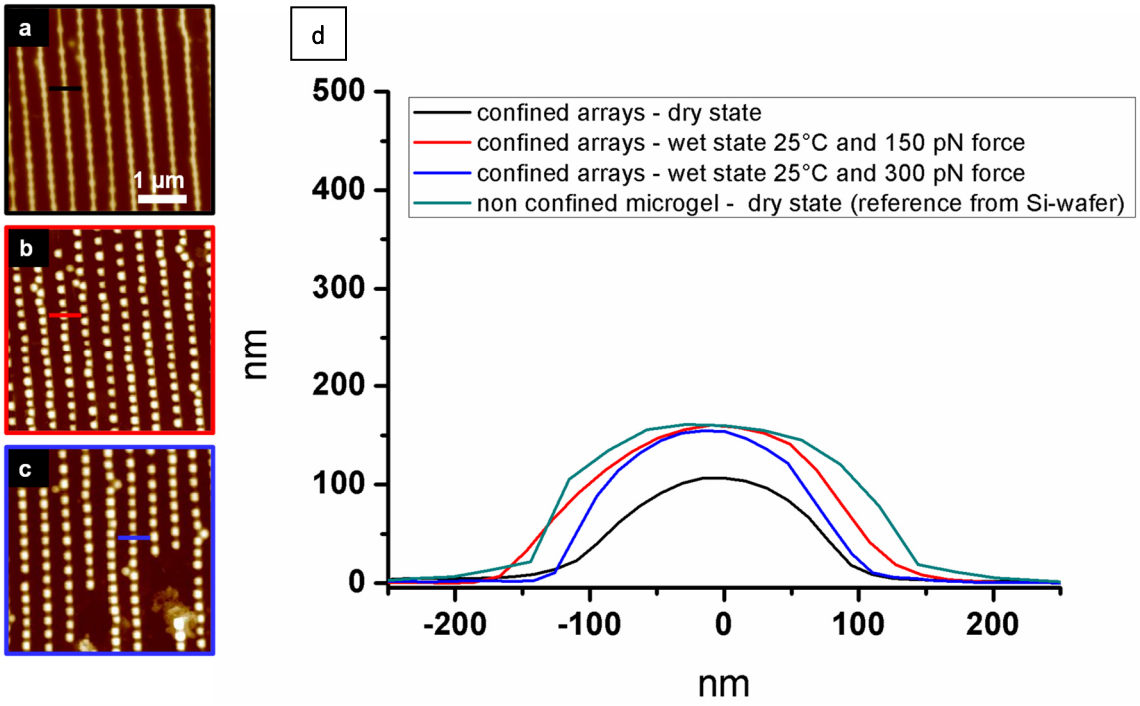

Figure 35: Deformability behavior of VCL/AAEM microgels after molding. All images were taken at 25°C and Δz = 250 nm. a: dry state, b: wet state and load force of 150 pN, c: wet state and load force of 300 pN. d: corresponding cross-sections.

Similar experiments were conducted with NIPAAm microgel arrays. As discussed above, these microgels change from continuous arrays into single spherical shapes losing their interparticle connectivity (Figure 38a-b). In contrast to the VCL/AAEM microgels, for the NIPAAm microgels the influence of the load force can be seen visually in the AFM images where the same vertical scaling was used (Figure 38b-c; z-axis = 350nm). PeakForce QNM also enables to compare the relative E-moduli of the microgel arrays (see Figure 35), indicated by the dark regions which represent the relatively soft areas compared to the substrate (Figure 36). The moduli of microgels in the dry state indicate that there is almost no apparent difference between the moduli of the Si-Wafer and the heavily collapsed microgels. After exposure to water, the arrays differ in terms of moduli from the Si wafer. The particles appear soft, even after deforming them.

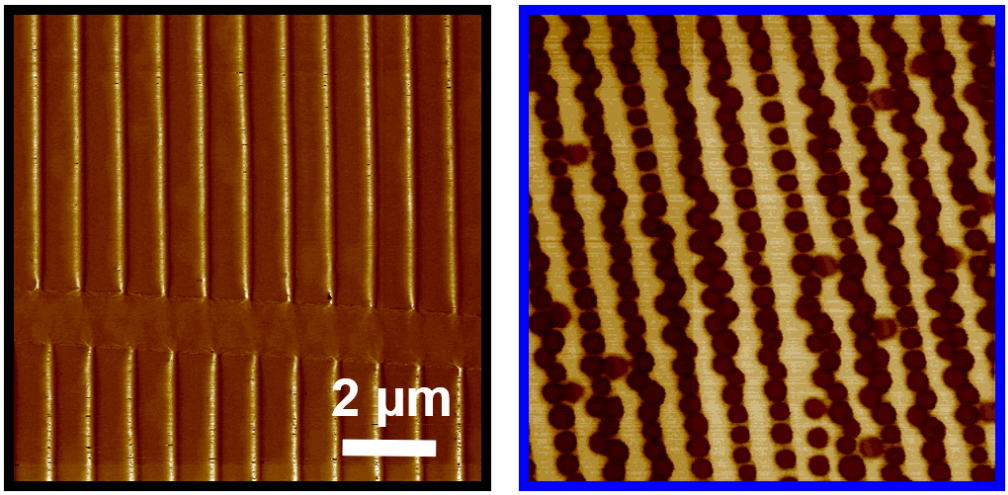

Figure 36: AFM PeakForce-QNM E-moduli mapping. left: NIPAAm in dry sate; right: NIPAAm microgels in the wet state. Dark areas indicate the softer regions.

Comparing the cross-section of the microgel arrays in dry and hydrated states, it was observed that the microgels change minor in height and grow laterally. This can be explained by the influence of the template during the molding process depicted in Figure 37. Herein, it is shown how the space within the wrinkle grooves decreases due to the applied force which is needed during the molding process. The flexible NIPAAm microgels

adapt to the confinement. This leads to their deformed state with them being taller and narrower in comparison to the unconfined NIPAAm microgels in the dry state, obtained through spin-coating. This is one of the reasons why the single microgels within the continuous NIPAAm microgel arrays regain their shape laterally while not swelling much vertically. It must be kept in mind that the real outline of the fuzzy outer shell in the hydrated state is difficult to visualize with invasive AFM. Loading force (150 pN) and tip radius (5 nm) are the crucial factors in determining the true shape of the fuzzy microgels as good as possible, see Figure 2.

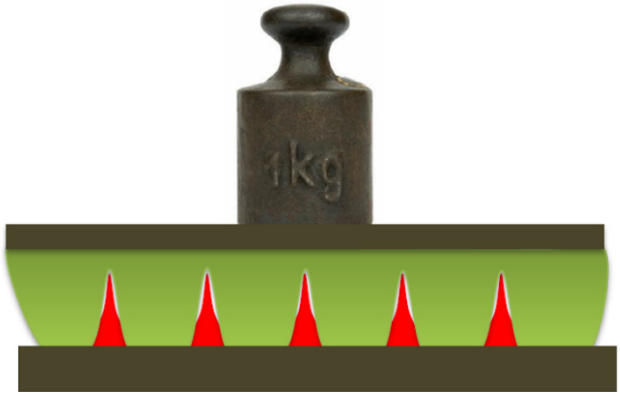

Figure 37: Schematic depiction how the molding process influences the shape of the NIPAAm microgel arrays forming continuous arrays.[94]

In contrast to the VCL/AAEM microgels, increasing the load force from 150pN to 300 pN leads to a homogeneous deformation of the NIPAAm microgels. In Figure 38b-c, it can be seen that the hydrated NIPAAm microgel shrank by 50% due to the increased loading. The microgels were able to re-swell again as shown by the cross-section of the previously deformed microgel taken after 10 min. In terms of a regain in height, they have reached 90% of their fully swollen state. However, the swelling in lateral dimensions is less pronounced (Figure 38). A reason for this behavior could be that during the deformation at 300 pN, the polymer matrix on the outer areas of the microgels was pressed against the silanol-rich substrate. Thus, during reswelling, the polymer in this region has to overcome adhesion on the substrate (Figure 25), leading to a delayed re-swelling behavior. Supporting

this argument is the fact that the polymer matrix of the microgels in the confined state in the same region were not flattened out that much (Figure 38).

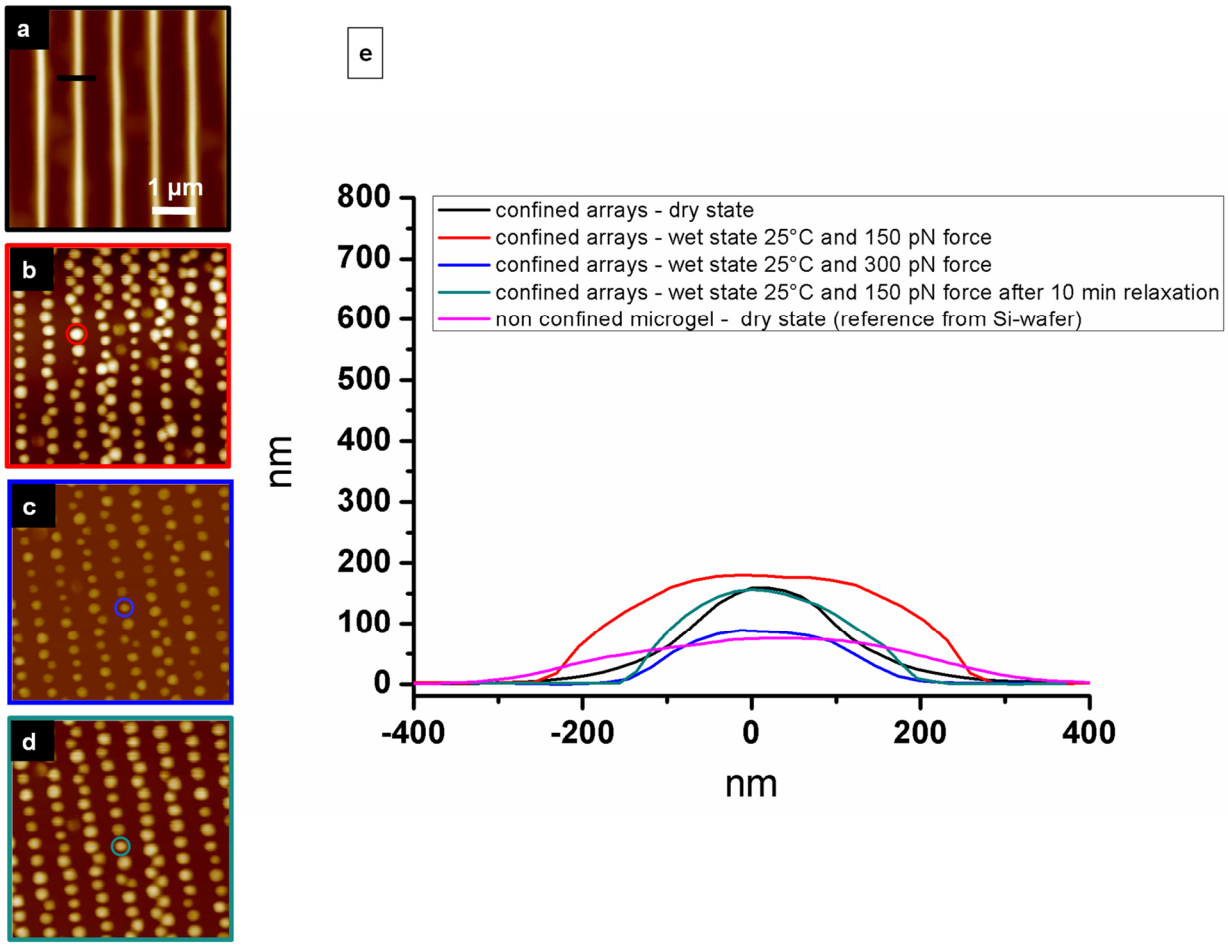

Figure 38: Deformability behavior of NIPAAm microgels after molding. All Images were taken at 25°C and Δz = 350nm. a: dry state, b: wet state and load force of 150 pN, c: wet state and load force of 300 pN, d: wet state and load force of 150 pN after 10 min relaxation. e: corresponding cross-sections.

To prove the assumption that the previously observed difference in deformability between VCL/AAEM microgels and NIPAAm microgels is based on their different intrinsic rigidity, E-moduli measurements in water were conducted in collaboration with the von Klitzing group (TU Berlin).[191] These measurements show that the E-modulus of the

VCL/AAEM microgel center (550 kPa ± 100 kPa) is twice as high as all pure NIPAAm and NIPAAm/VCL microgels (Figure 39).

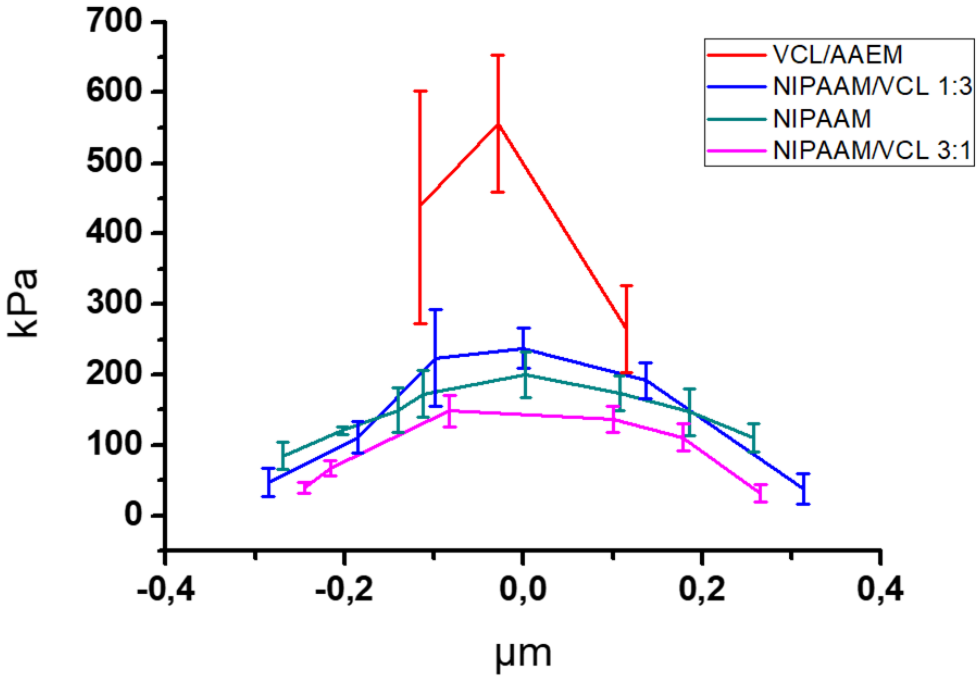

Figure 39: E-moduli measurements in water of the corresponding microgels from Figure 21 provided by the von Klitzing group (TU Berlin).

The E-moduli of latter microgels resided all in the same range of 100-200 kPa ± 30 kPa, which lies in the range of soft matters like gelatin or cells (Figure 39 vs Figure 40).[203]

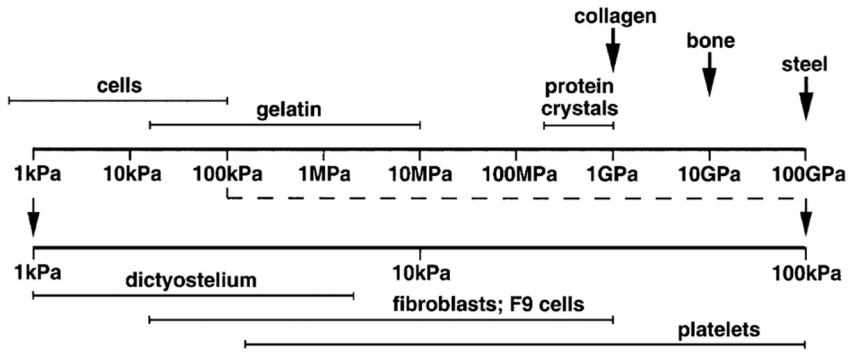

Figure 40: Young's (elastic) moduli of different materials. The diagram shows a spectrum from very hard to very soft: steel > bone > collagen > protein crystals > gelatin, rubber > cells. [203]

2.1.6 Wrinkle-microgel array interaction

In order to assess the wrinkle-microgel array interactions, in-situ stretching experiments were performed. This is important with regard to future cross-linking for the design of supramolecular 1D nanostructures.

With a self-made stretching apparatus, it was possible to measure in-situ the different stretching states of the wrinkled templates with the AFM. Details regarding the measurement method can be found in Chapter 4 and 5.

As can be seen in Figure 41, upon stretching of templates with a wavelength of λ = 1000 nm, the wrinkled structure diminished subsequently with increasing dilation. By exceeding 15% stretching, the amplitude of the wrinkled structures diminished drastically which can be seen in the relative difference in the image contrast. The 29 % stretching applied during this experiment corresponds to the initial stretching of the PDMS substrates during the fabrication of the wrinkles. Upon reaching this point, a flat surface is expected. The cross-sections seemed to confirm this. By each equidistant step of stretching, the amplitude of the wrinkles diminished linearly until reaching 15 % stretching. On the first glance, it seemed that after that the wrinkles were completely flattened out. However, after magnification, one could see that the wrinkled structures were still present but with very low amplitudes. This observation was confirmed by similar experiments with wrinkles which had λ = 800 nm and λ = 650 nm.

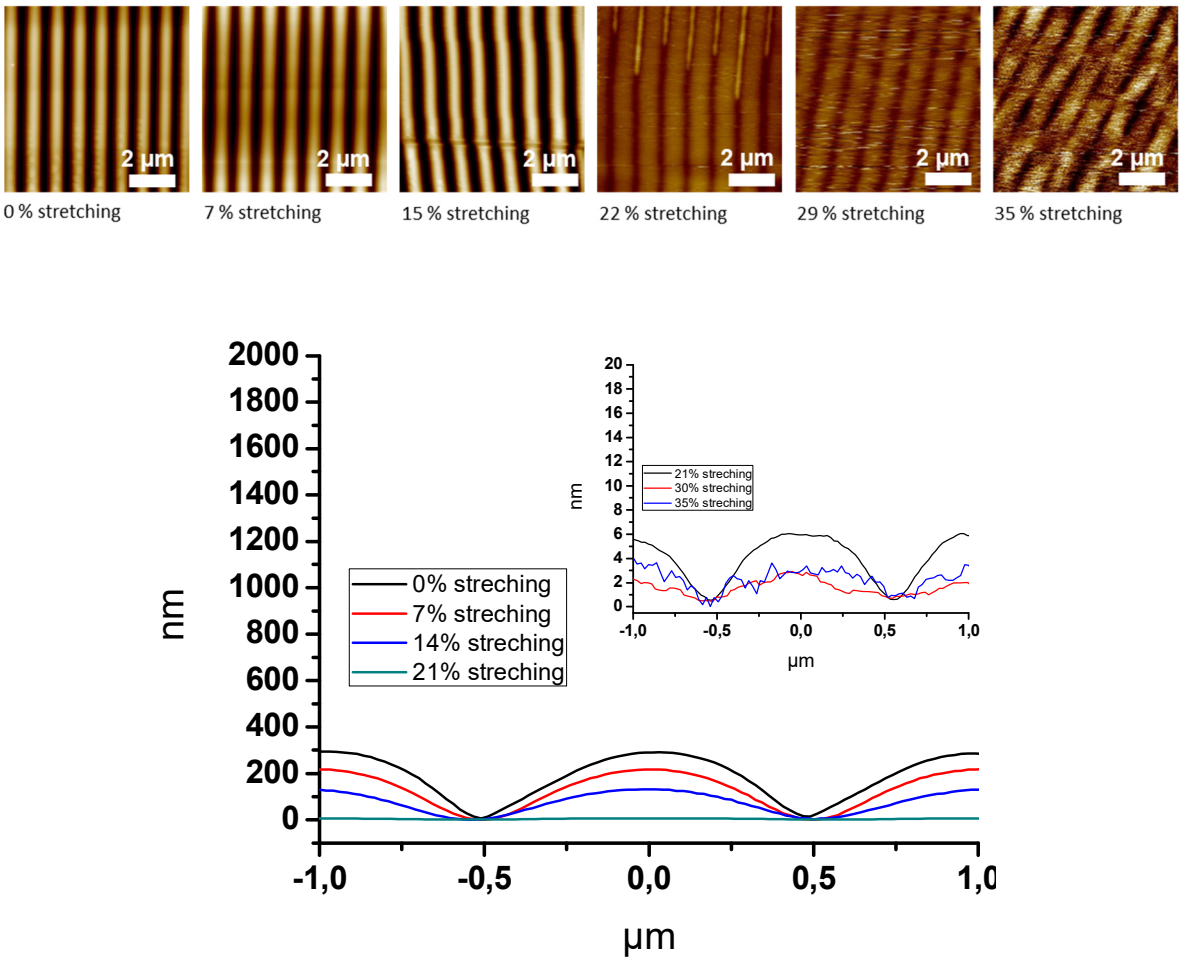

Figure 41: In-situ stretching experiments: AFM images of wrinkles with λ = 1000 nm in different stretching stages and corresponding cross-sections.

Based on this knowledge, it was assumed that microgels can be exposed to the surface by stretching the wrinkled templates filled with them to make the microgels more accessible for further studies and modifications. For this purpose, VCL/AAEM microgels were spin-coated onto wrinkles with wavelengths of $\lambda = 1000$ nm, $\lambda = 900$ nm and $\lambda = 800$ nm. The microgel arrays aligned via spin-coating were cross-linked using UV-light to ensure inter-particle connectivity.

First, the analysis of microgel arrays which were spin-coated into wrinkles with $\lambda = 1000$ nm is discussed. Initially, the microgels resided within the wrinkle grooves, as can be seen in Figure 42, giving no indication how the microgels were aligned within them. Upon

stretching, the microgel arrays were subsequently lifted towards the surface, which can be observed after 14% of stretching. At 21%, the arrays were residing on top of the surface. Interestingly, upon further stretching, it was found that additional microgels were residing deep in the wrinkle grooves and were now revealed to the surface. The 30% stretching applied during this experiment corresponds to the initial stretching of the PDMS substrates during the fabrication of the wrinkles which means that upon reaching this point, a flat surface should be obtained. The revealed microgel arrays will be later discussed as microgel ribbons after cross-linking them by UV-light under stretched conditions. Cross-linking the arrays in the stretched state of the wrinkles allows an unshielded irradiation. The cross-sections revealed that the aligned microgels were lifted subsequently towards the surface. The process started at approximately 150 nm below the surface at 0% stretching and reached approximately 50 nm on top of the surface at 30% stretching. Thus, approximately 100-150 nm of the single microgels remained submerged within the wrinkle grooves (cf. Figure 43 21-30% stretching). Interestingly, at 21% stretching, only microgel pairs were visible in the AFM image and in the corresponding cross section. They seemed to form zigzag arrays which resided by 50 nm on top of the surface revealing its true alignment as broad ribbon like arrays upon further stretching till 30% (initial stretching degree of the PDMS). At that stretching degree tree microgel particles resided next to each other forming the ribbon. At the same time, the former wrinkle tips (center of the sections in Figure 42) were flattened out by subsequently increasing the stretching until they inverted at 30% stretching, forming grooves with 50 nm depth. Stretching these kinds of wrinkles is crucial for later cross-linking experiments with the microgel arrays.

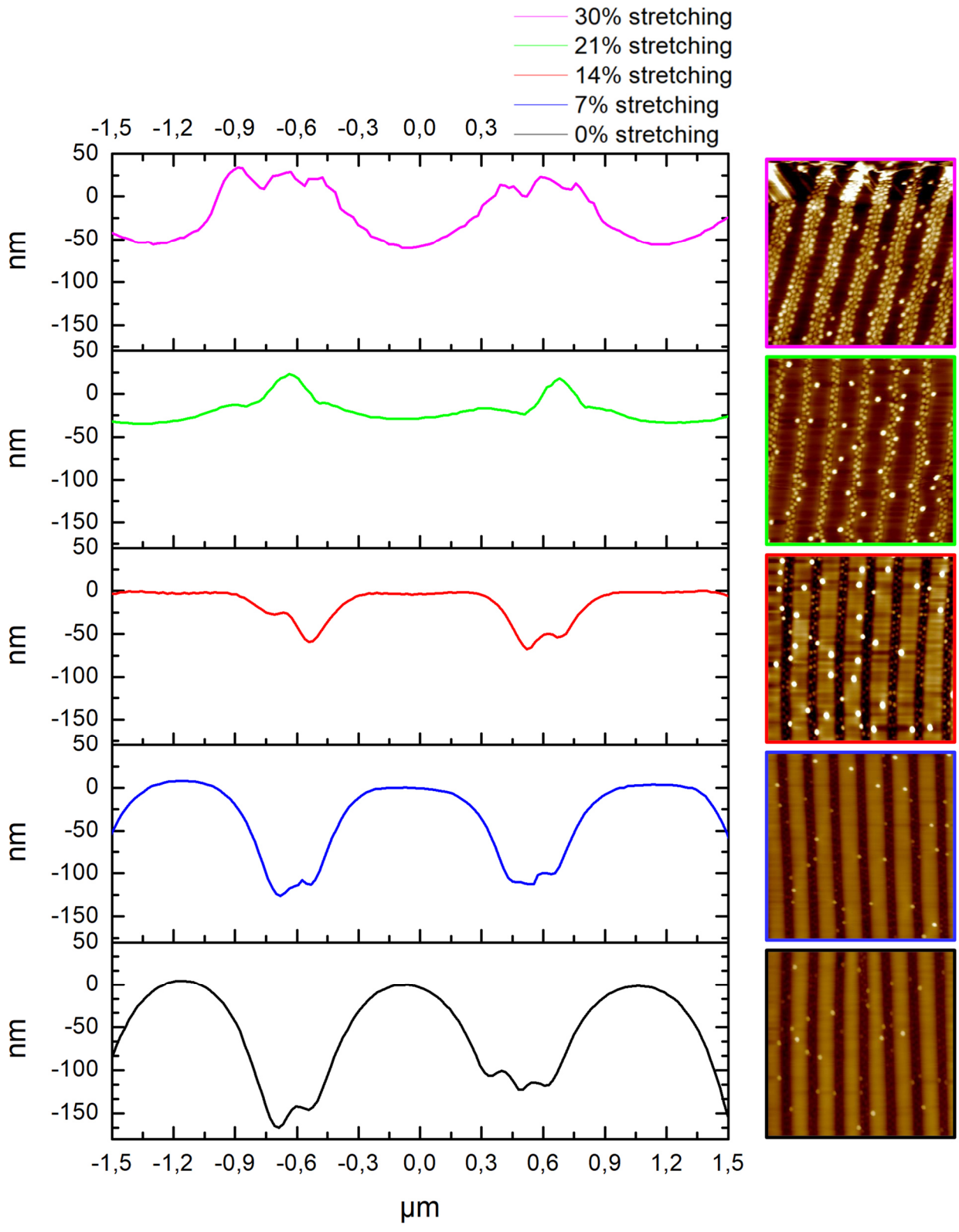

Figure 42: In-situ stretching experiments. AFM images of wrinkles with VCL/AAEM microgels with λ = 1000 nm in different stretching stages and corresponding cross-sections (Δz = 150 nm).

When applying the stretching method to wrinkles with 900 nm wavelength, one could observe a similar behavior (Figure 43). A flattening of the structures was already reached at 7 % stretching, due to the fact that the microgels at 0 % stretching nearly resided on top of the surface in a zigzag arrangement. Thus, there was no need for a prolonged transport of the microgels towards the surface. They fully emerged at 14 % stretching while wrinkle tips were inverted to grooves at the same time. Upon further stretching towards 30 % (initial stretching degree of the PDMS), a breakage of the oxidized layer of the PDMS surface occurred where the former wrinkle tips used to be (Figure 44). Interestingly, the microgels remained submerged with approximately 50 % of their total volume, which means that the microgel interactions with the surface was apparently stronger than the coherence of the oxidized surface layer of the PDMS wrinkles, leading to its breakage. Furthermore, by cross-linking the microgels before stretching, it was difficult to tear them apart. The connections between the particles could be observed as thin strains between the microgels (Figure 44). Otherwise there was no apparent difference in terms of morphology change between cross-linked and non-cross-linked microgel arrays.

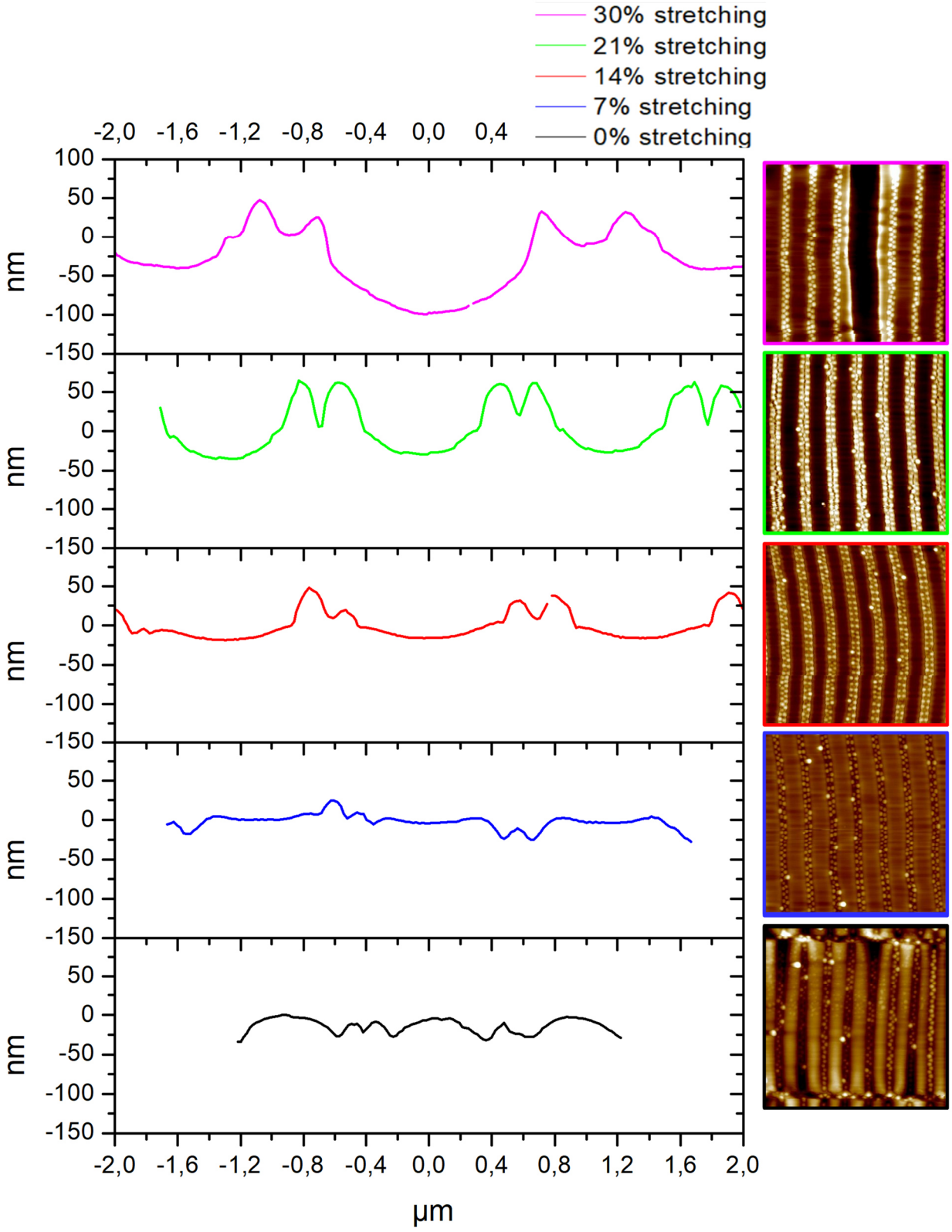

Figure 43: In-situ stretching experiments. AFM images of wrinkles with VCL/AAEM microgels with λ = 900 nm in different stretching stages and corresponding cross-sections (Δz = 150 nm).

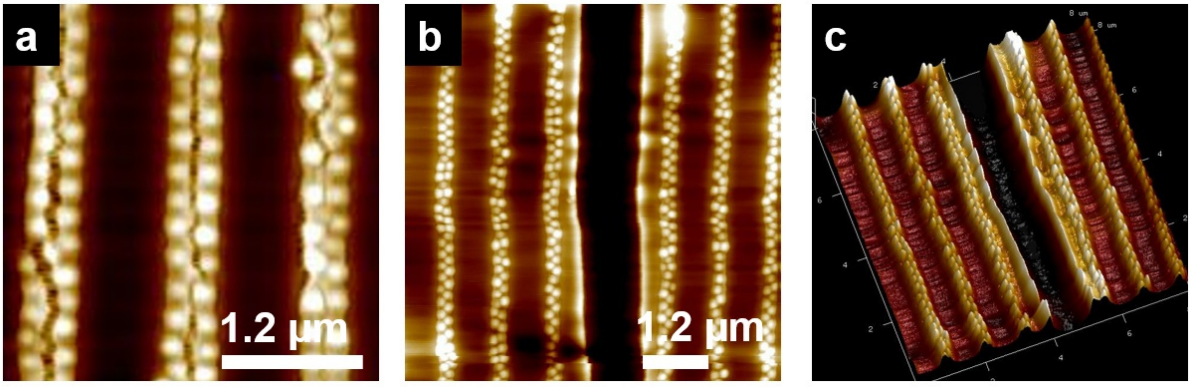

Figure 44a: AFM image of cross-linked microgel arrays which reside on top of an overstretched PDMS surface. The arrays show signs of tearing. b-c: AFM image and 3D representation of crack forming due to overstretching

In a last experiment, the whole procedure was repeated for wrinkles with 800 nm wavelength and microgels spin coated on top of them. Similarly, to the 900 nm wrinkles, the pearl-necklace like arrays were already residing on top of the surface before applying stretching. The whole experiment led to the same findings in terms of surface morphology as the experiment with 900 nm wrinkles. The only difference towards the latter experiment was that the pearl-necklace like arrays were also teared apart at a stretching of 30 % (Figure 45).

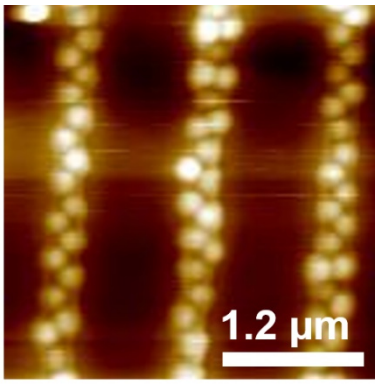

Figure 45: AFM image of cross-linked microgel arrays which reside on top of an overstretched PDMS surface (30% stretching). Analogous to the experiment with 900 nm wrinkles, the arrays show signs of tearing.

2.1.7 Conclusion

In this chapter, alignment methods for soft particles were tested with different microgel types in order to create an understanding of the crucial alignment parameters. By using Assembly Method 1 it has been shown that the alignment is highly dependent on the template wavelength λ. For example, to get a high yield of perfectly lined up VCL/AAEM microgel arrays, the templates had to provide enough space to ensure that the microgels remained within the wrinkle grooves during spin-coating. Increasing the wavelength led to a submerging of the aligned arrays into the grooves. By adjusting the wavelength according to the microgel dimensions (approx. 1.8 times the R_H), the alignment in zigzag formation was possible with the microgels remaining at the surface. A transfer onto different surfaces, e.g. a Si-wafer, was feasible thereby. Through this method it was possible to create a nanostructured surface with relatively low defect rates while ensuring a high periodicity, which has been proven by GISAXS measurements.

In addition, the microgel properties such as rigidity, their adhesion on surfaces and their interactions with electrostatic charges were crucial factors for the particle alignment using the examined methods. By using oxidized PDMS and Si-wafers, studies regarding the latter interactions focused on SiO_x surfaces.[204] This work has shown that there are distinct differences in flexibility between the studied microgels which are influenced by their

chemical composition. Although all microgels were synthesized by the same synthesis methods and conditions (e.g. cross-linker concentration), VCL/AAEM microgels showed an aligning behavior similar to that of solid particles (e.g. silica[140] or gold[132] particles). Through this property, the microgels could be easily aligned into densely packed arrays. In contrast to the latter microgels, NIPAAm based microgels showed a heavy deformation when spin-coated onto wrinkled templates and seemed to interact with the silanol groups of the template surface by covering the surface unspecifically while flattening out. By introducing VCL into the microgels matrix, they gained rigidity which led to an improved particle alignment. Even though these microgels showed a high defect rate when aligned onto wrinkled surfaces, they partially formed densely packed arrays. The combination of VCL with NIPAAm allowed furthermore to introduce a certain amount of flexibility to the microgels (shown by bending between two wrinkle tips) which has not been observed for the VCL/AAEM microgels. Based upon these findings, the interaction between the microgels and oxidized Si-surfaces were examined through AFM-tip-retraction experiments. These experiments showed that the adhesion energy of pure NIPAAm microgels was twice as high than the adhesion energy measured for VCL/AAEM microgels, explaining why NIPAAm microgels adhere to the wrinkled templates and cover them homogeneously. All NIPAAm/VCL microgels with mixed ratios showed adhesion energies which were comparable to the energy measured for VCL/AAEM microgels (Figure 25). In conclusion, it can be assumed that the interaction between the amide groups of NIPAAm with the silanol groups were responsible for this behavior. An introduction of positive surface charges to VCL/AAEM microgels via the incorporation of CTAB resulted in an unspecific alignment onto the templates with increasing charge density until covering it homogeneously like NIPAAm microgels. The silanol groups on the silica surfaces (e.g. oxidized PDMS wrinkles and Si-wafers) are responsible for a negative surface charge.[204]

In conclusion, the Assembly Method 1 is well suited for aligning rigid microgels (e.g. VCL/AAEM microgels). These microgels could also be transferred easily onto other surfaces. The method only showed weaknesses when facing particles which were capable to interact with the template through electrostatic interactions or via hydrogens bonds.

In contrast to Assembly Method 1, all examined microgels could be easily aligned by using Assembly Method 2. The used templates functioned as confinements for the microgels and surface interactions were negligible. By using this assembly method, a control of the spacing between the arrays was feasible by changing the wavelength of the wrinkles. This could be used to create controlled optical grids.[130, 185] However, the softer NIPAAm and NIPAAm/VCL microgels were heavily deformed by the template confinement, while only the rigid VCL/AAEM microgels retained their shape. Despite the rather harsh conditions of the molding process, the VCL/AAEM microgels exhibited a pronounced increase in size upon hydration and were able to experience temperature dependent swelling behavior. Thus, the Assembly Method 2 does not impart the formation of stimuli-responsive microgel 1D nanostructures.

At last, wrinkle-microgel interactions were examined by stretching of the wrinkled templates. By these experiments it was found that the stretching of wrinkles with microgels in the grooves led to an inversion of the structures exposing the microgels to the surface. This is an important finding for the efficient cross-linking of the aligned microgel strands since this method can ensure a sufficient exposure to UV-light. However, the strong interaction of the microgels with the wrinkle surface even led to a breakage of the wrinkles upon further stretching rather than to their flattening which was more expected and observed with empty wrinkles. Taken together, these findings are important factors for the development of supramolecular smart microgel strands. The fabrication of these is discussed in the following chapter.

2.2 Fabrication of 1D microgel arrays and strands via inter-particle cross-linking

Parts of this chapter have been published elsewhere.[141, 205]

2.2.1 Introduction

Template assisted or guided self-assembly of microgels is a necessary step towards the formation of 1D microgel nanostrands, which in turn could be used for different applications such as fast actuators (Figure 15).

The influence of the alignment procedure on the dimensions of the microgel arrays was discussed in the previous chapter. For this purpose, PDMS wrinkles were utilized as templates, which were prepared by plasma treatment of stretched PDMS surfaces as described in M. Ph. Schürings diploma thesis.[94] To ensure an appropriate microgel alignment within the grooves, the wavelength had to be adjusted in the same order of magnitude as the diameter of the microgels.[64, 103] In all following experiments the microgels were assembled onto wrinkled PDMS substrates by spin-coating (Figure 46).

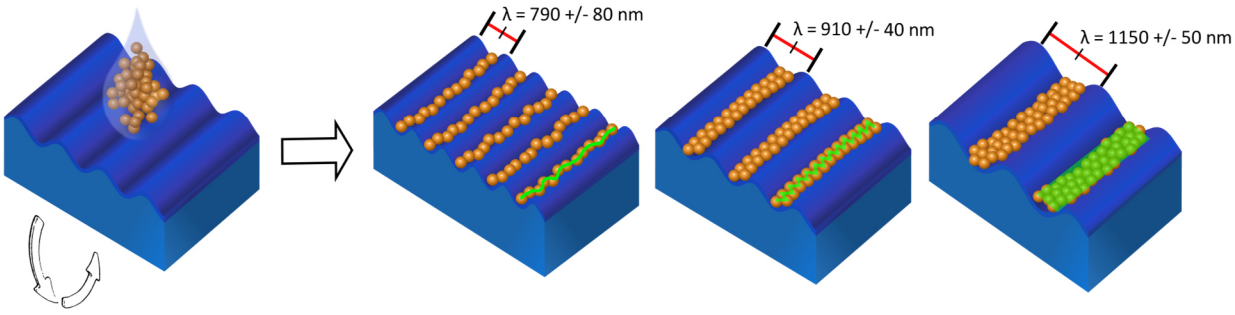

Figure 46: Schematic depiction of a spin-coating process with microgels which lead to a formation within the wrinkled grooves. The variation of the wrinkle wavelength λ lead to different microgel formations such as pearl necklace, zigzag and ribbon-like nanoarrays.

In the previous chapter it has been shown that depending on the wrinkle wavelength the VCL/AAEM microgel arrays form different formations, e.g. pearl necklace, zigzag and

ribbons. In contrast to NIPAAm microgels, the alignment of VCL/AAEM microgels is solely based on the de-wetting process during spin-coating.[173, 174]

By connecting neighboring particles within the formation via various cross-linking methods, the above-mentioned microgel arrays can be fixed permanently. In the following, different approaches for cross-linking microgel arrays towards stable microgel strands are discussed.

2.2.2 Cross-linking by UV-light

To achieve inter-particle cross-linking of VCL/AAEM microgels, it was initially tried to add a comonomer into the network which is known to cross-link via a UV activated 2+2 cycloaddition shown by Kuckling et al. (Figure 47).[206] Microgels functionalized with the Kuckling cross-linker showed no significant improvement in their inter particle cross-linking capability compared to standard VCL/AAEM microgels. One reason for that could be that nearly all known UV-cross-linkers are hydrophobic in nature. Thus, it can be assumed that the cross-linker was incorporated into the hydrophobic core of the VCL/AAEM microgels during precipitation synthesis in water.

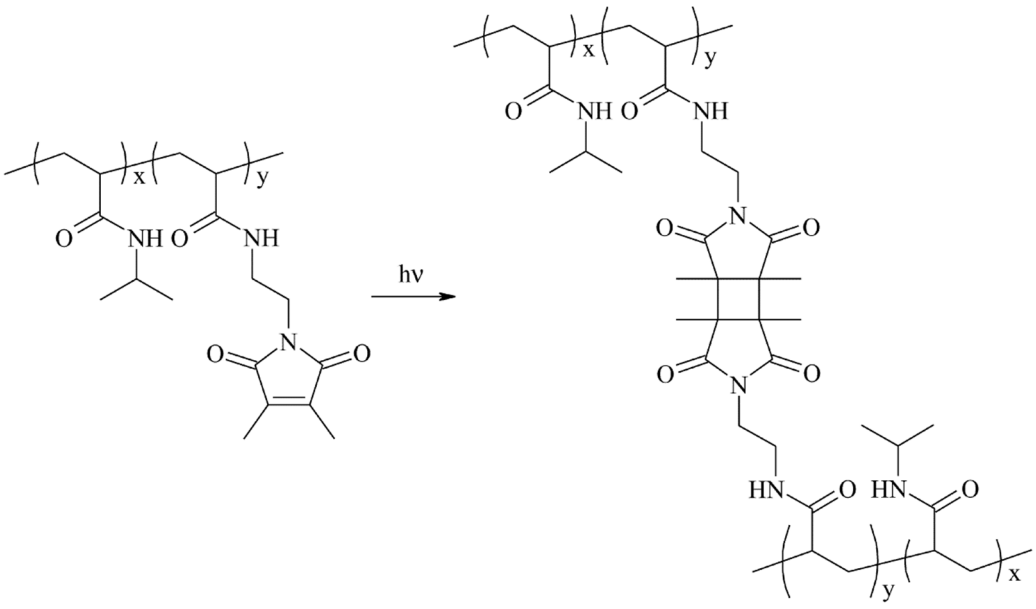

Figure 47: 2+2 photoinduced cyclo-addition of NIPAAm with maleimide copolymer.[206]

Approaches which involved unspecific cross-linking analogous to the radical polymerization of the microgels, e.g. using a solution of BIS and AMPA on pre-aligned microgels, yielded undefined agglomerates. By taking a closer look into the molecular composition of the VCL/AAEM microgels, it was proposed that the AAEM could provide UV-cross-linkable moieties since it undergoes keto-enol-tautomerism (Figure 5: β-diketone groups).[75, 207] The microgels used in the present study exhibit heterogeneity in their structure due to the predominant localization of AAEM units in the core.

Pich et al. showed that the majority of the AAEM resides in the microgel core.[56] Nevertheless, as the synthesis is based on a free radical polymerization, it leads to a nearly random distribution of both comonomers (VCL and AAEM) at the end of the synthesis. Statistically, this yields a low but still significant concentration of AAEM in the microgel corona. The reason for this is that the different polarities of the keto- and enol-form of AAEM significantly influence the incorporation of AAEM units into the microgel structure during precipitation polymerization. It is reasonable to assume that a considerable amount of the keto-form of AAEM, which readily forms hydrogen bonds with water molecules, will be incorporated in the microgel corona. Considering the fuzzy surface of microgels and the close alignment of the microgels in arrays before UV-irradiation, it justifies the assumption that β-diketone groups of neighboring microgels will be localized in close proximity to each other, providing sufficient conditions for inter-particle crosslinking.

It has been reported in literature that UV irradiation induces photo-tautomerization of β-diketones in water, thus influencing their reactivity.[75, 207] We assume that the β-diketone groups present in the keto or the enol form attached to the polymer chains of the microgel can act as substrates for the radical formation reaction under UV irradiation in the presence of oxygen and water. The activity of β-diketones as radical mediators was already observed in enzymatic radical polymerization.[208] Similar experiments with NIPAAm based microgels were not successful, due to the absence of AAEM in the polymer matrix.

The fabrication of 1D microgel strands by UV-cross-linking was conducted by two different approaches. In the first approach, the microgel arrays were printed on Si-wafers as described in the previous chapter. Subsequently, the arrays were successfully cross-linked using UV-light in a wavelength range from 190 to 310 nm to ensure inter-particle connectivity (Figure 48a). In the second approach, the arrays were directly cross-linked within the wrinkle grooves (Figure 48b).

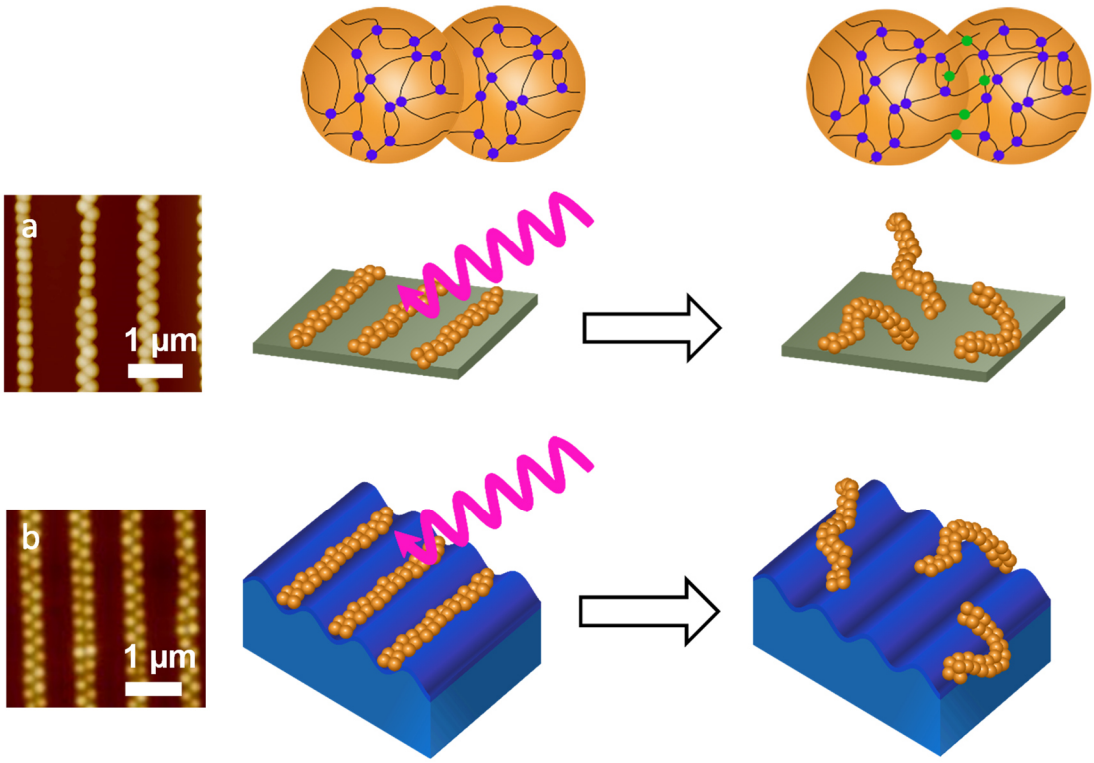

Figure 48: Two different approaches towards strand fabrication. a: microgels were printed on Si-wafers and subsequently cross-linked via UV-light to ensure interparticle connectivity (depicted in green cross-linking moieties), b: microgels were assembled into wrinkles directly followed UV cross-linking.[75, 207, 208]

By using the first method, microgels were transferred as arrays onto a flat Si-wafer depicted in Figure 48. After cross-linking, it was tried to detach the microgels from the surface by washing the glass slide with several microliters of water. However, the cross-linked microgel

strands could not be displaced, thus showing no changes in alignment on the AFM images. The mean distance between the strands remained equidistant and is determined by the wavelength λ of the wrinkles. One probable reason for the "sticky" behavior of the microgel strands could be that the silanol-groups at the surface are interacting with the microgels by forming hydrogen bonds with the amide group within the VCL ring. Furthermore, it must be considered that a wetting process at the water/silica interface is hindered by the microgel strands through their nano-structural dimension and the relatively high surface tension of water.[209] In contrast, ethanol as a substitute to water has two major advantages. (i) Ethanol has a lower surface tension, which is beneficial to the wetting process of nanostructured surfaces. (ii) Ethanol can form hydrophobic alkoxy-groups with the silanol on the silica surface at room temperature, which probably support the detachment process by reducing the mean number of active hydrogen bonds while increasing the hydrophobic repulsion.[210, 211]

As can be seen in Figure 49a and b, the microgels could be moved by applying a droplet of ethanol on top of a tilted substrate (Figure 49). While in the non-cross-linked state the microgel arrays lose their formation and form agglomerates (Figure 49a), the cross-linked microgels were moved as intact strands. Although the microgels could not be detached completely, this approach demonstrated the effectiveness of the cross-linking reaction.

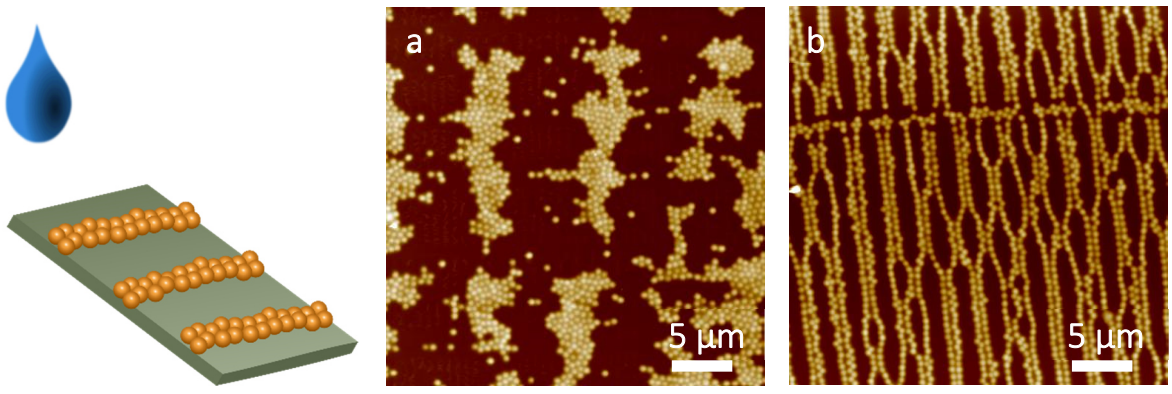

Figure 49: Schematic depiction of solvent-assisted strand detachment. Upon application of ethanol a: agglomerates formed due to the absence of UV cross-linking; b: microgel arrays retained their inter-particle connectivity after UV-irradiation, thus moving as collective nanostrands.

In the second approach, the microgel assemblies were cross-linked directly on the wrinkles by UV irradiation. Afterwards, it was unsuccessfully tried to detach them from the wrinkled surface with water. As explained above, a poor wetting of the wrinkled surface could have been the reason why the strands retained their position. Furthermore, preliminary work showed that the oxidized PDMS surface of the wrinkles turns hydrophobic over time which hinders the wetting even more.[94, 141] By re-stretching the wrinkles via the stretching apparatus to create a plane surface, the wrinkled structure inverts and lifts the microgel strands from the wrinkle grooves to the peaks (see Figure 43 - Chapter 2.1.6). Thereby, the strands were exposed to the solvent leading to a more efficient contact and hence a complete detachment of the strands. The hydrophobic surface properties of the PDMS substrate are in this case highly beneficial for the removal process. The transfer technique of the microgels strands is described in the experimental part (Chapter 4).

Analysis of the samples via AFM and TEM proved that stable microgel strands with a granular structure and lengths up to 100 µm were obtained (Figure 50). The fact that such large lengths can be found after transfer means that most of the links between adjacent microgels survive the shear forces effective during re-dispersal via a pipette in water and re-deposition. The granular structure of the strands, which can be clearly seen in the insets of Figure 51a, is determined by the surface curvatures of the constituent microgels and their center-to-center distances.

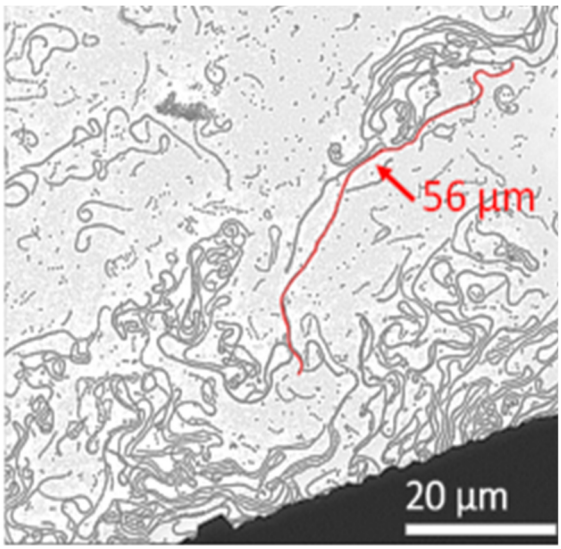

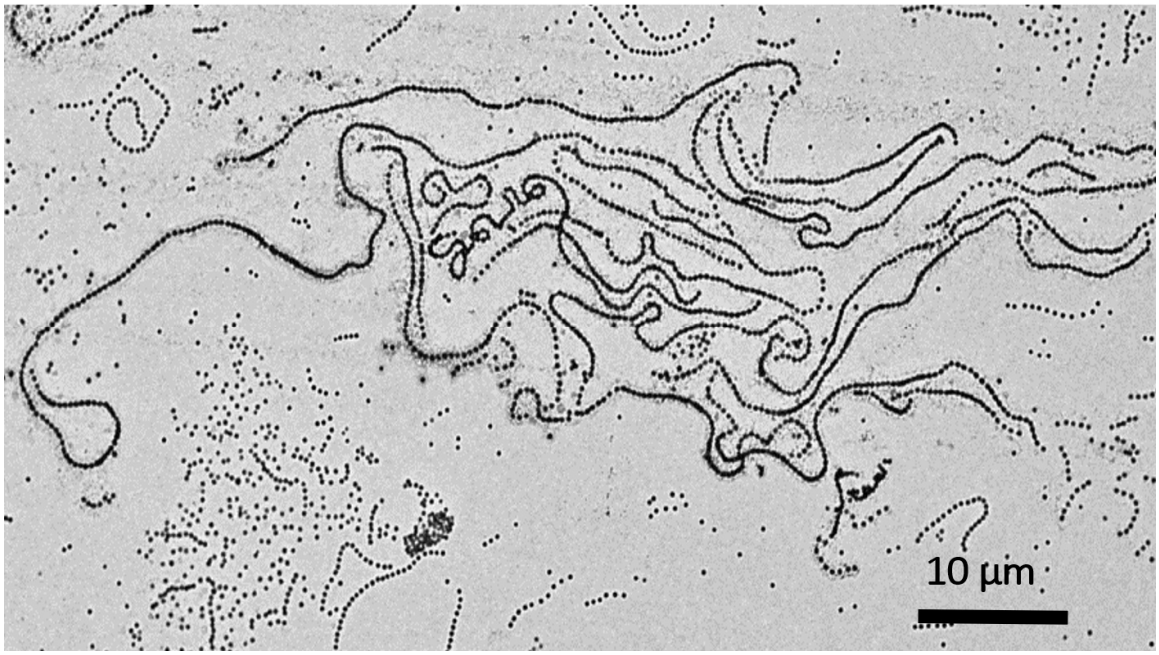

Figure 50: Various TEM images that show long microgel strands.[141]

Depending on the wavelength of the wrinkles, microgel strands with pearl necklace, zigzag, and ribbon-like formations can be obtained as shown in Figure 51. However, for the formation of stable semi-flexible strands, a high degree of overlap between the soft microgels is necessary. The pearl necklace formation has many breaking points since microgels are only connected via a few filaments, as can be seen in the magnified TEM image in Figure 51b. By increasing the wavelength λ of the templates, the width of the strands increases while the height remains unchanged. Independent of the offered space between the wrinkles, the microgels never stacked, thus they did not form double layers (Figure 51c-d). The reason for this phenomenon resides in the fact that the PVCL microgels are sterically stabilized, which avoids agglomeration in dispersion and hinders stacking on top of each other during spin-coating. The high inertia of the ribbon-like arrays leads to breakage already at low shear forces and faster precipitation due to their high mass (Figure 51d). For this reason, the zigzag alignment combines both good overlap between neighboring particles and a relatively low inertial mass (Figure 51c).

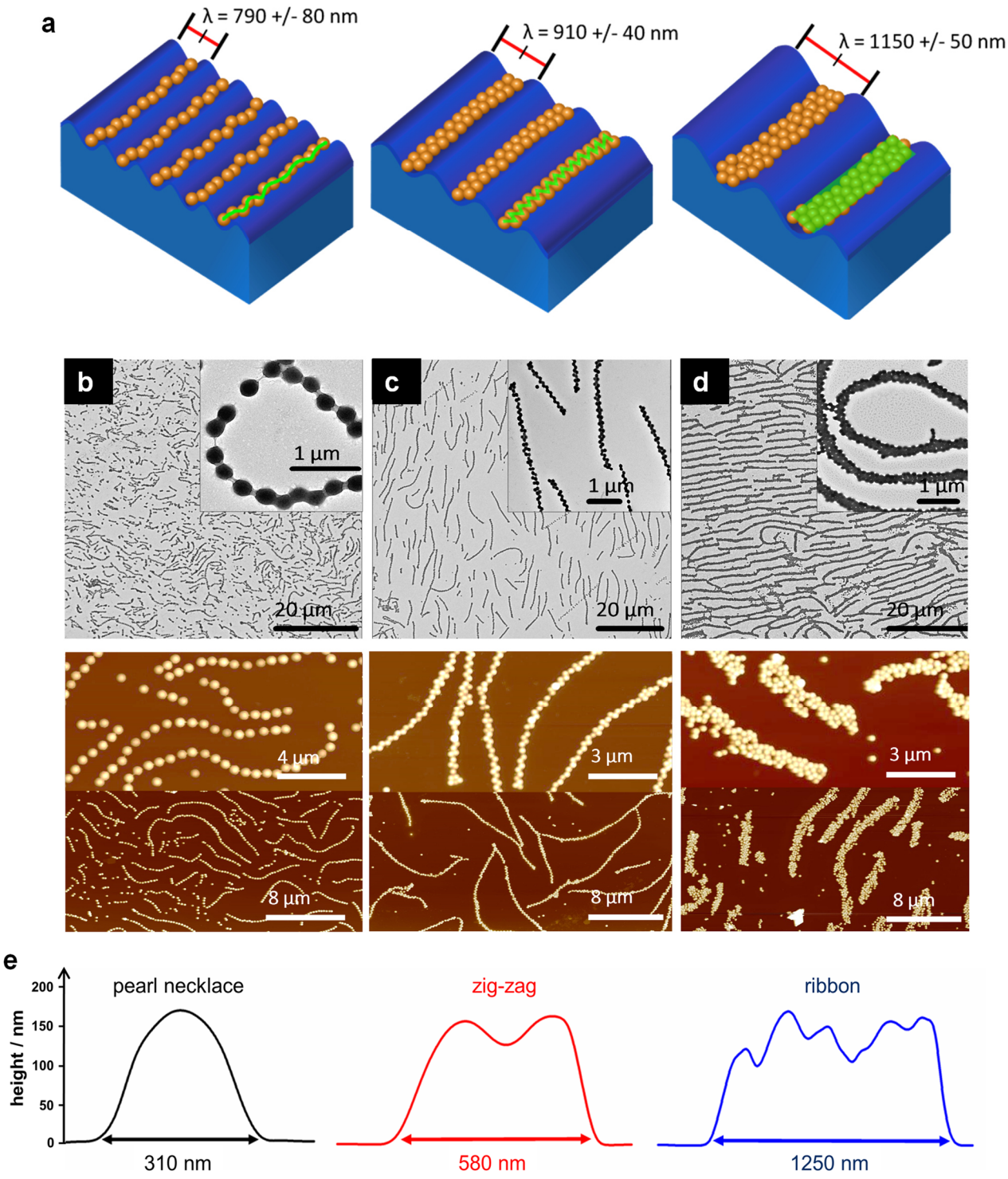

Figure 51: Scheme of sample preparation and corresponding AFM and TEM images. a: Schematic depiction of microgel alignment within the wrinkle grooves via spin-coating, UV irradiation of microgels strands. b-d: AFM and TEM images of redispersed microgel strands transferred onto a substrate (e.g. Si Wafer or TEM grid). e: Corresponding AFM-section which show the increase in strand width proportional to the increasing space within the wrinkle grooves while retaining their height (single layer).[141]

While the width and height of the microgel strands can be controlled by the wavelength λ of the templates, it has to be noted that the strand length varies as it is influenced by the density of the defects (i.e. cracks that are perpendicular to the wrinkles) in the template surface. Further investigations revolving around the motion of microgel strands in solution were all performed with microgels aligned in the zigzag formation (Figure 52).

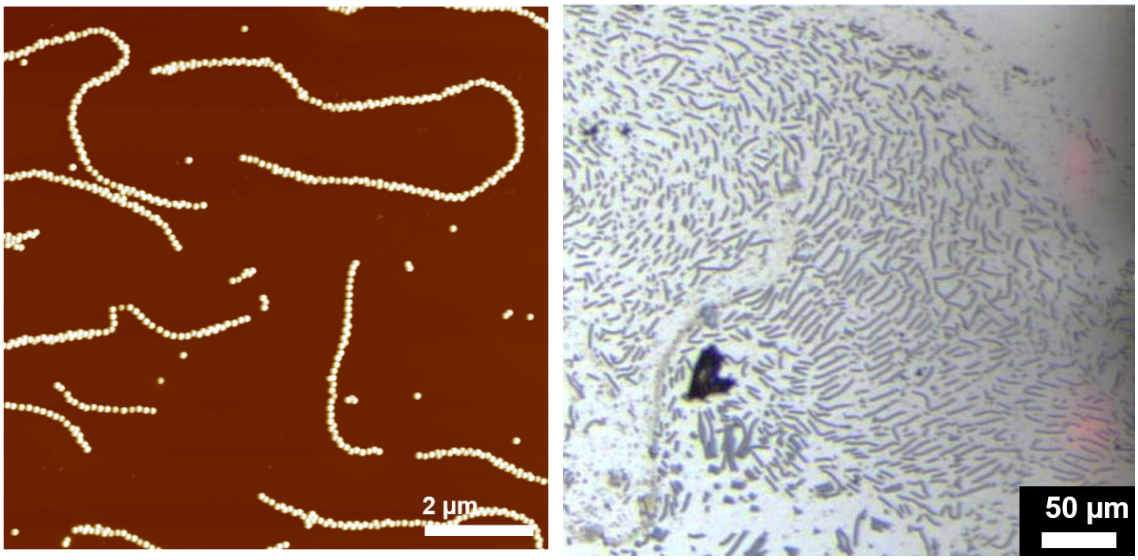

Figure 52: AFM image of microgel strands in zigzag formation (left) and optical microscopy image of microgel ribbons (right).

Based upon these findings, the potential of this particular alignment or preparation procedure was further explored by constructing more complex superstructures, like microgel meshes and double/triple strands with unique properties (Figure 53).

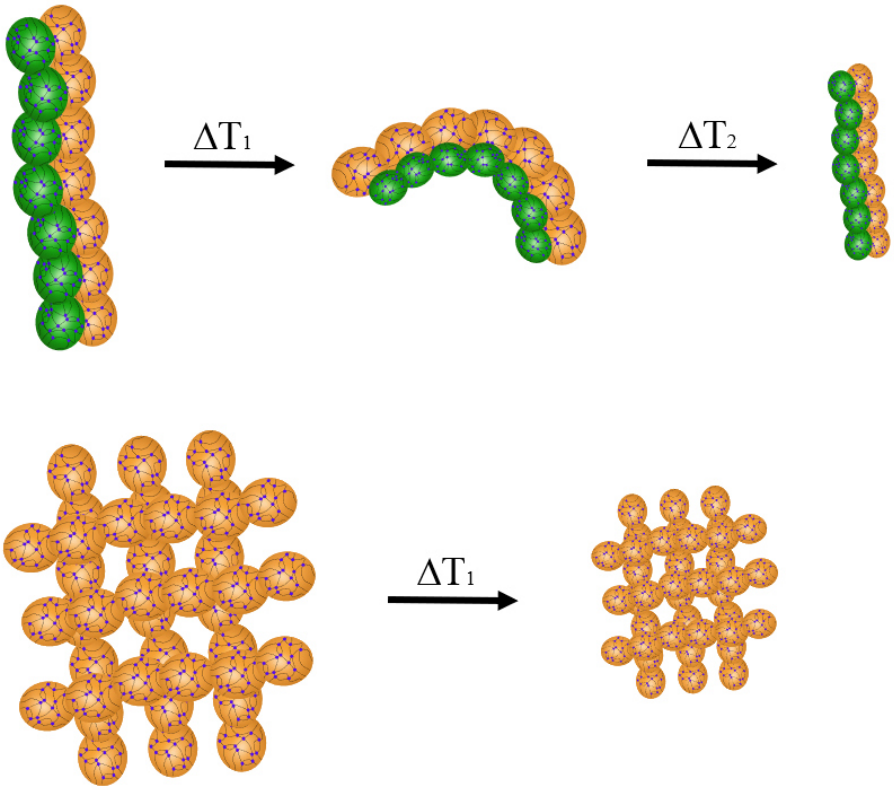

Figure 53: Schematic depiction of a double strands with two different VPTTs and microgel meshes.

The fabrication of meshes is shown in Figure 54. Initially, cross-linked strands were printed onto a Si-wafer forming the first generation of the already described microgel nanostructures. A second set of prealigned and cross-linked microgels were printed perpendicularly on top of the first-generation nanostructures, forming a mesh.

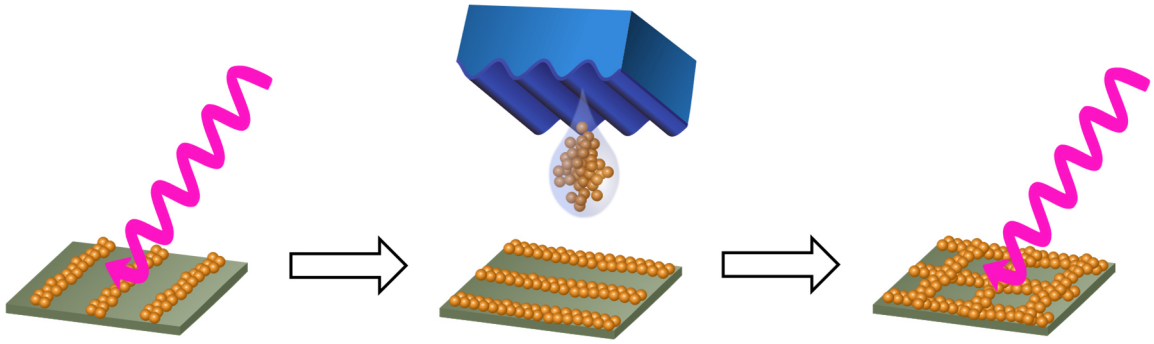

Figure 54: Schematic depiction of microgel mesh fabrication.

To ensure inter-particle connectivity, the newly formed mesh was UV cross-linked. Afterwards, the meshes were removed by applying a droplet of ethanol on the surface and the semi-detached meshes were transferred onto a TEM grid by a pipette. Large fragments of intact microgels meshes were found in TEM images after the transfer (Figure 55).

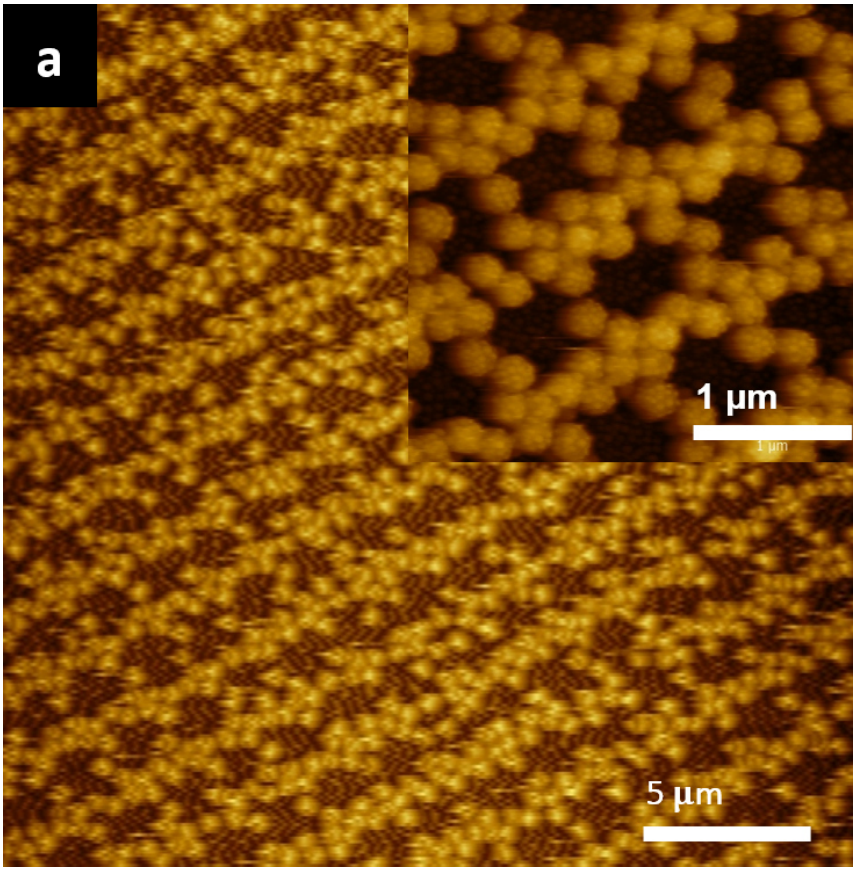

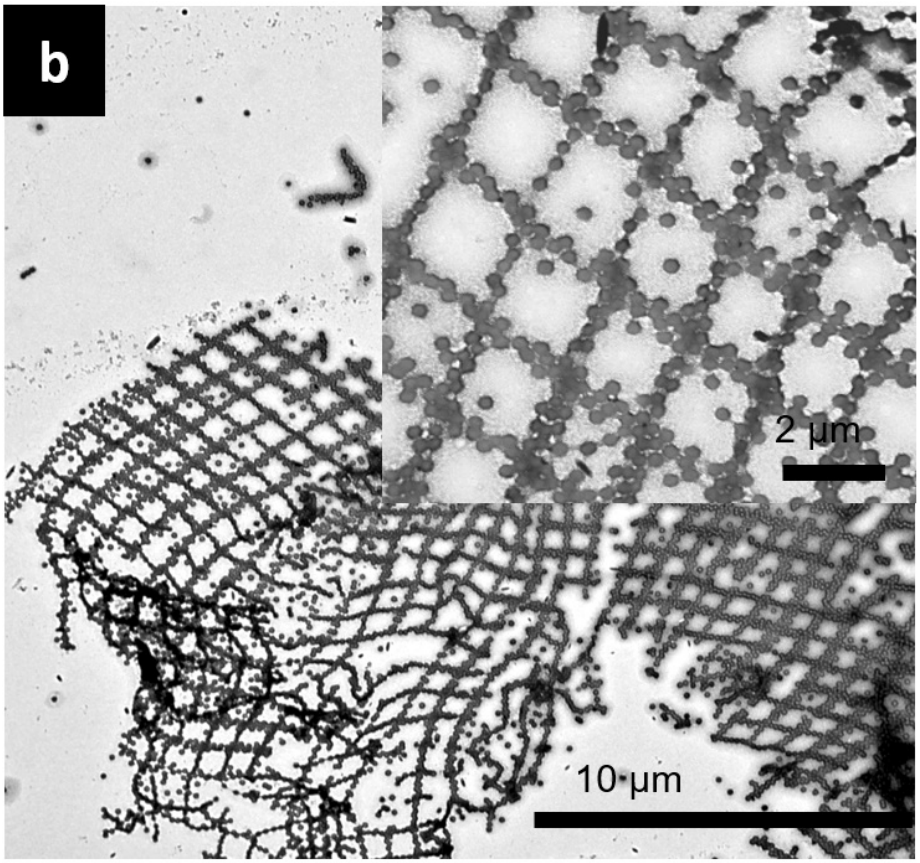

Figure 55: a: AFM image of a microgel mesh on a Si-wafer in water. b: TEM image of detached mesh.

One could imagine that the mesh size is tunable through the wavelength of the substrates (wrinkles) and external stimuli (e.g. temperature). The latter property could be used to create porous stimuli responsive membranes which change their porosity at the volume phase transition temperature of the microgels.

In order to fabricate microgel strands which have the potential for directed motion, microgels with different sizes, charge densities or VPTTs were combined into parallel aligned double or triple strands (Figure 56). Out of all conducted experiments two fabrication approaches showed promising results.

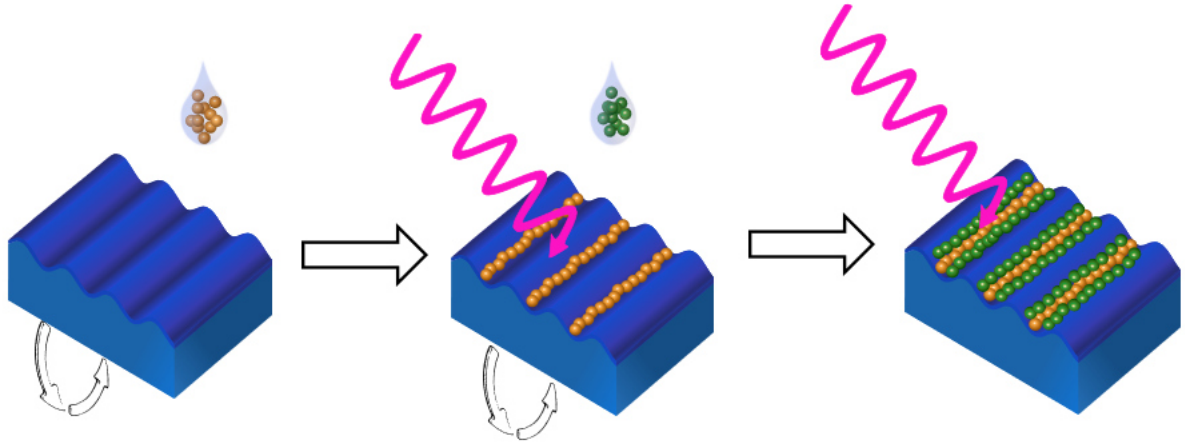

Figure 56: Schematic depiction of microgel triple strand fabrication via subsequent spin coating and UV cross-linking.

As a proof of principle, VCL/AAEM microgels were prealigned and cross-linked on a wrinkled substrate. Subsequently, smaller and charged VCL/AAEM/CTAB 10 mg microgels (see Chapter 2.1.2) were added by spin-coating and cross-linked via UV irradiation. The idea was to create a directed bending motion through a difference in the overall contraction length during VPT of the respective microgels (VCL/AAEM with R_H ~ 220 nm and a swelling degree of 4.3 combined with VCL/AAEM/CTAB 10 mg with R_H ~ 100 nm and a swelling degree of 3.1). Since the amount of smaller microgels has to be much higher to match the length of the neighboring strand composed of larger microgels, the change in overall contraction length is much more pronounced for the strand with smaller microgels. This could lead to a bending motion upon reaching the VPTT if the swelling degrees of both microgel types are comparable.

Although this was not the case in this work, the experiment was an important step to gain insight into the alignment process of multi strands. By observing the alignment of smaller microgels in respect to the already aligned arrays, no clear conclusions can be drawn by the analysis of the AFM-images taken of the wrinkled substrate after the second spin-coating process (Figure 57). The VCL/AAEM and VCL/AAEM/ CTAB 10 mg microgels seem to be randomly distributed. However, after the redispersion process it can be clearly seen, that the VCL/AAEM microgels form the previously described pearl-necklace microgel strands. Alongside to these strands, single VCL/AAEM/CTAB 10 mg microgels are attached. They

did not form continuous strands by themselves. These results show that a combination of these microgels was in principle feasible, but the aspired double strands could not be achieved through this approach.

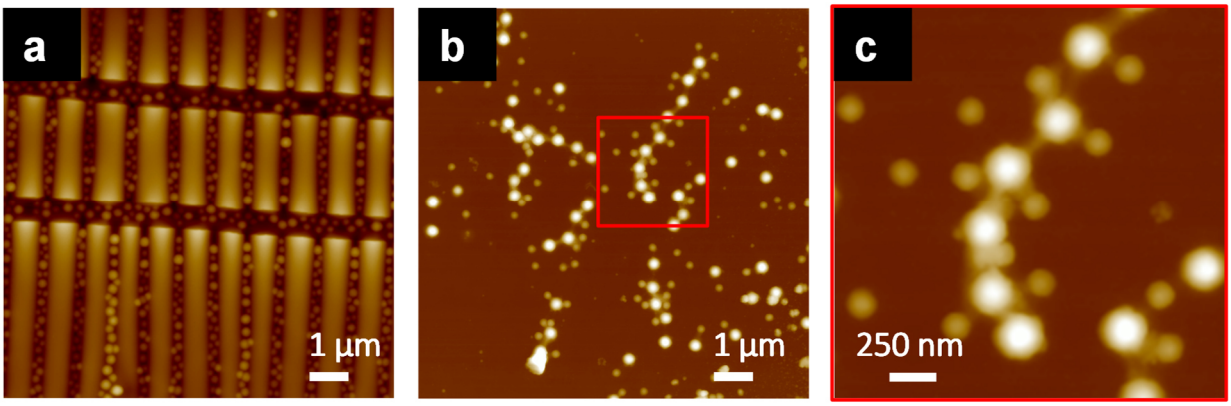

Figure 57: a: wrinkled substrates after 2nd spin-coating process with VCL/AAEM/10 mg CTAB microgels. b: redispersed microgel strands fabricated with this approach. c: magnified AFM image from b where the cross-links can be seen.

Due the strong adhesion of NIPAAm microgels on silica surfaces (Chapter 2.1.2), spin-coating was excluded in experiments with these microgels.

In the second approach, Assembly Method 2 was used with a wrinkled PDMS template which had prealigned and UV cross-linked VCL/AAEM microgel arrays residing it its grooves. The PDMS template was previoulsy prepared by spin coating VCL/AAEM microgels onto the wrinkled surface (Assembly Method 1). A droplet of VCL/AAEM/CTAB microgels was applied on a Si-wafer. The wrinkled substrate was pressed on top of the Si-wafer in order to transfer and fabricate double strands (Figure 57a). This molding process is described in the experimental part in Chapter 4. The idea here was that after removal of the wrinkled substrate the VCL/AAEM/CTAB 10 mg microgels would adhere onto the Si-wafer with the VCL/AAEM microgels stacked on top of them. The corresponding AFM images exactly confirmed this expectation (Figure 57b-c). It is clearly visible that the smaller VCL/AAEM/CTAB 10 mg microgels reside underneath the larger VCL/AAEM microgels. Although the formation of double strands was a success, detaching them was difficult. Even using ethanol as a solvent, the positively

charged VCL/AAEM/ CTAB 10 mg microgels would not move from the substrate. Dissolving the oxidized top layer of the Si-wafer was one possible way to detach the double strands. By using NaOH to dissolve the glassy layer of the substrate and washing the substrate multiple times with distilled water, a considerably high amount of salt crystals remained on the surfaces. This made further studies through AFM and TEM microscopy impossible.

In an analogous approach, wrinkled substrates with prealigned and UV-cross-linked VCL/AAEM microgels were used. Instead of applying a droplet of VCL/AAEM/CTAB 10 mg microgels on to a Si-wafer, NIPAAm/VCL microgels with different NIPAAm:VCL ratios (3:1 and 1:3) were used. Analogous to the previously described experiments, the wrinkled substrate was pressed on top of the Si-wafer in order to fabricate double strands (Figure 58a).

Using NIPAAm/VCL with a ratio of 1:3, the arrays were formed by the VCL/AAEM microgels. The NIPAAm/VCL 1:3 microgels disturbed the VCL/AAEM array formation. They were either included within in the arrays as single randomly distributed particles (Figure 58e) or they tore up the VCL/AAEM arrays formation by their sheer amount (Figure 58d). Figure 58d also shows that there was no interparticle connection between NIPAAm/VCL 1:3 microgels after UV irradiation, because no two NIPAAm/VCL 1:3 microgels were aligned next to each other. Inverting the NIPAAm:VCL ratio towards three parts NIPAAm, led to a formation of a thick, physically entangled microgel sheet consisting of NIPAAm/VCL 3:1 and VCL/AAEM microgels depicted Figure 58f-g. To conclude, by using a combination of NIPAAm/VCL and VCL/AAEM microgels a formation which resemble a double or multi strands could not be achieved.

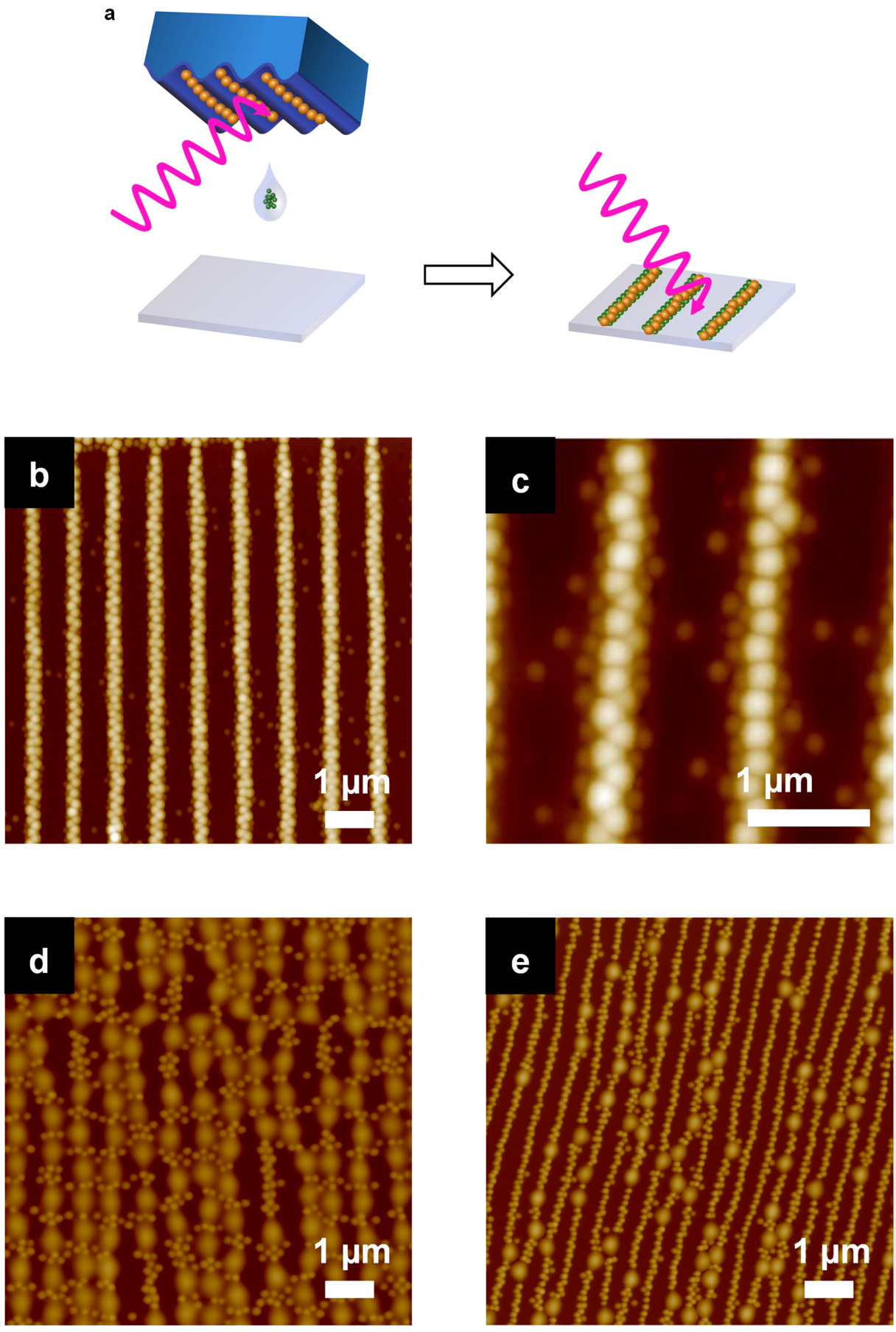
a
b
1 µm
c
1 µm
d
1 µm
e
1 µm

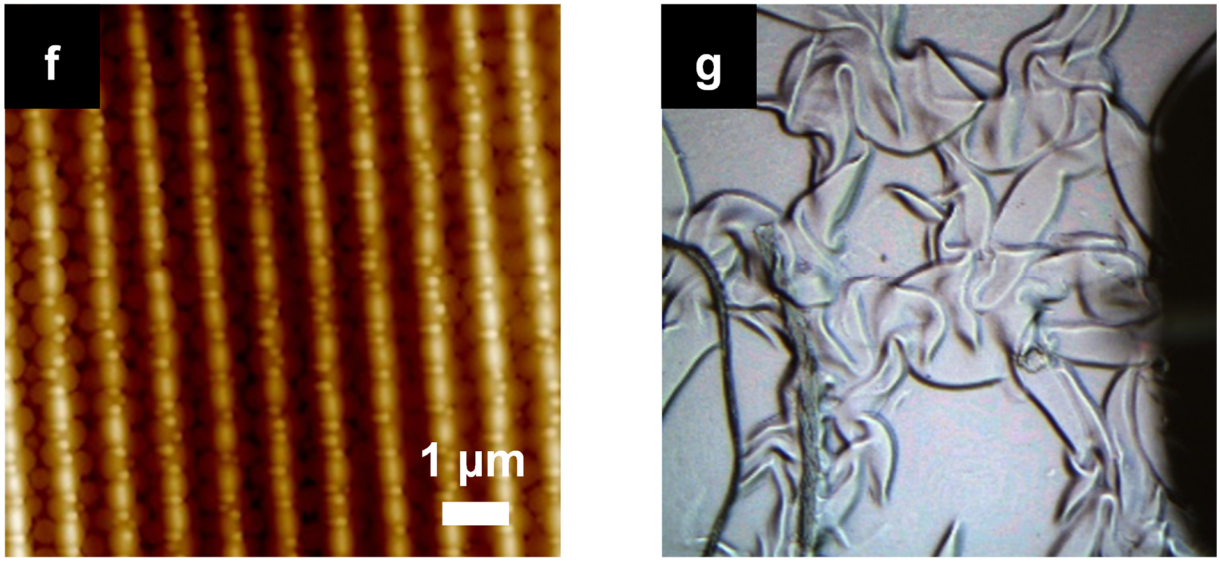

Figure 58: a: Schematic depiction of double strand fabrication via molding by using prealigned and UV-cross-linked microgels. b: AFM image of stacked microgel double strands after molding with prealigned VCL/AAEM and VCL/AAEM/CTAB 10 mg microgels. c: magnification of AFM image a which shows that the bottom layer consists out of VCL/AAEM/CTAB 10 mg. d-e: AFM images of a Si-substrate after molding with prealigned VCL/AAEM and NIPAAm/VCL 1:3 microgels; f: AFM image of a Si-substrate after molding with prealigned VCL/AAEM and NIPAAm/VCL 3:1 microgels; g: optical microscopy image of a microgel sheet consisting of NIPAAm/VCL 3:1 and VCL/AAEM microgels.

In summary, UV cross-linking of microgel arrays proved to be a feasible method towards the fabrication of 1D nanostructures. By testing different approaches, the most efficient method was found by cross-linking the arrays while they were aligned within the grooves of the wrinkled templates. Since this approach is limited to VCL/AAEM microgels, an alternative cross-linking method is introduced in the next subchapter based on a host-guest complexation. This provides a more general approach and can be transferred to various polymer systems (e.g. NIPAAm microgels) and also applied to inorganic particles.

2.2.3 Interparticle cross-linking through host-guest inclusion complexation with β-cyclodextrin

To increase the stability against lateral shear forces of the previously described VCL/AAEM microgel strands, a well-known host-guest system, based on the complexation between β-cyclodextrin and azobenzene, was used. Pich et al. showed that copolymerization of β-cyclodextrin with VCL and AAEM was feasible.[77] In this work Dominic Schmitz from the Pich group substituted one OH-group of the β-cyclodextrin with an acrylic-moiety for copolymerization (Figure 59).[212]

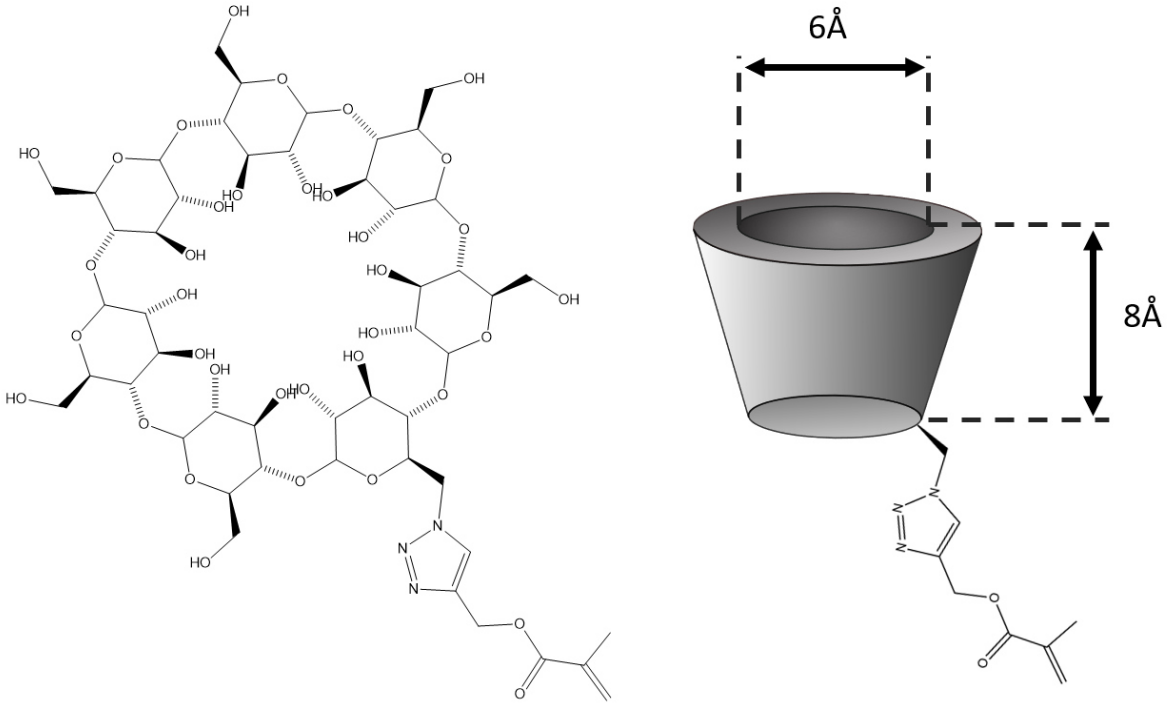

Figure 59: Chemical structure of β-cyclodextrin mono-functionalized with an acrylate moiety (left); schematic depiction of the toroid structure of β-cyclodextrin with lipophilic cavity and hydrophilic outer region.

The aim of this idea was to create β-cyclodextrin-functionalized microgels which could be cross-linked via molecular or oligomeric azobenzene cross-linkers. In theory, cross-linking should be feasible via addition of di- or polyazobenzene linkers (Figure 60).[13]

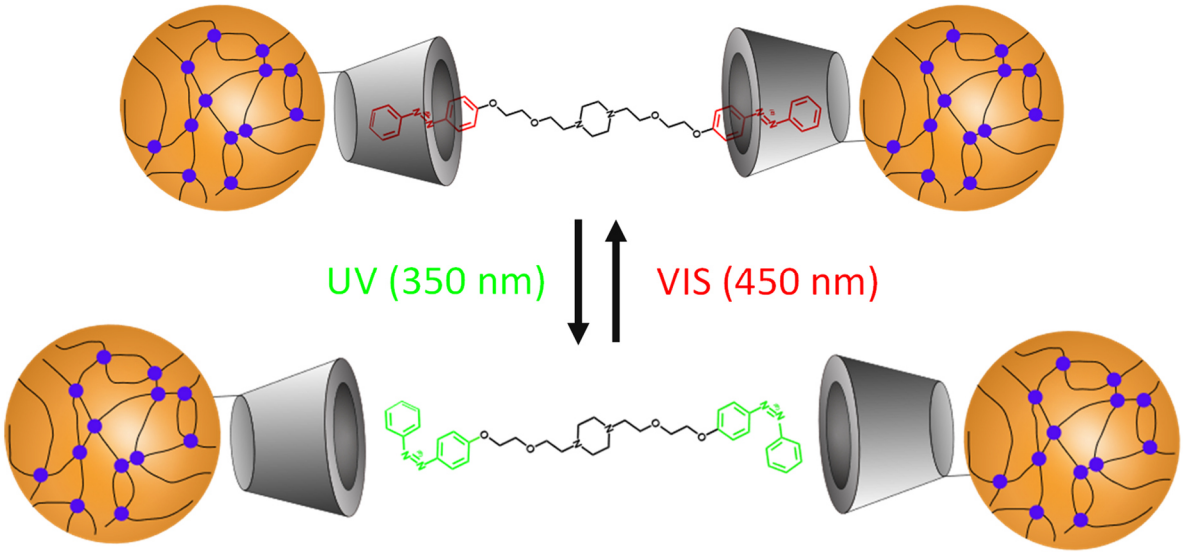

Figure 60: Model description of photo-switchable cross-linking between β-cyclodextrin functionalized microgels.

β-cyclodextrin forms cone shaped cavities of 6 Å in diameter, where the interior is hydrophobic and the outer layer hydrophilic.[213] It can thus act as a host for various guest molecules. This complexation via inclusion is used for smell removal, scavenging of drugs and nanoparticles etc.[214, 215] The synthesis of microgels by precipitation polymerization of VCL in the presence of monoacrylate substituted β-cyclodextrin has been reported by Pich et al.[77]

In the toroid of the β-cyclodextrin the trans-conformation of azobenzene can be complexed with a strong binding constant of 770 M^{-1} due to its rod-like and apolar form.[13,216] Azobenzenes are well-known light-responsive compounds which can be reversibly isomerized from the cis- to the trans-isomer by irradiation with light.[217] By applying UV light of 330 nm, azobenzene switches to the cis-conformation, which has a low binding constant due to its sterically demanding structure. This leads to a dissolution of the complex (Figure 60). Under visible light (440 nm), the trans-conformation is favored. The reversible cross-linking of the VCL/AAEM/CD microgels with a polyazobenzene linker was characterized by turbidity measurements (see Chapter 5.7 below).[218]

Additionally, with this cross-linking system it is possible to combine different microgel types and this approach is not only limited to VCL/AAEM microgels. Incorporation of β-cyclodextrin functionalized monomers in various types of microgels allows a controllable and reversible inter-particle connectivity, shown by Ravoo et al.[219, 220] Thus, this construction kit-like approach enables the combination of microgels which react upon different stimuli and enables access to a broad spectrum of microgel nanostructures (Figure 61).

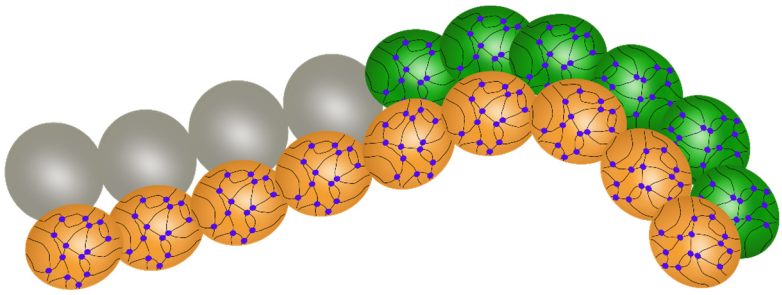

Figure 61: Schematic depiction of 1D nanostructures based on different combination of particle types.

Synthesis and characterization

The synthesis was carried out by Dominic Schmitz from the Pich group analogous to previously published protocols.[12, 77, 212] The molecular and oligomeric cross-linkers were synthesized and characterized by Jenny Krings from the Ravoo Group.[221]

Table 1: β-cyclodextrin functionalized microgels used in this work. For reasons of clarity, the β-cyclodextrin content is specified through weight percent in regard to the VCL polymer matrix of the respective microgel.

sample	VCL/AAEM /BIS [g]	β-CD [g]	β-CD [wt%]	β-CD [µmol]
VCL/AAEM/CD1	1.877/0.338/0.06	0.039	**2.1**	34
VCL/AAEM/CD2	1.877/0.338/0.06	0.081	**4.3**	71
VCL/AAEM/CD3	1.877/0.338/0.06	0.235	**12.5**	207

Microgel dimensions at air/solid interfaces and in aqueous dispersion

The particle dimensions of the β-cyclodextrin functionalized microgel samples (VCL/AAEM/CD1-3) were characterized via dynamic light scattering (DLS – hydrodynamic radii) and atomic force microscopy (AFM – dimension aspect of the spheroids on flat surfaces). In the previous Chapter 2.1, investigations regarding surface interactions, absorption behavior, cross-linking density of VCL/AAEM microgels on flat silica surfaces provided a crucial understanding for the fabrication of supramolecular nanostructures.

The microgel samples VCL/AAEM/CD1-3 were characterized analogous to the VCL/AAEM microgels described in Chapter 2.1. The standard characterization can be found in Chapter 4.

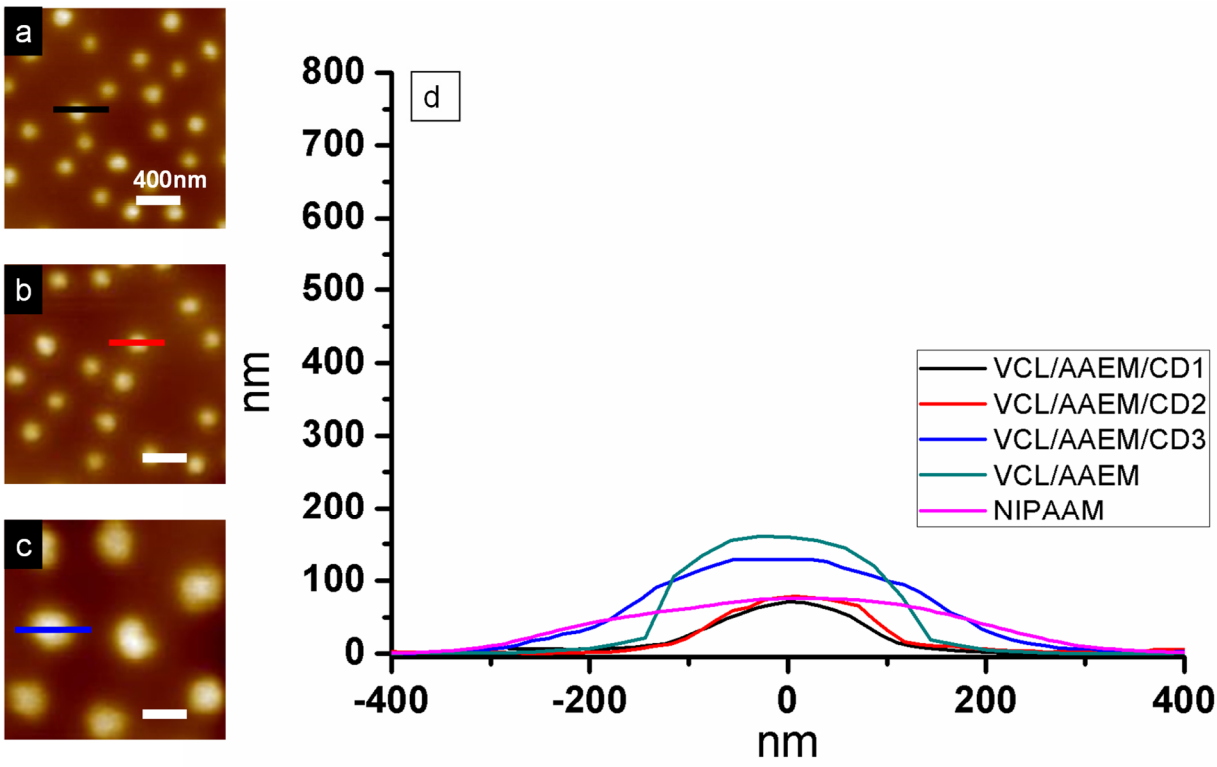

Figure 62: AFM images from VCL/AAEM/CD1-3 (a-c, Δz = 180 nm). d: corresponding cross-sections.

The aspect ratios of the VCL/AAEM/CD1-3 samples were determined by evaluating a statistically relevant amount of AFM cross-sections (> 100 microgel sections/sample).

Table 2: Microgel dimensions obtained via AFM cross-section evaluation versus hydrodynamic radius obtained via Zetasizer.

samples	AFM			Zetasizer
	XY-plane [nm]	Z-axis [nm]	Z/XY ratio	R_H [nm]
VCL/AAEM/CD1	368 ± 32	70± 7	0.19	160 ± 46
VCL/AAEM/CD2	386 ± 20	78 ± 6	0.20	210 ± 73
VCL/AAEM/CD3	708 ± 60	142 ± 8	0.20	364 ± 52

The microgels with a β-cyclodextrin content between 2.1 and 4.3 wt% showed similar size dimensions being adsorbed on a Si-wafer (Table 2). In contrast, the microgels with a relatively high β-cyclodextrin content of 12.5 wt% were twice as big (Table 2). This finding stands in contradiction to previously published literature in which growing amounts of cyclodextrin led to a decrease in size of the microgels.[77] Since the VCL/AAEM/CD3 microgels contained nearly three times the amount of β-cyclodextrin compared to the VCL/AAEM/CD2 microgels, this leads to the conclusion that below a certain β-cyclodextrin concentration (e.g. between 71 – 207 μmol) the dimensions of the microgels at the air/solid interface are predominantly determined by the VCL-matrix. A possible reason for this observation could be that at a specific concentration below 207 μmol of β-cyclodextrin, the hydrophilic β-cyclodextrin moieties predominantly reside at the outer shell of the microgels. A saturation of the outer microgel shell at concentrations between 71 μmol and 207 μmol could lead to an incorporation of the excess amounts of β-cyclodextrin groups into the inner sections of the microgels during the copolymerization. Due to the relatively high steric demand of the β-cyclodextrin monomers compared to VCL and their good capability to bind water, the VCL/AAEM/CD3 microgels are double in size

compared to the VCL/AAEM/CD2 microgels. Latter property could also hinder the de-wetting process during spin coating through water complexation. The previously stated theory is supported by AFM- and Zetasizer measurements, see Table 2**.** All samples which were characterized via AFM showed a calculated aspect ratio of about 0.2, which indicates that the deformation behavior at air/solid interfaces and thereby also the rigidity of the microgels was not significantly influenced by the different β-cyclodextrin concentrations.

Pich et al. have shown that the hydrodynamic radius of VCL/AAEM microgels is temperature dependent.[5] The cyclodextrin-functionalized microgels used in this work also showed the ability of a reversible collapse at a defined temperature (see Chapter 7). Furthermore, the VCL/AAEM/CD1-3 microgels showed a pH-dependent change in volume (Figure 63). Charged residues could have been complexed by the β-cyclodextrin during synthesis (e.g. sodium ascorbate derivatives). A similar observation has been reported by Ravoo et al.[222] A detailed characterization of the microgel properties has been carried out by the cooperation partner from the Pich group and goes beyond the scope of this work.

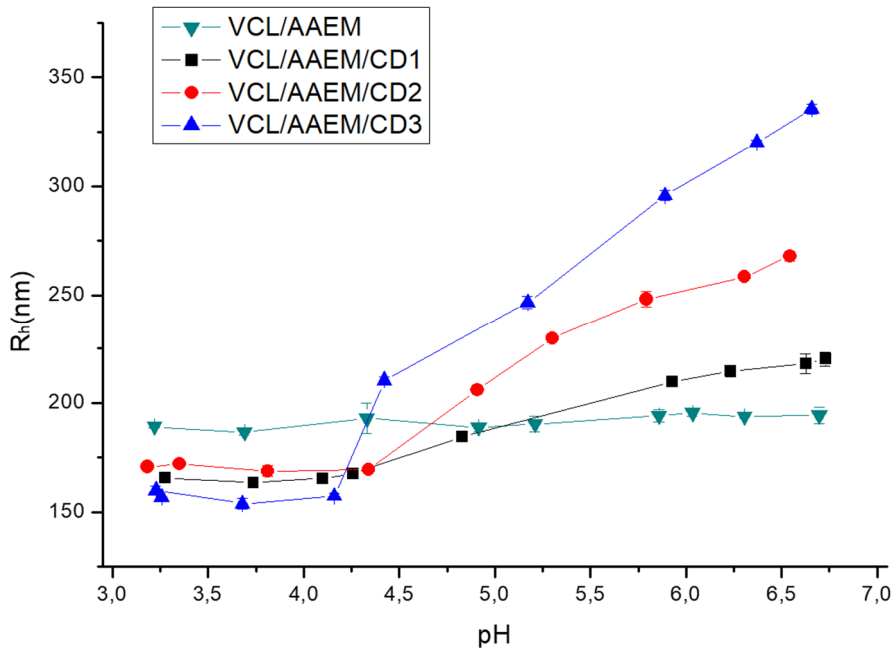

Figure 63: pH dependent measurements of the hydrodynamic microgel radii.

Focusing on the cross-linking properties of the CD functionalized microgels, cross-linking experiments in solution were conducted via turbidity measurements with the diazobenzene-linker depicted in Figure 64.

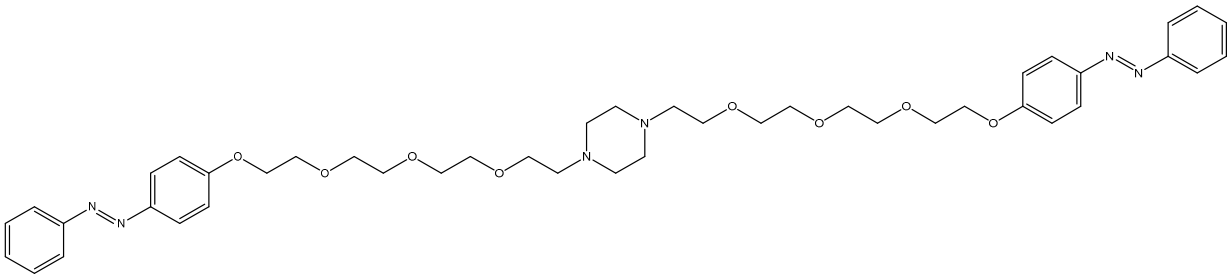

1,4-bis(2-(2-(2-(2-(4-((E)-phenyldiazenyl)phenoxy)ethoxy)ethoxy)ethoxy)ethyl)-piperazine

Figure 64: Chemical structure of the diazobenzene-linker.

The optical density measurements showed that all three microgel types can be cross-linked with the diazobenzene cross-linker . For cross-linking, the sample was irradiated with 600 nm light so that the azobenzene groups of the linker would switch from cis- to trans-conformation. This led to an immediate change in turbidity/optical density, which is shown in Figure 65 for all three microgel types. Even though the results show a correlation between CD-concentration and the optical density, the absolute values regarding the optical density were at the verge of the lower sensitivity limit of the device. The successful cross-linking can also be observed visually as shown in the photograph in Figure 65.

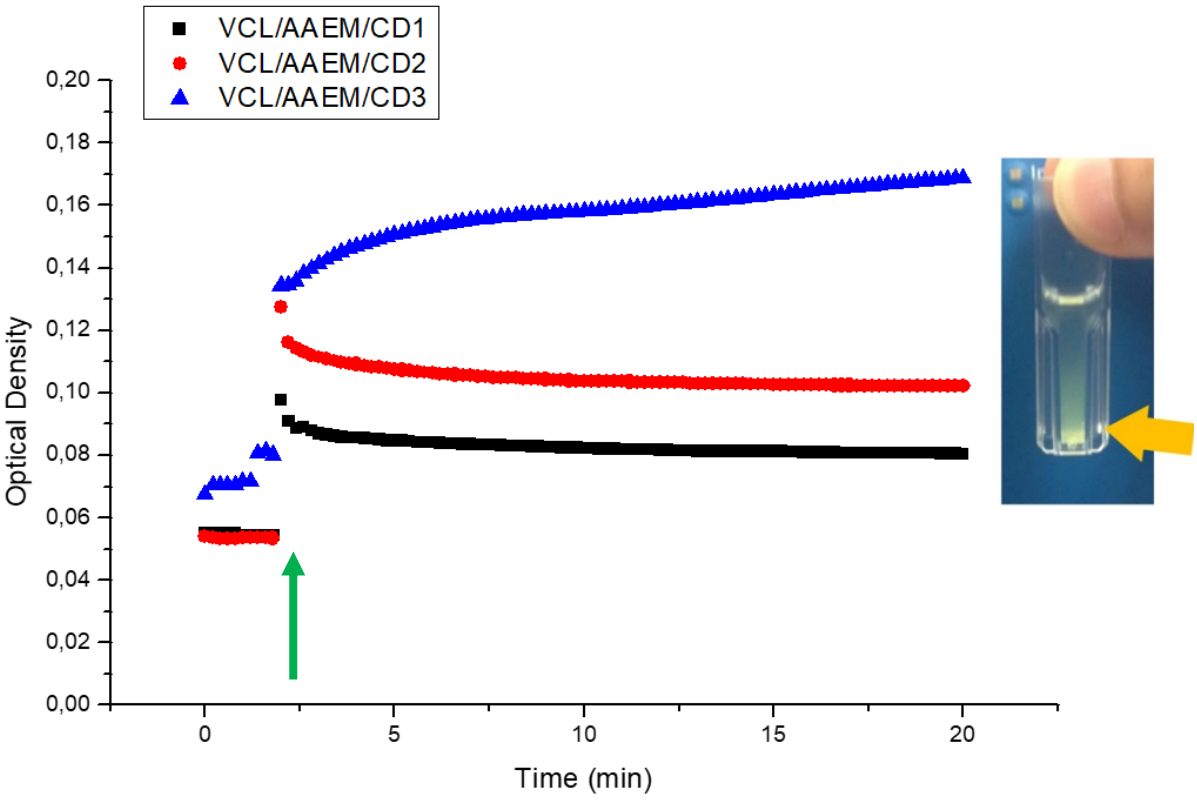

Figure 65: Optical density measurements with VCL/AAEM/CD1-3 microgels cross-linked with the diazobenzene-linker. The green arrow indicates the moment when the cross-linker was injected to the experiment. Inset: picture of the turbid dispersion.

Guided self-assembly of β-cyclodextrin functionalized microgels

To determine the optimal assembly conditions for the β-cyclodextrin functionalized microgels used in this work, preliminary assembly experiments towards 1D nanostructures, analogous to those discussed in previous chapters, were conducted. The aim of these preliminary experiments was to determine the most suitable microgel sample for a given alignment method. A knowledge of the hydrodynamic radii, the structural behavior of the microgels at air/solid interfaces and the surface charge of the microgels were crucial to understand their assembly behavior at hydrophilic and negatively charged wrinkled surfaces. Based upon the microgel size wrinkled substrates with suitable wavelengths (500-900 nm) were chosen. Spin-coating and molding conditions can be found in Chapter 4.

Using water as a dispersant, it was found that the quality of the assembly decreased with increasing particle charges (Figure 66g). This is the reason why VCL/AAEM/CD1 showed the best alignment results due to the low β-cyclodextrin content (Figure 66c), while for VCL/AAEM/CD3, the particles were several hundred nanometers apart from each other (Figure 66a).

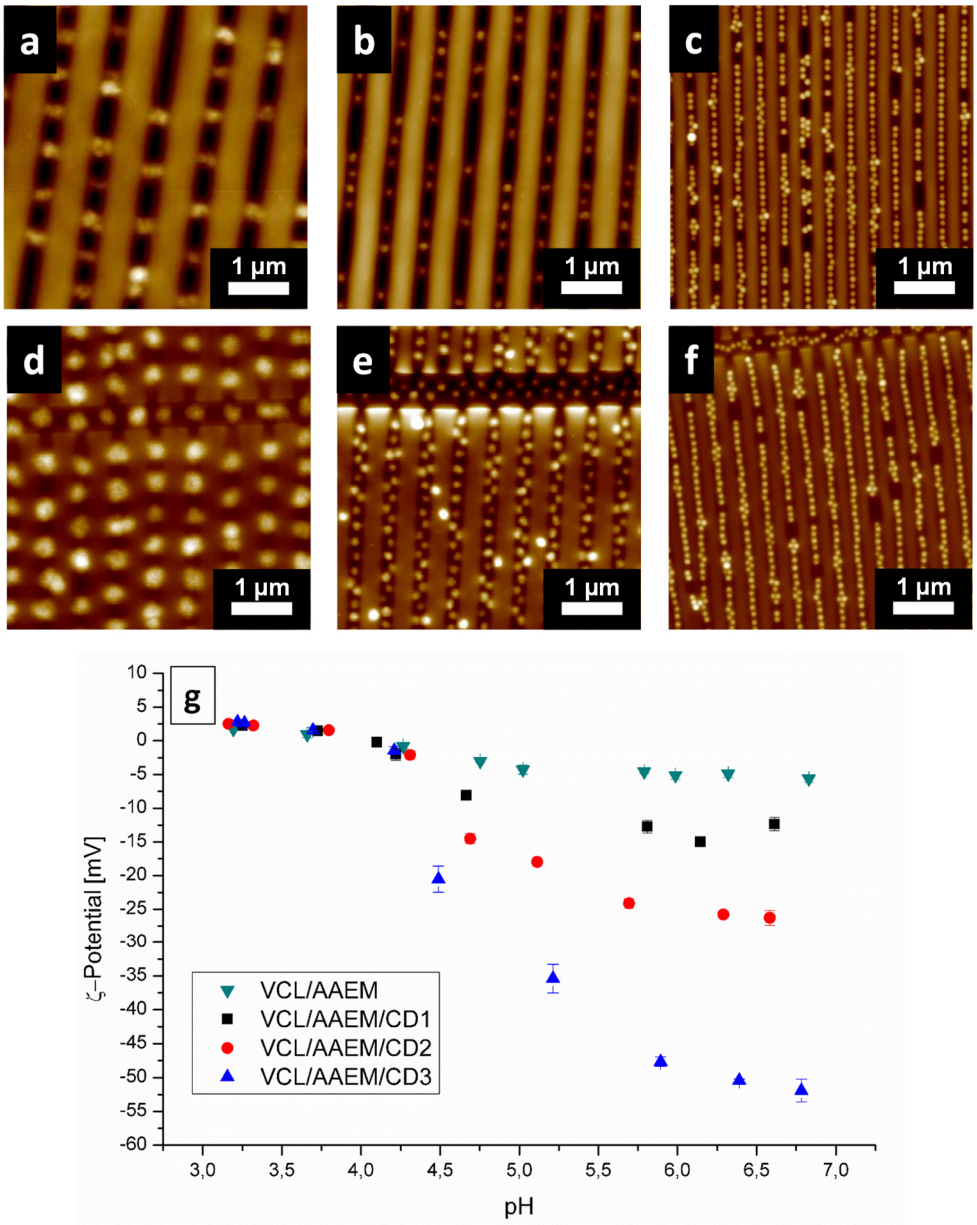

Figure 66: Spin-coating experiments onto wrinkled substrates with VCL/AAEM/CD microgels dispersed in water → a: VCL/AAEM/CD3, b: VCL/AAEM/CD2, c: VCL/AAEM/CD1, Δz=120nm and ethanol → d: VCL/AAEM/CD3, e: VCL/AAEM/CD 2, f: VCL/AAEM/CD1, Δz=200nm. g: corresponding ζ-potentials in water.

The alignment of the microgels could be optimized by using ethanol as the dispersant. While Figure 66f is showing nearly no difference to the corresponding experiment with water, in Figure 66d and Figure 66e a closer microgel packing is obtained through spin-coating with ethanol. Through this method VCL/AAEM/CD2 microgels are forced into close proximity to each other, while the particle charges of the VCL/AAEM/CD3 microgels still hinder close packing but leads to an equidistant alignment (space between microgels ~ 100 nm). The low surface tension of ethanol contributes to a better wetting of the wrinkles which in turn results in a more efficient distribution of the microgel particles into the grooves during spin-coating.

Assembly Method 1 – spin coating and printing

In Figure 66 it can be seen that microgel alignment via spin-coating in not suitable for the fabrication of 1D nanostrands, due to the high defect rate and the repulsion between the microgels. The Assembly Method 1 was not further pursued for these microgel types.

Assembly Method 2 – template assisted molding

In order to circumvent an interference of the physical properties with the alignment of the microgels, the template assisted molding process described in Chapter 2.1 was used (Experimental setup see Chapter 4). This method is forcing the microgels to occupy the space in between the grooves, which leads to a dense packing despite repulsion through surface charges and steric hindrance. The charged VCL/AAEM/CD3 microgels with a $\zeta-$ potential around -60 mV (Figure 67a) were forced to align in close proximity, even though the single microgels were still visible due to the electrostatic repulsion. With decreasing particle charge, the alignment quality improves and the individual microgels merge into homogeneous strands (Figure 67b-c). The aimed inter-particle connectivity through cross-linking could benefit from latter observation due to a high overlap of the single microgels with neighboring particles. Based upon these findings, VCL/AAEM/CD1

showed the best compromise between alignment quality and concentration of cross-linkable moieties. In Figure 67d, the relatively high long-range order of the microgel arrays is shown. For this reason, further investigation towards cross-linking of the aligned microgel arrays were conducted with VCL/AAEM/CD1 microgels. It was postulated that if a successful cross-linking can be achieved by using microgels with the lowest concentration of CD-moieties, the microgels with higher CD concentrations will work as well.

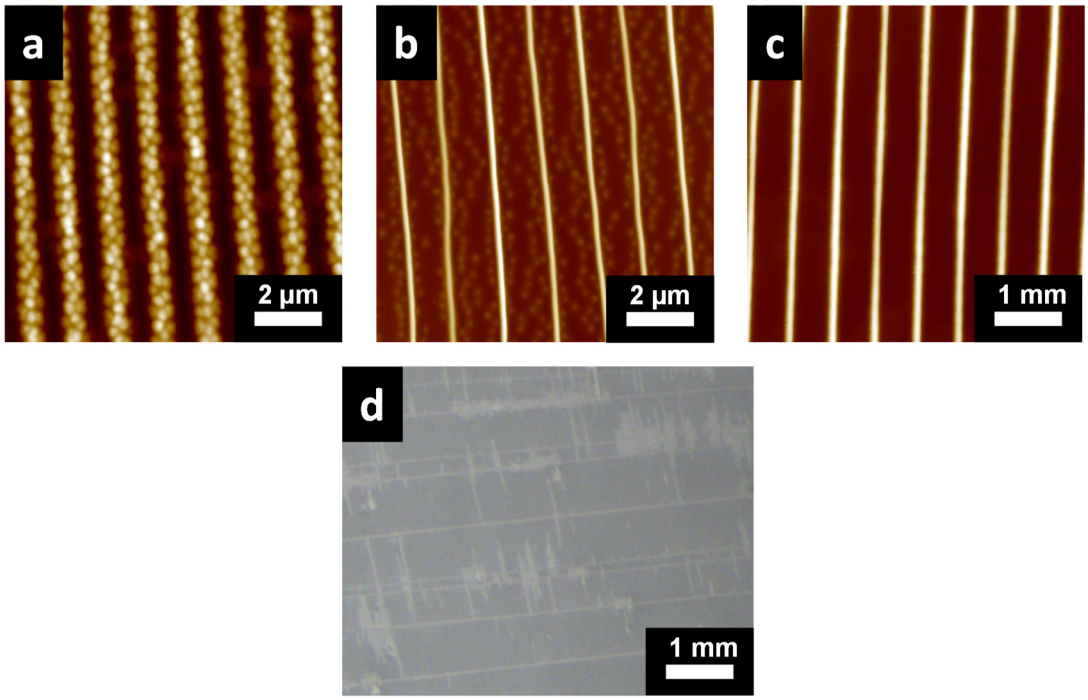

Figure 67: AFM and optical microscopy images of: a: VCL/AAEM/CD3 microgel arrays, b: VCL/AAEM/CD2 microgel arrays, c: VCL/AAEM/CD1 microgel arrays and d: VCL/AAEM/CD1 optical microscopy image of aligned arrays.

As already mentioned, the VCL/AAEM/CD1 microgels showed the most promising results in terms of alignment through molding and spin-coating while maintaining the minimal amount of cross-linking capability. In this chapter, both approaches towards the fabrication of stable microgel strands are discussed.

Cross-linking of microgel arrays on top of the wrinkles

VCL/AAEM/CD1 microgels were spin-coated onto a suitable wrinkled substrate. Experimental details are described in Chapter 4. In short, the diazobenzene-linker was dissolved in DMSO. A droplet of the dissolved linker was applied onto the wrinkled substrates to cross-link the microgel arrays. Note: The trans-configuration, which is necessary to induce cross-linking via host-guest complexation with the cyclodextrin moieties, is thermodynamically favored. After 10 min, water was used to transfer the cross-linked microgel strands from the wrinkled surface to a flat Si-wafer. Analysis by AFM showed that the microgels agglomerated. It can be assumed that the cross-linking was in principle successful, but upon redispersion of the cross-linked strands, non-complexed CD moieties led to further cross-linking between neighboring particles and agglomeration occurred. This assumption was experimentally proven in the following.

Cross-linking of template confined arrays

Since the latter approach was not suitable, substrates with molded VCL/AAEM/CD1 microgels on Si-wafers were used. Experimental details are described in Chapter 4. Applying a droplet of dissolved diazobenzene-linker onto the molded microgel arrays led to a similar agglomeration as described above. This was the reason to change the cross-linking method towards an in-situ cross-linking during the molding process. For this method, the Assembly Method 2 was undertaken up to the point where the wrinkled substrate had to be removed from the Si-wafer. Before taking off the wrinkled mold, the diazobenzene-crosslinker was applied on both sides of the wrinkles as shown in Figure 68. For this approach, wrinkles with a wavelength around 1 μm were used to ensure that capillary forces were strong enough for DMSO to penetrate the wrinkled grooves and thereby carry the cross-linker as far as possible into the grooves. At the same time, the wrinkled substrate hindered the single microgel strands to move towards each other and agglomerate. It must be kept in mind that capillary forces are still effective submicron scale.[223]

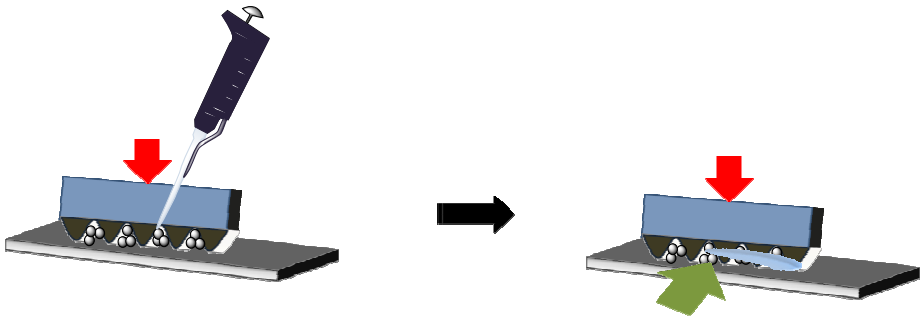

Figure 68: Schematic depiction of cross-linking via diazobenzene-linker of VCL/AAEM/CD1 microgels during molding.[205]

To test whether the cross-linking procedure towards microgel strands was successful, a droplet of ethanol was applied on a tilted sample analogous to the experiment depicted in Figure 49 of the previous chapter. As described before, the ethanol should be able to detach the microgel strands to the extent that the single strands start moving with the droplet flow determined by the tilted angle. Analysis of the samples obtained through the preparation described in Figure 68 via AFM imaging showed equidistantly aligned strands (see Figure 69a). Due to the detachment of the wrinkled templates, the single microgel strands were moved on a microscopic scale. Traces of the original position can be observed in Figure 69a. In Figure 69c it can be clearly seen that the microgels moved as predicted alongside the flow direction of the applied ethanol droplet. Their original position and perpendicular alignment were disbanded. Figure 69c also showed that the microgels were able to bend to a great extend without breaking apart, which in turn verified successful cross-linking. However, the magnification in Figure 69c also showed that the strands stick together once they reach close proximity to each other. This can be considered as the main reason why all the previous fabrication methods failed in yielding single microgel strands comparable to the UV-cross-linking experiments discussed in Chapter 2.2.2. Without applying the diazobenzene-crosslinker, the prealigned arrays shown in Figure 69b, were completely disbanded by ethanol.

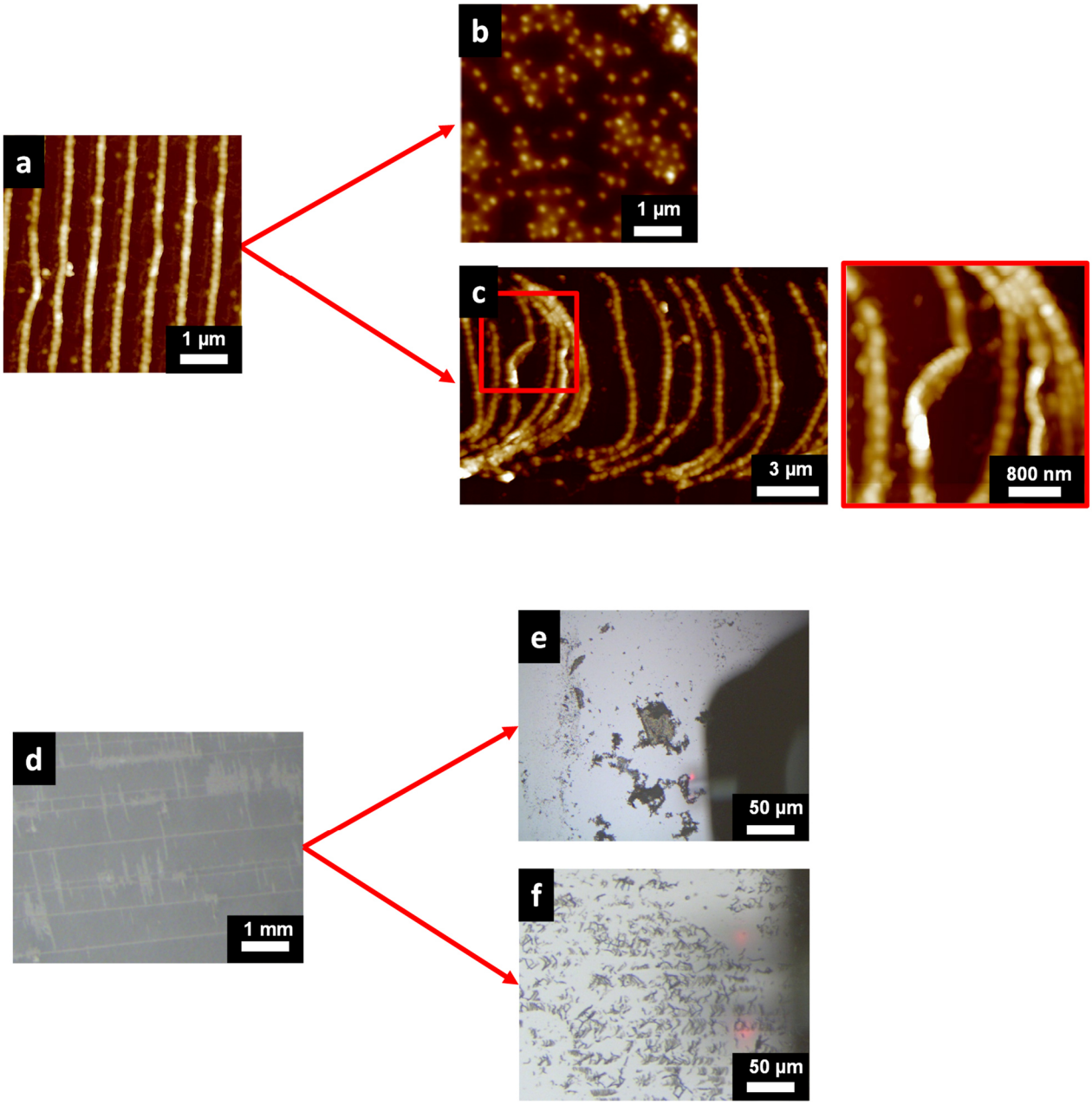

Figure 69: AFM and optical microscopy images of the tilt-experiment. a and d: VCL/AAEM/CD1 microgel aligned via Assembly Method 2 after cross-linking, c and f: cross-linked microgels after the tilt-experiment. b and e: reference sample of non-cross-linked microgel arrays after tilt-experiment.

The magnification in Figure 69c shows how several strands, here 4-5 strands, form a bundle. These bundles were a frequent phenomenon, which is shown in the optical microscopy image in Figure 70. A large amount of these bundles can be seen in this image. Their length

is determined by the perpendicularly aligned cracks of the wrinkled mold (approx. 10 µm, see Chapter 2.1). The bundle formation is highlighted in 3D-extrapolation (Figure 70). Based on the height information from the AFM data, bundles are formed by strands stacking in all three dimensions. This finding stands in contrast to the VCL/AAEM ribbons discussed in Figure 51d which formed flat structures due to steric repulsion. Additionally, in Figure 70can be seen where the original positions of the single strands were before they were pushed together.

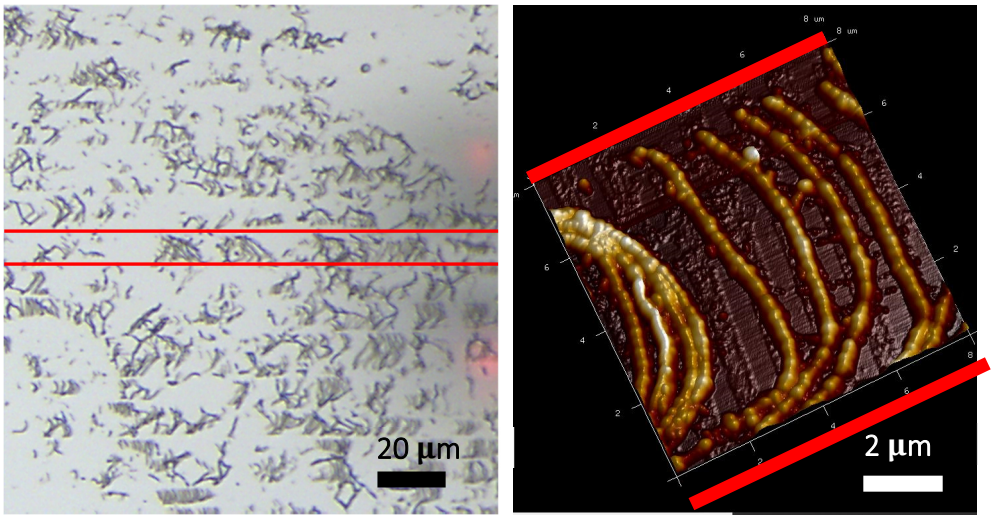

Figure 70: left: optical microscopy image of bundles of microgel strands. Right: 3D- extrapolation of an AFM image which shows the formation of microgel bundles when the single strands were moved towards close proximity. Red bars show the ca. 10 µm distant voids which were determined through the perpendicular cracks on wrinkled templates. In contrast to single strands that were barely detectable via optical microscopy (Figure 67c), here microgel bundles are clearly visible.

One can assume that since this bundle formation was not observed for the UV-cross-linked strands (Figure 49), the reason must be found in the cross-linking system by host guest complexation with β-cyclodextrin. The previously speculated abundance in β-cyclodextrin moieties which interact with free diazobenzene-linkers from the neighboring strands could be one explanation for these bundles and random agglomerations in the previously described experiments. The more probable reason, however, could lie in an entropy gain.

When two CD moieties which are only occupied with one diazobenzene-linker meet, they could release one diazobenzene-linker molecule while sharing the other one. This can happen between neighboring strands or single microgels, respectively, which in turn explains the bundle formation and agglomeration through cross-linking.

Capping through cyclodextrin abundance

To circumvent the bundle formation, several approaches were pursued. One approach was conducted by using excess β-cyclodextrin in solution to end-cap single bonded diazobenzene-linkers. Therefore, the cross-linked microgel strands were subjected to β-cyclodextrin solutions with different concentrations to find the minimal concentration required to end-cap the single bonded diazobenzene-linkers. Afterwards, the substrates with the cross-linked strands were analyzed by AFM and optical microscopy.

All optical microscopy images showed that the substrates were covered by crystallized β-cyclodextrin and microgel nanostructures, as seen in Figure 67c, were not visible at all (Figure 71). Therefore, AFM imaging could not be performed.

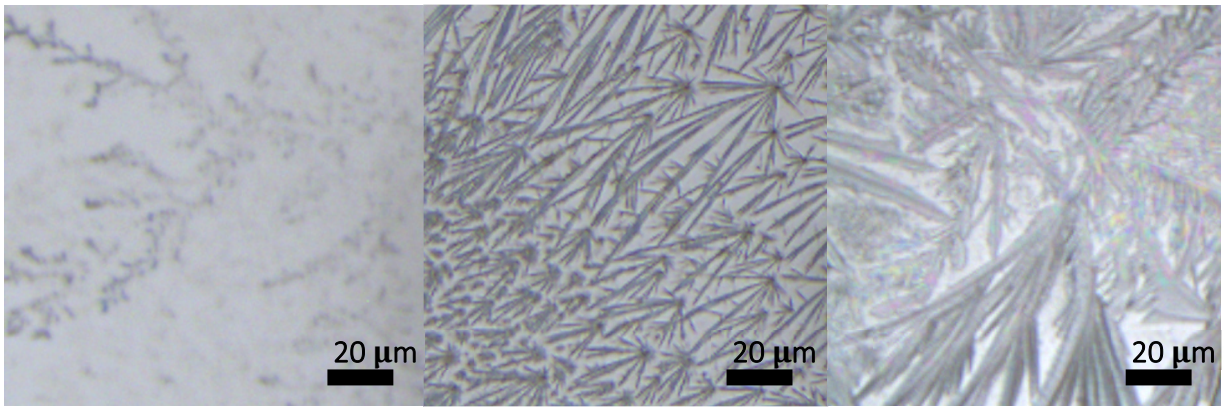

Figure 71: Substrates with crystallized β-cyclodextrin: left: c(CD) = 0.7 mmol/L; middle: c(CD) = 10 mmol/L; right c(CD) = 16 mmol/L.

In dependence of the β-cyclodextrin concentration, larger crystallites were obtained. Even the lowest concentration of 0.7 mmol/L yielded a crystalline β-cyclodextrin layer. If there were strands left, they had to be underneath this layer. To uncover the microgel strands, all substrates were carefully rinsed with distilled water. Despite this measure, no strands were detected, probably due to detachment of the microgel strands during the crystallization process.[224]

To conclude, this method requires a very delicate balancing of all process parameters to be successful and goes beyond the limits of experimental feasibility.

Capping through azobenzene functionalized Au-NPs

In another approach, nanoparticles were used for end-capping the microgel strands. The aim was to wrap the microgel strands in a dense particle layer and thereby hinder further cross-linking with neighboring strands through steric repulsion. The idea behind this approach was to use polyfunctional Au-NPs to replace single bonded azobenzene in the CD-moieties at the surface and occupy free CD-moieties at the same time. The resulting gain in entropy, which was described above, should be the driving force behind this reaction.

Therefore, 10 μL of 30 nm Au-NPs which were functionalized with azobenzene end-groups, was pipetted onto a substrate with cross-linked microgel strands (Figure 72, left). After drying and careful rinsing with distilled water, AFM images were taken. At low magnifications, few differences between the cross-linked microgel strands and the end-capped gels were visible. It seemed that the rinsing detached some segments of the aligned strands without moving the remaining ones. Furthermore, parts of the microgel strands appeared broader in comparison to the strands without Au-nanoparticles.

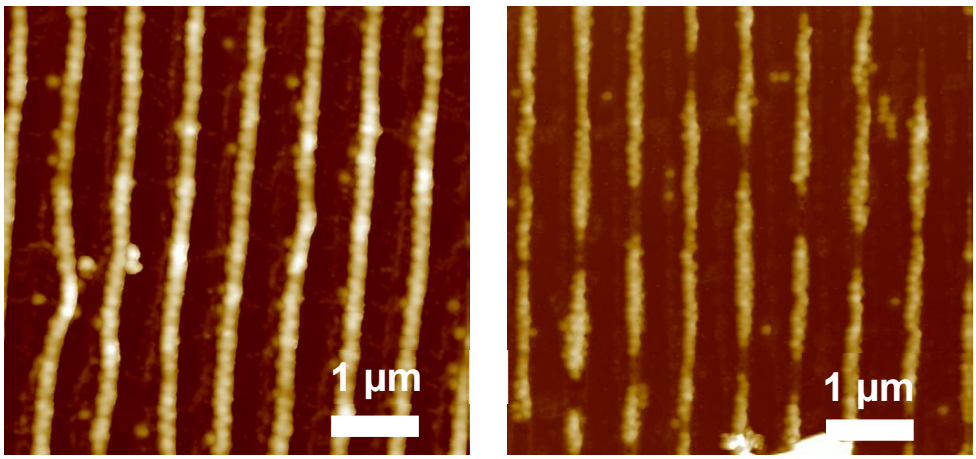

Figure 72: left: AFM images of VCL/AAEM/CD1 microgel strands cross-linked with the diazobenzene cross-linker; right: cross-linked gels end-capped with azobenzene functionalized Au-NPs (Δz = 250 nm).

After magnification of single strands, the differences in the surface structure becomes more apparent (Figure 73). One can see that the surface structure became less smooth compared to the microgel strands without particle end-capping. In conclusion, covering the microgel strands with Au-particles was successful.

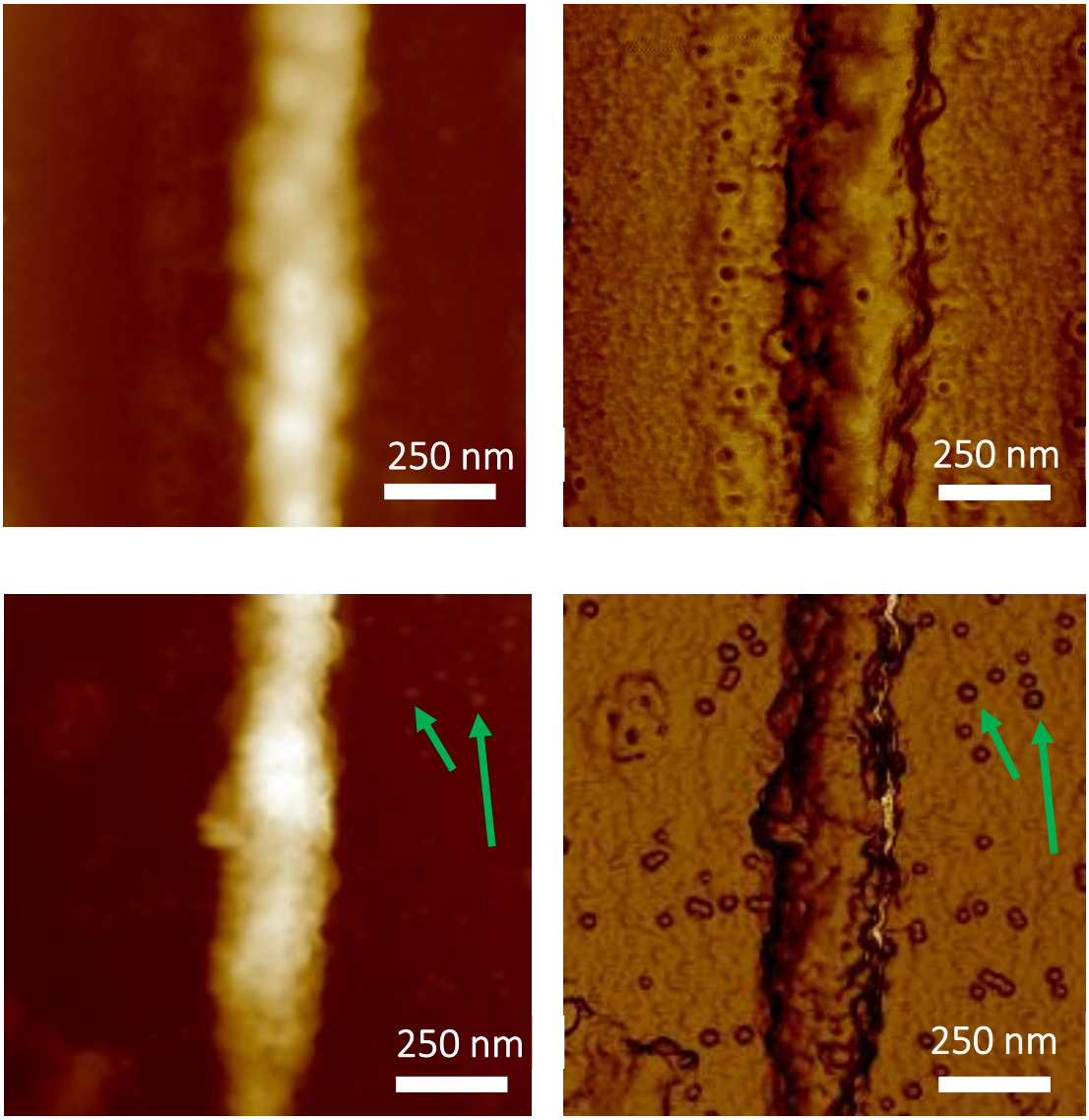

Figure 73: top: AFM height and phase image of cross-linked VLC/AAEM/CD1 microgels. Bottom: AFM height and phase image of VCL/AAEM/CD1 microgel strands end-capped with 30 nm Au-particles. Green arrows indicate two examples of Au-NPs.

In Figure 73 bottom, free 30 nm Au-particles can be seen, which could indicate that a surface saturation at the given Au-particle concentration was reached.

After conducting the tilted-substrate experiment with ethanol, described in the previous section of this chapter, AFM images were taken. Figure 74 shows that the single strands were not displaced by the ethanol droplet. Even the Au-agglomerates were still present. A possible reason could be that after covering the microgel strands with Au-particles the strands were too heavy to be moved by the solvent. Even a detachment via a pipette, analogous to the experiments described in the previous chapter was not successful.

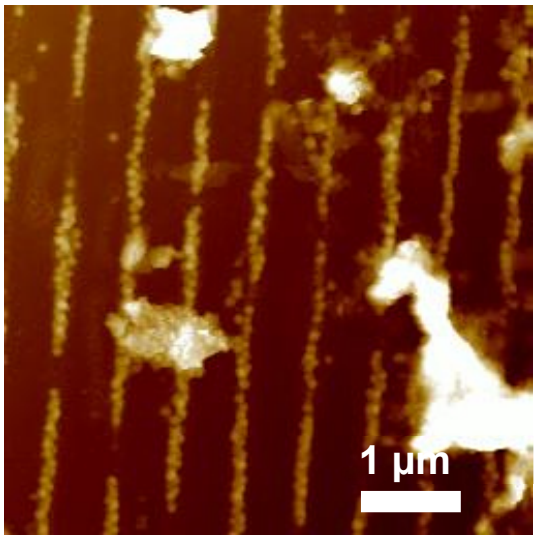

Figure 74: AFM image of the VCL/AAEM/CD1 microgels end-capped with Au-NPs taken after the tilted-substrate experiment.

Harada Polymer

Combining the insights of all previous described experiments, one can conclude that the entropy-driven exclusion of diazobenzene linkers is the main antagonist towards the fabrication of single microgel strands using the host-guest complexation for cross-linking.

Based upon these findings, a diazobenzene functionalized polymer was introduced as a cross-linker instead of the molecular diazobenzene linker. This combines three advantages. First, by using the cross-linking method analogous to the diazobenzene linkers, the single strands will be covered by polymer coils shielding potentially remaining CD-moieties. Thereby, a formation of microgel bundles through cross-linking with neighboring strands during the tilted-substrate experiment is hindered significantly (Figure 70). Second, there is no entropy gain by exchange of azobenzene groups attached to the same polymer. Even if free azobenzene groups of neighboring strands are accessible, still no significant entropy gain is expected. Third, in contrast to polyfunctionalized Au-particles, the polymer is much lighter. Thus, after covering the strand surfaces with the polymer, the strands should still remain displaceable with ethanol. The cross-linking strength should depend on the azobenzene ratio within the polymer. For the following experiments, a polymer consisting out of acrylamide and azobenzene-acrylamide with a ratio of 50:50 was used based on the work of Harada et al. (Figure 75).[212, 221, 225] The polymer was synthesized and characterized by Jenny Krings from the Ravoo group.

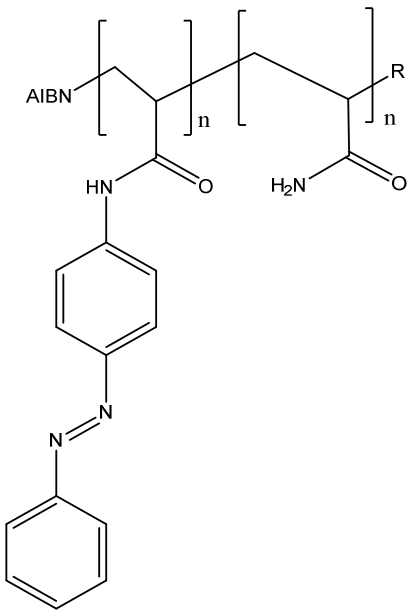

Figure 75: Structure of the Harada polymer.

Due to the high content of azobenzene, the polymer was no longer soluble in water. Therefore, ethanol was used as the solvent. Similar to the characterization of the cross-linking capability of the microgels with the molecular diazobenzene linker, optical density measurements were performed.

The optical density measurements show that all three microgel types can be cross-linked with the Harada polymer leading to an immediate change in turbidity/optical density which is shown in Figure 76. In contrast to the diazobenzene linker, the Harada polymer leads to significantly higher optical density. Compared to the molecular diazobenzene, the large size of the polymer linker enables the formation of larger agglomerates, which are easier detectable optically. Additionally, one single polymer molecule can cross-link several microgels simultaneously. The successful cross-linking can also be observed visually via the photographs in Figure 76.

With increasing CD-concentration of the VCL/AAEM/CD1-CD3 microgels, the turbidity increases since the VCL/AAEM/CD3 microgels are nearly twice as large as VCL/AAEM/CD1 and CD2 (Table 2).

Despite the large polymer, the cross-linking speed is high, and the saturation is reached in several minutes. A comparison of the cross-linking speeds between these two cross-linkers is not possible, since the optical density obtained with the diazobenzene linker was at the verge of the lower sensitivity limit of the device, providing unprecise values. To summarize, all three microgel samples were cross-linkable with the Harada polymer.

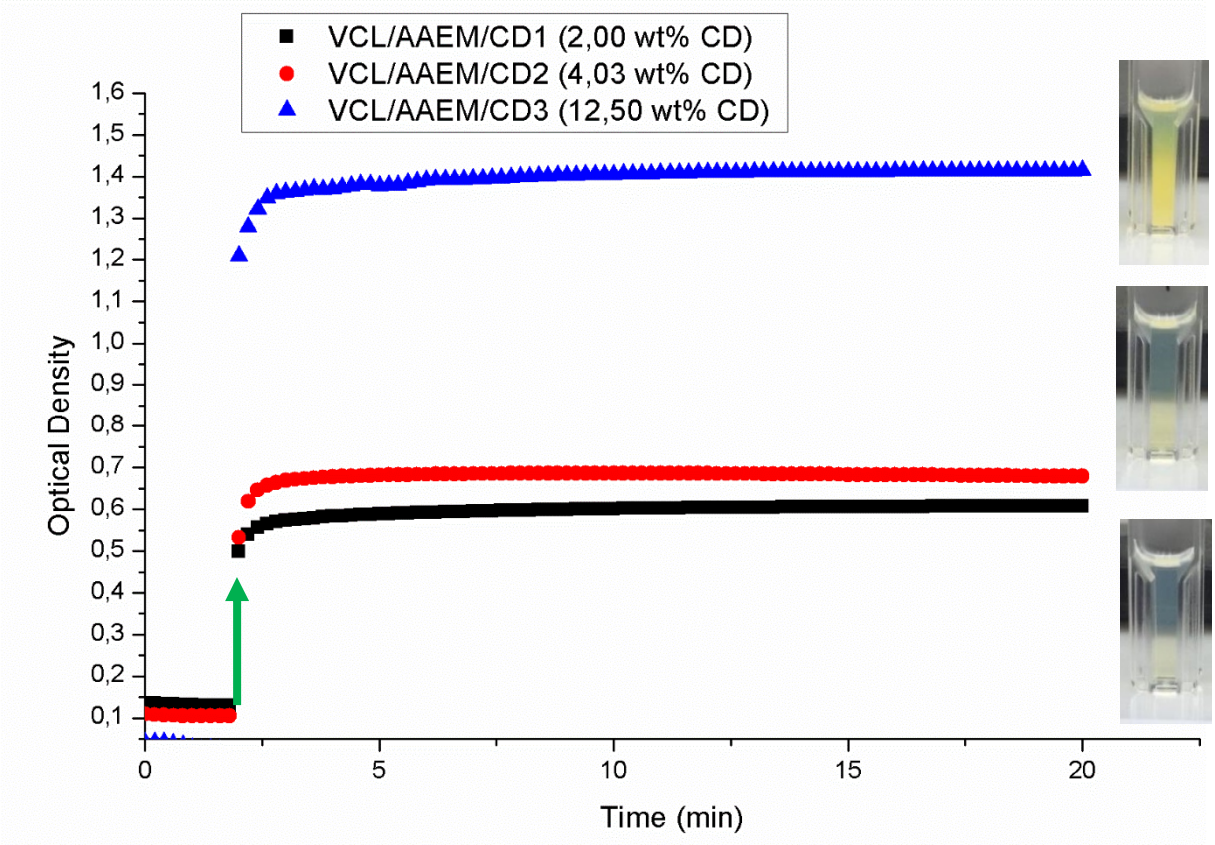

Figure 76: Optical density measurements with VCL/AAEM/CD 1-3 cross linked with the Harada polymer. Inset: pictures of turbid dispersions. The green arrow indicates the moment when the cross-linker was injected to the experiment. Inset: picture of the turbid dispersion.

Cross-linking of template confined arrays by the Harada polymer

Based upon these findings, substrates with molded VCL/AAEM/CD1 microgel arrays were cross-linked with a small amount of the Harada polymer dissolved in ethanol. Again, the Assembly Method 2 was undertaken up to the point where the wrinkled substrate had to be removed from the Si-wafer. Before lifting off the wrinkle mold, the Harada polymer solution was applied on both sides of the wrinkles as shown in Figure 68. Experimental details are described in Chapter 4.

A droplet of ethanol was applied on the tilted sample analogous to the tilted-sample experiment depicted in Figure 49 of the previous subchapter. Afterwards, AFM and optical

microscopy images were taken. The image taken by optical microscopy (Figure 77 left) shows that agglomeration was less pronounced compared to the microgel strands which were cross-linked by the diazobenzene cross-linker (Figure 70 left). AFM images of the non-agglomerated areas show promising results. Some strands, which were displaced towards each other, showed no cross-linking with the neighboring strand, despite being in close proximity.

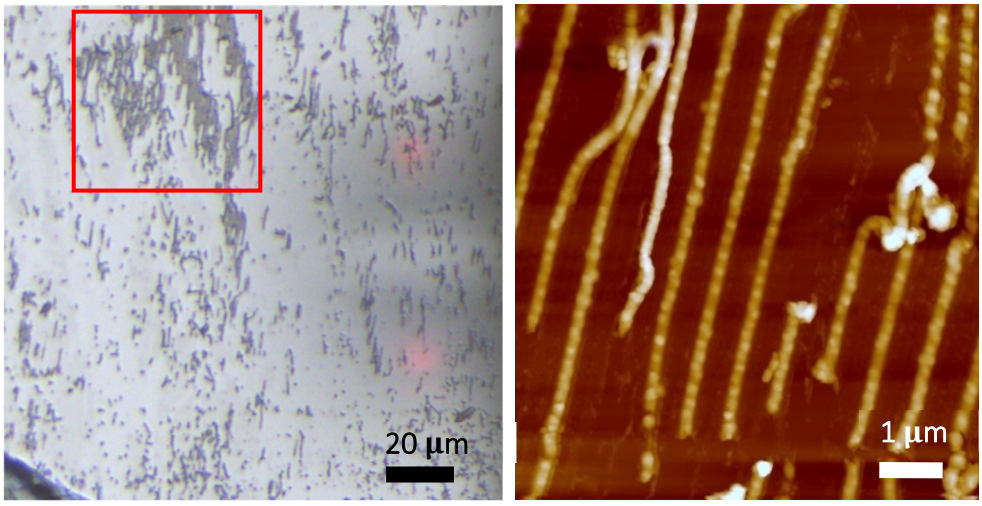

Figure 77: left: optical microscopy image of microgel strands and bundles. The red rectangle depicts the area in which the AFM image was taken. Right: AFM height image which shows microgel strands which were cross-linked by the Harada polymer.

Nevertheless, these results must be considered with caution, since the differences between the results obtained through these two cross-linking systems are not that pronounced. Therefore, more careful examination would be necessary to confirm these first very promising results. However, further experiments would have exceeded the time frame of this work.

To conclude, the fabrication of microgels strands via host-guest complexation was achieved. Optical density measurements confirmed that microgels were cross-linkable by using a bi-functional azobenzene linker and a multifunctional azobenzene functionalized polymer (Harada polymer). In summary, when using the host-guest complexation system

based on cyclodextrins to fabricate 1D microgel strands, the azobenzene functionalized Harada polymer is the most promising candidate towards the fabrication of multifunctional nanostructures based on a construction kit-like approach.

2.2.4 Conclusion

In summary, the fabrication of 1D nanostructures was feasible with both cross-linking methods.

For UV cross-linking, the most efficient method was found to be the cross-linking while the microgel arrays were aligned within the grooves of the wrinkled substrate. Studies regarding the control of the strand dimensions (strand length and width) showed that the strand width is controllable via the wavelength λ of the wrinkled template. By increasing the wavelength, different strand structures were obtained, starting with pearl-necklace like microgel strands. These strands were sensitive towards shear forces due to insufficient interparticle overlap. By exceeding a certain substrate wavelength, the strand alignment changed towards a zigzag formation, ensuring a larger overlap area between neighboring microgels and thus increasing the cross-linking stability significantly while losing flexibility. Surprisingly, increasing the wavelength even further led to flat 2D-microgel strands with a width of one micron or bigger. The space the wrinkles grooves provided was potentially sufficient enough to stack or pile microgels on top of each other. Due to the steric repulsion between the microgels, a stacking was prohibited by de-wetting processes during spin-coating, leading to the formation of flat ribbon like strands. However, due to the inertial mass of these strands, even weak shear forces led to a disintegration of the ribbons into fragments. In conclusion, the alignment of microgels in zigzag formation provided the best compromise in terms of flexibility and inter-particle connectivity.

Controlling the length of the microgel strands turned out to be more challenging. The length of the relatively stable zigzag strands where limited by the distance between the cracks of the wrinkled substrates, leading to microgel strands of several hundred micrometers. One way of controlling the length of the microgel strands is to control the

perpendicular defects (e.g. cracks). By creating ceramic rhombs shown by Böker et al.,[226] the alignment space for the microgels can be defined for both lateral directions on a planar surface.

By combining different alignment methods even complex structures like microgels meshes and microgel double/triple strands, consisting out of two different AAEM/VCL microgels, were feasible with this cross-linking approach.

Since similar experiments with NIPAAm based microgels were not successful, presumably due to the absence of AAEM in the shell, a more general cross-linking approach was searched for. Host-guest complexation provides therefore a suitable tool, since the β–cyclodextrin used herein was functionalized with an acrylic group for copolymerization.

The fabrication of microgels strands via host-guest complexation was achieved. β–cyclodextrin modified VCL/AAEM microgels showed a concentration dependent change in hydrodynamic radii. At a certain threshold concentration of β–cyclodextrin, a surface saturation with the latter comonomer could have been the reason for a drastic increase in size. While VCL/AAEM/CD1 and CD2 with 2.1 wt-% and 4.3 wt-% β–cyclodextrin were similar in size, VCL/AAEM/CD3 with 12.5 wt-% was nearly twice as big as the other microgels.

Optical density measurements confirmed that microgels were cross-linkable by using a bi-functional azobenzene linker and a multifunctional azobenzene functionalized polymer (Harada polymer). Due to the large size of the polymer and the subsequent formation of larger agglomerates, the change in optical density was more pronounced compared to the reaction with the diazobenzene linker. Nevertheless, the complexation reactions for both cross-linkers were sufficiently fast for experimental handling, and both were suitable for the formation of 1D-microgel strands.

With increasing β–cyclodextrin content, the surface charge of the microgels increased, respectively. As a result, the standard alignment process was affected by the cyclodextrin loading. VCL/AAEM/CD3 microgels with 12.5 wt-% of β–cyclodextrin showed the highest repulsion of each other, which inhibited a close proximity alignment and thus strand

formation. Interestingly, using ethanol as a dispersant for VCL/AAEM/CD3 microgels, a nearly equidistant alignment of single particles on wrinkles was achieved. Best alignment results for strand formation were feasible by using the microgels with the lowest β–cyclodextrin loading. Despite the low content of β–cyclodextrin, these microgels still yielded a sufficient cross-linking reaction for strand formation.

Based upon these results, cross-linking experiments via inclusion complexation with both cross-linkers were successfully conducted after optimizing the cross-linking procedure. For the diazobenzene linker, large agglomerates and strand bundles formed when neighboring strands came in contact with each other. It was postulated that two factors were responsible for these bundles: unoccupied β–cyclodextrin moieties and an entropy gain through exclusion of single bonded diazobenzene linkers during cross-linking of neighboring strands. To circumvent these secondary reactions, end-capping by a solution with excess β–cyclodextrin was tried. However, heavy crystallization of β–cyclodextrin on the substrate surface hindered further examination. As an alternative, Au-nanoparticles which were functionalized with azobenzene moieties were used for end-capping the microgel strands. However, the heavy Au-NPs hindered the strand detachment, rendering further characterization of the single 1D microgel strands impossible. Last, the Harada polymer was used, which provided a solution for both factors of strand agglomeration and bundle formation. In contrast to the molecular diazobenzene linker, the Harada polymer, by being a larger molecule, could shield remaining unoccupied CD-moieties on the microgel strands more efficiently. Thus, it could prevent a post-cross-linking of neighboring strands during the tilted-substrate experiment (Figure 70). Additionally, an exchange of azobenzene groups attached to the same polymer would not alter the entropy of the system in a significant manner. Compared to polyfunctionalized Au-NPs, the polymer is much lighter, thus not hindering a detachment of the microgel strands with ethanol after covering their surface. In summary, when using the host-guest complexation system based on cyclodextrins to fabricate 1D microgel strands, the azobenzene functionalized Harada polymer is the most promising candidate.

Comparing the cross-linking via UV irradiation with the inclusion complexation, the latter is a more elaborate tool, versatile in terms of transfer to other systems (e.g. polymer or inorganic) and reversible by the photo-switchable linker. However, it requires more fine-tuning of the experimental setup, because the host and guest molecules remain active after strand formation resulting in agglomeration which is difficult to avoid. In contrast, UV cross-linking functions only during irradiation with UV-light. Thus, reactive groups are not present after treatment. This cross-linking method provided stable strands which did not agglomerate. However, this method was limited to VCL/AAEM microgels.

For further studies towards the properties of the microgels strands in solution (e.g. diffusion, flexibility, capability of anisotropic contraction) the UV cross-linking method was used. Zigzag microgels were used as a model system.

2.3 Characterization of 1D microgel strands in solution

Parts of this chapter have been published elsewhere.[141]

2.3.1 Introduction

Due to their anisotropic shape and their ability to respond to external stimuli, linear strands of microgels are promising for biomimetic applications such as artificial muscles.[126] In this chapter, the synthesis and characterization of freely dispersed one and two-dimensional poly(N-vinylcaprolactam) microgel strands is reported, which were fabricated by utilizing wrinkled surfaces as templates and subsequent UV cross-linking of the microgels. The fabrication of the strands is explained in Chapter 2.2. Their shapes include pearl necklace-like, zigzag and ribbon-like formations. In this subchapter these strands were visualized using various microscopy methods as atomic force microscopy (AFM), dark-field microscopy confocal fluorescence microscopy and wide-field fluorescence microscopy, respectively. The aim of this work was to observe the lateral and rotational motion of microgel strands in solution and on flat surfaces (Figure 78).

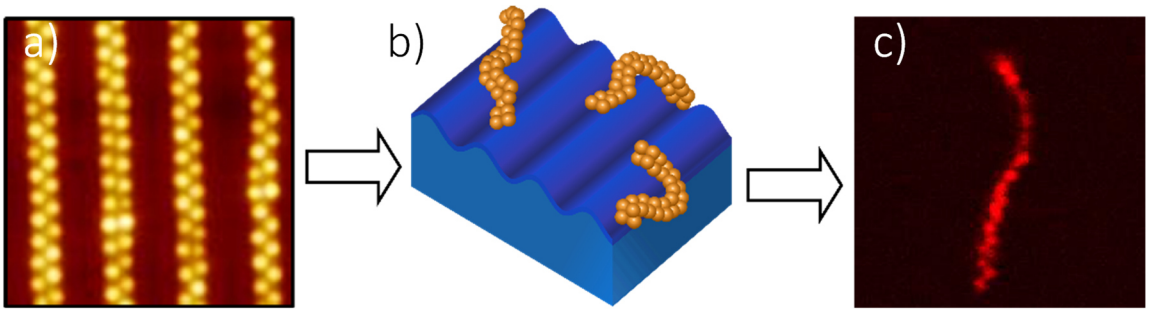

Figure 78: Schematic depiction of freely moving microgel strands. a: guided self-assembly and UV cross-linking; b: transfer into solution; c: Characterization via confocal fluorescence microscopy.[141]

2.3.2 Characterization via liquid cell AFM

Self-assembled VCL/AAEM microgels on PDMS wrinkles with a wavelength of approximately 800 nm were cross-linked via UV-light (experimental details see Chapter 4). The transfer of the cross-linked strands onto Si-wafers was conducted with pipettes. The sample was analyzed in peak-force QNM mode via liquid cell AFM (Figure 79) by using cantilevers with low spring constants (0.6 N/m and 0.1 N/m).

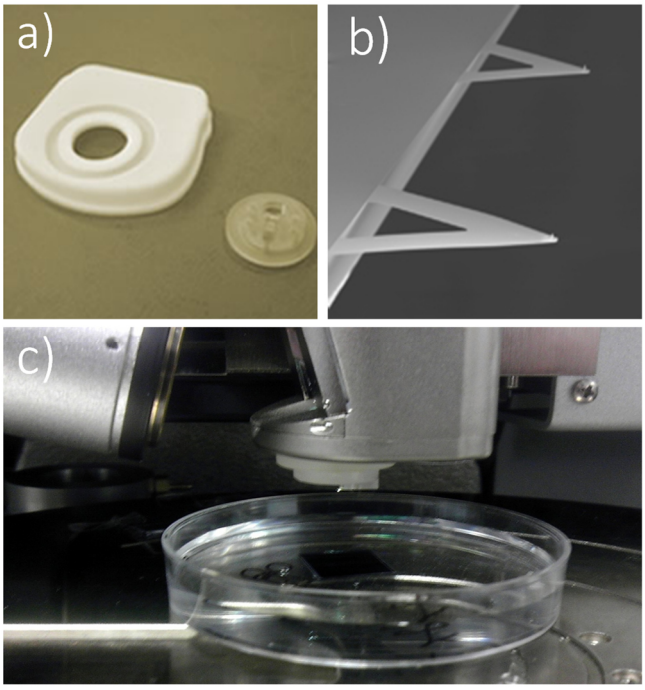

Figure 79: Experimental setup of the liquid cell AFM. a: insulation for the sensor head and insulated cantilever holder. b: soft cantilevers with spring constants of ~0.1 N/m and ~0.6 N/m, c: photo of experimental setup (measurement head, cantilever holder and sample in water).

The aim of this experiment was to determine whether the adsorbed single microgels and microgel strands could be detached from or moved on top of the substrate surface via nano-manipulation by contact mode AFM. This step was necessary for further studies of the behavior of freely dispersed microgel strands. The challenge here was to overcome the previously described adhesion energy between the silanol-rich surfaces and the VCL-matrix of the microgels (~40 mJ/m²). Therefore, cantilevers with a spring constant of 0.1 N/m

and 0.6 N/m were used to move or detach single particles or whole microgel strands. For these experiments, the software NanoMan from Bruker was used to define the cantilever pathway along the substrate surface. A start and stop position of a linear path was chosen in a way that the targeted particle or strand was located along the path. It turned out that single microgels could be detached by using cantilevers with a rather low spring constant of 0.1 N/m (Figure 80). However, it was not possible to move parts of a whole microgel strand by using the same cantilever. The calculate maximum loading force for the given cantilever was around 250 pN.

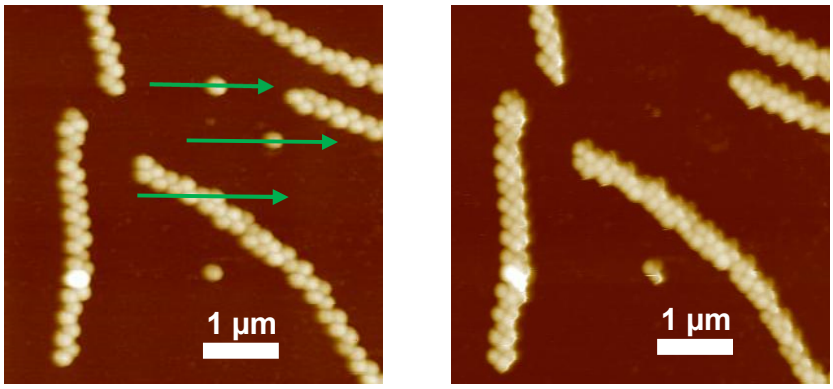

Figure 80: Nano-manipulation of VCL/AAEM microgel strands via AFM cantilever, k~ 0.1 N/m. The green arrow depicts the direction in which the cantilever was moved in-plane after contact with the surface.

Due to the cross-linking of the microgels into strands, more force was needed to move or detach the collective strand from the surface. Therefore, a cantilever with the second lowest spring constant of 0.6 N/m was used to perform the analogous experiment. The calculate maximum loading force for the given cantilever was around 500 pN. In Figure 81 can be seen that the whole strand was teared from the surface. Thus, it was proven that the strand could be detached from the surface. However, it was not possible to only displace the strand slightly, which would have been helpful for the examination of the contraction or bending capabilities of the loose strands.

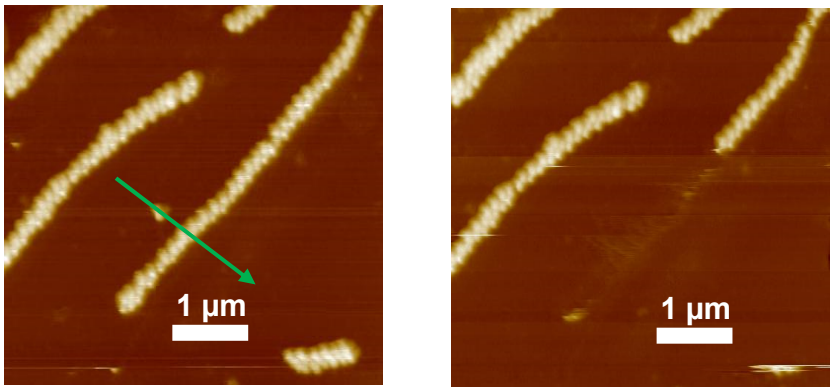

Figure 81: Nano-manipulation of VCL/AAEM microgel strands via AFM cantilever, k~ 0.6 N/m. The green arrow depicts the direction in which the cantilever was moved in-plane after contact with the surface. Residues of the strand are clearly visible in the right image.

In a similar experiment, microgel meshes were used, in the hope that after moving the microgels in between the grids they would loosely float slightly above the surface while being held from the neighboring particles, thus staying detectable for the AFM. The experiment partially worked, because the moved microgel was still detectable (Figure 82), but due to the nature of the measurement method, by scanning only in two dimensions, it could not be determined whether the microgel is floating between its neighbors or has been sliced due to the sharp 5 nm tip of the cantilever.

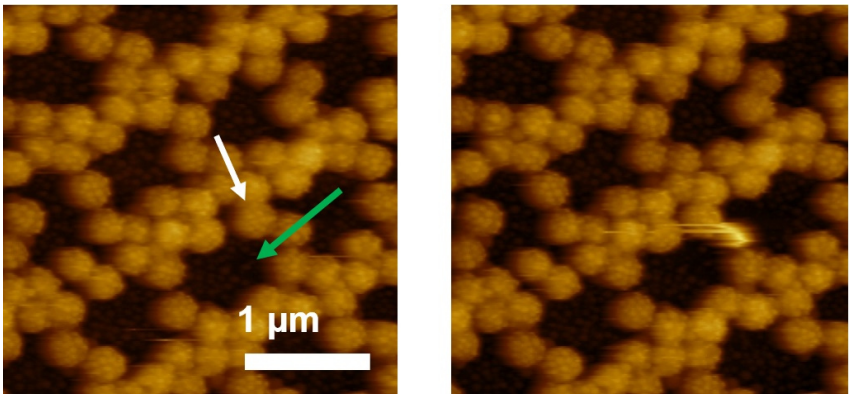

Figure 82: Nano-manipulation of a VCL/AAEM microgel mesh via AFM cantilever, k~ 0.6 N/m. The green arrow depicts the direction in which the cantilever was moved in plane after contact with the surface. The white arrow shows the displaced microgel.

Experiments conducted on microgel strands without any liquid medium surrounding them showed that the rather sharp tip (tip radius ~5 nm) slices through the polymer network without moving the collective strand (Figure 83). The sharp tip radius was necessary for the image resolution but is not beneficial for the manipulation of the microgel strands.

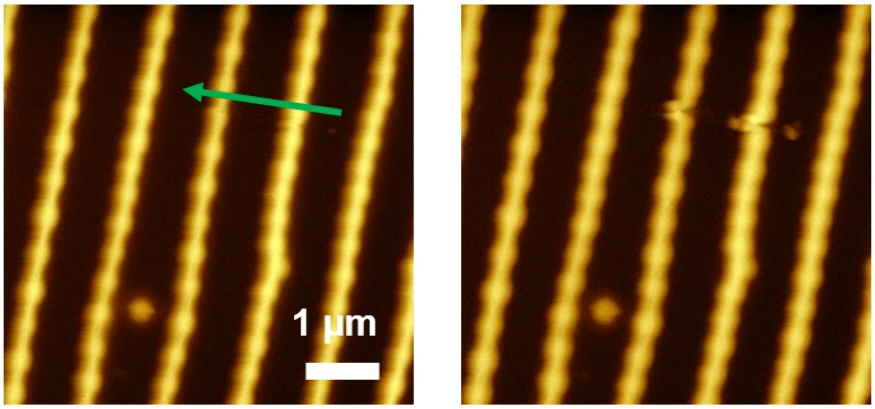

Figure 83: Nano-manipulation of VCL/AAEM microgel strands via AFM cantilever, k~ 0.6 N/m. The green arrow depicts the direction in which the cantilever was moved in-plane after contact with the surface. The tip slices through the polymer network.

In this experimental sequence, a partial detachment of strands was aimed for, but could not be achieved through this method. For further investigations into the motion behavior of microgel strands, the analysis methods had to be switched from an invasive surface method (AFM contact mode) towards non-invasive spectral methods, e.g. liquid cell TEM, dark field, wide-field and fluorescence microscopy.

2.3.3 Characterization via dark-field microscopy

Using the non-invasive dark-field and confocal microscopy in-situ imaging of microgel strands in solution became feasible. With the kind help of Kamil Eliasch from the von Plessen group (Lehrstuhl für Experimentalphysik I A und I. Physikalisches Institut Lehr-

und Forschungsgebiet Physik) dark-field microscopy was conducted on microgel strands which were dispersed in water.

The difference in refractive index between water and the microgels was big enough to track them in solution via this method. Similar experiments showed that the dark-field microscope was able to image microgel strands which were transferred onto glass slides (Figure 84) without significant difficulties.

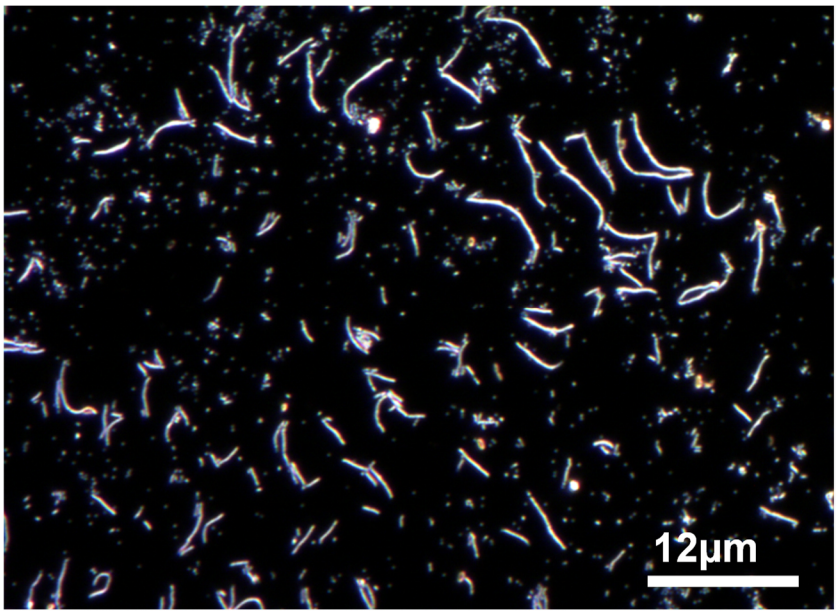

Figure 84: Dark field microscopy of VCL/AAEM microgel strands at solid/liquid (bottom of the glass substrate) interface.

Due to the imaging technique and the resolution limit of this microscope, which is analogous to the wide-field microscope described in Chapter 5.4, single microgels within the strands cannot be distinguished. Although the difference between the refractive index of water and PVCL was high to track the strands, all taken images showed a low optical contrast and were thereby unusable for further analysis. Therefore, all images had to be taken in the dry state of the microgel strands. This method is intrinsically more suitable to track particles in solution which differ greatly in their refractive index, e.g. inorganic compounds like microgels with gold cores.[227]

AFM and dark field microscopy showed that most of the microgel strands were adsorbed on the silica surface (e.g. Si-wafer and glass slides) more or less permanently. In order to solve this issue, the surface of the substrates had to be functionalized in a way that the microgels were not able to adsorb to the surface. Coating of the surfaces with linear polymerized PVCL via spin-coating was found to be a suitable solution. Due to steric repulsion between the N-vinylcaprolactam rings, the adsorption of the microgels could be reduced to a minimum.

Nevertheless, dark field microcopy was not suited to obtain analyzable images and videos of the microgel strands as all images of moving particles were blurry. For this reason, the analysis technique was switched to confocal and wide-field microscopy.

2.3.4 Characterization via confocal microscopy and wide-field fluorescence microscopy

The direct observation of the microgel strands in aqueous medium was a key step for the characterization of their physical properties. The resolution of optical microscopy is restricted to the Abbe limit which means that structures below approximately half the wavelength of the observation light cannot be resolved. Superresolved fluorescence microscopy methods allow a circumvention of the diffraction limit,[228] but are restricted by their time resolution. Thus, in this work (diffraction-limited) confocal microscopy and wide-field fluorescence microscopy was used to observe the fluorescence-labeled microgel assemblies. The former possesses a higher spatial resolution, in particular in z-direction. This allows for resolving single microgels in the microgel assembly as demonstrated in Figure 85b. For the visualization by fluorescence microscopy, rhodamine B (RhB) was added to the VCL/AAEM microgel strands as a fluorescent marker. Rhodamine B infiltrated the VCL/AAEM microgel network overnight under constant stirring (for experimental details see Chapters 4 and 5). Presumably, the hydrophobic Rhodamine B was able to diffuse into the hydrophobic compartment of the microgel. Analogous to the

experiments conducted via dark-field microscopy, the glass slide surfaces were functionalized with PVCL by spin-coating a thin polymer layer onto the substrate surface. Subsequently, a small amount of cross-linked zigzag microgel strands dispersed in water were transferred onto the polymer functionalized glass substrate, and confocal or wide-field fluorescence microscopy images were taken, respectively. Without the surface functionalization, the microgels adsorb to the surface. The fact that the microgels are visible with the confocal microscope showed that the Rhodamine B was absorbed into the polymeric network. In contrast to the characterization in two dimensions (e.g. AFM, TEM) the characterization of the same amount of 1D strands in three dimensions (e.g. confocal microcopy in water) was more challenging, due to the reduced concentration.

For the experimental sequence, glass substrates with a concave curvature were used to maximize the examined amount of the microgel strands. Microgel strands were found to be both semi-attached to the glass surface as well as freely dispersed in the solution. The motion of semi-attached microgel strands is schematically shown in Figure 85a and experimentally in Figure 85b (Image sequences were taken from the respective video found in Chapter 7).

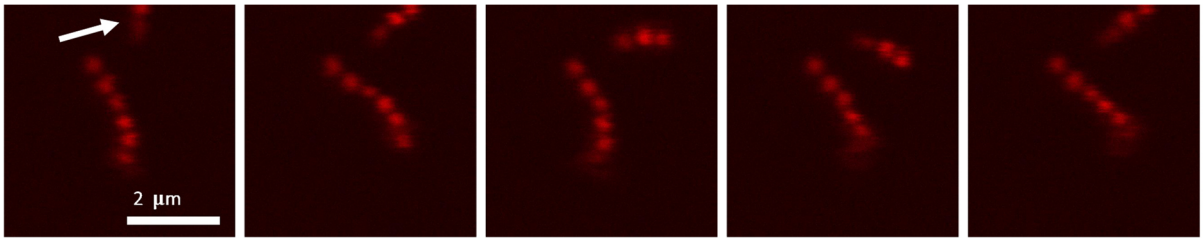

Figure 85: Images from a video taken of moving microgel strands which were semi attached to the substrate surface.

As can be seen in Figure 85, the microgel strands have a certain stability that withstands lateral shear forces through turbulent and lamellar flow which occur during the evaporation of water during measurement. The lamellar flow promotes the motion of the microgel strands. Furthermore, the images show that the adhesion energy between VCL-microgels and silanol rich surfaces (e.g. glass slides) is strong enough (~40 mJ/m^2) to anchor microgel strands which are several microns long. In Figure 86 can be seen that even larger microgel

strands, in this case a whole loop, can be fixed by adhesion energies between several microgels and the cover slip surface. To be able to find these semi-adsorbed microgel structures can be seen as a proof that the PVCL-coating is not homogenously distributed on the substrates. This leads to the conclusion that the spin coating process must be optimized in future work. Further examples for semi-attached microgel strands in motion can be found in the attachments.

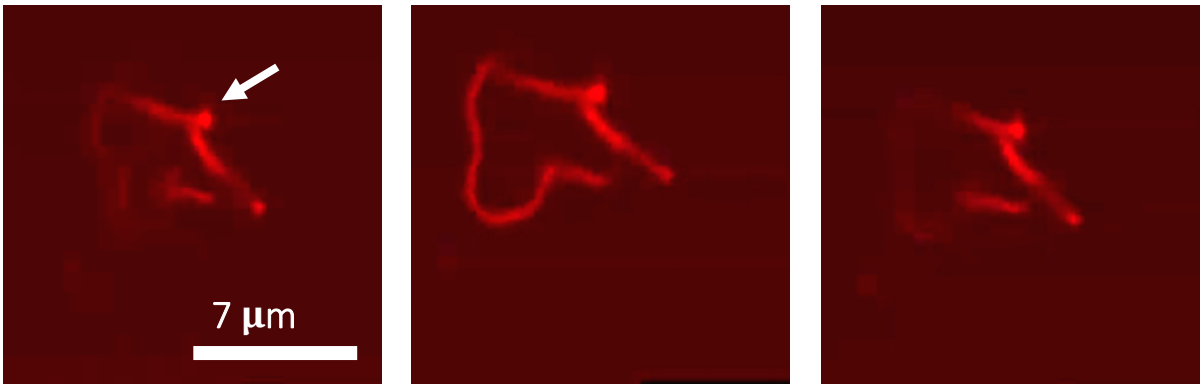

Figure 86: Images from a video taken of moving microgel loop which was semi attached to the cover slip at a fixed spot (white arrow).

Although the polymer coating was inhomogeneously distributed on the glass slides and cover slips, it was still effective enough to observe several free moving microgel strands (Figure 87). In contrast to the semi-attached microgels, which were limited in their movement in respect to the z-axis, the free moving microgel strands were able to use all three dimensions freely. Considering the high spatial resolution of the confocal microscope, in particular in z-direction, observing their fast motion turned out to be challenging. The z-position of the objective had to be constantly adapted in order to keep track of the strand motion. In contrast, wide-field fluorescence microscopy is less sensitive to the motion of microgel strands along the z-direction. Despite the higher background noise and the fact that individual microgels could not be resolved (Figure 88), long movies of single microgel strands floating in water were obtained and could be readily analyzed.

A number of free moving microgel strands could be observed using both methods, providing information on the diffusion behavior of the microgel strands (Figure 87). Based

on the video data obtained through confocal microscopy, it could be determined that microgel strands were flexible to a certain degree, as can be seen in the worm like form in Figure 87. Furthermore, the videos provide the irrefutable proof that UV cross-linking provides a sufficiently stable connection between single particles, that allow them translational and rotational motion without tearing them apart into fragments or single microgels.

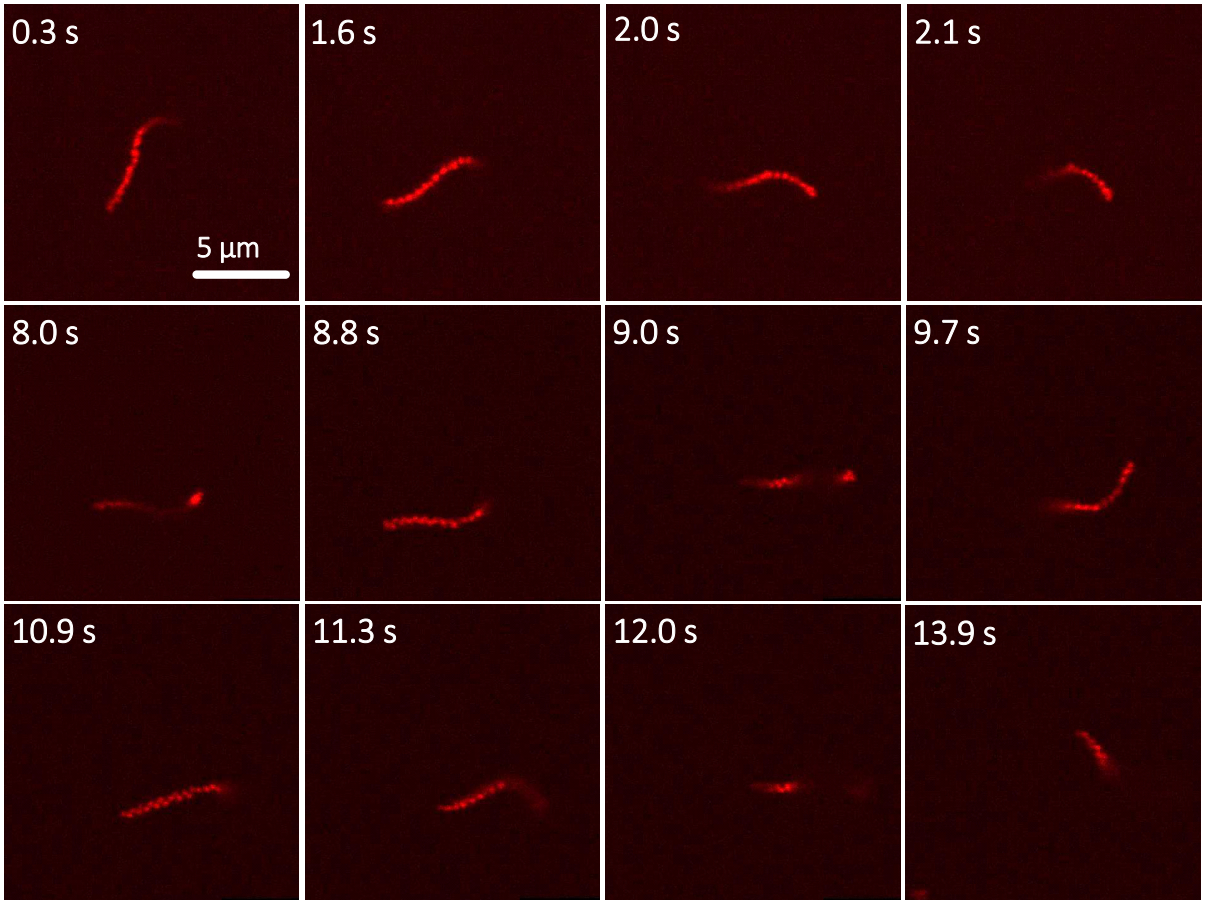

Figure 87: Free moving VCL/AAEM microgel strand (with adsorbed rhodamine B) observed by confocal microscopy.[141]

Based on these findings, questions regarding the degree of flexibility and the diffusion behavior of the microgel strands can be finally addressed.

2.3.5 Diffusive motion of strands in solution

In cooperation with Oleksii Nevskyi of the Wöll group (Institute of Physical Chemistry, RWTH Aachen), detailed information about the motion and the flexibility of the microgel strands was extracted via image analysis as discussed in the following section. Further examples of image series and movies can be found in the attachments.

Conformational analysis via 2D projections of microgel strands

In order to gain a better understanding of the conformations/flexibility of the synthesized microgel strands and their dynamics, the recorded movies were analyzed using image analysis tools provided by the Easyworm software package.[229] Herein, the shape of each analyzed microgel strand was determined by fitting it to a spline after appropriate image filtering.

Since the time resolution of confocal microscopy does not allow sufficiently rapid 3D scanning and wide-field fluorescence microscopy does not resolve the axial z-direction better than a few micrometers, only 2D projections of the 3D orientation of the microgel strands could be recorded. The analysis of these 2D projections is presented in the following section.

As shown in Figure 87, the different 2D shapes in the microscopy images were observed to vary over time. This variation is caused by Brownian motion, as will be confirmed in the following subsections. More examples of such variations are given in Figure 88, which shows the splines for the three microgel chains from Figure 88 a-c.

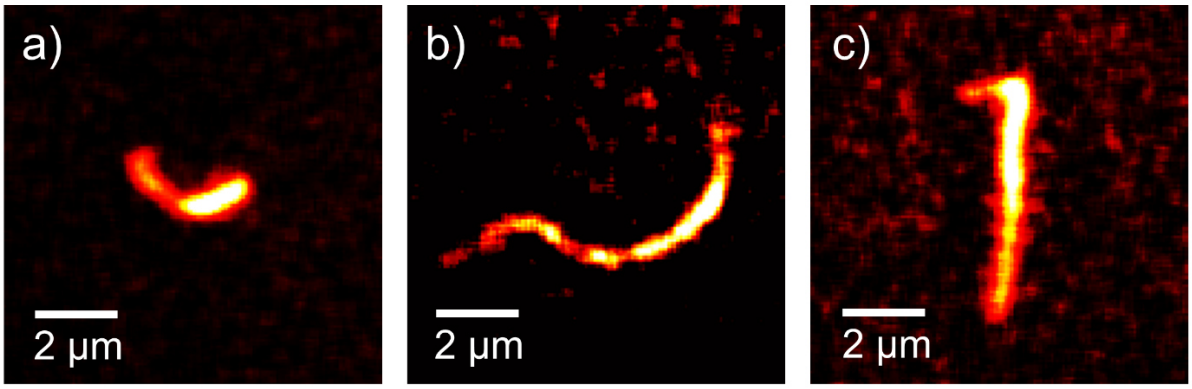

Figure 88: a-c: Typical shapes of microgel strands observed during widefield and fluorescence microscopy measurements. The three strands show a C-shape, S-shape and an L-shape form, respectively. The grey scale is inverted for better contrast. The following contour lengths L were obtained by Easyworm. a: L = 3.8 µm; b: L = 11.4 µm; c: L = 7.6 µm. The images were filtered as described in Chapter 5 and the corresponding movies can be found in the attachements.[141]

The observed microgel shapes can be categorized into three different groups: C-shape, S-shape and L-shape (Figure 88). The curvature of the C- and S-shapes might be caused by the maximum bending capability of the strands in the free dispersed state determined by the strength of the interparticle connectivity and the strand structure. A possible origin of the unusual L-shaped microgel strands might be the lateral cracks in the wrinkled substrate (Figure 89).

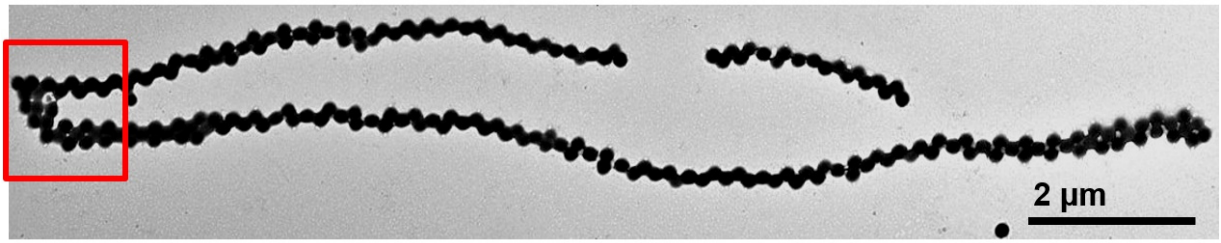

Figure 89: TEM image of a cross-linked microgels strand were on the left side (red) the L-shaped structure can be seen.

From the 2D projections obtained by both fluorescence microscopy methods, the characteristic parameters for each single analyzed strand were determined using the software Easyworm (see Figure 90).[229] In particular, the contour length L_{xy} of the 2D

projection of the strand in each frame was determined from the spline fit. Due to the perspective-induced shortening of the strand during 3D rotation, the values of L_{xy} can vary from frame to frame. To determine the contour lengths L of the strand itself, for each strand the maximum value of L_{xy} was selected, corresponding to the frame with the minimum perspective-induced shortening. This procedure yields, for example, the following contour lengths for the microgel strands shown in Figure 88a–c: (a) L = 3.8 μm; (b) L = 11.4 μm; and (c) L = 7.6 μm.

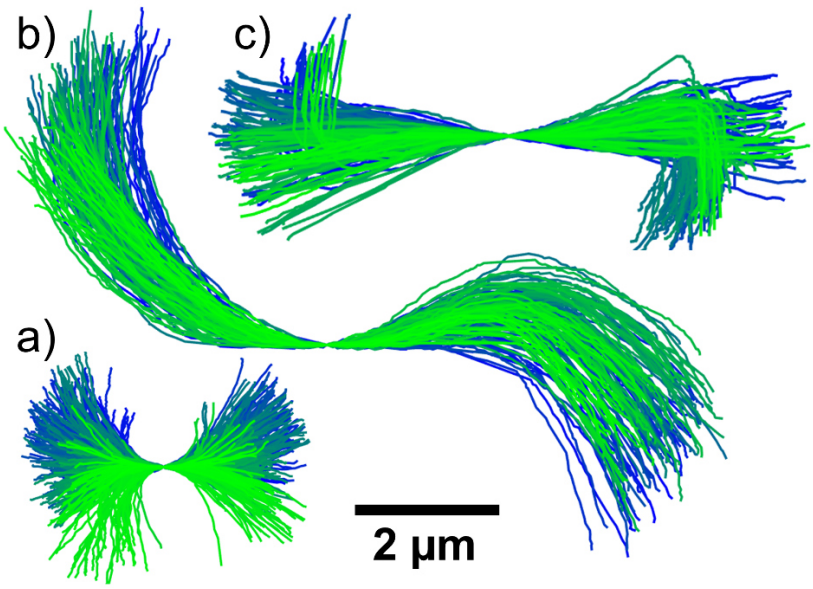

Figure 90: Temporal evolution of the 2D projections of the microgel strands also shown in the fluorescence microscopy images in Figure 88. For a clearer representation, the centers of the strands were positioned in the same point and the microgels were rotated so that the slope in this point equals zero. The color change from blue to green represents the evolution through different frames.[141]

For a clearer representation, the centers of the strands have been positioned in the same point and the splines rotated in-plane so that their slope in this point equals zero; these manipulations effectively remove effects of the center-of-mass motion and in-plane rotation from the representation. A careful analysis shows that the remaining variations in length and shape of the splines, i.e., their apparent shortenings and changes of curvature, are consistent with out-of-plane rotations of the strands, i.e., rotations around axes in the

object plane. In contrast, their 3D conformation does not seem to change significantly within our observation time window. This implies that they are much stiffer than the single-walled carbon nanotubes studied by Fakhri et al.[162] which showed considerable bending at comparable lengths but much smaller thicknesses.

The fact that the microgel strands show no perceptible bending dynamics on the time scale of the experiment means that the persistence lengths of the strands, L_p, are much greater than their contour lengths, $L_p >> L$. For the bending stiffness $k = k_BT \cdot L_p$, this implies that $k >> k_BT \cdot L$, where kB is the Boltzmann constant. For example, this inequality yields $5 \cdot 10^{-26}$ Nm² as a rough lower limit on the bending stiffness of the strand with a contour length of L = 11.4 μm in Figure 88b and Figure 90b. At present, no comparison of this value with theory is possible due to the unknown cross-linking strength between adjacent microgels. It is interesting to note that this lower limit lies in the order of magnitude range spanned by the k values that were determined for chains of linked magnetic colloids by Biswal et al.[149] and Goubault et al. [151] (k between $1.1 \cdot 10^{-26}$ and $1.1 \cdot 10^{-21}$ Nm²). In the magnetic-colloid chains, k depends exclusively on the kind of molecule used to link the colloids, because the latter are not deformable. In the following sections, the translational and rotational motion of the linear microgel assemblies was analyzed.

Translation diffusion of microgel strands

The translational motion of the microgel strands was studied by analyzing in each frame the center-of-mass position of the projection of the strand. This position was obtained from the shape of the projection using auxiliary points homogeneously distributed over each spline. An example of the temporal evolution of the mean square displacement $\langle \Delta x^2 + \Delta y^2 \rangle$ of the center-of-mass of the projection is presented in Figure 91 for the strands shown in Figure 88a and Figure 90a (see the attachments in Chapter 7 for the movie which shows the motion of this strand).

The time dependence of the mean square displacement can be approximately described by a linear fit (blue line), showing that the microgel strands diffuse normally due to Brownian motion. Using the relation $\langle \Delta x^2 + \Delta y^2 \rangle = 4D_t \cdot t$, which is valid for 2D projections of 3D diffusive motions,[230] the isotropic translational diffusion coefficient is determined to be $D_t = 0.15\ \mu m^2 \cdot s^{-1}$ from the slope of the fit in Figure 91.

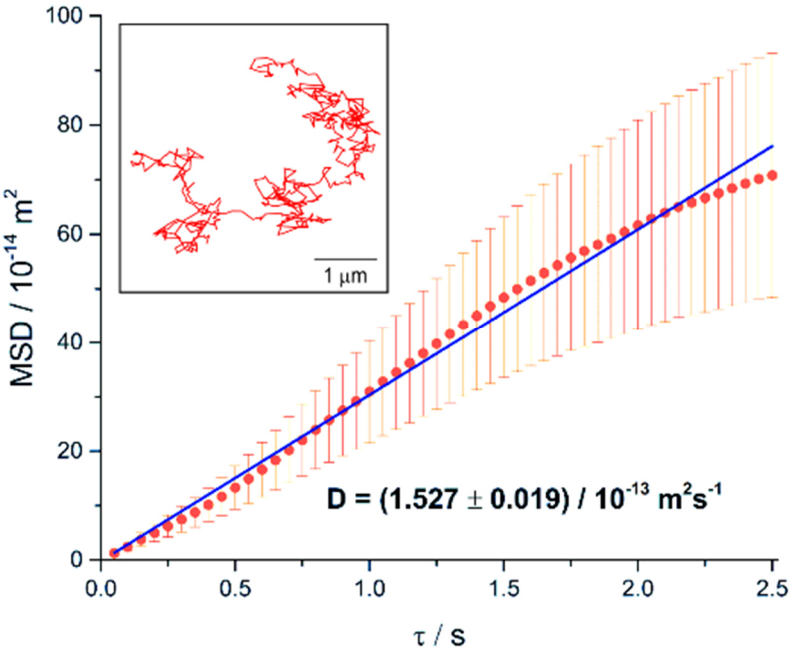

Figure 91: Temporal evolution of the mean square displacement of the center-of-mass of the microgel strand from Figure 88a and Figure 90a. Blue line: linear fit. Inset: single track of the center-of-mass. The corresponding diagrams for the other two examples of microgel strands in Figure 88b-c and Figure 90b-c are shown in the corresponding attachment see Figure 108 and Figure 109.[141]

It is instructive to compare this experimental result to theory using a model for the translational and rotational diffusion of cylinders developed by Broersma.[231, 232] Such models have been experimentally validated for rod-like particles.[163, 233, 234] The translational and rotational diffusion coefficients of a cylindrical rod are depicted in Equation 3.

Equation 3

$$D_i^{(th)} = \frac{k_B T}{\pi \eta L} a_i \left(\ln\left(\frac{L}{d}\right) + \nu_i \right)$$

where the index i = ∥ stands for translational diffusion along the direction of the rod axis, i = ⊥ for translational diffusion in a sidewise direction, i = t for isotropic translational diffusion and i = R for rotational diffusion, i.e., diffusive re-orientation of the rod axis. T is the temperature, η is the viscosity of the solution, L is the rod length, and d is the rod diameter. The a_i are given by $a_\parallel = 1/2$, $a_\perp = 1/4$, $a_t = 1/3$ and $a_R = 3/L^2$. The end correction coefficients ν_i are polynomials in $(\ln 2(L/d))^{-1}$ and listed by Broersma.[231, 232] The comparison between the model calculation and the experiment is complicated by the shape of the microgel strand, which is not strictly cylindrical. In particular, the zigzag arrangement of microgels in the assemblies studied here (Figure 78a) means that the cross-section of the strands perpendicular to their axis is anisometric with dimensions $d_1 \approx 0.50$ μm (i.e. the diameter of an individual microgel) and $d_2 \approx 0.93$ μm. To simplify the comparison between calculation and experiment, an effective rod diameter d by fitting Equation 3 to the measured value of the isotropic translational diffusion coefficient D_t and using d as a fit parameter has been determined. For example, inserting T = 293 K, η = 1.00 mPa s and L = 3.8 μm into Equation 3, the fit yields a perfect match with the measured value $D_t = 0.15$ $\mu m^2 \cdot s^{-1}$ for d = 1.08 μm. Fits for the other microgel strands studied here yield d values within 10% of 1.08 μm. This effective diameter is close to $d_2 \approx 0.93$ μm, the thick dimension of the cross-section measured by AFM. One of the goals of the present work is to determine a value for the translational mobility. The isotropic translational mobility μ_t can be calculated from D_t using the Einstein relation $\mu_t = D_t/k_BT$. Inserting the experimental result $D_t = 0.15$ $\mu m^2 \cdot s^{-1}$ into this equation yields $\mu_t = 3.8 \cdot 10^7$ $s \cdot kg^{-1}$. It is important to note that the isotropic translational mobility μ_t obtained in this way describes the translational motion of the microgel strand only in conditions in which the orientation of the individual strand varies randomly. If, in contrast, a situation with a fixed orientation of the strand is of

interest, e.g. in an actuation application, then the translational mobilities along and perpendicular to the direction of the rod axis, $\mu_{\parallel}$ and $\mu_{\perp}$, are relevant. While the experiment is not able to determine them separately, they can be calculated by inserting the effective diameter d = 1.08 μm, which has been determined above, into Equation 3 for i =∥ and ⊥, and inserting the resultant values of $D_{\parallel}^{(th)}$ k and $D_{\perp}^{(th)}$ into the Einstein relation $\mu_i = D_i/k_BT$. Thus, we obtain $\mu_{\parallel} = 4.1 \cdot 10^7\ s \cdot kg^{-1}$ and $\mu_{\perp} = 3.6 \cdot 10^7\ s \cdot kg^{-1}$.

Rotational diffusion of microgel strands

The rotational diffusion can be determined from the temporal evolution of orientations in successive wide-field fluorescence microscopy frames. Even though the full 3D orientation of objects is accessible under certain conditions, in the current study only 2D projections cloud be determined and analyzed. From the temporal evolution of such 2D projections, the rotational diffusion coefficient D_R can be estimated.[235] For this, the time-average angle ψ of 2D-projected orientations at different time delays τ is determined and fitted according to

Equation 4

$$\langle \cos \psi \rangle (\tau) \approx e^{-2\tau D_R}$$

The temporal evolution of the orientational correlation function of the microgel strand from Figure 91 is shown in Figure 92. An excerpt from a movie of this microgel can be found in the attachments. Fitting an exponential function according to Equation 4 yields a rotational diffusion coefficient $D_R = 0.10\ s^{-1}$.

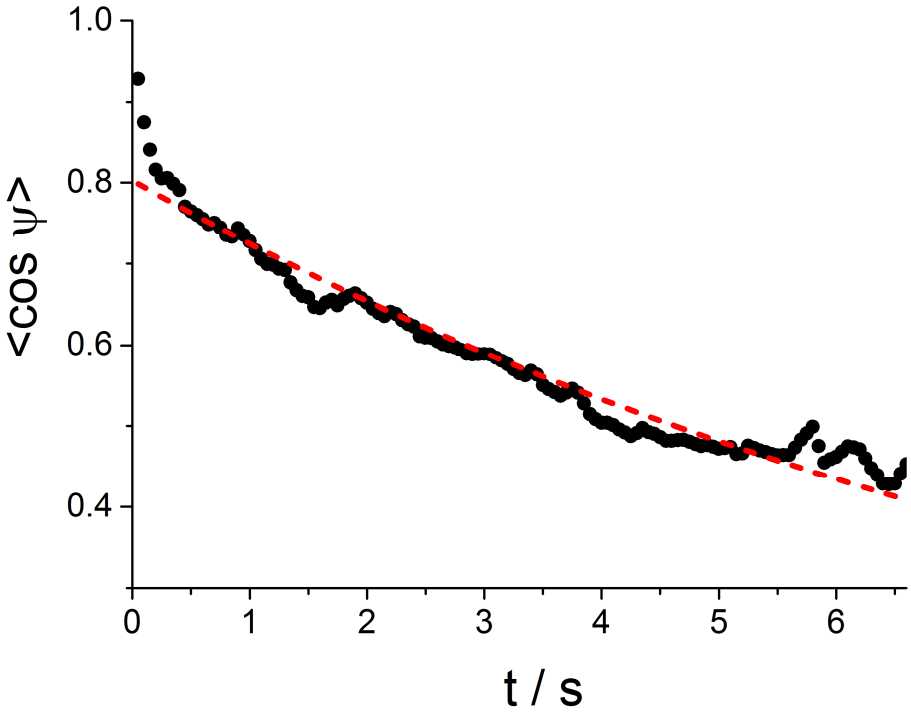

Figure 92: Temporal evolution of the mean square displacement of the center-of-mass of a microgel strand. Red line: linear fit.[141]

For a comparison with theory, Equation 3 was used with i = R and the end correction coefficient for rotational diffusion from Broersma.[231, 232] Due to the anisometric cross-section of the microgel strands, the same approach as above was followed and an effective rod diameter d was determined by fitting Equation 3 to the measured value = 0.10 s^{-1}, using d as a fit parameter. The fit yields d = 0.46 µm, a result close to $d_1 \approx 0.50$ µm which is comparable to the diameter of a single microgel determined by AFM cross-section. The discrepancy between this result and that obtained from the fit to D_t (d = 1.08 µm) may be attributed to the curved shape, non-circular cross section, and granular structure of the microgel strand, which are not contained in the cylinder model that was used here. Fortunately, the discrepancy is not of critical importance, because the dependencies of $D_t^{(th)}$ and $D_R^{(th)}$ on the value of d are relatively weak in this range of diameters; when d is varied freely between the two fit results, i.e., in the range 0.46–1.08 µm, the model calculation gives that $D_t^{(th)}$ varies between 0.23 and 0.15 $\mu m^2 \cdot s^{-1}$, and $D_R^{(th)}$ between 0.10 and 0.05 s^{-1}. In particular, all values in this $D_t^{(th)}$ range still lie reasonably close to the experimental result

D_t = 0.15 $\mu m^2 \cdot s^{-1}$. Similarly, the uncertainty in the effective diameter d translates into relatively narrow ranges $\mu = 3.8 \cdot 10^7 – 5.8 \cdot 10^7\ s \cdot kg^{-1}$, $\mu_{\parallel} = 4.1 \cdot 10^7 – 6.5 \cdot 10^7\ s \cdot kg^{-1}$ and $\mu\perp = 3.6 \cdot 10^7 – 5.4 \cdot 10^7\ s \cdot kg^{-1}$ of the calculated isotropic, lengthwise and sidewise translational mobilities, respectively.

2.3.6 Conclusion

In this chapter, microgel strands in solution were characterized by various microscopy methods. The experiments showed that AFM as the standard analyzing method in a setup suited for measurement in liquids is not able to characterize microgel strands in free moving state. Experiments in which the surface manipulation of single microgel particles and strands have given proof that adhesion forces between the microgels and the substrate surface (e.g. glass slides, oxidized Silica wafer) are strong enough for the microgels to adhere on surface but weak enough to allow detachment via relatively weak AFM cantilevers. Furthermore, it was found out that whole strands could be detached. These findings showed that the inter-particle cross-linking via UV light was successful.

To examine freely moving microgel strands without the restrictions that a surface depended method like AFM dictates, the method was switched to spectral based microscopy. Dark-field microscopy provided only limited insight into the nature of the freely dispersed microgel strands, due to its dependency on a high difference in refractive indices. No sharp/analyzable images of microgel strands could be obtained. Nevertheless, a very small amount of freely dispersed strands could be detected but the majority of the transferred strands were attached at the surface of the glass slide.

Based on the findings of latter methods, the surface was modified with a repulsive polymer (PVCL) for confocal and wide-field microscopy in order to increase the concentration of the freely dispersed microgels. By infiltrating microgel strands with Rhodamine B, a visualization via confocal microscopy with a high in-plane resolution was possible. The challenge here was to locate and track the dynamically moving strands within a three-

dimensional space. Nevertheless, the method did not only enable a high-resolution video-tracking of the free moving microgel strands but also gave insights into their physical properties in terms of strand flexibility, inter-particle cross-linking and diffusion behavior. In order to deepen the knowledge regarding the latter properties, wide-field microscopy was used. Due to its less sensitive depth of field, the strand motion itself was better trackable with an acceptable loss of in-plane resolution. The strands were observed to execute translational and rotational diffusive motion in solution, without bending motion. Unfortunately, with confocal and wide-field microscopy, the detection of the anisotropic stimuli responsive contraction of the free moving microgel strands was not possible. Either the microgel strands which were partially detached stopped moving and adhered permanently to the surface upon temperature increase, or upon reaching the VPTT, the free moving microgel strands precipitated and thus could not be tracked anymore.

Evaluation of the motions has yielded translational and rotational diffusion coefficients that are in reasonably good agreement with the results of a model calculation for cylindrical rods in solution. From the translational diffusion coefficient, the strand mobility has been calculated. The microgel strands show no perceptible bending, which yields a lower limit on their bending stiffness. If one looks for a comparable behavior in the common life, then the flexibility of a single microgel strand corresponds more to that of a cable than to that of a yarn. The strands studied here consist of dozens or even hundreds of discrete submicron units strung together by cross-linking. As such, they have few parallels in nanotechnology, the most notable being the microfilaments made of linked magnetic colloids that have recently been studied for actuation applications in microfluidics.[149, 164] In comparison to the latter, microgel strands may have specific potential for possible actuation applications that necessitate contraction and expansion along the strand axis and the possibility of triggering movements by temperature and pH changes. Before this potential can be realized, however, more research is needed, with particular attention to controlling the bending stiffness of the strands and their overall shapes and lengths, as well as investigating their contraction and the forces exerted by them.

3 Summary and Outlook

The fabrication of 1D nanostrands composed of stimuli responsive microgels has been shown in this work.

Microgels are well known materials able to respond to various stimuli from outer environment. Since these microgels respond via a volume change to an external stimulus, a targeted mechanical response can be achieved. Through carefully choosing the right composition of the polymer matrix, microgels can be designed to react precisely to the targeted stimuli (e.g. drug delivery via pH and temperature changes, or selective contractions through changes in electrical current[126]).

In this work, it was aimed to create flexible nano-filaments which are capable of fast anisotropic contractions similar to muscle filaments. For the fabrication of such filaments or strands, nanostructured templates (PDMS wrinkles) were chosen due to a facile and low-cost fabrication and versatile tunability of their dimensions. Additionally, wrinkling is a well-known lithography-free method which enables the fabrication of nanostructures in a reproducible manner and with a high long-range periodicity.

In Chapter 2.1, it was shown for the first time that microgels as soft matter particles can be aligned to densely packed microgel arrays of various lateral dimensions. The alignment of microgels with different compositions (e.g. VCL/AAEM, NIPAAm, NIPAAm/VCL and charged microgels) was shown by using different assembly techniques (e.g. spin-coating, template confined molding). It was chosen to set one experimental parameter constant which was the SiO_x surface composition of the templates and substrates (e.g. oxidized PDMS wrinkles, Si-wafers and glass slides). It was shown that the fabrication of nanoarrays was feasible with all tested microgel types. Although the microgels exhibited different deformability when aligned on a flat surface, they retained their thermo-responsivity and swelling behavior.

Towards the fabrication of 1D microgel strands interparticle connectivity was aspired. This was achieved via different cross-linking methods (i.e. cross-linking via UV-irradiation and host-guest complexation) discussed in Chapter 2.2. The microgel arrays created by different

assembly methods and microgel types were tested for their cross-linking suitability. It was observed that NIPAAm based microgels cannot be cross-linked with UV light. Furthermore, it was found that these microgels exhibit a strong surface-particle-interaction and therefore could not be detached from the given substrates. In contrast to the latter, with VCL/AAEM based microgels it was possible to both UV cross-link them based on the keto-enol tautomerism of the AAEM copolymer, and to detach them from the substrate due to the lower adhesion energy towards SiO_x surfaces. With VCL/AAEM microgels long, one-dimensional microgel strands could be re-dispersed in water for further analysis. It has also been shown that at least one lateral dimension of the free dispersed 1D microgel strands is easily controllable by adjusting the wavelength of the wrinkled template. For further work, only VCL/AAEM based microgels were used to focus on the main aim of this work, i.e. the fabrication of 1D microgel nanostrands.

As an alternative to the unspecific and harsh UV cross-linking, the host-guest complexation via diazobenzene cross-linkers and cyclodextrin hosts was explored. The idea behind this approach was to give means to a future construction kit-like approach by incorporation of cyclodextrin comonomers in a broad variety of particle systems (e.g. microgels, nanoparticles). For this purpose, VCL/AAEM microgels were copolymerized with different amounts of mono-acrylate functionalized β-cyclodextrin (CD). After successfully testing the cross-linking capability in solution, the cross-linking of aligned VCL/AAEM/CD microgels was tried. Although the cross-linking worked well, once the single arrays came into contact to each other, they agglomerated. As a reason for this behavior residual amounts of mono-complexed diazobenzene linkers were suspected. Thus, end-capping strategies were tried out (e.g. excess amounts of β-cyclodextrin and coverage with azobenzene functionalized AuNPs) but were unsuccessful. With deeper thought, entropy effects were taken into consideration which favor the release of complexed diazobenzene linker leading to agglomerations. To circumvent this entropy driven effect, a multifunctional polymer with 50% azobenzene groups (Harada polymer) was used. First experiments with this polymer showed promising results regarding a less pronounced agglomeration (Figure 77). Thus, this approach could be pursued in the future. In this chapter it was found out that in contrast to pearl necklace and ribbon like

formations, particle alignment in zigzag formation provided the best compromise in terms of stability in dispersion (see Figure 44a and Figure 51) while maintaining sufficient flexibility.

For this reason, microgel strands in zigzag formation were used for the motion analysis described in Chapter 2.3. The aim was to observe the properties of unrestrained microgel strands in solution (e.g. diffusion behavior, rotational properties and ideally, anisotropic contraction after temperature increase). Initially, 1D microgel strands were manipulated via AFM in a liquid cell setup. It could be observed that the strands required a higher load force compared to single microgels to be detached from the surface. However, with the AFM it was not possible to detach the strands in a controllable manner but resulted in a complete removal of single microgel particles and a tearing off the strands from the surface, respectively. For this reason, to observe the motion behavior of unrestrained microgel strands in solution, confocal microscopy was used. Furthermore, to hinder an adhesion of the strands, it was found out that coating the surface of the substrates with a repulsive polymer film was beneficial. Confocal and wide-field microscopy videos showed that the microgel strands exhibit translational and rotational diffusive motion in solution without perceptible bending. Unfortunately, with these methods the detection of the anisotropic stimuli responsive contraction of the free moving microgel strands was not possible. To summarize, the flexibility of microgel strands is more comparable to the mechanical behavior of a semi flexible cable than to a yarn. The strands studied here consist of dozens or even hundreds of discrete submicron units strung together by cross-linking, having few parallels in nanotechnology.

With the insights gained in this work on microgel-surface interactions, in the future, a targeted functionalization of the template and substrate surfaces can be conducted to actively prevent unwanted microgel adhesion for a given microgel system (e.g. PVCL and polystyrene coating[236]). This measure would make the discussed alignment methods more diverse. As shown herein, the assembly methods enable a versatile microgel alignment (e.g. microgel meshes, double and triple strands). To go further, one could use more complex templates (e.g. ceramic rhombs and star shaped wrinkles (Figure 14) to expand the

possibilities of microgel alignment and to precisely control their aspect ratios (e.g. microgel rods with homogeneous size distributions).

4 Experimental part

4.1 Microgel synthesis

The following chemicals were used for standard microgel synthesis. If not mentioned otherwise, all chemicals were ordered at Sigma Aldrich. VCL was purified by distillation prior to use.

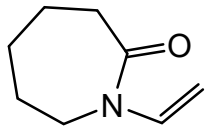

N-Vinylcaprolactam (VCL)

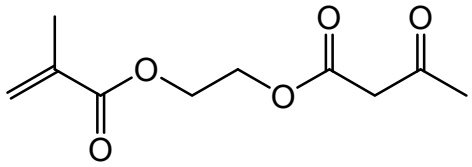

Acetoacetoxyethylmethacrylate (AAEM)

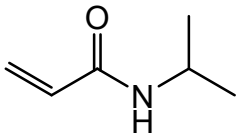

N-Isopropylacrylamide (NIPAAm)

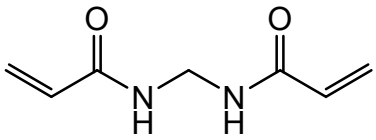

N,N-Methylenebisacrylamide (BIS

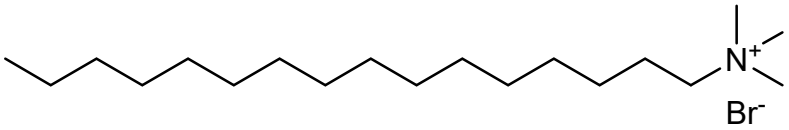

Cetyltrimethylammoniumbromide (CTAB)

4.1.1 VCL/AAEM

The poly(N-vinylcaprolactam) (PVCL/AAEM) based microgels were synthesized as described in the following. In particular, 1.877 g N-vinylcaprolactam (VCL, 13.5 mmol), 0.338 g acetoacetoxyethyl methacrylate (AAEM, 1.58 mmol), and 0.06 g N,N-methylene bisacrylamide (BIS, 0.39 mmol, 3 mol-% based on the amount of VCL) were added to 150

mL deionized water. A double-walled glass reactor equipped with stirrer and reflux condenser was purged with nitrogen for several minutes. After placing the monomer solution in the reactor, it was stirred for 1 h at 70°C under constant nitrogen flow. Subsequently, 5 mL of aqueous initiator solution (5 $g \cdot L^{-1}$) were added under constant stirring and the reaction took place for 7 h. Microgels were formed via precipitation polymerization. The dispersion was then purified by a Millipore Dialysis System (cellulose membrane, molecular weight cut-off (MWCO) 100.000, Darmstadt, Germany) for 4 days before characterization.

4.1.2 VCL/AAEM/CTAB

In a double-walled glass reactor equipped with stirrer and reflux condenser suitable amounts of previously dissolved VCL, AAEM and 0.06 g of the cross-linker N,N´-methylenebis(acrylamide) (BIS, 0.39 mmol, 3 mol-% based on the amount of VCL) were placed in 150 mL deionized water. The solution was heated up to 70°C and stirred for 1h under constant nitrogen purging. For the size variation of the microgels, different amounts of cetyltrimethylammonium bromide (CTAB) were added to the preheated solution which is shown in Table 3. The polymerization was started by adding 5 mL of the initiator 2,2´-azobis(2-methylpropyonamidine) dihydrochloride (AMPA) to the reaction under stirring. After 6 h, the reaction was stopped, and the dispersion was purified via dialysis membrane (Spectra/Por- Dialysis Membrane, MWCO:12-14.000) for 4 days before characterization.

Table 3: VCL/AAEM microgel sample composition.

sample	VCL [g]	AAEM [g]	BIS [g]	CTAB [g]
VCL/AAEM	1.877	0.338	0.06	
VCL/AAEM/5 mg CTAB	1.877	0.338	0.06	0.005
VCL/AAEM/10 mg CTAB	1.877	0.338	0.06	0.010

VCL/AAEM/20 mg CTAB	1.877	0.338	0.06	0.020
VCL/AAEM/50 mg CTAB	1.877	0.338	0.06	0.050

4.1.3 NIPAAm/VCL microgels

In a double-walled glass reactor equipped with a stirrer and a reflux condenser, suitable amounts (see Table 4) of previously dissolved VCL, NIPAAm and 0.06 g of the cross-linker N,N´-methylenebis(acrylamide) (BIS, 0.39 mmol, 3 mol-% based on the amount of VCL) were placed in 150 mL deionized water. The solution was heated up to 70 °C and stirred for 1 h under constant nitrogen purging. The polymerization was started by adding 5 mL of the initiator 2,2´-azobis(2-methylpropyonamidine) dihydrochloride (AMPA) to the reaction under stirring. After 6 h the reaction was stopped, and the dispersion was purified via dialysis membrane (Spectra/Por- Dialysis Membrane, MWCO:12-14.000) for 4 days before characterization.

Table 4: VCL/ NIPAAm microgel sample composition.

sample	NIPAAm:VCL [mol ratio]	VCL [g]	NIPAAm [g]
NIPAAm/VCL	1:3	1.742	0.472
NIPAAm/VCL	1:1	1.220	0.993
NIPAAm/VCL	3:1	0.644	1.571

4.1.4 VCL/AAEM/CD microgels

The synthesis of the polymerizable β-cyclodextrin monomer was performed by Dominic Schmitz from the Pich group. The procedure is described in the following.

50,0 g β-cyclodextrin (44,0 mmol) were dried in a two necked flask at 100 °C over night. 500 mL of a 0.4 M NaOH solution was added under nitrogen. The solution was cooled down to 0 °C. Under heavy stirring, 35.0 g p-toluenesulfonic-chloride (203 mmol) was added and the mixture was stirred for 30 min under cooling. The suspension was filtered, and the filtrate was neutralized via HCl. The solid was filtered off, washed with water and dried.

From the obtained product mono(6-O-(p-toluenesulfonic))-β-cyclodextrin, 10 g (7,76 mmol) were suspended in 100 mL degassed water and heated to 80 °C. 2.53 g (38.5 mmol) NaN_3 were slowly added and the mixture was stirred for 4 h at 80 °C. Afterwards, the mixture was cooled down and filtered. The product was felled in 600 mL of acetone. After washing with acetone, the product was recrystallized in a 2:1 acetone/water mixture and dried subsequently.

5,0 g (4,30 mmol) of the obtained mono(6-azido-6-desoxy)-β-cyclodextrin were dissolved in 100 mL degassed DMF. After addition of 1.09 g propargyl-methacrylate (8.60 mmol) and 0.11 g of $CuSO_4 \cdot 5\ H_2O$ and 0.17 g sodium ascorbate (0.86 mmol), the mixture was stirred for 6 h at 140 °C. The brown solution was felled with 800 mL of cold acetone. The solid was filtered off and washed multiple times with acetone. For purification, the product was dissolved in water and dialyzed for 3 days.

For the CD-functionalized microgel synthesis, a double-walled glass reactor equipped with a stirrer and reflux condenser was used. Suitable amounts of previously dissolved VCL, AAEM and 0.06 g of the cross-linker N,N´-methylenebis(acrylamide) (BIS, 0.39 mmol, 3 mol-% based on the amount of VCL) were placed in 150 mL deionized water. The solution was heated up to 70 °C and stirred for 1 h under constant nitrogen purging. The different amounts of β-cyclodextrin (CD) were added to the preheated solution, which is shown in Table 5. The polymerization was started by adding 5 mL of the initiator 2,2´-azobis(2-

methylpropyonamidine) dihydrochloride (AMPA) to the reaction under stirring. After 12 h, the reaction was stopped, and the dispersion was purified via dialysis membrane (Spectra/Por- Dialysis Membrane, MWCO:12-14.000) for 4 days before characterization.

Table 5: VCL/AAEM/CD microgel sample composition.

sample	VCL/AAEM /BIS [g]	β-CD [g]	β-CD [wt%]	β-CD [μmol]
VCL/AAEM/CD1	1.877/0.338/0.06	0.039	**2.1**	34
VCL/AAEM/CD2	1.877/0.338/0.06	0.081	**4.3**	71
VCL/AAEM/CD3	1.877/0.338/0.06	0.235	**12.5**	207

4.2 Wrinkle preparation

The microgels were assembled on wrinkled substrates based on elastomeric polydimethylsiloxane (PDMS).[64] For the wrinkle preparation, the commercially available elastomer kit Sylgard® 184 was used which contained the siloxane oligomers (Sylgard® 184 Base) and a siloxane-based curing agent (Sylgard® 184 curing agent) in a ratio of 10:1. The mixture was poured into a clean, flat petri dish and filled until a 3 mm thick film was obtained. The petri dish was then placed into an oven and was cured for 2 h at 80 °C after degassing overnight. With a scalpel, a 0.6·3 cm^2 area was cut out from the elastomeric film, which subsequently was placed into a custom-made stretching apparatus. Preferentially uniaxial stretching up to 130% of the initial length was applied before the substrate was placed into a plasma cleaner (Plasma active ecto 10usb-MFC) where the surface of the substrate was oxidized by air plasma under 0.2 mbar pressure (Figure 93). As previously shown by Genzer et al.,[85] the plasma treatment time is strongly correlated to the thickness of the porous oxide layer, which in turn defines the wavelength and amplitude (i.e., the height of the structure) of the resulting sinusoidal wrinkles after relaxation. To prevent defects of the nanostructure due to substrate handling, the wrinkled elastomers were placed on adapted glass slides. Based on the porous character of the oxide layer, free PDMS oligomers are able to diffuse to the surface, which in turn switches the surface properties

from hydrophilic to hydrophobic within minutes. Thus, before all aqueous experiments, the nanostructured substrates had to be plasma activated for 15 s.

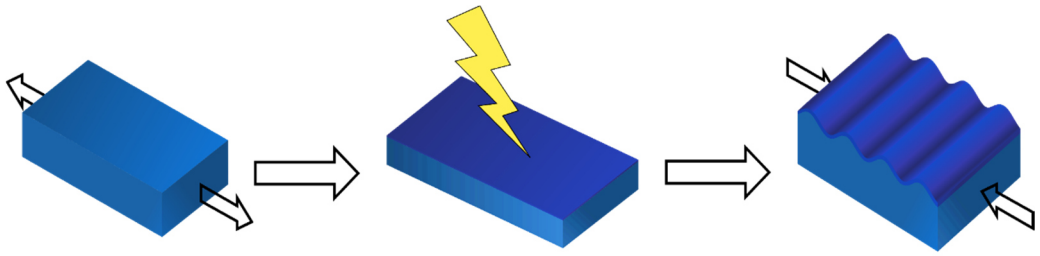

Figure 93: Uniaxial stretching followed by air plasma oxidation and strain relaxation.

For the in-situ stretching experiments the wrinkles were adjusted in a PTFE stretching apparatus. The stretching apparatus had a scale bar implemented in order to determine the stretching degree. The whole setup could be directly placed underneath the AFM measurement head. This way the samples could be observed in different stretching states via AFM.

4.3 Preparation of microgel arrays and 1D nanostrands

Assembly Method 1: Spin-coating setup, UV cross-linking and strand detachment

The assembly of microgels within the grooves of the wrinkles was carried out via spin-coating. To ensure the optimal occupancy of the wrinkle grooves with soft matter particles in the range of R_H 250-600 nm, the experimental setting for spin coating was prompted at 3000 rpm with an acceleration of 800 rpm and a total rotation time of 60 s. The amount of dispersion ranged from 5-30 µL. To cross-link the microgel assembly, PDMS wrinkles with microgels were placed under a custom-built UV lamp (450 W Xenon short-arc, L.O.T.-ORIEL GmbH & Co. KG (Darmstadt, Germany), irradiation area A = 6 cm^2; wavelength λ(lamp) = 190-350 nm; distance to source δ = 55 cm) and irradiated for 30 min.* To transfer

the microgel assemblies to TEM grids or glass substrates for microscopy, the sample had to be placed into the stretching apparatus again. After stretching the sample to 130 % of its initial length, 10 µL water was placed onto the stretched surface. After 1 min, a pipette was placed at the droplet and pressed onto the surface with a slight pressure before absorbing the droplet. The microgel assembly dispersion was transferred to TEM grids, glass slides or Si-wafers for further investigations.

*Exception: Arrays which were aligned within wrinkles with $\lambda \geq 1000$ nm were placed in a stretching apparatus and stretched to 130 % of its initial length to ensure an unshielded irradiation. After that the microgel strand could be transferred directly on to TEM grids for analysis.

Assembly Method 2: Molding conditions

The flat substrate (e.g. Si-wafer, glass slides) were cleaned by Snow Jet (compressed CO_2).[237] After exposure to air plasma for 20 s at 0.2 mbar (Plasma Activate Flecto 10 USB) 5-30 µL of the microgel dispersions were applied on the substrate surface. The PDMS template was pressed onto the prepared sample. After drying for 24 h the PDMS template was removed.

4.4 Cross-linking conditions and cross-linkers

Cross-linking VCL/AAEM microgels with UV light on wrinkles:

To cross-link the microgel assembly, PDMS wrinkles with microgels were placed under a custom-built UV lamp (450 W Xenon short-arc, L.O.T.-ORIEL GmbH & Co. KG (Darmstadt, Germany), irradiation area A = 6 cm^2; wavelength λ(lamp) = 190-350 nm; distance to source δ = 55 cm) and irradiated for 30 min.

Cross-linking VCL/AAEM/CD microgels with the azobenzene cross-linkers in solution:

For the cross-linking experiments, light with a wavelength of 600 nm was used. The diazobenzene cross-linker was dissolved in DMSO with a concentration of 2 mmol/L. 20 µL of the respective microgels were diluted to 1 mL with distilled water. After two minutes, 10 µL, respectively 30 µL of the cross-linker were added. and the extinction was measured. The Harada polymer was dissolved in ethanol to a concentration of 12 g/L. Further steps were equivalent to the experiments with the Azobenzene cross-linker. For the experimental setup see Chapter 5.7.

Cross-linking VCL/AAEM/CD microgels with the azobenzene cross-linkers under wrinkled substrates (Assembly Method 2):

The cross-linker was dissolved (in DMSO for the diazobenzene cross-linker, in EtOH for the Harada polymer) and added to the wrinkles in a way that the whole substrate was covered by the solution. For this purpose, 10 µL of the respective cross-linker was placed carefully with an Eppendorf pipette on the sample. After 15 minutes, the cross-linked microgels were dispersed in 20 µL of water. After additional 20 min, they were taken up by a pipette for transfer onto an activated Si-wafer for AFM analysis.

Sample rinsing was carried out by tilting the sample by 45° and repetitively rinsing the sample for 2-5 times. Afterwards, the sample was left to dry for 24 h at room temperature.

Harada polymer and diazobenzene-cross-linker

The cross-linkers were kindly provided by the Ravoo group. Synthesis and characterization can be found in literature.[220, 221]

5 Methods

5.1 AFM tapping mode, PeakForce QNM and liquid cell measurements

Atomic Force Microscopy (AFM) measurements in tapping mode (Veeco Dimension ICON from Bruker, Billerica, MA, USA) were performed with OTESPA tips (278–357 kHz, spring constant 12–103 $N \cdot m^{-1}$, tip radius 7-12 nm) in tapping mode at an air solid interface on flat silicon surfaces and wrinkles. The samples were prepared by spin coating 10 µL of the respective microgel dispersion onto a plasma activated silicon wafer. Subsequently, the substrates were dried at room temperature for at least 24 h. Nanoscope 8.10 (Build R1.60476) software was used to analyze the AFM data.

PeakForce QNM imaging in fluid were performed with the Veeco Dimension ICON from Bruker, Billerica, MA, USA. The silicon cantilever holder was equipped with SNL - 10 nitride probes (B triangular cantilever, 16–28 kHz, spring constant 0.06 – 0.24 Nm^{-1} and 2 -12 nm tip radius) or OTR8-10 probes (A triangular cantilever, 45–95 kHz, spring constant 0.28 – 1.14 Nm^{-1} ; B triangular cantilever, 16–932 kHz, spring constant 0.07 – 0.3 Nm^{-1} and 15 -20 nm tip radius. The samples were prepared by spin coating 10 µL of the respective microgel dispersion onto a plasma activated silicon wafer. Subsequently, the substrates were hydrated in water at room temperature for at least 24 h. The setup of the liquid cell measurement is described in Figure 79 from Chapter 2.3.2. Nanoscope 8.10 (Build R1.60476) software was used to analyze the AFM data.

5.2 Transmission electron microscopy

10 µL of the microgel dispersions were placed onto a carbon-coated copper grid, dried and examined by Transmission Electron Microscopy (TEM) (Zeiss Libra 120, Carl Zeiss NTS GmbH, Oberkochen, Germany) at 80 kV in bright field mode.

5.3 Confocal microscopy

Microgel strands were visualized by confocal laser scanning microscopy (Leica TCS SP8, Leica Microsystems GmbH, Wetzlar, Germany, Detector HyD). The samples were diluted, dropped onto a glass substrate and covered with a cover slide. Since the excitation maximum of rhodamine B is 540 nm, the microgel samples were excited with a diode-pumped solid state (DPSS) laser at 561 nm.

Fluorescence-labelling of microgel assemblies

One microgram of Rhodamine B was added to 50 mL of a VCL/AAEM microgel dispersion in a 100 mL flask. The fluorescent marker was adsorbed into the microgel network during 24 h of stirring. Right before adding 50 mL of the fluorescently marked microgel dispersion onto a wrinkled substrate, the wrinkles had to be activated by air plasma for 15 s at 0.2 mbar pressure to ensure a hydrophilic surface. Subsequently, the sample was spin-coated at 3000 rpm for 60 s (800 rpm acceleration). Afterwards, the sample was prepared analogous to Assembly Method 1.

5.4 Widefield fluorescence microscopy

A 561 nm DPSS laser (Cobolt Jive, 150 mW, Cobolt AB, Solna, Sweden) was used for the excitation of the dye molecules in the widefield fluorescence microscopy. The laser intensity was adjusted by neutral density filters to ca. 1–2 kW/cm^2. The laser was coupled into a multi-mode fiber (UM22-600 Thorlabs, NA 0.22 ± 0.02, 0.6 mm core diameter), which was shaken to destroy the coherence and suppress interference effects in order to obtain homogeneous sample illumination. The end of the fiber was imaged onto a ca. 40·40 μm^2 area of the sample using a 100×/1.49 NA oil immersion objective (UAPON100×OTIRF, Olympus, Olympus Deutschland GmbH, Hamburg, Germany). The samples were placed on a xyz-piezo table (P-545.3R7, Physik Instrumente, Karlsruhe, Germany), which fits into a commercial microscope (Olympus IX83, Olympus Deutschland GmbH, Hamburg,

Germany). The fluorescence was collected using the same objective and was spectrally separated from the excitation laser light by a quad line beam splitter (zt405/488/561/640rpc, AHF Analysentechnik, Tübingen, Germany), further magnified by two lenses (f1 = 200 mm AC254-200-A, Thorlabs and f2 = 400 mm AC254-400-A, Thorlabs, Thorlabs, Dachau, Germany) and imaged onto the chip of an EMCCD camera (Andor iXON Ultra 897, Andor Technology Ltd., Belfast, UK). To increase the S/N-ratio, a notch filter (E grade, 561 nm, AHF Analysentechnik) and a bandpass filter (Brightline HC 617/73, AHF Analysentechnik) were placed between the two lenses, and a cleanup filter (z561/10, AHF Analysentechnik) was placed in front of the laser. The total magnification was 200-fold, resulting in an image with 77 nm per pixel of the CCD camera. All measurements were performed at 294 K with an integration time per frame of 50 ms.

5.5 Analysis of microgel assembly conformation

The shape fluctuation contour analysis based on widefield images was performed with the Easyworm software package.[229] Parametric splines were used to approximate the contour, while the persistence length was evaluated within the framework of a worm-like strand model for a semi-flexible polymer.[229, 238]

5.6 Dynamic light scattering

The hydrodynamic radius and the VPTT of the microgel dispersion were measured by dynamic light scattering (ALV Goniometer with scattering detection at an angle of 90°, ALV-Laser Vertriebsgesellschaft m-b.H., Langen/Hessen, Germany).

The hydrodynamic radii (R_H) of the microgel dispersions at different temperatures (20 to 50 °C) and pH values (3-7) were measured with a Mastersizer Instruments Zetasizer 2000 with MPT-2 add-on (Malvern, UK). The temperature of the dispersions was equilibrated at each new temperature setpoint for a minimum of 2 min before data collection.

5.7 Optical density

Optical density measurements were carried out with a Uvikon 923 double beam spectrophotometer (Kontron Instruments) using 1.5 mL disposable cuvettes with dimensions 12.5 × 12.5 × 45 mm and 10 mm path length. The wavelength of 600 nm was used (OD600). Measurements were performed for 55 min with data points collected every 11 s.

6 Literature

1. N. Kellaris, V. G. Venkata, G. M. Smith, S. K. Mitchell and C. Keplinger, *Science Robotics*, 2018, **3**, eaar3276.
2. W. Obrecht, U. Seitz and W. Funke, 1976.
3. T. Tanaka and D. J. Fillmore, *The Journal of Chemical Physics*, 1979, **70**, 1214-1218.
4. I. Berndt, J. S. Pedersen and W. Richtering, *Angewandte Chemie*, 2006, **118**, 1769-1773.
5. A. Pich, A. Tessier, V. Boyko, Y. Lu and H.-J. P. Adler, *Macromolecules*, 2006, **39**, 7701-7707.
6. G. M. Eichenbaum, P. F. Kiser, D. Shah, W. P. Meuer, D. Needham and S. A. Simon, *Macromolecules*, 2000, **33**, 4087-4093.
7. S. Nayak and L. A. Lyon, *Angewandte chemie international edition*, 2005, **44**, 7686-7708.
8. A. Balaceanu, V. Mayorga, W. Lin, M.-P. Schürings, D. E. Demco, A. Böker, M. A. Winnik and A. Pich, *Colloid and Polymer Science*, 2013, **291**, 21-31.
9. S. Durkut, *International Journal of Polymeric Materials and Polymeric Biomaterials*, 2018, 1-14.
10. R. Pelton, *Advances in colloid and interface science*, 2000, **85**, 1-33.
11. N. A. Cortez-Lemus and A. Licea-Claverie, *Progress in Polymer Science*, 2016, **53**, 1-51.
12. V. Boyko, A. Pich, Y. Lu, S. Richter, K.-F. Arndt and H.-J. P. Adler, *Polymer*, 2003, **44**, 7821-7827.
13. B. R. Saunders, N. Laajam, E. Daly, S. Teow, X. Hu and R. Stepto, *Advances in colloid and interface science*, 2009, **147**, 251-262.
14. D. A. Pich.
15. L. Y. Chu, J. W. Kim, R. K. Shah and D. A. Weitz, *Advanced Functional Materials*, 2007, **17**, 3499-3504.
16. B. Mallikarjuna, K. M. S. Rao, C. Prasad, K. Rao, K. K. Rao and M. Subha, *Journal of Applied Pharmaceutical Science*, 2011, **1**, 171.
17. V. Boyko, S. Richter, A. Pich and K.-F. Arndt, *Colloid and Polymer Science*, 2003, **282**, 127-132.
18. J. Hain, A. Pich, H. J. Adler, D. Rais and S. Nešpůrek, 2008.
19. L. Shen, A. Pich, D. Fava, M. Wang, S. Kumar, C. Wu, G. D. Scholes and M. A. Winnik, *Journal of Materials Chemistry*, 2008, **18**, 763-770.
20. A. Pich, A. Karak, Y. Lu, A. K. Ghosh and H. J. P. Adler, *Macromolecular rapid communications*, 2006, **27**, 344-350.
21. A. Pich, A. Karak, Y. Lu, A. K. Ghosh and H.-J. P. Adler, *e-Polymers*, 2006, **6**, 226-241.
22. J. Hain, M. Schrinner, Y. Lu and A. Pich, *Small*, 2008, **4**, 2016-2024.
23. J. Zhang, S. Xu and E. Kumacheva, *Journal of the American Chemical Society*, 2004, **126**, 7908-7914.
24. M. Agrawal, A. Pich, S. Gupta, N. E. Zafeiropoulos, J. Rubio-Retama, F. Simon and M. Stamm, *Journal of Materials Chemistry*, 2008, **18**, 2581-2586.
25. N. Häntzschel, F. Zhang, F. Eckert, A. Pich and M. A. Winnik, *Langmuir*, 2007, **23**, 10793-10800.

26. S. F. Medeiros, A. M. Santos, H. Fessi and A. Elaissari, *Journal of Polymer Science Part A: Polymer Chemistry*, 2010, **48**, 3932-3941.
27. A. Fernandez-Nieves, H. Wyss, J. Mattsson and D. A. Weitz, *Microgel suspensions: fundamentals and applications*, John Wiley & Sons, 2011.
28. I. U. Ė. Kirsh and Y. E. Kirsh, *Water soluble poly-N-vinylamides: synthesis and physicochemical properties*, John Wiley & Sons, 1998.
29. H. Vihola, A. Laukkanen, L. Valtola, H. Tenhu and J. Hirvonen, *Biomaterials*, 2005, **26**, 3055-3064.
30. W. Tian, X. Lv, L. Huang, N. Ali and J. Kong, *Macromolecular Chemistry and Physics*, 2012, **213**, 2450-2463.
31. J. Liu, A. Debuigne, C. Detrembleur and C. Jérôme, *Advanced healthcare materials*, 2014, **3**, 1941-1968.
32. A. Imaz and J. Forcada, *Journal of Polymer Science Part A: Polymer Chemistry*, 2010, **48**, 1173-1181.
33. M. N. Mohammed, K. B. Yusoh and J. H. B. H. Shariffuddin, *Materials Express*, 2018, **8**, 21-34.
34. H. Vihola, 2007.
35. E. D. Goddard and J. V. Gruber, *Principles of polymer science and technology in cosmetics and personal care*, CRC Press, 1999.
36. H. Sefidroodi, P. C. Chua and M. A. Kelland, *Chemical Engineering Science*, 2011, **66**, 2050-2056.
37. D. Menne, F. Pitsch, J. E. Wong, A. Pich and M. Wessling, *Angewandte Chemie International Edition*, 2014, **53**, 5706-5710.
38. E. A. Markvicheva, V. I. Lozinsky, F. M. Plieva, K. A. Kochetkov, L. D. Rumsh, V. P. Zubov, J. Maity, R. Kumar, V. S. Parmar and Y. N. Belokon, *Pure and applied chemistry*, 2005, **77**, 227-236.
39. S. Kuptsova, E. Markvicheva, K. Kochetkov, Y. Belokon, L. Rumsh and V. Zubov, *Biocatalysis and Biotransformation*, 2000, **18**, 133-149.
40. E. Markvicheva, I. Kuz'kina, I. Pashkin, T. Plechko, Y. E. Kirsh and V. Zubov, *Biotechnology Techniques*, 1991, **5**, 223-226.
41. B. Mallikarjuna, 2012.
42. R. C. Mundargi, V. Rangaswamy and T. M. Aminabhavi, *Designed Monomers and Polymers*, 2010, **13**, 325-336.
43. Y. H. Roh, J. Y. Moon, E. J. Hong, H. U. Kim, M. S. Shim and K. W. Bong, *Colloids and Surfaces B: Biointerfaces*, 2018, **172**, 380-386.
44. X.-Z. Sun, X. Wang and J.-Z. Wu, *Applied Surface Science*, 2017, **403**, 509-518.
45. G. Agrawal, R. Agrawal and A. Pich, *Particle & Particle Systems Characterization*, 2017, **34**, 1700132.
46. R. L. Sala, M. Y. Kwon, M. Kim, S. E. Gullbrand, E. A. Henning, R. L. Mauck, E. R. Camargo and J. A. Burdick, *Tissue Engineering Part A*, 2017, **23**, 935-945.
47. B. Lynch, K. Crawford, O. Baruti, A. Abdulahad, M. Webster, J. Puetzer, C. Ryu, L. J. Bonassar and J. Mendenhall, *Journal of Biomedical Materials Research Part B: Applied Biomaterials*, 2017, **105**, 1863-1873.

48. A. K. Shakya, R. Holmdahl, K. S. Nandakumar and A. Kumar, *Journal of Biomedical Materials Research Part A*, 2014, **102**, 3409-3418.
49. B. Lee, A. Jiao, S. Yu, J. B. You, D.-H. Kim and S. G. Im, *Acta biomaterialia*, 2013, **9**, 7691-7698.
50. K. Takahashi and T. Imato, *Analytical sciences*, 1999, **15**, 181-184.
51. W. Wu, N. Mitra, E. C. Yan and S. Zhou, *Acs Nano*, 2010, **4**, 4831-4839.
52. V. Lapeyre, I. Gosse, S. Chevreux and V. Ravaine, *Biomacromolecules*, 2006, **7**, 3356-3363.
53. J.-z. Wu, D. H. Bremner, H.-y. Li, X.-z. Sun and L.-M. Zhu, *Materials Science and Engineering: C*, 2016, **69**, 1026-1035.
54. E. E. Makhaeva, L. T. M. Thanh, S. G. Starodoubtsev and A. R. Khokhlov, *Macromolecular Chemistry and Physics*, 1996, **197**, 1973-1982.
55. I. M. Okhapkin, I. R. Nasimova, E. E. Makhaeva and A. R. Khokhlov, *Macromolecules*, 2003, **36**, 8130-8138.
56. A. Balaceanu, D. E. Demco, M. Möller and A. Pich, *Macromolecules*, 2011, **44**, 2161-2169.
57. N. Nun, S. Hinrichs, M. A. Schroer, D. Sheyfer, G. Grübel and B. Fischer, *Gels*, 2017, **3**, 34.
58. A. Tager, A. Safronov, S. Sharina and I. Y. Galaev, *Colloid and Polymer Science*, 1993, **271**, 868-872.
59. F. Meeussen, E. Nies, H. Berghmans, S. Verbrugghe, E. Goethals and F. Du Prez, *Polymer*, 2000, **41**, 8597-8602.
60. S. F. Medeiros, J. C. Barboza, M. I. Ré, R. Giudici and A. M. Santos, *Journal of applied polymer science*, 2010, **118**, 229-240.
61. A. Laukkanen, L. Valtola, F. M. Winnik and H. Tenhu, *Macromolecules*, 2004, **37**, 2268-2274.
62. A. Tager, A. Safronov, S. Sharina and I. Y. Galaev, *Polym SciUSSR* 1990, 469–474.
63. C. Chee, S. Rimmer, I. Soutar and L. Swanson, *Reactive and Functional Polymers*, 2006, **66**, 1-11.
64. S. Hiltl, M.-P. Schürings, A. Balaceanu, V. Mayorga, C. Liedel, A. Pich and A. Böker, *Soft Matter*, 2011, **7**, 8231-8238.
65. M. Zeiser, I. Freudensprung and T. Hellweg, *Polymer*, 2012, **53**, 6096-6101.
66. G. Agrawal, M. P. Schürings, P. van Rijn and A. Pich, *Journal of Materials Chemistry A*, 2013, **1**, 13244-13251.
67. S. Thies, P. Simon, I. Zelenina, L. Mertens and A. Pich, *Small*, 2018, **14**, 1803589.
68. K. Wiemer, K. Dörmbach, I. Slabu, G. Agrawal, F. Schrader, T. Caumanns, S. Bourone, J. Mayer, J. Steitz and U. Simon, *Journal of Materials Chemistry B*, 2017, **5**, 1284-1292.
69. W. Sun, S. Thies, J. Zhang, C. Peng, G. Tang, M. Shen, A. Pich and X. Shi, *ACS applied materials & interfaces*, 2017, **9**, 3411-3418.
70. S. Schachschal, A. Pich and H.-J. Adler, in *Surface and Interfacial Forces–From Fundamentals to Applications*, Springer, 2008, pp. 141-148.
71. S. Schachschal, A. Pich and H.-J. Adler, *Langmuir*, 2008, **24**, 5129-5134.
72. A. Pich, S. Bhattacharya, Y. Lu, V. Boyko and H.-J. P. Adler, *Langmuir*, 2004, **20**, 10706-10711.

73. K. Herman, M. Lang and A. Pich, *Nanoscale*, 2018, **10**, 3884-3892.
74. A. Pich, J. Hain, Y. Lu, V. Boyko, Y. Prots and H.-J. Adler, *Macromolecules*, 2005, **38**, 6610-6619.
75. G. Tillet, B. Boutevin and B. Ameduri, *Progress in Polymer Science*, 2011, **36**, 191-217.
76. X. SU and Y. LIU, *Acta Polymerica Sinica*, 2009, **4**.
77. M. J. Kettel, F. Dierkes, K. Schaefer, M. Moeller and A. Pich, *Polymer*, 2011, **52**, 1917-1924.
78. A. Biswas, I. S. Bayer, A. S. Biris, T. Wang, E. Dervishi and F. Faupel, *Advances in colloid and interface science*, 2012, **170**, 2-27.
79. S. Sacanna, W. T. Irvine, P. M. Chaikin and D. J. Pine, *Nature*, 2010, **464**, 575.
80. D. Ortiz, K. L. Kohlstedt, T. D. Nguyen and S. C. Glotzer, *Soft Matter*, 2014, **10**, 3541-3552.
81. Y. Wang, Y. Wang, X. Zheng, G.-R. Yi, S. Sacanna, D. J. Pine and M. Weck, *Journal of the American Chemical Society*, 2014, **136**, 6866-6869.
82. Q. Ji, S. Acharya, J. P. Hill, G. J. Richards and K. Ariga, *Advanced Materials*, 2008, **20**, 4027-4032.
83. S. Acharya, J. P. Hill and K. Ariga, *Advanced Materials*, 2009, **21**, 2959-2981.
84. D. Tuerp, M. Baumgarten and K. Müllen, *New Journal of Chemistry*, 2012, **36**, 282-298.
85. J. Genzer and J. Groenewold, *Soft Matter*, 2006, **2**, 310-323.
86. I. L. Kruglikov and P. E. Scherer, *Nutrition and healthy aging*, 2017, 1-17.
87. E. Cerda, K. Ravi-Chandar and L. Mahadevan, *Nature*, 2002, **419**, 579-580.
88. E. Cerda and L. Mahadevan, *Physical review letters*, 2003, **90**, 074302.
89. N. Bowden, W. T. Huck, K. E. Paul and G. M. Whitesides, *Applied Physics Letters*, 1999, **75**, 2557-2559.
90. K. Efimenko, M. Rackaitis, E. Manias, A. Vaziri, L. Mahadevan and J. Genzer, *Nature materials*, 2005, **4**, 293-297.
91. W. T. Huck, N. Bowden, P. Onck, T. Pardoen, J. W. Hutchinson and G. M. Whitesides, *Langmuir*, 2000, **16**, 3497-3501.
92. M. Pretzl, A. Schweikart, C. Hanske, A. Chiche, U. Zettl, A. Horn, A. Böker and A. Fery, *Langmuir*, 2008, **24**, 12748-12753.
93. A. Chiche, C. M. Stafford and J. T. Cabral, *Soft Matter*, 2008, **4**, 2360-2364.
94. M.-P. Schürings, 2010.
95. A. Tóth, I. Bertóti, M. Blazsó, G. Bánhegyi, A. Bognar and P. Szaplonczay, *Journal of applied polymer science*, 1994, **52**, 1293-1307.
96. G. Curthoys, V. Y. Davydov, A. Kiselev, S. Kiselev and B. Kuznetsov, *Journal of Colloid and Interface Science*, 1974, **48**, 58-72.
97. K. Efimenko, W. E. Wallace and J. Genzer, *Journal of colloid and interface science*, 2002, **254**, 306-315.
98. E. Everaert, H. Van der Mei and H. Busscher, *American Chemical Society, Polym. Prepr.(USA)*, 1995, **36**, 89-90.
99. N. Bowden, S. Brittain, A. G. Evans, J. W. Hutchinson and G. M. Whitesides, *Nature*, 1998, **393**, 146-149.

100. G. Lin, Q. Zhang, C. Lv, Y. Tang and J. Yin, *Soft matter*, 2018, **14**, 1517-1529.
101. Z.-C. Shao, Y. Zhao, W. Zhang, Y. Cao and X.-Q. Feng, *Soft Matter*, 2016, **12**, 7977-7982.
102. C. Zong, U. Azhar, C. Zhou, J. Wang, L. Zhang, Y. Cao, S. Zhang, S. Jiang and C. Lu, *Langmuir*, 2019.
103. S. Hiltl, J. Oltmanns and A. Böker, *Nanoscale*, 2012, **4**, 7338-7345.
104. S. Hiltl and A. Böker, *Langmuir*, 2016, **32**, 8882-8888.
105. P. Wünnemann, 2011.
106. I. E. Khodasevych, L. Wang, A. Mitchell and G. Rosengarten, *Advanced Optical Materials*, 2015, **3**, 852-881.
107. Q. Zhou, P. Wünnemann, P. T. Kühn, J. de Vries, M. Helmin, A. Böker, T. G. van Kooten and P. van Rijn, *Advanced Materials Interfaces*, 2016, **3**, 1600275.
108. A. Sechi, J. M. Freitas, P. Wünnemann, A. Töpel, R. T. Paschoalin, S. Ullmann, R. Schröder, G. Aydin, S. Rütten and A. Böker, *Advanced Materials Interfaces*, 2016, **3**, 1600455.
109. Y. Luan, S. Liu, M. Pihl, H. C. van der Mei, J. Liu, F. Hizal, C.-H. Choi, H. Chen, Y. Ren and H. J. Busscher, *Current Opinion in Colloid & Interface Science*, 2018.
110. K. Efimenko, J. Finlay, M. E. Callow, J. A. Callow and J. Genzer, *ACS applied materials & interfaces*, 2009, **1**, 1031-1040.
111. K. Khare, J. Zhou and S. Yang, *Langmuir*, 2009, **25**, 12794-12799.
112. J. Mu, C. Hou, G. Wang, X. Wang, Q. Zhang, Y. Li, H. Wang and M. Zhu, *Advanced Materials*, 2016, **28**, 9491-9497.
113. W.-K. Lee, J. Kang, K.-S. Chen, C. J. Engel, W.-B. Jung, D. Rhee, M. C. Hersam and T. W. Odom, *Nano letters*, 2016, **16**, 7121-7127.
114. Q. Wang and X. Zhao, *Mrs Bulletin*, 2016, **41**, 115-122.
115. M. A. C. Stuart, W. T. Huck, J. Genzer, M. Müller, C. Ober, M. Stamm, G. B. Sukhorukov, I. Szleifer, V. V. Tsukruk and M. Urban, *Nature materials*, 2010, **9**, 101.
116. Y.-B. Kim, J.-K. Choi, J.-A. Yu and J.-W. Hong, *Synthetic metals*, 2002, **131**, 79-85.
117. Y.-B. Kim, C.-h. Park and J.-W. Hong, *Journal*, 2002.
118. J. Clara-Rahola, R. Contreras-Caceres, B. Sierra-Martin, A. Maldonado-Valdivia, M. Hund, A. Fery, T. Hellweg and A. Fernandez-Barbero, *Colloids and Surfaces A: Physicochemical and Engineering Aspects*, 2014, **463**, 18-27.
119. M. Müller, M. Karg, A. Fortini, T. Hellweg and A. Fery, *Nanoscale*, 2012, **4**, 2491-2499.
120. S. Xu, J. Zhang, C. Paquet, Y. Lin and E. Kumacheva, *Advanced Functional Materials*, 2003, **13**, 468-472.
121. A. P. Napolitano, P. Chai, D. M. Dean and J. R. Morgan, *Tissue engineering*, 2007, **13**, 2087-2094.
122. Y. Xia, X. He, M. Cao, X. Wang, Y. Sun, H. He, H. Xu and J. R. Lu, *Biomacromolecules*, 2014, **15**, 4021-4031.
123. A. C. Saito, T. S. Matsui, M. Sato and S. Deguchi, *Biotechnology letters*, 2014, **36**, 391-396.
124. M. E. Harmon, M. Tang and C. W. Frank, *Polymer*, 2003, **44**, 4547-4556.

125. R. H. Liu, Q. Yu and D. J. Beebe, *Microelectromechanical Systems, Journal of*, 2002, **11**, 45-53.
126. Z. Liu and P. Calvert, *Advanced Materials*, 2000, **12**, 288-291.
127. A. Tadimety, K. M. Kready, H. T. Chorsi, L. Zhang, T. J. Palinski and J. X. Zhang, *Microfluidics and Nanofluidics*, 2019, **23**, 17.
128. K. Park, M.-A. Woo, J.-A. Lim, Y.-R. Kim, S.-W. Choi and M.-C. Lim, *Colloids and Surfaces A: Physicochemical and Engineering Aspects*, 2018, **558**, 186-191.
129. C. Hanske, M. Tebbe, C. Kuttner, V. Bieber, V. V. Tsukruk, M. Chanana, T. A. König and A. Fery, *Nano letters*, 2014, **14**, 6863-6871.
130. M. Tebbe, M. Mayer, B. A. Glatz, C. Hanske, P. T. Probst, M. B. Müller, M. Karg, M. Chanana, T. A. König and C. Kuttner, *Faraday discussions*, 2015, **181**, 243-260.
131. M. Mayer, M. Tebbe, C. Kuttner, M. J. Schnepf, T. A. König and A. Fery, *Faraday discussions*, 2016, **191**, 159-176.
132. A. Schweikart, N. Pazos-Pérez, R. A. Alvarez-Puebla and A. Fery, *Soft Matter*, 2011, **7**, 4093-4100.
133. A. Schweikart, A. Fortini, A. Wittemann, M. Schmidt and A. Fery, *Soft Matter*, 2010, **6**, 5860-5863.
134. H. Endo, Y. Mochizuki, M. Tamura and T. Kawai, *Langmuir*, 2013, **29**, 15058-15064.
135. R. Brüx, S. Hiltl, V. Schröder, C. von Essen and A. Böker, *Particle & Particle Systems Characterization*, 2014, **31**, 871-878.
136. Y. Wang, A. D. Hollingsworth, S. K. Yang, S. Patel, D. J. Pine and M. Weck, *Journal of the American Chemical Society*, 2013, **135**, 14064-14067.
137. Y. Wang, Y. Wang, D. R. Breed, V. N. Manoharan, L. Feng, A. D. Hollingsworth, M. Weck and D. J. Pine, *Nature*, 2012, **491**, 51.
138. S. Ni, J. Leemann, I. Buttinoni, L. Isa and H. Wolf, *Science advances*, 2016, **2**, e1501779.
139. C. Lu, H. Möhwald and A. Fery, *Soft Matter*, 2007, **3**, 1530-1536.
140. H. Endo, Y. Mochizuki, M. Tamura and T. Kawai, *Colloids and Surfaces A: Physicochemical and Engineering Aspects*, 2014, **443**, 576-582.
141. M.-P. Schürings, O. Nevskyi, K. Eliasch, A.-K. Michel, B. Liu, A. Pich, A. Böker, G. von Plessen and D. Wöll, *Polymers*, 2016, **8**, 413.
142. M. Mueller, M. Tebbe, D. V. Andreeva, M. Karg, R. A. Alvarez Puebla, N. Pazos Perez and A. Fery, *Langmuir*, 2012, **28**, 9168-9173.
143. T. Wagner, A. Nedilko, M. Linn, D. N. Chigrin, G. von Plessen and A. Böker, *Small*, 2017, **13**, 1603054.
144. P. Wünnemann, M. Noyong, K. Kreuels, R. Brüx, P. Gordiichuk, P. van Rijn, F. A. Plamper, U. Simon and A. Böker, *Macromolecular rapid communications*, 2016, **37**, 1446-1452.
145. A. Horn, S. Hiltl, A. Fery and A. Böker, *Small*, 2010, **6**, 2122-2125.
146. A. Horn, H. G. Schoberth, S. Hiltl, A. Chiche, Q. Wang, A. Schweikart, A. Fery and A. Böker, *Faraday discussions*, 2009, **143**, 143-150.
147. M. Das, S. Mardyani, W. C. Chan and E. Kumacheva, *Advanced Materials*, 2006, **18**, 80-83.

148. A. Gestos, P. G. Whitten, G. G. Wallace and G. M. Spinks, *Soft Matter*, 2012, **8**, 8082-8087.
149. S. L. Biswal and A. P. Gast, *Physical Review E*, 2003, **68**, 021402.
150. R. Dreyfus, J. Baudry, M. L. Roper, M. Fermigier, H. A. Stone and J. Bibette, *Nature*, 2005, **437**, 862.
151. C. Goubault, P. Jop, M. Fermigier, J. Baudry, E. Bertrand and J. Bibette, *Physical review letters*, 2003, **91**, 260802.
152. P. Reineck, G. P. Lee, D. Brick, M. Karg, P. Mulvaney and U. Bach, *Advanced Materials*, 2012, **24**, 4750-4755.
153. J. Y. Cheng, C. T. Rettner, D. P. Sanders, H. C. Kim and W. D. Hinsberg, *Advanced Materials*, 2008, **20**, 3155-3158.
154. S. Srinivasan, V. K. Praveen, R. Philip and A. Ajayaghosh, *Angewandte Chemie*, 2008, **120**, 5834-5838.
155. R. Sakamoto, Y. Hataguchi, R. Kimura, K. Tsuchiya and Y. Mori, *Chemistry Letters*, 2012, **41**, 1207-1209.
156. W. Han, M. Byun and Z. Lin, *Journal of Materials Chemistry*, 2011, **21**, 16968-16972.
157. Y. Xia, Y. Yin, Y. Lu and J. McLellan, *Advanced Functional Materials*, 2003, **13**, 907-918.
158. Y. Yin, Y. Lu, B. Gates and Y. Xia, *Journal of the American Chemical Society*, 2001, **123**, 8718-8729.
159. Y. Yin, Y. Lu and Y. Xia, *Journal of Materials Chemistry*, 2001, **11**, 987-989.
160. Y. Yin and Y. Xia, *Journal of the American Chemical Society*, 2003, **125**, 2048-2049.
161. F. Gittes, B. Mickey, J. Nettleton and J. Howard, *The Journal of cell biology*, 1993, **120**, 923-934.
162. N. Fakhri, D. A. Tsyboulski, L. Cognet, R. B. Weisman and M. Pasquali, *Proceedings of the National Academy of Sciences*, 2009, **106**, 14219-14223.
163. D. A. Tsyboulski, S. M. Bachilo, A. B. Kolomeisky and R. B. Weisman, *Acs Nano*, 2008, **2**, 1770-1776.
164. E. E. Keaveny and M. J. Shelley, *Physical Review E*, 2009, **79**, 051405.
165. B. Varghese, F. C. Cheong, S. Sindhu, T. Yu, C.-T. Lim, S. Valiyaveettil and C.-H. Sow, *Langmuir*, 2006, **22**, 8248-8252.
166. E. Kumacheva, R. K. Golding, M. Allard and E. H. Sargent, *Advanced Materials*, 2002, **14**, 221.
167. F. Ramiro-Manzano, E. Bonet, I. Rodriguez and F. Meseguer, *Langmuir*, 2010, **26**, 4559-4562.
168. N. N. Khanh and K. B. Yoon, *Journal of the American Chemical Society*, 2009, **131**, 14228-14230.
169. G. A. Ozin and S. M. Yang, *Advanced Functional Materials*, 2001, **11**, 95-104.
170. H. n. M. San Ming Yang and G. A. Ozin, 2002.
171. F. Juillerat, H. H. Solak, P. Bowen and H. Hofmann, *Nanotechnology*, 2005, **16**, 1311.
172. X. Y. Ling, I. Y. Phang, D. N. Reinhoudt, G. J. Vancso and J. Huskens, *ACS applied materials & interfaces*, 2009, **1**, 960-968.
173. A. Mathur, A.-D. Brown and J. Erlebacher, *Langmuir*, 2006, **22**, 582-589.
174. K. Norrman, A. Ghanbari-Siahkali and N. Larsen, *Annual Reports Section" C"(Physical Chemistry)*, 2005, **101**, 174-201.
175. E. Fisslthaler, A. Blümel, K. Landfester, U. Scherf and E. J. List, *Soft Matter*, 2008, **4**, 2448-2453.

176. M. A. Meitl, Z.-T. Zhu, V. Kumar, K. J. Lee, X. Feng, Y. Y. Huang, I. Adesida, R. G. Nuzzo and J. A. Rogers, *Nature Materials*, 2006, **5**, 33-38.
177. S. Wagner, S. P. Lacour, J. Jones, I. H. Pai-hui, J. C. Sturm, T. Li and Z. Suo, *Physica E: Low-dimensional Systems and Nanostructures*, 2004, **25**, 326-334.
178. D.-Y. Khang, H. Jiang, Y. Huang and J. A. Rogers, *science*, 2006, **311**, 208-212.
179. C. Harrison, C. M. Stafford, W. Zhang and A. Karim, *Applied Physics Letters*, 2004, **85**, 4016-4018.
180. L. Hoipkemeier-Wilson, J. F. Schumacher, M. L. Carman, A. L. Gibson, A. W. Feinberg, M. E. Callow, J. A. Finlay, J. A. Callow and A. B. Brennan, *Biofouling*, 2004, **20**, 53-63.
181. P.-C. Lin and S. Yang, *Soft Matter*, 2009, **5**, 1011-1018.
182. S. Zhao, H. Xia, D. Wu, C. Lv, Q.-D. Chen, K. Ariga, L.-Q. Liu and H.-B. Sun, *Soft Matter*, 2013, **9**, 4236-4240.
183. S. Schmidt, T. Hellweg and R. von Klitzing, *Langmuir*, 2008, **24**, 12595-12602.
184. S. Schmidt, H. Motschmann, T. Hellweg and R. von Klitzing, *Polymer*, 2008, **49**, 749-756.
185. T. Hellweg, C. Dewhurst, E. Brückner, K. Kratz and W. Eimer, *Colloid and Polymer Science*, 2000, **278**, 972-978.
186. S. H. Cohen and M. L. Lightbody, *Atomic force microscopy/scanning tunneling microscopy 3*, Springer Science & Business Media, 2007.
187. S. Morita, *Roadmap of scanning probe microscopy*, Springer Science & Business Media, 2006.
188. D. Sarid, *Scanning force microscopy: with applications to electric, magnetic, and atomic forces*, Oxford University Press on Demand, 1994.
189. G. Binnig, C. F. Quate and C. Gerber, *Physical review letters*, 1986, **56**, 930.
190. C. A. Putman, K. O. Van der Werf, B. G. De Grooth, N. F. Van Hulst and J. Greve, *Applied physics letters*, 1994, **64**, 2454-2456.
191. S. Wellert, M. Richter, T. Hellweg, R. von Klitzing and Y. Hertle, *Zeitschrift für Physikalische Chemie*, 2015, **229**, 1225-1250.
192. L. Kailas, E. Ratcliffe, E. Hayhurst, M. Walker, S. Foster and J. Hobbs, *Ultramicroscopy*, 2009, **109**, 775-780.
193. V. I. Inc, 2009.
194. B. Pittenger, N. Erina and C. Su, *Application Note Veeco Instruments Inc*, 2010, 1-2.
195. B. Zhao, Y. Song, S. Wang, B. Dai, L. Zhang, Y. Dong, J. Lü and J. Hu, *Soft Matter*, 2013, **9**, 8837-8843.
196. M. Enachescu, R. Van Den Oetelaar, R. W. Carpick, D. Ogletree, C. Flipse and M. Salmeron, *Physical review letters*, 1998, **81**, 1877.
197. D. J. Henry, C. A. Lukey, E. Evans and I. Yarovsky, *Molecular Simulation*, 2005, **31**, 449-455.
198. R. Horn, D. Smith and W. Haller, *Chemical Physics Letters*, 1989, **162**, 404-408.
199. L.-O. Heim, J. Blum, M. Preuss and H.-J. Butt, *Physical Review Letters*, 1999, **83**, 3328.
200. R. W. Rice, *Mechanical properties of ceramics and composites: grain and particle effects*, CRC Press, 2000.

201. A. Laukkanen, S. Wiedmer, S. Varjo, M.-L. Riekkola and H. Tenhu, *Colloid and Polymer Science*, 2002, **280**, 65-70.
202. Y. Guan and Y. Zhang, *Soft Matter*, 2011, **7**, 6375-6384.
203. J. L. Alonso and W. H. Goldmann, *Life sciences*, 2003, **72**, 2553-2560.
204. E. Papirer, *Adsorption on silica surfaces*, CRC Press, 2000.
205. J. R. Höhner, 2014.
206. D. Kuckling, J. Hoffmann, M. Plötner, D. Ferse, K. Kretschmer, H.-J. P. Adler, K.-F. Arndt and R. Reichelt, *Polymer*, 2003, **44**, 4455-4462.
207. T. Watanabe, M. Akiyama, K. Totani, S. M. Kuebler, F. Stellacci, W. Wenseleers, K. Braun, S. R. Marder and J. W. Perry, *Advanced Functional Materials*, 2002, **12**, 611-614.
208. F. Hollmann and I. W. Arends, *Polymers*, 2012, **4**, 759-793.
209. D. Murakami, H. Jinnai and A. Takahara, *Langmuir*, 2014, **30**, 2061-2067.
210. R. G. Azrak and C. Angell, *The Journal of Physical Chemistry*, 1973, **77**, 3048-3052.
211. S. Björklund and V. Kocherbitov, *Scientific reports*, 2017, **7**, 9960.
212. A. Harada, M. Furue and S.-i. Nozakura, *Macromolecules*, 1976, **9**, 701-704.
213. G. Wenz, *Angewandte Chemie*, 1994, **106**, 851-870.
214. H. Dodziuk, *Cyclodextrins and their complexes: chemistry, analytical methods, applications*, John Wiley & Sons, 2006.
215. D. Duchêne, G. Ponchel and D. Wouessidjewe, *Advanced Drug Delivery Reviews*, 1999, **36**, 29-40.
216. P. J. Zheng, C. Wang, X. Hu, K. C. Tam and L. Li, *Macromolecules*, 2005, **38**, 2859-2864.
217. H. D. Bandara and S. C. Burdette, *Chemical Society Reviews*, 2012, **41**, 1809-1825.
218. S. K. M. Nalluri, J. Voskuhl, J. B. Bultema, E. J. Boekema and B. J. Ravoo, *Angewandte Chemie International Edition*, 2011, **50**, 9747-9751.
219. S. Engel, N. Möller and B. J. Ravoo, *Chemistry–A European Journal*, 2018, **24**, 4741-4748.
220. S. K. M. Nalluri, 2011.
221. H. Yamaguchi, Y. Kobayashi, R. Kobayashi, Y. Takashima, A. Hashidzume and A. Harada, *Nature communications*, 2012, **3**, 603.
222. P. Falvey, C. W. Lim, R. Darcy, T. Revermann, U. Karst, M. Giesbers, A. T. Marcelis, A. Lazar, A. W. Coleman and D. N. Reinhoudt, *Chemistry–A European Journal*, 2005, **11**, 1171-1180.
223. Y. Mei, S. Kiravittaya, S. Harazim and O. G. Schmidt, *Materials Science and Engineering: R: Reports*, 2010, **70**, 209-224.
224. M. R. Caira, E. J. De Vries and L. R. Nassimbeni, *Chemical Communications*, 2003, 2058-2059.
225. S. Tamesue, Y. Takashima, H. Yamaguchi, S. Shinkai and A. Harada, *Angewandte Chemie International Edition*, 2010, **49**, 7461-7464.
226. S. Park and A. Böker, *Journal of Materials Chemistry*, 2011, **21**, 11734-11736.

227. M. Hu, C. Novo, A. Funston, H. Wang, H. Staleva, S. Zou, P. Mulvaney, Y. Xia and G. V. Hartland, *Journal of materials chemistry*, 2008, **18**, 1949-1960.
228. B. Huang, M. Bates and X. Zhuang, *Annual review of biochemistry*, 2009, **78**, 993-1016.
229. G. Lamour, J. B. Kirkegaard, H. Li, T. P. Knowles and J. Gsponer, *Source code for biology and medicine*, 2014, **9**, 1-6.
230. M. J. Saxton, *Biophysical journal*, 1997, **72**, 1744-1753.
231. S. Broersma, *The Journal of Chemical Physics*, 1960, **32**, 1632-1635.
232. S. Broersma, *The Journal of Chemical Physics*, 1981, **74**, 6989-6990.
233. R. Duggal and M. Pasquali, *Physical Review Letters*, 2006, **96**, 246104.
234. J. G. De La Torre and M. C. L. Martinez, *Biopolymers*, 1984, **23**, 611-615.
235. J. Saragosti, P. Silberzan and A. Buguin, *PloS one*, 2012, **7**, e35412.
236. D. C. Hyun, G. D. Moon, E. C. Cho and U. Jeong, *Advanced Functional Materials*, 2009, **19**, 2155-2162.
237. R. Sherman, D. Hirt and R. Vane, *Journal of Vacuum Science & Technology A: Vacuum, Surfaces, and Films*, 1994, **12**, 1876-1881.
238. T. P. Knowles, A. W. Fitzpatrick, S. Meehan, H. R. Mott, M. Vendruscolo, C. M. Dobson and M. E. Welland, *Science*, 2007, **318**, 1900-1903.

7 Attachment

Guided self-assembly of microgels into 1D nanoarrays

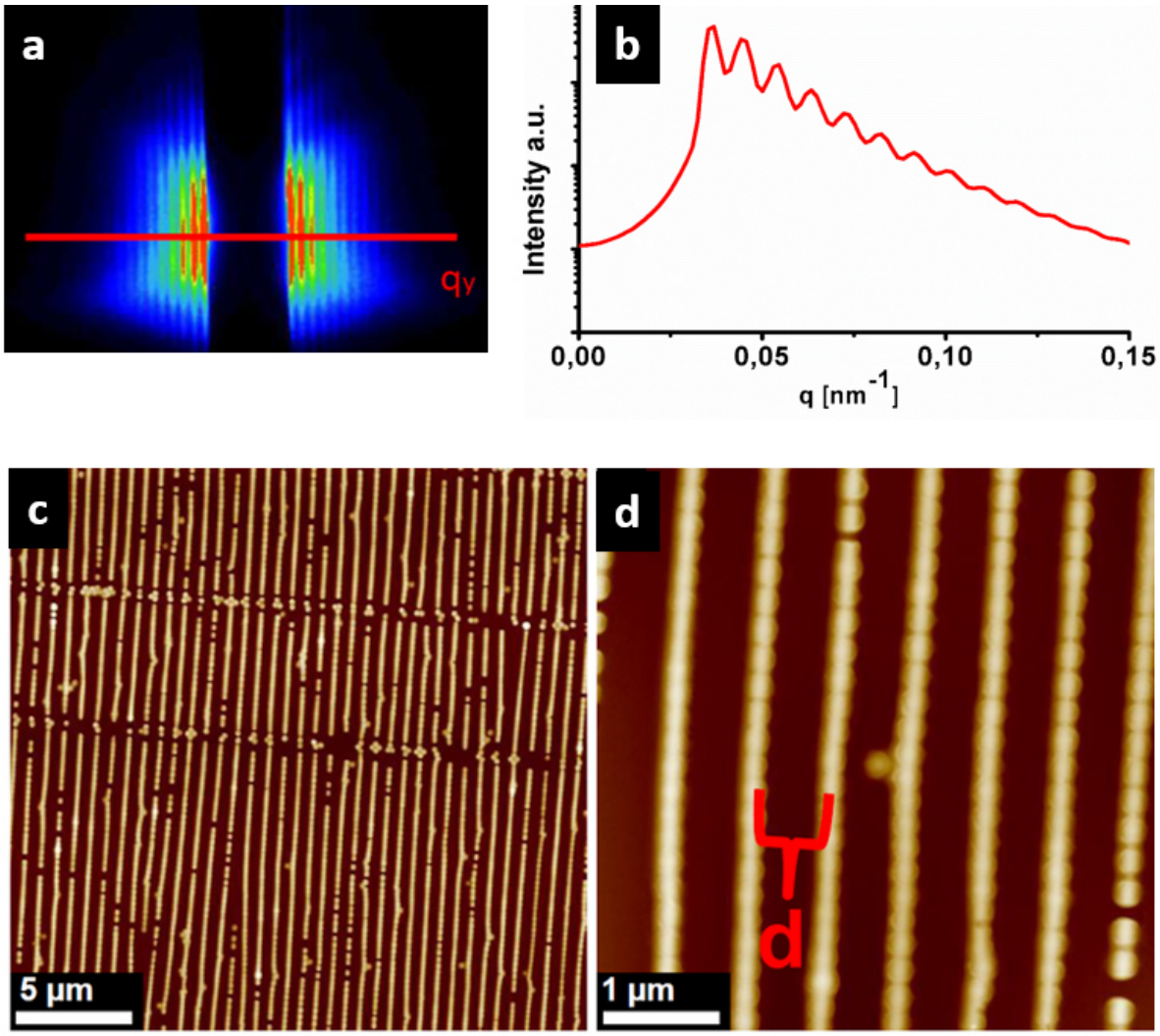

Figure 94a: Diffraction data of a one-dimensional nanostructure made of VCL/AAEM -microgels transferred on a Si wafer. b: q_y - section of the diffraction data. The calculated mean distance between the collective arrays over 2 cm² correlates to the measured distance d obtained via AFM. c-d: AFM images of VCL/AAEM microgels (Δz=200nm; incident angle α=0.2°).[64]

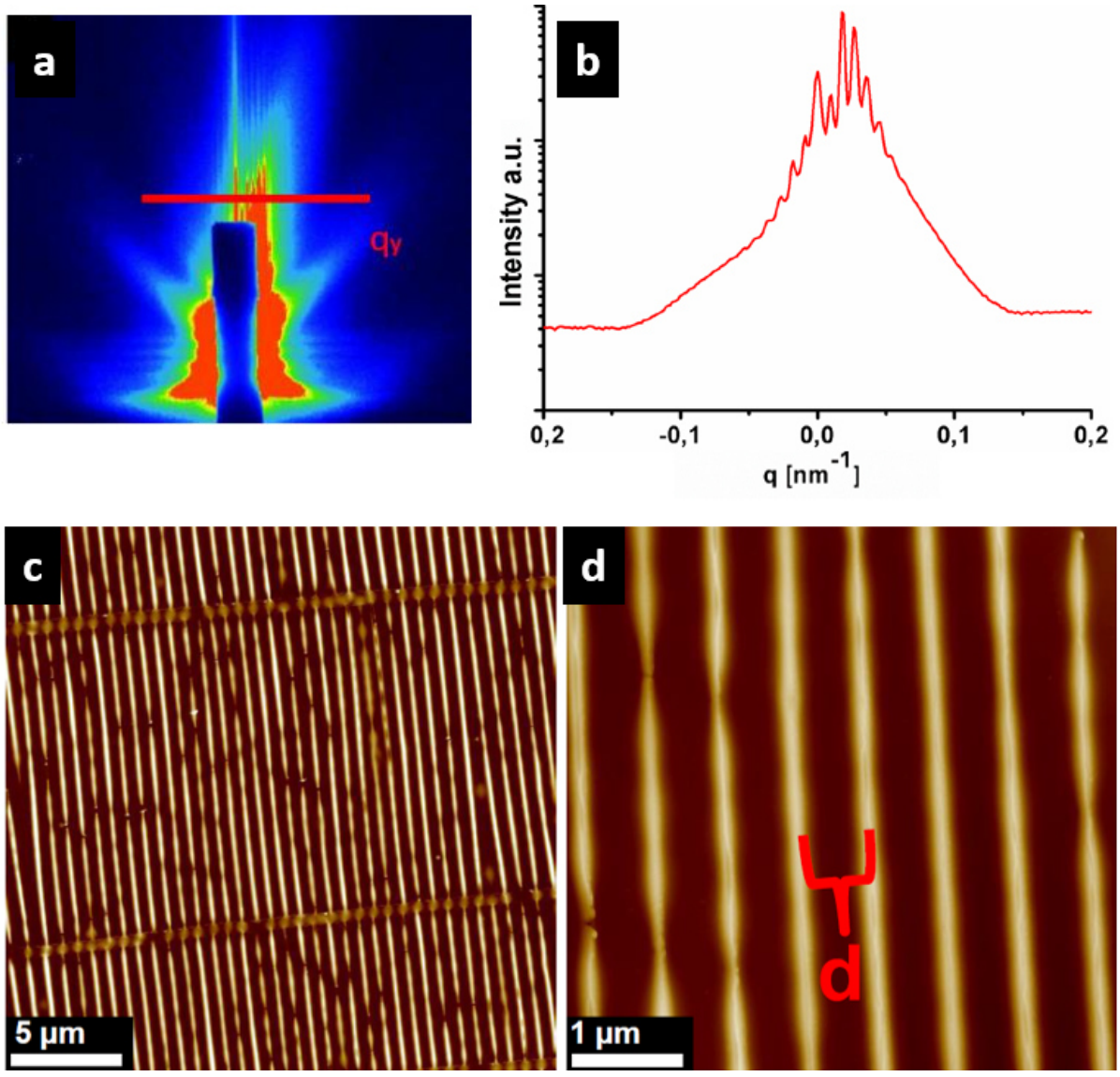

Figure 95a: Diffraction data of a one-dimensional nanostructure made of NIPAAm/VCL 1:3 microgels transferred on a Si wafer. b: q_y - section of the diffraction data. The calculated mean distance between the collective arrays over 2 cm² correlates to the measured distance d obtained via AFM. c-d: AFM images of NIPAAm/VCL 1:3 microgels (Δz=200nm; incident angle α=0.2°).

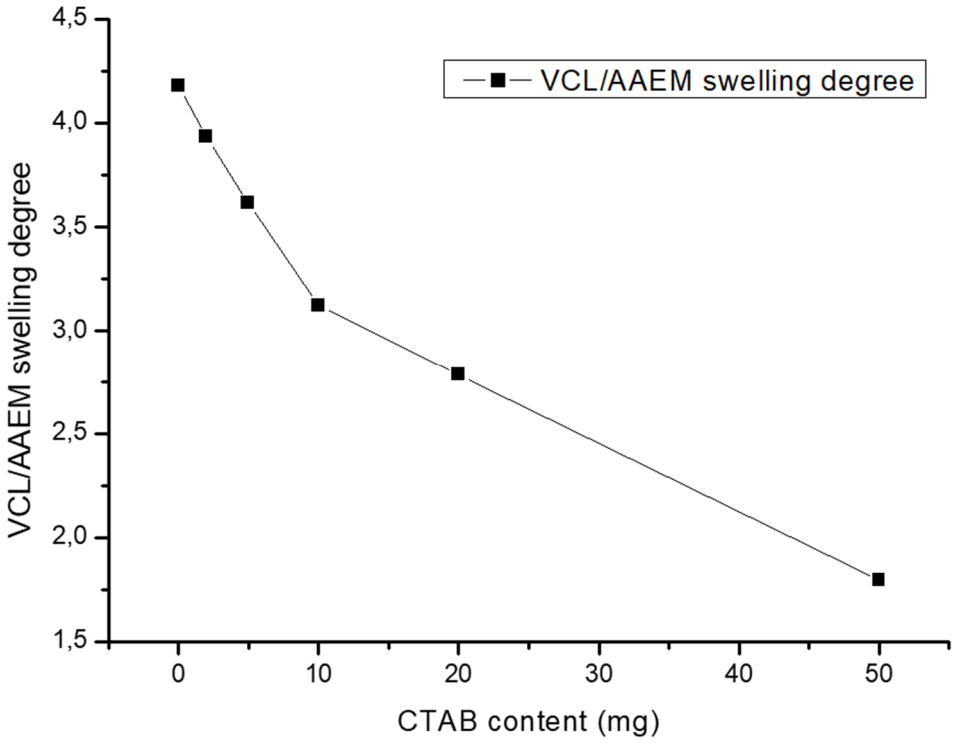

Figure 96: Swelling degree of VCL/AAEM microgels synthesized with different amounts of CTAB at 20°C. The swelling degree is calculated form hydrodynamic radii measures at 20°C and 40°C.

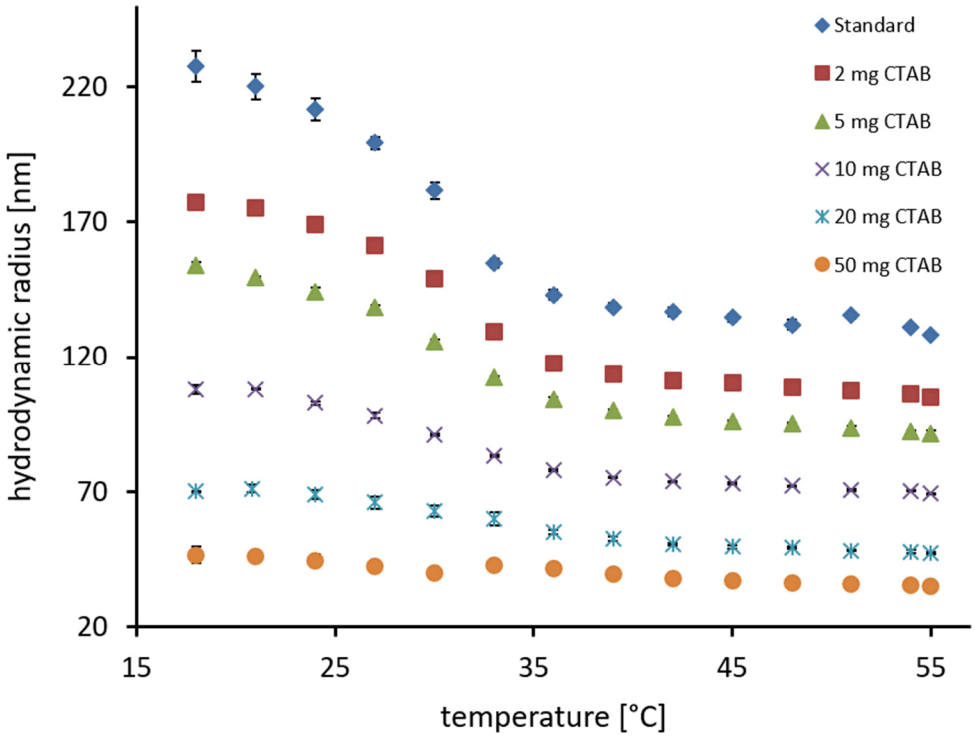

Figure 97: DLS measurements of VCL/AAEM microgels with different amounts of CTAB.

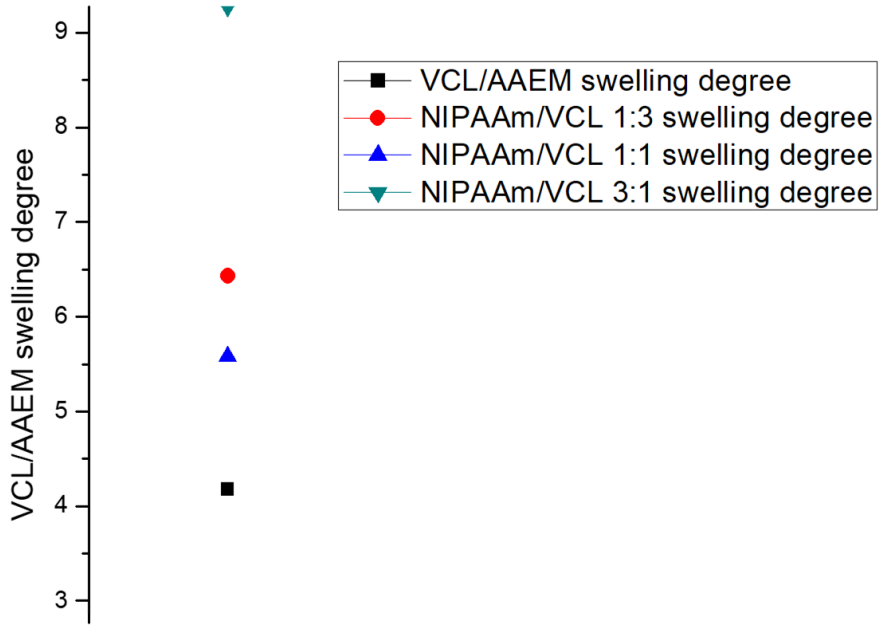

Figure 98: Swelling degree of VCL/AAEM, NIPAAm/VCL 1:1, NIPAAm/VCL 3:1 and NIPAAm/VCL 1:3 microgels at 20°C. The swelling degree is calculated form hydrodynamic radii measured at 20°C and 40°C.

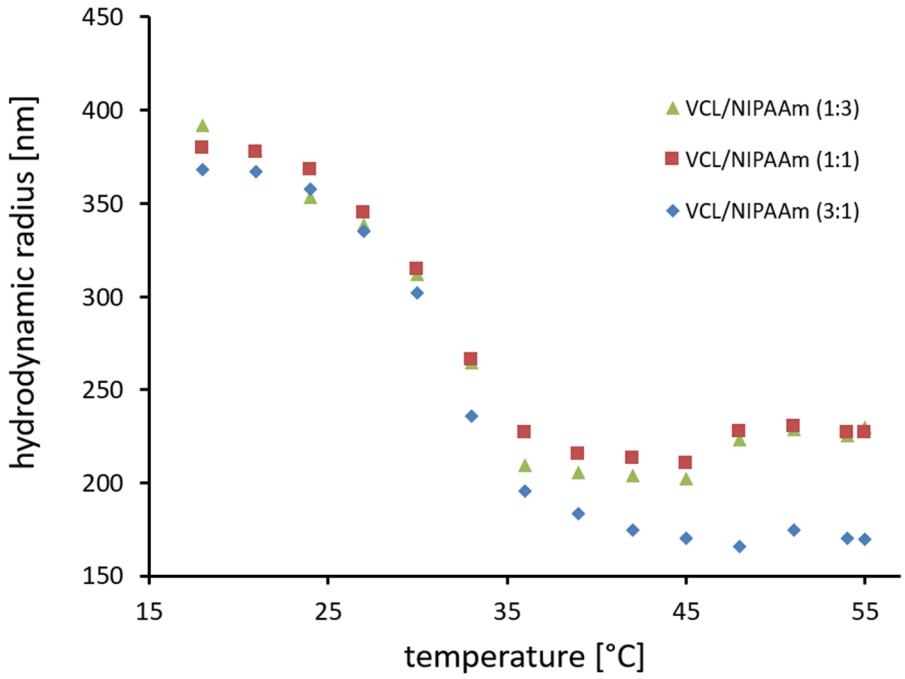

Figure 99: DLS measurements of NIPAAm/VCL 1:1, NIPAAm/VCL 3:1 and microgels.

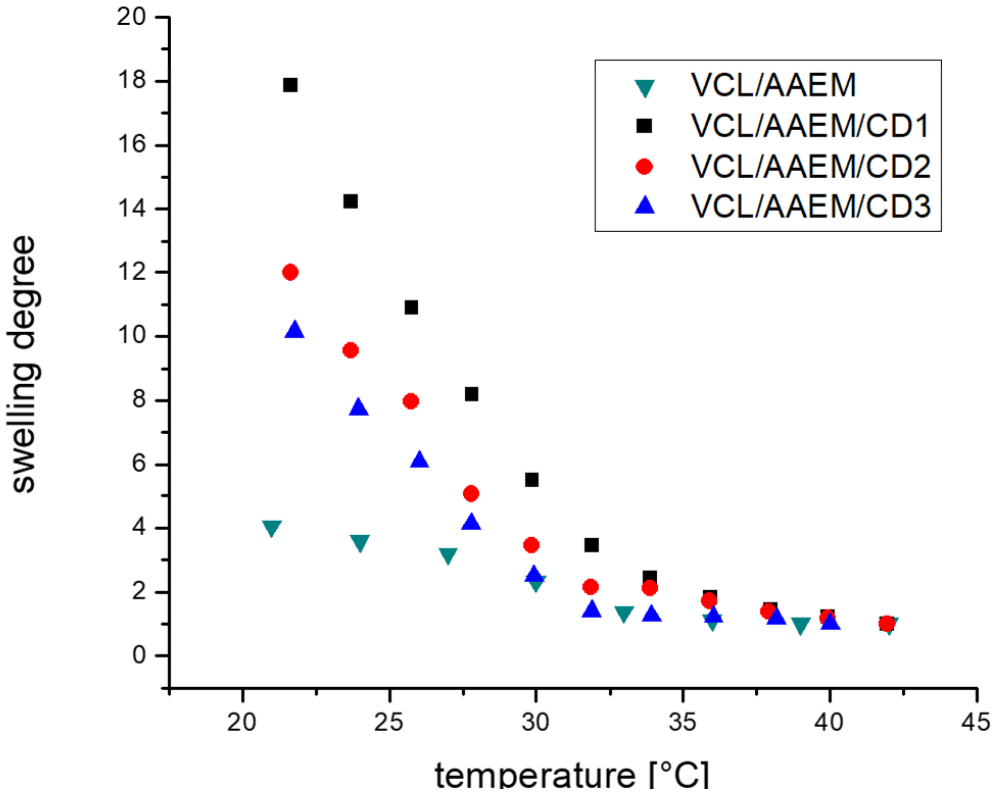

Figure 100: Swelling degree of VCL/AAEM/CD 1-3 microgels calculated for different temperatures. The swelling degree is calculated form hydrodynamic radii measured at 20°C and 40°C of the corresponding microgels.

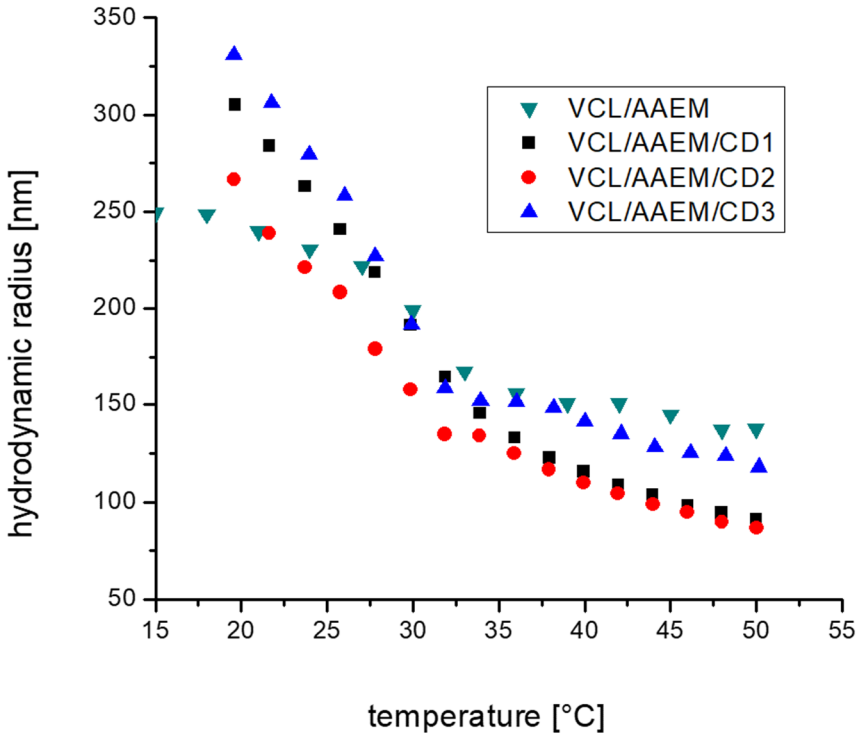

Figure 101: Hydrodynamic radii of VCL/AAEM/CD1-3 measured at different temperatures compared to contraction behavior of standard VCL/AAEM microgels.

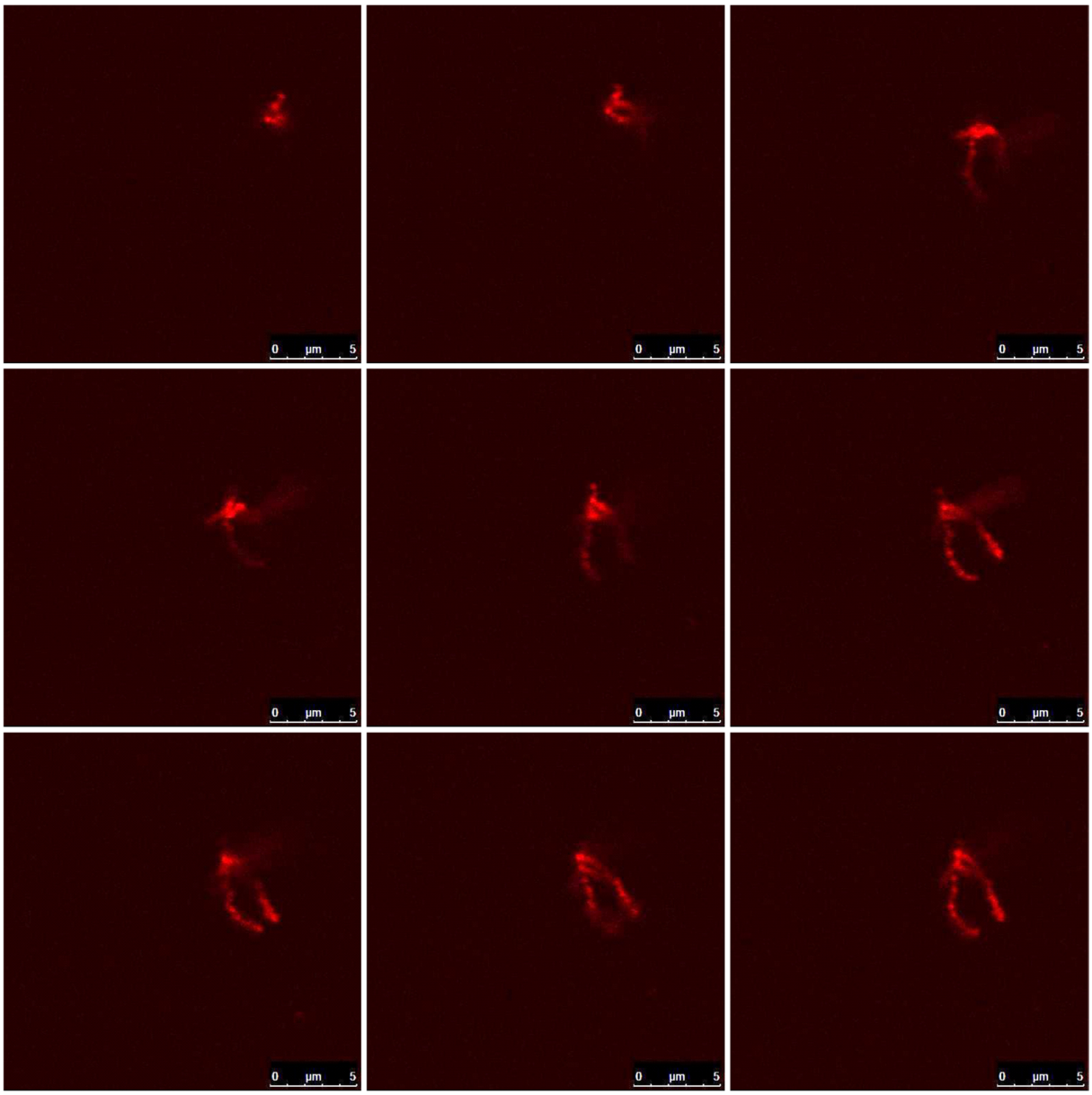

Figure 102: Another example of collective moving VCL/AAEM microgel strands (with adsorbed rhodamine B) observed by confocal microscopy.

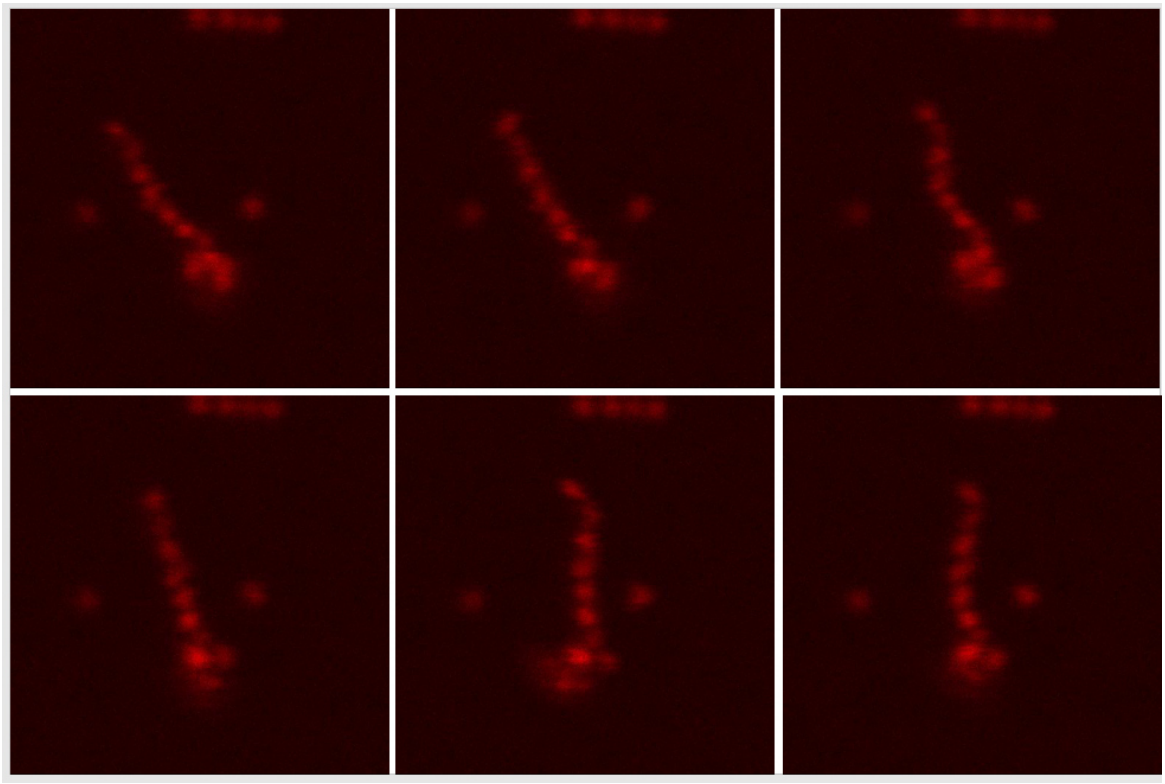

Figure 103: Images from a video taken of another moving microgel strad which was semi attached to the cover slip at a fixed spot.

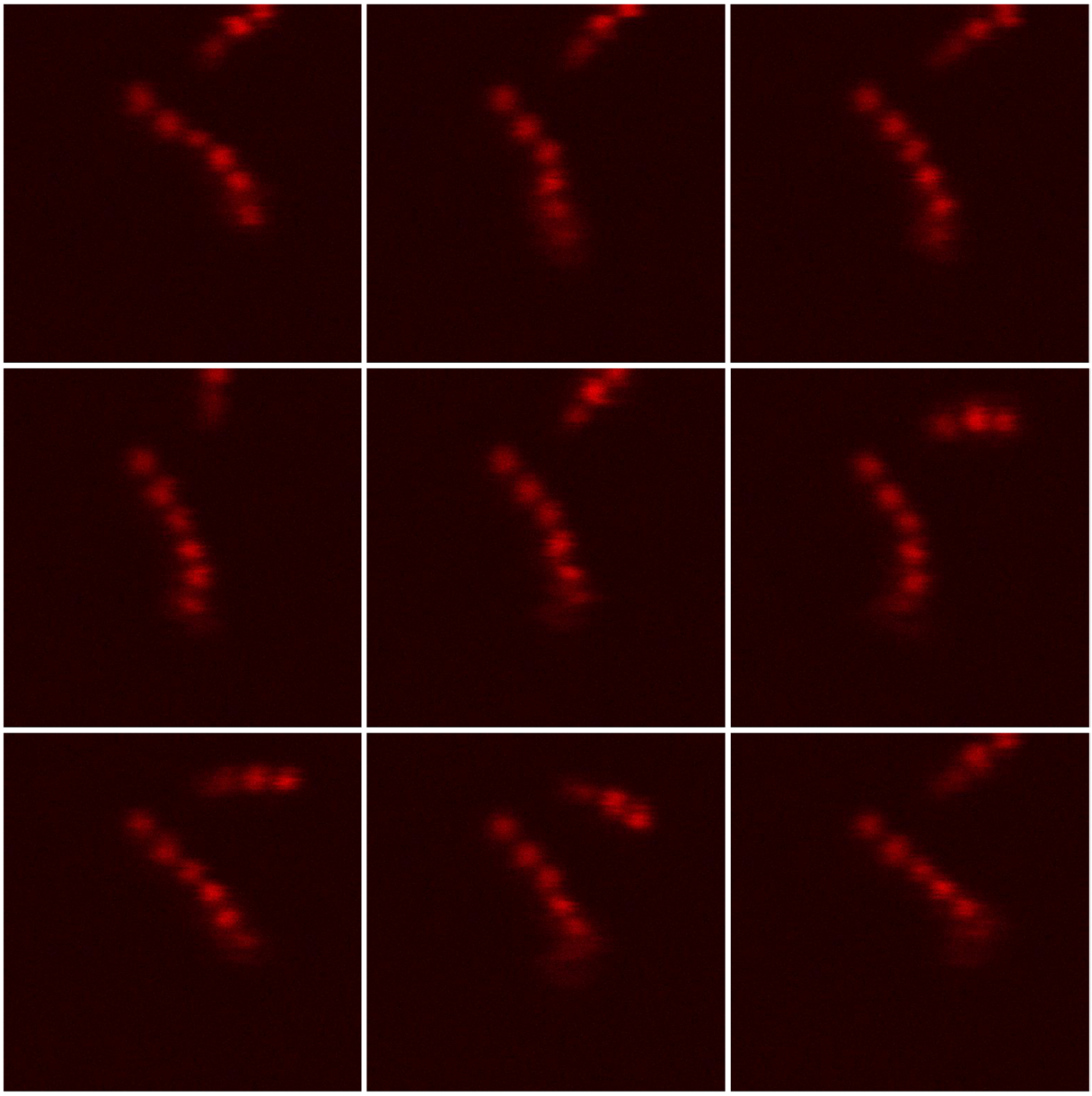

Figure 104: Detailed images from a video taken of moving microgel loop which was semi attached to the cover slip at a fixed spot.

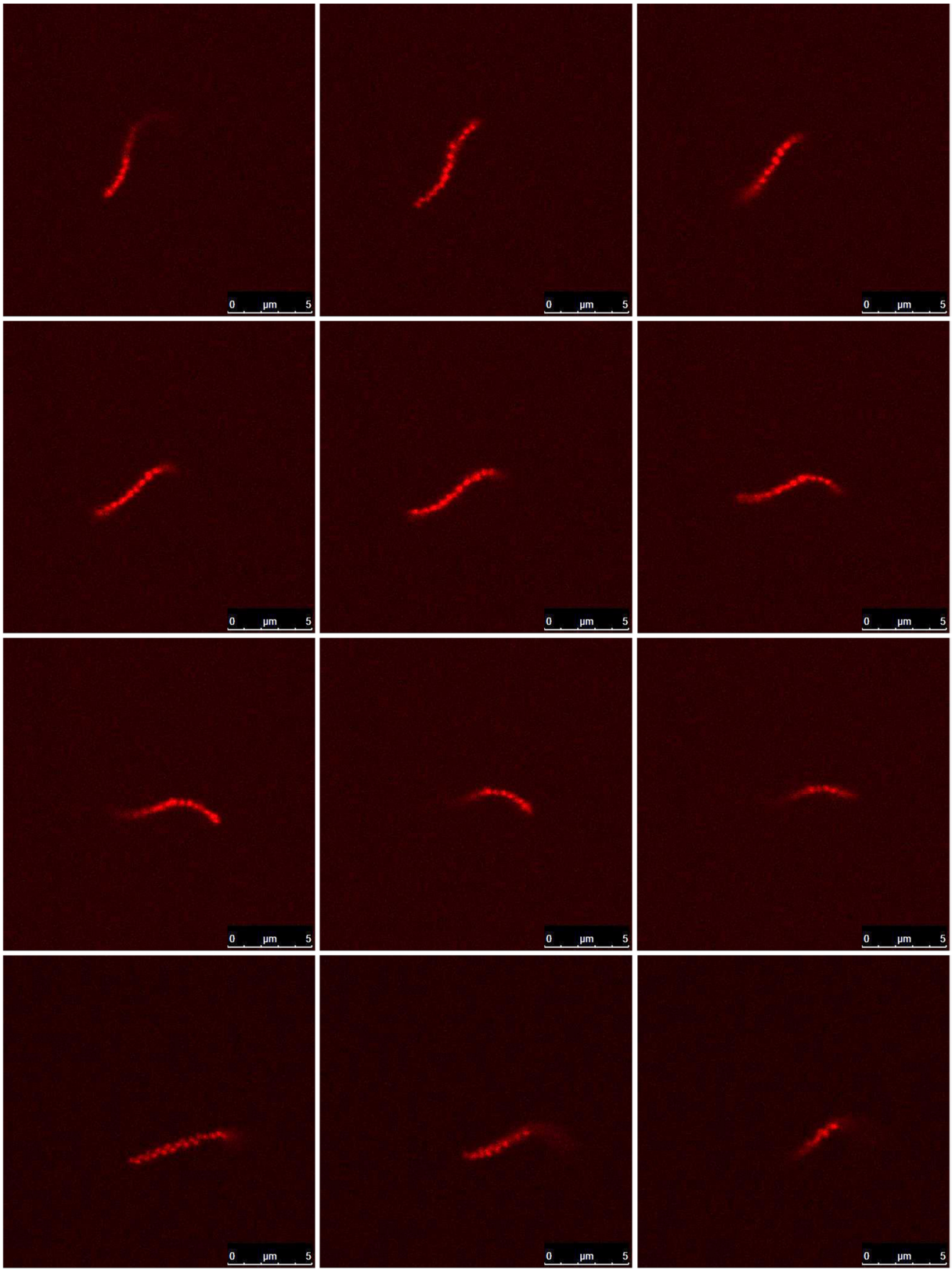

Figure 105: Detailed images of a free moving VCL/AAEM microgel strand (with adsorbed rhodamine B) observed by confocal microscopy.

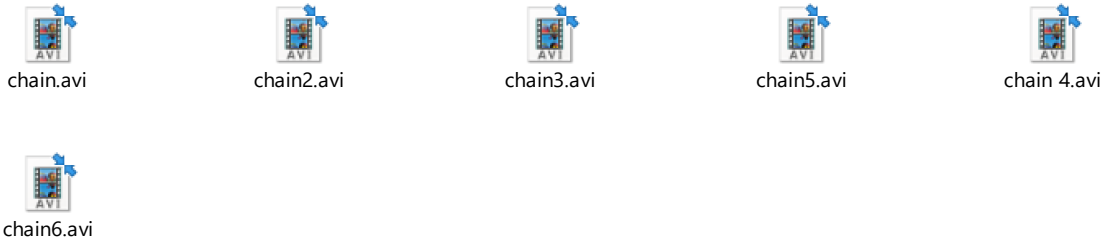

Figure 106: Videos of strands which will be attached to this doctoral thesis.

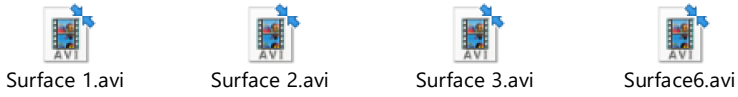

Figure 107: Videos of strands semi attached to the surface which will be attached to this doctoral thesis.

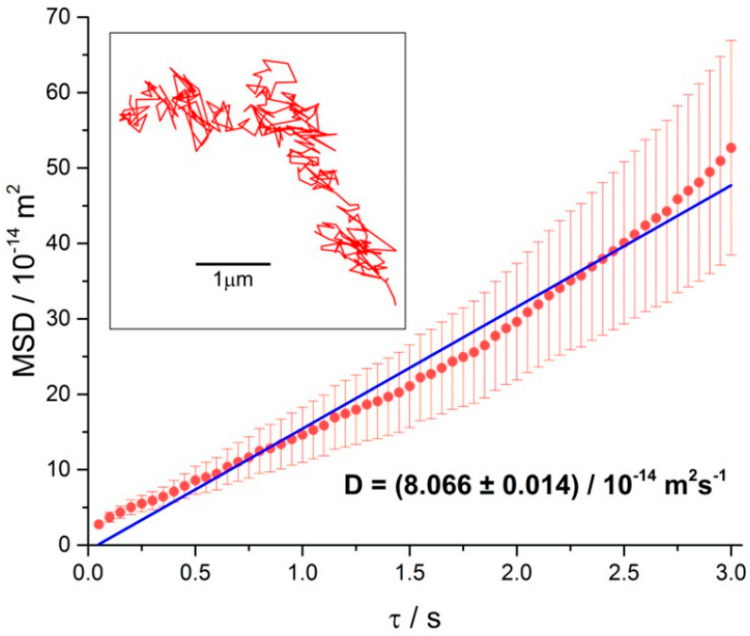

Figure 108: Temporal evolution of the mean square displacement for the center-of-mass of microgel chain b. Inset: single track of the center-of-mass of the same microgel chain.[141]

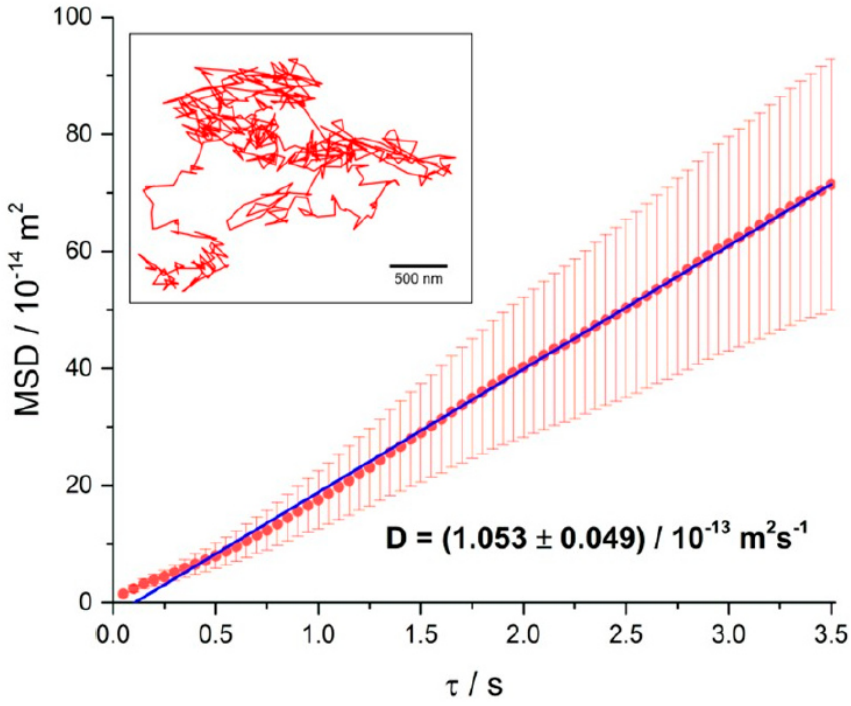

Figure 109: Temporal evolution of the mean square displacement for the center-of-mass of microgel chain c. Inset: single track of the center-of-mass of the same microgel chain.[141]